UNIVERSITÀ DEGLI STUDI DI PARMA

Dottorato di ricerca in Scienze Chimiche

Ciclo XXIX (2014-2016)

CHELATING LIGANDS: NEW APPROACHES IN BIOINORGANIC CHEMISTRY

Coordinatore:

Chiar.mo Prof. Roberto Cammi

Tutor:

Chiar.mo Prof. Mauro Carcelli

Dottoranda: Anna Gatti

“So many people along the way, whatever it is you aspire to do, will tell you it can’t be done. But all it takes is imagination. You dream. You plan. You reach. There will be obstacles. There will doubters. There will be mistakes. But with hard work, with belief, with confidence and trust in yourself and those around you, there are no limits.”

Michael Phelps

SUMMARY

1 *HYDRAZONES COMPOUNDS AS POTENTIAL ANTIVIRAL AGENTS*

ABBREVIATIONS

2'-FdG 2'-Deoxy-2'-fluoroguanosine

ATR Attenuated Total Reflectance

CC_{50} 50% Cytotoxic Concentration

cRNA Complementary Ribonucleic Acid

DEP Direct Exposure Probe

DKA Diketoacid

DMEM Dulbecco's Modified Eagle Medium

EC_{50} Half maximum effective concentration

EC_{90} Compound concentration causing a 1-$\log_{10}$ reduction in virus yield at 24 h p.i.

EC_{99} Compound concentration causing a 2-$\log_{10}$ reduction in virus yield at 24 h p.i.

EDTA Ethylenediaminetetraacetic acid

EGCG Epigallocatechin-3-gallate

ER Endoplasmic Reticulum

ESI-MS Electron Spray Ionization Mass Spectrometry

FSC Fetal Bovine Serum

FT Fourier Transform

HA Haemagglutinin

HEK293T Human Embryonic Kidney 293T

IC_{50} Compound concentration to obtain 50% inhibition of cleavage

IPTG Isopropyl-β-thiogalactopyranoside

IR Infrared Spectroscopy

LB Luria-Bertani

M1 Matrix protein 1

M2 Matrix protein 2

MDCK Madin-Darby Canine Kidney

mRNA Messenger Ribonucleic acid

MTS 3-(4,5-dimethylthiazol-2-yl)-5-(3-carboxymethoxyphenyl)-2-(4-sulfophenyl)-2H-tetrazolium

NA Neuraminidase

NAI Neuraminidase Inhibitor

ND Not Determined

NEP Nuclear Export Protein

NMR Nuclear Magnetic Resonance

NP Nucleoprotein

NS Non-structural protein

PA Acidic Protein

PA_C C-terminal acidic protein

PA_N N-terminal acidic protein

PB1 Basic Protein 1

PB2 Basic Protein 2

qRT-PCR Quantitative Real-Time Reverse Transcription Polymerase Chain Reaction

RdPR RNA-dependent RNA polymerase

RNP Ribonucleoprotein

SAR Structure-Activity Relationship

SERCAT Southeast Regional Collaborative Access Team

TCEP *tris*(2-carboxyethyl)phosphine

TPCK Tosylphenylalanylchloromethylketon

vRNA Viral Ribonucleic Acid

vRNP Viral Nucleoprotein

1.1 INTRODUCTION

1.1.1 General introduction

Influenza A, B and C virus are enveloped viruses with a segmented negative-oriented single-stranded RNA genome, belonging to the *Orthomyxoviridae*[1]. The classification of the virus type is based on the antigenic specificity of the nucleoprotein (NP) antigen (type A, B or C)[2]. The clinical epidemiological aspects of influenza C infections remain poorly characterise and rely mainly on a few studies in paediatric population[3]. Seasonal influenza A and B viruses, instead, affect each year approximately 5-10% of the adult and 20-30% of the paediatric population[4] causing significant morbidity and mortality, particularly in infants, elderly people, pregnant woman and those suffering from immunodeficiency or chronic diseases. In addition, there is a permanent risk of sudden influenza pandemics such as the notorious 'Spanish flu' in 1918, the most deadly pandemic in the history of mankind[5], and the swine-origin H1N1 pandemic in 2009[6]. Two classes of anti-influenza virus drugs are currently available, but they have limited clinical utility due to their central nervous system side effects and widespread resistance. Therefore, there is an urgent need for new antiviral drugs with an entirely different mode of action.

The influenza virions form spherical capsules with a diameter of approximately 100 nm (Fig. 1.1)[7].

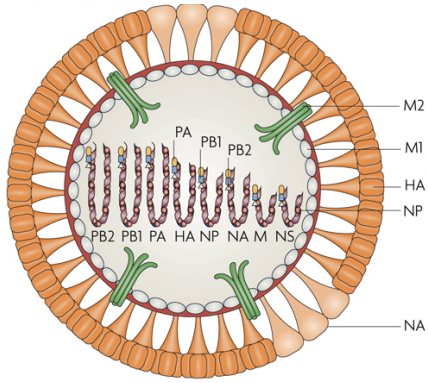

Fig. 1.1 Structure of Influenza virus particle. The influenza A virus particle has a lipid envelope derived from the host cell membrane. Three envelope proteins –haemagglutinin (HA), neuraminidase (NA) and an ion channel protein (matrix protein 2, M2) – are embedded in the lipid bilayer of the viral envelope. [Taken from Karlsson Hedestam at al.[8]]

The viral envelope is made up of a lipid bilayer membrane that contains three of the viral transmembrane proteins: hemagglutinin (HA), neuraminidase (NA), and matrix protein 2 (M2). HA is the most abundant envelope protein and is responsible for binding of the virus to sialic acid residues on the host cell surface, and for fusion of the viral envelope with the endosomal membrane during virus uncoating. NA glycoprotein cleaves sialic acid receptors from the cell membrane and thereby releases new virions from the cell surface; NA proteins are essential for the release of progeny virons. M2 is a proton channel, a multifunctional protein that functions as a pH-activated ion channel: it enables acidification of the interior of the virion, leading to uncoating of the virion itself [9, 10]. Sitting just underneath the viral lipid membrane is matrix protein 1 (M1), which mediates the encapsidation of the viral genome in the viral particle by bridging the interaction between the membrane and the genomic material[11]. The influenza virus genome is segmented in eight vRNA strands, which occurs in the viron in the form of ribonucleoprotein complexes (vRNPs) (Fig. 1.2). Each

vRNP consists of one negative-oriented RNA segment, coated by multiple copies of the nucleoprotein (NP) and bound to the polymerase proteins (PB1, PB2 and PA) involved in the replication process[12, 13, 14].

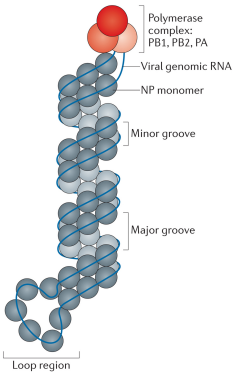

Fig. 1.2 Structure of vRNPs. Each influenza viral ribonucleoprotein (vRNP) consists of one single-stranded, negative-sense genomic RNA associated with multiple nucleoprotein (NP) monomers and a single trimeric polymerase complex (composed of PB1, PB2 and PA). The 5′ and 3′ vRNA ends are complementary and base pair to form a double-stranded structure, which is bound by the polymerase complex at one end of the vRNP filament. The internal vRNA region is organized into an antiparallel double helix, the formation of which is driven by contacts between NP monomers (known as the 'minor' groove) and a loop can be observed at the end of the filament, opposite to that bound by the polymerase complex. [Taken from Elsfeld et al.[15]]

The three largest RNA segments encoded the three viral RNA-dependent RNA polymerase (RdRP) proteins: polymerase acidic protein (PA), polymerase basic protein 1 (PB1) and polymerase basic protein 2 (PB2). The three intermediate size RNAs encoded HA, NA end nucleoprotein. The larger of the remaining two segments encodes the M1 matrix protein and the M2 ion-channel protein, the smaller segment encodes the two non-structural proteins NS1 and NS2/NEP[16].

1.1.2 Influenza virus life cycle

The influenza virus life cycle (Fig. 1.3) can be divided into the following stages:

(i) entry into the host cell;

(ii) entry of the vRNPs into the nucleus;

(iii) transcription and replication of the viral genome;

(iv) export of the vRNPs from the nucleus;

(v) assembly and budding at the host cell plasma membrane.

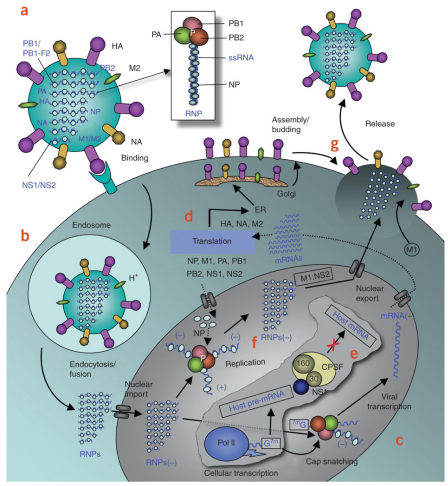

Fig. 1.3 The Influenza virus replication cycle. (a) The viral surface glycoprotein HA binds the host cell-surface sialic acid receptors and the virus is transported into the cell in endocytic vesicles. (b) The low pH causes the release of vRNPs in the cytoplasm. (c) Once transported in the nucleus, the viral polymerase initiates viral mRNA synthesis through the 'cap snatching' process. (d) Viral mRNAs are transported to the cytoplasm for translation into viral proteins. (e) The NS1 protein of influenza A virus serves a critical role in suppressing the production of host mRNAs. (f) The viral polymerase is responsible for RNA synthesis. The resulting vRNPs are subsequently transported to the cytoplasm. (g) The vRNPs reach the cell membrane to be incorporated into new viruses that are budded out. [Taken from Das et al.[17]]

The influenza virus particle adheres to the target cell with its HA, which recognises the terminal sialic acid of glycoproteins or glycolipids coated at the host cell surface (step a). Upon binding to the host cell sialic acid residues, receptor-mediated endocytosis occurs and the virus enters the host cell in an endosome: this is the process by which the new genetic materials enter in the cells. Acidification of the vesicle (pH around 5), thanks to the protein M2, leads to fusion of the viral and endosomal membranes. The low pH also activates the M2 ion channel, and leads to the release of the viral RNA and core proteins (vRNP) into the cytoplasm of the cell (step b)[18]. After being released into the cytoplasm, the vRNP must enter the nucleus[19]. Once in the nucleus, the primary roles of vRNPs are to transcribe viral mRNAs for the production of viral proteins and to replicate full-length complementary genomic RNA (cRNA) for amplification of vRNA and generation of progeny vRNPs. After nuclear import, influenza vRNPs are transcribed to produce viral mRNAs (this is known as primary transcription) in a process that is independent of *de novo* viral protein synthesis[20]. Primary transcription is primer-dependent and the primers, which are used for this purpose, are obtained by the viral polymerase complex via 'cap-snatching' of cellular mRNAs[21, 22, 23].

The PB2 subunit binds the 5'-7-methylguanosine cap of a cellular pre-mRNA, which is cleaved 10–15 nucleotides downstream by the PA endonuclease catalytic site. The obtained RNA primer is used to initiate the polymerization by the PB1 subunit, which uses the vRNA as a template. In this way, chimeric mRNA molecules are synthesised and subsequently transported into the cytoplasm to be translated into viral proteins (Fig. 1.4). Once the new polymerase proteins are created, they are transported back to the nucleus, where other transcription and replication cycles take place.

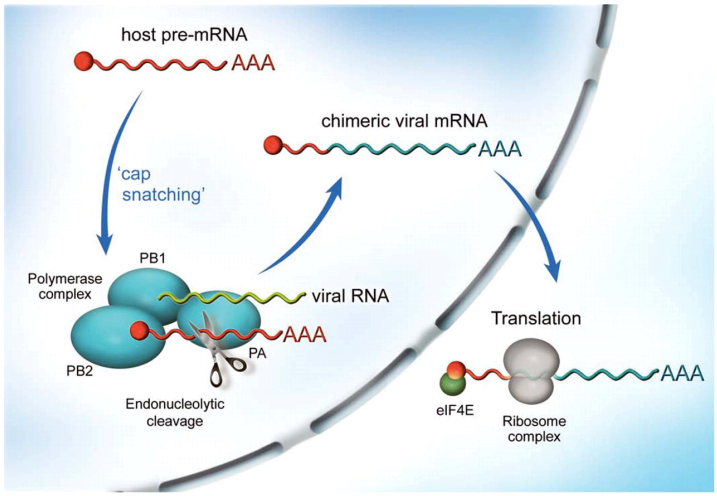

Fig. 1.4 Cap-snatching transcription mechanism of influenza polymerase. Within the nucleus of the infected cell, the PB2 subunit binds the 5',7-methylguanosine cap of a host pre-mRNA molecule (red). The PA endonuclease subunit cuts the host DNA 10–15 nucleotides downstream, obtaining a short-capped RNA primer. This primer is used to initiate polymerization by the RNA-dependent RNA polymerase of the PB1 subunit, that uses a 5'- and 3'-bound vRNA (green) as template. In this way, capped, polyadenylated, chimeric mRNA molecules (red and light blue) are obtained, that are exported to the cytoplasm for translation into viral proteins.

The surface proteins HA, M2 and NA are processed in the endoplasmic reticulum (ER), glycosylated in the Golgi apparatus and transported to the cell membrane (step d). The NS1 protein of influenza A virus serves a critical role in suppressing the production of host mRNAs by inhibiting the 3′-end processing of host pre-mRNAs[24, 25]. The protein components of the vRNP complex are subsequently imported into the nucleus, where progeny vRNP complexes are assembled (step e)[26, 27]. Replication of vRNPs proceeds via complementary RNP (cRNP) intermediates (made up of complementary RNA, a single polymerase heterotrimer and a multiple NPs), which act as a template

for RNA synthesis. Replication of cRNA into vRNA requires an additional polymerase unit: since vRNA and cRNA do not carry a 5'cap, their production requires a different initiation mechanism than that used for mRNA synthesis. Replication is initiated *de novo* in a primer-independent manner. In the next replication rounds the pppApG dinucleotide, produced on the resultant cRNA, is used as primer (step f)[28]. During replication, the nascent replicates are immediately packaged into new vRNPs. These newly synthesised vRNP complexes are then exported from the nucleus to the cytoplasm. Together with host-cell phospholipids and the viral membrane proteins HA, NA and M2, the new virus is packed from the host cell membrane and released from the cell surface by the enzyme Neuraminidase (NA) (step g).

1.1.3 Prevention and treatments of influenza virus infection

Vaccination is widely considered as the most effective way to prevent morbidity and mortality caused by severe influenza virus infections. However, the influenza virus polymerase lacks proofreading activity, resulting in a continuous appearance of mutation in the influenza RNA genome. This is the reason why existing influenza vaccines require annual updating and are only partially protective in some target population such as the elderly and immunocompromised[29] as well as pregnant women[30]. The currently used seasonal influenza vaccines have a trivalent composition necessary to contain the circulating A/H1N1, A/H3N2 and B strains but they failed to provide a broadly protective and long lasting immunity. Vaccine strain selection is based on surveillance and prediction: minor mismatch between vaccine strains and circulating viruses result in a sharp drop of efficacy[31]. Additionally, current vaccines do not provide protection against zoonotic influenza viruses that may cause devastating pandemics. A universal influenza vaccine that confers broad-spectrum and long-term protection remains the "Holy Grail" in influenza research.

Whereas vaccination is the most effective way to prevent influenza virus infections, antiviral drugs are required for prophylaxis and therapy. These agents are crucial in the first period of a pandemic, when large-scale production of the new vaccine is lagging behind. Current antivirals are classified according to their molecular target (Table 1.1):

(i) M2 ion channel blockers;

(ii) NA inhibitors;

(iii) RNA polymerase or endonuclease inhibitors.

1.1.3.1 M2 ion channel blockers

The M2 protein is a multifunctional protein with roles in the virus entry, assembly and budding. The M2 function, as a homotetramer, is to form a proton-selective ion channel in the centre of four helices[32]. This pH activated proton channel is responsible for the acidification of the interior of viral particles, which is necessary for unpacking of the viral genome[33, 34]. A second function of M2 is to prevent premature conformational rearrangement of newly synthesised hemagglutinin molecules in the trans-Golgi network, by equilibrating the pH with that of the host cytoplasm[35]. The adamantanes amantadine and rimantadine (Fig. 1.5) are able to block the M2 channel of influenza A virus.

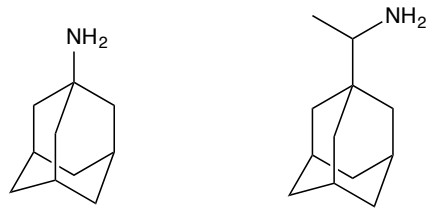

Amantadine Rimantadine

Fig. 1.5 Chemical structure of M2 ion blocker Amantadine and Rimantadine.

They bind in a pocket within the M2 proton channel, thereby physically occluding the pore[36, 37]. The M2 inhibitors have limited clinical utility due to widespread resistance, as in the case of the 2009 pandemic H1N1 virus[38, 39, 40] caused by a mutation in the transmembrane domain of the M2 protein[41, 42].

1.1.3.2 Neuraminidase inhibitors

The influenza virus neuraminidase is a mushroom-shaped homotetrameric glycoprotein with a stalk domain anchored to the viral membrane and a globular

head that contains the catalytic site. This enzyme cleaves off the terminal sialic acid moiety from surface glycans on the host cell membrane and progeny virions, preventing their aggregation and facilitating virus release from infected cells[43]. NA cleavage of sialylated mucins also plays a role in virus penetration through the mucus layer during initial infection[44, 45]. Additionally, NA has been implicated in the enhancement of HA-mediated cell-cell fusion and virus entry[46]. Neuraminidase inhibitors (Fig. 1.6) mimic the natural substrate of the NA enzyme, blocking NA cleavage activity.

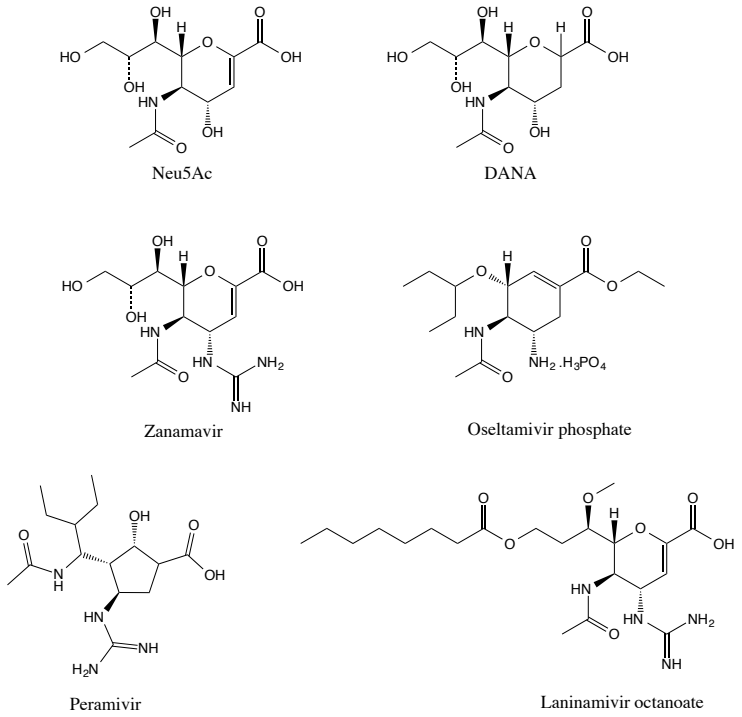

Fig. 1.6 Chemical structures of neuraminidase inhibitors.

Zanamavir was the first globally licensed NAI[47] but has the limitation of requiring administration by powder inhalation due to its poor oral bioavailability. Oseltamivir, orally administrable**,** was subsequently

discovered[48, 49]. However, resistance rapidly appeared due to inter-individual transmission of resistant viruses carrying a mutant form of NA.

Peramivir and Laninamivir are the two newer NAIs which have proceeded to clinical trials[50, 51]. Peramivir shares structural features with both oseltamivir and zanamivir; hence, mutations in NA that affect the activity of oseltamivir and zanamivir can also reduce peramivir activity[52].

1.1.3.3 RNA polymerase inhibitors

The influenza polymerase (Fig. 1.7) is a 250 kDa-dependent RNA polymerase involved in the synthesis of the viral RNA. Structurally, the enzyme is a heterotrimer, composed of three subunits: two basic proteins PB1 and PB2 and the acidic protein PA[53, 54]. The PA subunit performs the 'cap-snatching' endonuclease reaction in which cellular capped RNAs are cleaved to yield capped primers for vRNA transcription to mRNA. The PB2 subunit is responsible for initial binding of the capped RNAs, while the actual RNA synthesis is performed by the PB1 protein.

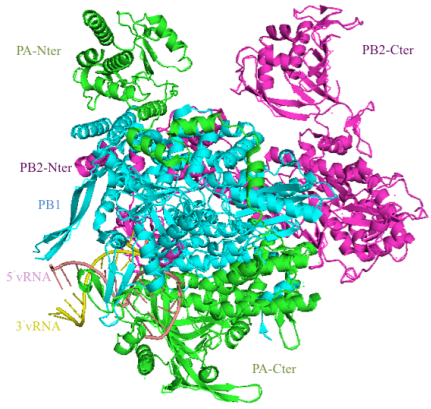

Fig. 1.7 The three different subunits of polymerase. PA, PB1 and PB2 are depicted in green, light blue and pink respectively. The vRNA promoter is shown in pale pink (5'end) and in yellow (3'end) [PDB entry 4WSB[53]].

Crystallographic studies have showed that PB1 works as the central structural component of the polymerase, with no direct interactions with PA and PB2[54, 55]. High-resolution structural studies have confirmed a direct interaction between the PA and PB1 subunits as well as between PB1 and PB2[55, 56]. The PB1 subunit contains the conserved motifs, characteristic of RNA-dependent RNA polymerases, and catalyses the sequential addition of nucleotides during RNA chain elongation.

Ribavirin

The purine analogue ribavirin 1-(β-D-ribofuranosyl)-1,2,4-triazole-3-carboxiamide (see Fig. 1.8) was discovered in 1972.[57] Its mode of action is rather complex, since it appears to inhibit viral replication through a combination of different mechanisms. It was only recently demonstrated that ribavirin induces lethal mutagenesis in the influenza virus genome by acting as an ambiguous purine analogue[58]. The clinical utility of ribavirin, in the management of influenza virus infection, is limited due to its potential severe side effects and teratogenic properties[59].

2'-Deoxy-2'-fluoroguanosine

2'-Deoxy-2'-fluoroguanosine (2'-FdG) (see Fig. 1.8) is a broad *in vitro* inhibitor of influenza viruses, giving equipotent inhibition of influenza A H1N1, H2N2, H3N2 and influenza B viruses. The mechanism of action passes through the inhibition of the polymerase complex by non-obligate chain termination. This mechanism was confirmed when the polymerase, from partially resistant virus, was found to be 10-fold less susceptible to 2'-FdG-triphosphate[60].

Favipiravir

Favipiravir (see Fig. 1.8), also known as T-705, is a nucleobase mimetic that is recognized by influenza virus RNA polymerase as a purine nucleotide[61]. However, the precise mechanism of action of favipiravir remains to be fully elucidated. Favipiravir appears to cause lethal virus mutagenesis. Baranovich et al. [62] observed a reduction in virus infectivity without a corresponding decrease in the number of viral RNA copies. Jin et al. [63] proposed the "non-obligate chain termination" mechanism since it was shown that incorporation of a single molecule of favipiravir into nascent RNA strand causes inhibition of viral RNA extension. Favipiravir is currently in phase 3 clinical trial in the USA and Europe. The compound has broad *in vitro* activity against influenza A, B and C viruses[64], including the 2009 pandemic A/H1N1 virus, the highly pathogenic avian influenza H5N1[65] and H7N9[66] viruses, and virus strain with resistance to M2 blockers or neuraminidase inhibitors[67]. Next to its activity against influenza virus[68] favipiravir inhibits the replication of various other viruses, including Ebolavirus[69, 70], bunyaviruses[71], arenaviruses[72], flaviviruses[73], alphaviruses[74], picornaviruses[75] and noroviruses[55].

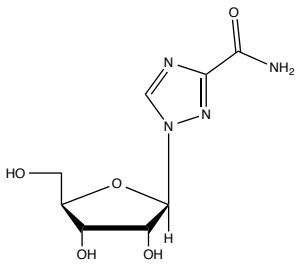

Ribavirin

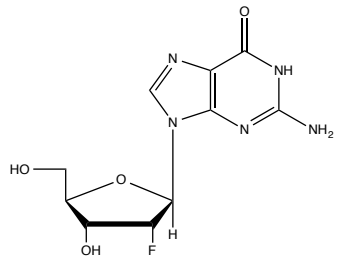

2'-FdG

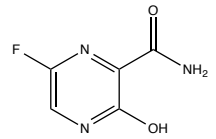

Favipiravir

Fig. 1.8 Chemical structures of the nucleobase or nucleoside analogue inhibitors Ribavirin, 2'-Deoxy-2'-fluoroguanosine and Favipiravir.

Protein-protein interaction inhibitors

The assembly of the three subunits (PB1, PB2, PA) into a functional viral polymerase complex is an essential step for influenza RNA synthesis and virus replication. Interference with its correct assembly, through inhibition of a crucial protein-protein interaction, is currently being explored as an innovative antiviral strategy. Design of small molecules, able to inhibit the formation of influenza virus polymerase complex, has been already possible based on available crystal structure[55, 56] of polymerase heterotrimer that enabled drug design of small molecules that inhibit PA-PB1 complex formation.

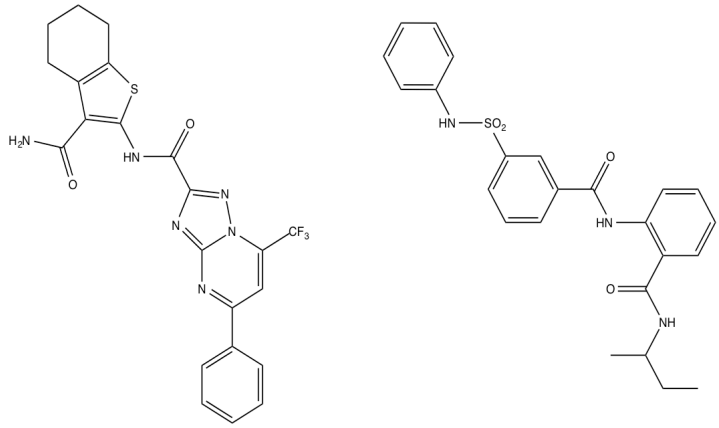

Fig. 1.9 Chemical structures of two PPI inhibitors.

The chemical structures of current lead compounds are shown in Fig. 1.9. Structural analyses of influenza A virus in the absence of PB1 revealed a number of structural changes compared to the previously reported structures for the PB1-peptide bound protein, suggesting that the PB1-binding interface may be quite plastic.

1.1.4 An attractive pharmacological target: PA endonuclease

Despite the availability of efficient antiviral, novel drugs are needed to overcome viral resistance. This problem is particularly serious since "antigenic drift" and "antigenic shift" can occur and widespread resistance to commercially available drugs has been verified for circulating influenza viruses[76, 77, 78, 79]. In this scenario, the influenza virus polymerase is widely recognized as a superior target for antiviral drug development and, in particular, inhibition of the PA endonuclease has deserved much attention in recent years. Since the host cell has no analogous activity, it should be feasible to design PA inhibitors that are non-toxic, as they do not interfere with normal host cell functions. The catalytic site of PA is highly conserved, hence inhibitors are expected to be active against all influenza virus (sub)types and oseltamivir-resistant mutants; in contrast, the neuraminidase inhibitors do not prevent the formation of new virus particles[80].

The PA subunit can be divided into the N-terminal (PA_N) and C-terminal (PA_C) domain, which are linked by a long flexible peptide. Recently, the crystallographic structure of the PA_N unit has been reported by several groups: it is a 25 kDa domain with α/β architecture. It consists of five β strands surrounded by seven α helices, forming a highly negative charged active pocket that binds divalent metal ions. It is a metal-dependent enzyme, but it is still not clear the number and type of divalent metal ions required for the endonuclease activity. The structure by Yuan et al.[81] contains a single Mg^{2+} ion coordinated by residues Glu80, Asp180 and three water molecules, which are stabilized by His41, Glu119, and the carbonyl oxygens of Leu106 and Pro107; the second plausible binding site is occupied by water molecules. Zao et al.[82] also identified only one Mg^{2+} metal coordinated by Glu80, His41, and the carbonyl oxygen of Ile38. Tefsen ad colleagues[83] described another PA-Nter *apo*

structure with one metal ion (Mn^{2+}), coordinated by one oxygen of Glu80 and Glu119 side chains, both oxygens of the Asp108 side chain and one His41 nitrogen. In contrast, Dias et al.[84] reported two Mn^{2+} ions in the active pocket. The first Mn^{2+} is equivalent to the magnesium ion in the structure by Yuan et al. and is coordinated by E80, D108 and four water molecules. On the other hand, the second Mn^{2+} is coordinated by D108 and E119, I120 and three water molecules. The discrepancy in the number of divalent ions can be explained in view of the results of the metal binding experiments by Crépin and co-workers[85]. They found that PA_N contains two divalent metal binding sites, one with a higher affinity than the other, and that the active pocket shows higher affinity for Mn^{2+} than for Mg^{2+} ions. In absence of the substrate, Mg^{2+} binds preferentially to site 2, whereas Mn is more favoured at site 1, most likely due to the presence of H41. In other words, site 1 is a low affinity site for Mg but a high affinity site for Mn, as magnesium ions have lower affinity for histidine than manganese[86, 87, 88].

The exact role of the influenza polymerase PA subunit remains unclear, although it is implicated in cap-binding, endonuclease activity, viral RNA binding and replication. The endonuclease catalytic site residues are located in the amino-terminal domain of PA. The first step, in phosphodiester hydrolysis, is activation of the water nucleophile. The lysine residue is essential for catalysis: it acts as general base by increasing the electrophilicity of the P atom and/or by lowering the PK_a of the nearby nucleophilic water by neutralizing the negative charge of the phosphodiester group. In the two Mg^{2+}-PA_N-RNA complexes, the coordinated water molecule is the attacking nucleophile that is activated by a metal ion, or a basic residue, to yield a hydroxyl ion that performs a nucleophilic attack on the phosphodiester bond. A new phosphoryl bond is formed between the nucleophile and the scissile phosphate and the 3'

leaving group is re-protonated, yielding an oligonucleotide carrying a 3'OH group. Finally, to serve as primer for viral mRNA synthesis, capped oligonucleotides are most likely further selected on the basis of their complementarity to the 3' end of the vRNA template[89, 90, 91, 92].

The first class of influenza endonuclease inhibitors belongs to the α,β-diketoacid family, discovered at Merck about two decades ago in the course of an intense drug discovery program targeting several metallo-enzymes within the superfamily of nucleases and polynucleotidyl transferase. Among this series of 4-substituted-2,4-dioxobutanoic acids, compound L-742,001 (Fig. 1.10), which contains a characteristic β-diketo acid (DKA) motif, was identified as particularly potent small molecule inhibitor of the influenza virus endonuclease reaction. Studies on this pharmacophore have revealed that a chelating moiety is required for the activity, and that the presence of lipophilic groups improves potency[93]. Other classes of reported endonuclease inhibitors include 2,4-dioxobutanoic acid derivatives[93, 94], flutimide and its derivatives[95], 2-hydroxyphenyl amide derivatives[96], as well as tetramic acids[97], 5-hydroxypyrimidin-4-one derivative[98], marchantins[99] and green tea catechins, like epigallocatechin-3-gallate (EGCG)[100, 101] (see Fig. 1.10).

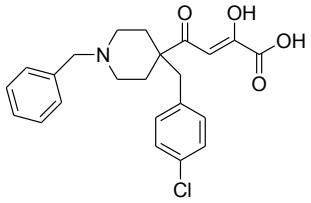

L-742,001

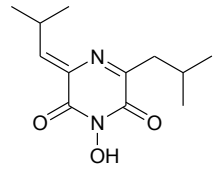

Flutimide

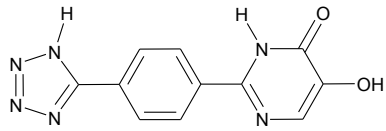

2-(4-(1H-tetrazol-5-yl)phenyl)-
5-hydroxypyrimidin-4(3H)-one

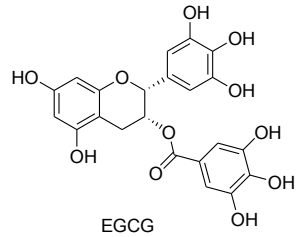

EGCG

Fig. 1.10 Chemical structures of some prototype inhibitors of influenza virus endonuclease.

These metal-chelating inhibitors of influenza virus endonuclease share a common pharmacophoric motif that is likely responsible for functional sequestration of the metal ion(s) in the active site of PA-Nter. Metal chelation has emerged as an efficient strategy to develop new inhibitors of metal-dependent viral enzymes: the most illustrious example has been the class of HIV integrase inhibitors, some of which have already been approved as drugs[102]. In this sense, the minimal pharmacophore motif is composed of two or three (nitrogen or oxygen) atoms capable of chelating the metal ion(s) in the active site of the protein[103]. In this way the activity of the protein is completely blocked.

Compound Name	Mechanism of action	Antiviral activity (EC_{50})	Resistance
M2 ion blocker			
Amantadine	Bind in a pocket of M2 proton channel	49	Mutation in transmembrane domain, side effects
Rimantadine		19	Mutation in transmembrane domain
NA Inhibitors			
Zanamivir	Mimic the substrate of NA	0.57-11 nM	Admininstration by powder
Oseltamivir		0.49-13 nM	Virus with H274Y mutant form
Peramivir		0.06-3.2	Virus with H274Y mutant form
Laninamivir		0.24-2.4 nM	None
Inhibitors targeting the PB1			
Ribavirin	Nucleoside analogue	2.5-23 µM	Side effects, teratogenic properties, PB1 and V43I mutant form
2'-FdG		2-22 µM	
T-705		0.083-3.1 µM	PB1 and V43I mutant form
PP Interaction			
PPI1	PA-PB1 interface inhibitors	11-43 µM	
PPI2		11-43 µM	
Flutaamide	Metal-chelating endonuclease inhibitors	5.9 µM	
L 742,001		0.35-11 µM	PA T20A form
2-(4-(1H-tetrazol-5-yl)phenyl)-5-hydroxypyrimidine-4(3H)-one		11 µM	

Table 1.1 General overview of published approaches to inhibit influenza virus.

1.1.5 Objective of the research: development of novel metal chelating inhibitors of PA Nter

In recent years we have focused our research on the study of new original chemical scaffolds, potentially able to inhibit the virus replication: the idea was to synthesised compounds able to occupy the active site of metal-dependent viral enzymes and to interact with their metal cofactors[94, 96, 102, 104, 105, 106, 107, 108, 109, 110]. We therefore exploited the metal-chelating abilities to highlight the important structural and electronic features to achieve effective enzymatic inhibition.

In the last 20 years, a broad spectrum of biological activities have been attributed to N-acylhydrazones including analgesic, anti-inflammatory, anti-tumoral, anti-(myco)bacterial, antiparasitic and antiviral activity[111]. A number of N-acylhydrazones (Fig. 1.11) have been demonstrated to display potent anti-HIV activity with a mechanism of action that involves the inhibition of the RNA-dependent DNA polymerase, the inhibition of the RNase H activity of HIV-1 reverse transcriptase and the binding to the HIV-1 capside protein[112, 113].

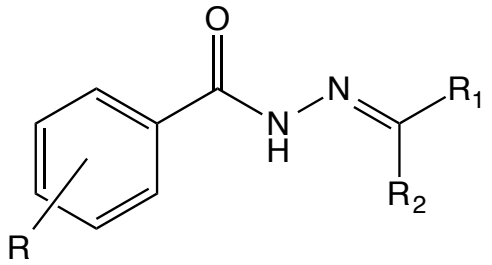

Fig. 1.11 Chemical structure of a general N-acylhydrazone.

In the present work the syntheses of a series of N-acylhydrazones differently substituted, both on the aromatic ring and on the R_1 and R_2 terminal moieties, are firstly reported. The general idea was to rationalise the influence that

different substituents plays on the chelating abilities and on the inhibitory activity of these compounds. The biological profile of these compounds was determined in an enzymatic assay with PA-Nter endonuclease as well as in cell-based influenza vRNP reconstitution and virus yield assays. Structure-activity relationship (SAR) was investigated and rationalised, considering the metal chelation as mechanism of action. Computational docking studies were set for two candidate ligands in the PA-Nter active site: they revealed the key features that determine inhibition of endonuclease activity by these N-acylhydrazones as well as the versatility of their scaffold. Furthermore these hypotheses were confirmed by the X-ray crystal structure of the protein co-crystallized with one of the synthesised ligands.

Finally, we further investigated the coordination versatility of a model N-acylhydrazone ligand towards manganese(II), nickel(II), cobalt(II), copper(II) and zinc(II): the corresponding coordination compounds were fully characterised and their biological activity was investigated in a broad-spectrum antiviral screening.

1.2 RESULTS AND DISCUSSION

1.2.1 N-acylhydrazonic inhibitors of influenza virus PA endonuclease

The influenza PA endonuclease active site can be targeted by compounds with metal-chelating scaffolds, potentially able to efficiently bind metal cofactors in the catalytic site: in this sense, metal coordination can be used as a strategy to block the activity of PA endonuclease and the influenza virus proliferation.

The attention was focused on a panel of differently substituted N-acylhydrazones reported in Fig. 1.12.

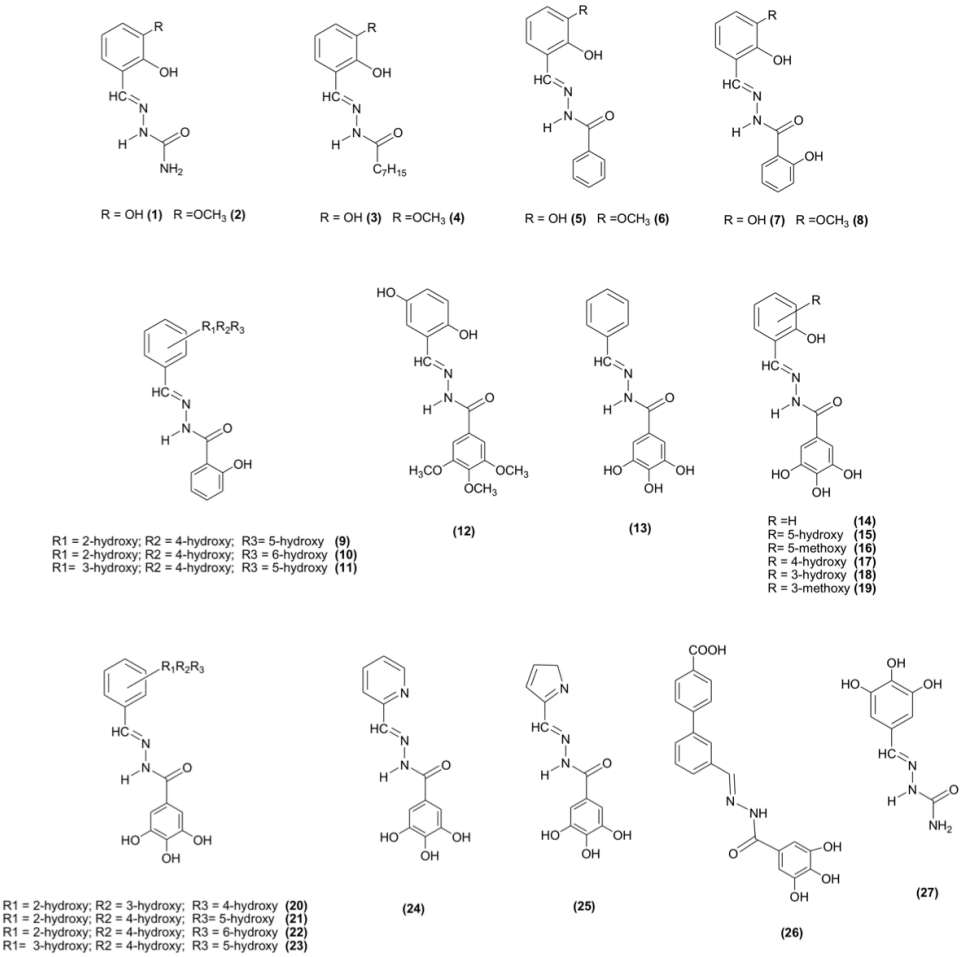

Fig. 1.12 Chemical structures of the synthesised ligands.

When R1 (Fig. 1.13) is a 2-hydroxy substituted phenyl ring, the corresponding N-acylhydrazone can coordinate one or, depending on denticity, two metal centres (modes A and B in Fig. 1.13). Therefore, 2-hydroxy substituted N-acylhydrazones seem interesting for the development of novel chelating inhibitors towards the PA endonuclease.

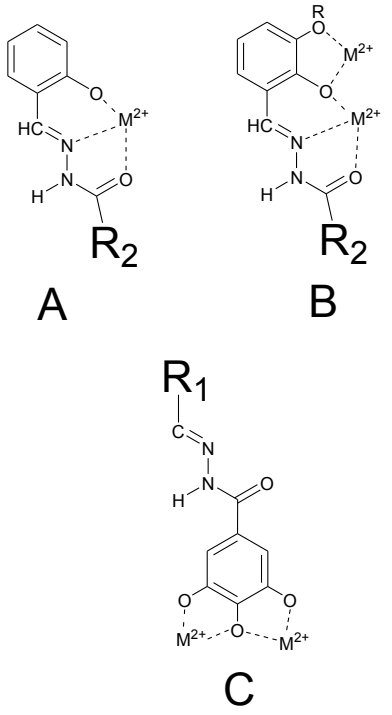

Fig. 1.13 Scheme of possible binding modes of the studied N-acylhydrazones.

Starting from N'-(2,3-dihydroxybenzylidene)-semicarbazide (**1**) and its methoxy-analogue (**2**), we modified the acylhydrazonic substituent R2 by introducing heptyl (**3** and **4**), phenyl **(5** and **6**), 2-hydroxyphenyl (**7** and **8**) and 3,4,5-trihydroxyphenyl moieties (**18** and **19**), in order to modulate the lipophilicity and hydrogen-bonding capabilities of the compounds. Of particular interest are **18** and **19,** where the gallic moiety can be involved in the chelation of the metal cofactors (mode C in Fig. 1.11). In order to investigate the role of hydroxyl substituents, and to confirm the importance of the gallic moiety, compounds **9-11**, **13-17**, **20-23** and **27,** which all carry a 3,4,5-trihydroxy moiety, were synthesised, as well as compound **12**. Furthermore, a nitrogen donor atom was introduced in R1 as a 2-pyridyl (**24**) and a 2-pyrrolidyl (**25**)

ring. Compound **26** was reported in a study on new inhibitors of HIV RNase H, another enzyme with two magnesium ions in its active site[112].

N-acylhydrazones **1-27** (Fig. 1.12) were prepared in high yields by condensation reaction between the hydrazide and the proper aldehyde (see experimental section). All compounds were completely characterised with the common spectroscopic and spectrometric analyses such as IR, ^{1}H-NMR, EI-MS and elemental analysis. The most important feature that influences the inhibitory activity seems to be the position and the number of hydroxyl groups in both R_1 and R_2: differences in the biological activity can be related to different possible mechanisms of action. On one hand, the hydroxyl groups can interact with the aminoacidic residues of the PA protein through hydrogen bonds; otherwise, the hydroxyl groups can interact with a second metal ion in the active site of the protein.

Structure-activity relationship is described in the “biological studies” section.

1.2.2 N-acylhydrazonic ligands

1.2.2.1 Chemistry

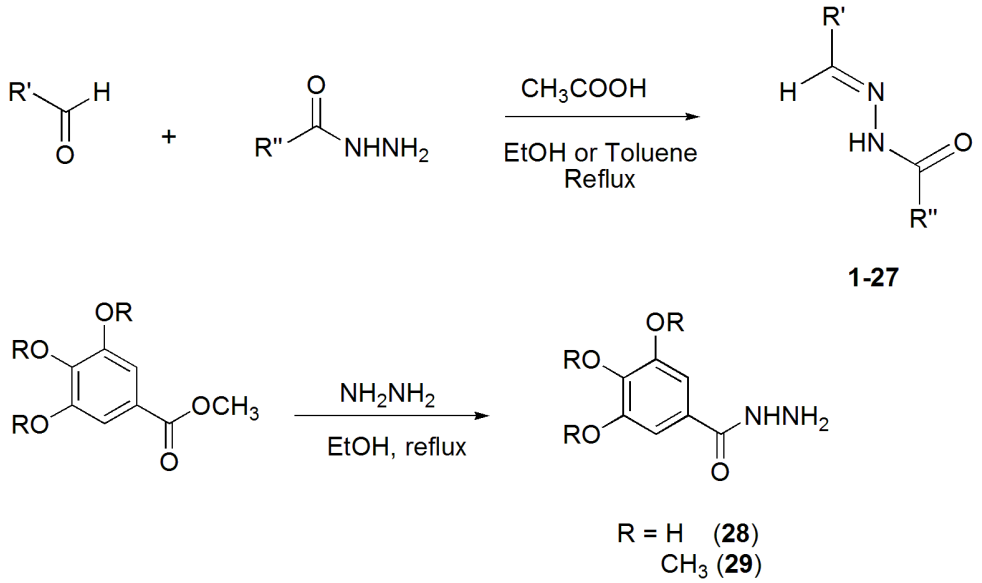

Fig. 1.14 Generic scheme for the synthesis of the N-acylhydrazones ligands (1-27) and the hydrazides 28 and 29.

The reaction (Fig. 1.14) between the proper aldehyde and the proper hydrazide was carried out in ethanol at 85°C and led to the isolation of the desired ligand. In the IR spectra of the ligands, absorption peaks at about 1630-1660 cm^{-1} can be related to the C=O stretching of the hydrazone. The stretching vibrations of the NH and OH groups are displayed in the range 3100-3300 cm^{-1}.

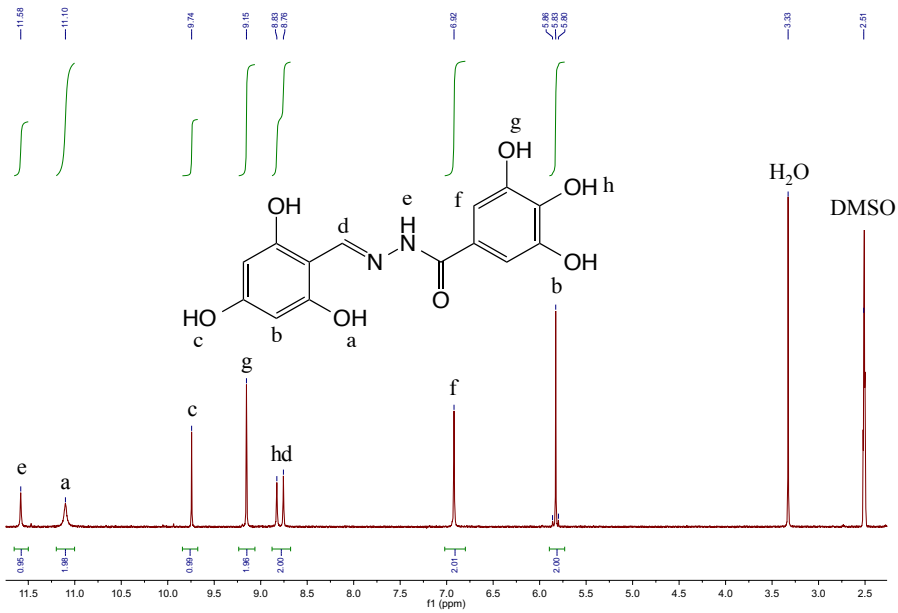

Fig. 1.15 ^{1}H-NMR of ligand 22 recorded in DMSO. Example of ^{1}H-NMR spectrum of one of the N-acylhydrazone ligands.

In the ^{1}H-NMR spectra (for a representative spectrum, see Fig. 1.15), recorded in DMSO-d_6, the resonances of the iminic (about 8.0 ppm) and of the acidic protons (NH and OH, 9-12 ppm) can be observed in the expected spectral range. All other signals are in agreement with the expected chemical shifts.

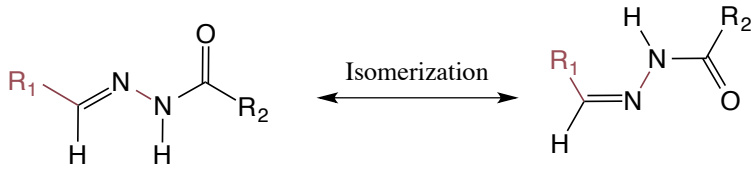

E form Z form

Fig. 1.16 E and Z isomerization of N-acylhydrazones.

In literature, it is well established that hydrazones can exist as cis/trans conformers around the C(O)-N bond, and as E/Z isomers with respect to the C=N double bond (Fig. 1.16). Stereochemistry of hydrazones is mainly decided by the steric effects of the various substituents in the hydrazone moiety, and favoured by intra-molecular hydrogen interactions. There are literature evidences[114, 115] that, for hydrazones compounds derived from aldehyde, the $Z_{C=N}$ isomer is always disfavoured because of the steric hindrance: the position of R_1 group is found to be on the same side of the acidic NH proton. In agreement with that, the Z isomer is disfavoured and all the synthesised ligands adopt the most stable E conformation in solution: in the ^{1}H-NMR spectra just one single set of signals is displayed related to the E isomer.

A different situation is observed in the alkyl-derivatives **3** and **4**. The ^{1}H-NMR spectra recorded in DMSO-d_6 show two sets of signals in a 2:1 and 5:3 *ratio*, respectively: the chemical shift of both the iminic and NH protons of the new set are shifted to lower fields, due to their close proximity with the carbonyl oxygen. The different nature of the R_2 substituent plays the major role in the cis-trans isomerization process (Fig. 1.17).

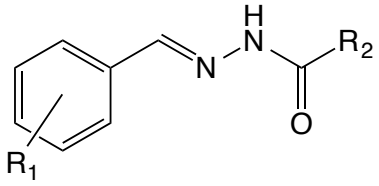

Trans-amide configuration

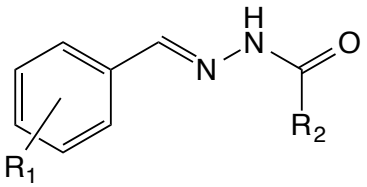

Cis-amide configuration

Fig. 1.17 Cis and trans possible configuration of the amide moiety.

The stabilisation of the anionic charge on the carbonyl oxygen atom (Fig. 1.18) leads to the formation of a double C=N(O) bond: when this situation is stabilized by aromatic and nitrogen substituents, the rotation is blocked.

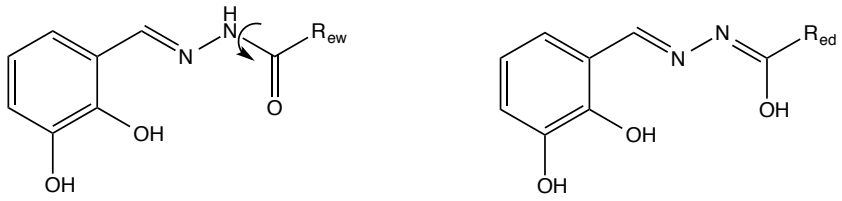

Fig. 1.18 Mechanism for cis-trans isomerization.

Different situations were obtained when the proton NMR spectra of the differently substituted compounds were recorded in the d_4-methanol instead of d_6-DMSO (Fig. 1.19).

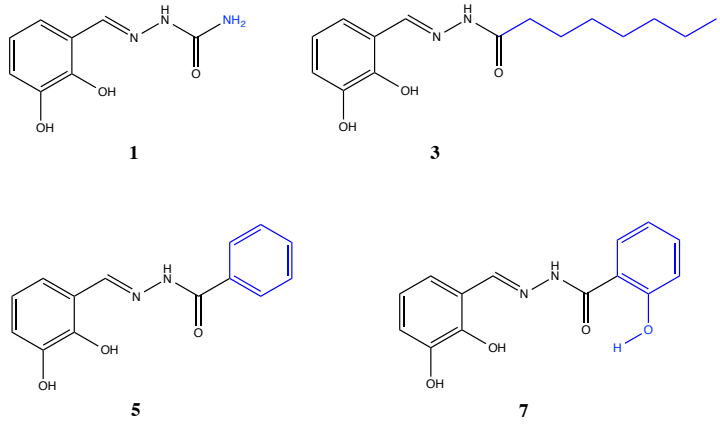

Fig. 1.19 Structure of compounds taken into account for the study of the cis-trans isomerisation process.

The role of a protic solvent is essential in the rotation around the N-C(O) bond, rotation that leads to the cis-trans interconversion. The spectra of compounds **1**,

3 and **5** showed two set of signals: the presence of a protic solvent leads to the stabilization, through hydrogen bond, of a negative charge on the carbonyl oxygen and to the rotation around the single bond N-C(O). The situation is different for compound **7**. Here, the presence of the hydrogen bond between the hydroxyl group in position 2 and the carbonyl oxygen, blocks any interaction with the solvent. This is why the spectrum shows just one set of signals. The same situation can be seen for derivatives **2**, **4**, **6** and **8**.

1.2.2.2 Docking studies

In order to explore the possible binding modes of the synthesised compounds, docking simulations by GOLD program[116] were performed by using the structural coordinates (PDB code 4AWM) of PA-Nter endonuclease in complex with epigallocatechin-3-gallate[50]. The analysis of the docking results put in evidence that different binding modes are possible and are influenced by different affinities within the amino acid pocket, located near the catalytic site, that includes the following residues: Thr20, Glu23, tyr24, Glu26, Lys34, Ile38, His41, Glu80, Gly81, Arg82, Asp83, Arg84, Thp88, Lys104, Phe105, Leu106, Asp108, Phe117, Glu119, Ile120, Gly121, Val122, Tyr130, Lys134, Lys137 and Ile138. The residues His41, Asp108, Glu119 and Lys134 are involved in metal binding and play a role in the catalytic process. Considering that the position of the side-chains of some residues changes depending on which pocket the ligand is occupying, we superimposed some X-ray structures of complexes between PA-Nter endonuclease and known active ligands. The PA-Nter active site is quite spacious and, therefore, able to accommodate large variation in ligand size and shape with different binding affinities. It was observed that the side-chain of amino acid Tyr24 shows greater movement than

the other residues and, for this reason, we considered it as a flexible residue during the docking procedure.

Docking calculations using epigallocatechin-3-gallate, L-742,001 and 2-(4-(1*H*-tetrazol-5-yl)phenyl)-5-hydroxypyrimidin-4(3*H*)-one (see chemical structure Fig. 1.10) were carried out to compare experimental data and predict binding modes as well as to validate our docking procedure. Their best docking poses agreed well with the experimental binding modes, with root-mean-square deviation of atomic position (rmsd) values of 0.8, 1.2 and 0.7, respectively. In particular, the chelating motif of H_2L strictly overlap with the three coplanar oxygen atoms of L-742,001, which are involved in metal chelation of divalent ions.

Next, docking studies of several N-acylhydrazone derivatives were performed and this generated a number of possible binding conformations. This highlighted that the active site cavity of the PA endonuclease is quite spacious, as already demonstrated by crystallographic studies[19, 50], and confirmed the ability of this scaffold to chelate the two M^{2+} ions in different ways, as already suggested (mode A-C in Fig. 1.13).

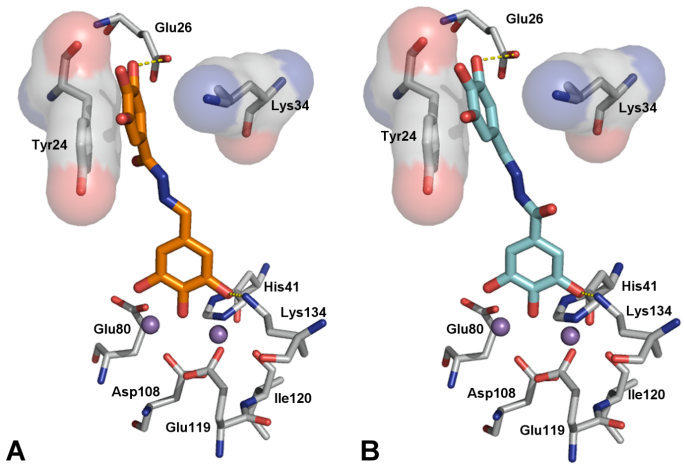

Fig. 1.20 First (A) and second (B) GOLD cluster docked solutions of compound 23 (orange and cyan, respectively) in complex with PA endonuclease. Key residues of the pocket are presented using PyMOL [http://www.pymol.org] and LIGPLUS [R.A. Laskowski, M.B. Swindells; *Journal of chemical information and modeling*; **2011**; 51; 2778]. Hydrogen bonds are illustrated by dotted lines while the divalent metal ions are shown as purple spheres.

Fig. 1.20 displays the first (panel A) and second (panel B) GOLD cluster docked solutions for compound **23**. These two complex structures represent the largest clusters with similar fitness values (59.20 and 58.65, respectively) and led us to consider both of them as plausible binding modes for compound **23**. In both cases, **23** appears able to coordinate the two M^{2+} ions in the active site through the three contiguous OH groups. In addition, **23** was predicted to form two hydrogen interactions, i.e. with the catalytic Lys134[85] on the one side and Glu26 on the other side. Furthermore, in these two different binding modes, compound **23** forms π–π interactions with the aromatic ring of Tyr24, in a way similar to that described for other endonuclease inhibitors, i.e. epigallocatechin-3-gallate[50] and L-742,001[19].

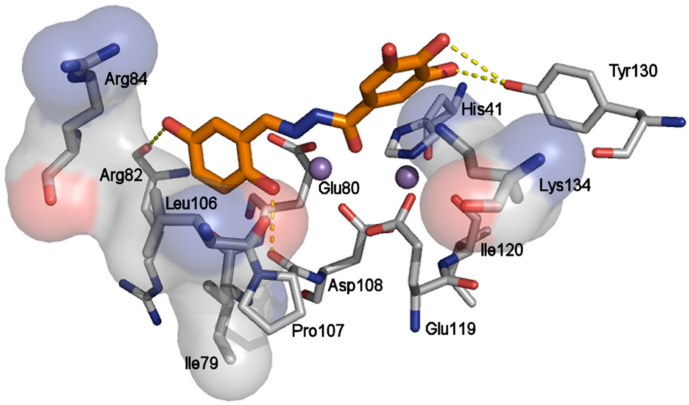

Fig. 1.21 Binding mode of compound 15 (orange) in complex with PA endonuclease. Key residues of the pocket are presented using PyMOL [http://www.pymol.org] and LIGPLUS [R.A. Laskowski, M.B. Swindells; *Journal of chemical information and modeling*; 2011; 51; 2778]. Hydrogen bonds are illustrated by dotted lines while the divalent metal ions are shown as purple spheres.

On the other hand, the best docked conformation for **15** (Fig. 1.21, fitness value 68.56), which has an activity slightly lower than **23**, reveals an entirely different role of the gallic moiety. In this case the ligand seems to form two hydrogen bond interactions with Tyr130 as well as a cation–π interaction with Lys134. Tyr130 lies in a pocket that also contains Arg124, a residue that was proposed to have a crucial role in binding of the RNA substrate[16, 144]. Arg124 was shown to be critical for enzymatic fitness in our mutational analysis in cell culture models[49]. Compound **15** appears further stabilised by hydrogen bond interactions between the two hydroxyl groups on its benzylidene ring and Arg82 and Asp108. In this case, chelation of the two M^{2+} ions is carried out by involving the imine group as in mode A in figure 1.13.

1.2.2.3 Biological results

1.2.2.3.1 Structure-activity relationship for the inhibition of the PA-Nter enzyme.

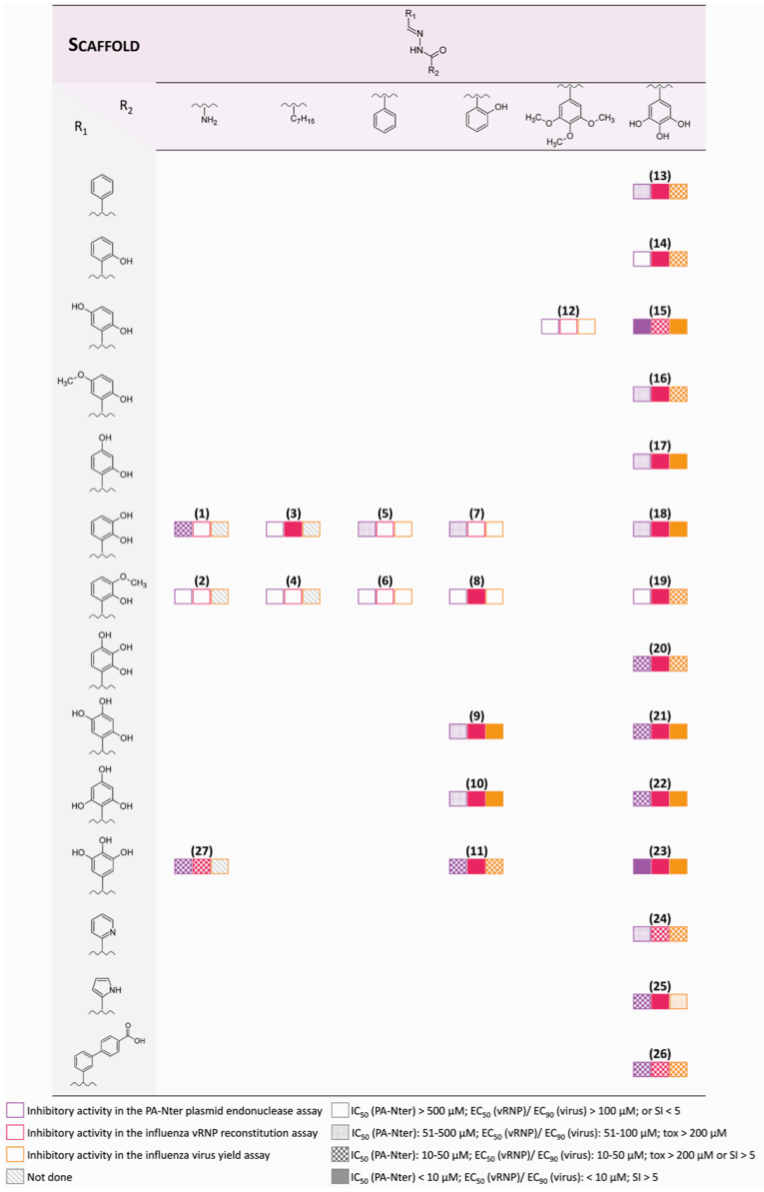

Table 1.2 Overview of the structure-activity relationship for compounds 1-27.

All the synthesised molecules were tested for their ability to inhibit the influenza endonuclease in an enzymatic plasmid-based assay with recombinant PA-Nter[117], as well as in cell-based influenza methods (i.e. virus yield and vRNP reconstitution assays[105]). The results are shown in Table 1.2, to visualise the structure-activity relationship (SAR).

Analysis of the IC_{50} data from the enzymatic studies revealed that the inhibitor activity against PA-Nter depends on the following determinants. The first analysed parameters are the effect of hydroxyl substituents in R1 and the nature of the R2 moiety. Moderate activity (IC_{50}= 24 mM) was seen for N'-2,3-dihydroxybenzylidene semicarbazide (**1**). This activity is completely lost when the NH_2 moiety is replaced by a hydrophobic heptyl chain (compound **3**), but is less affected with a phenyl or a 2-hydroxyphenyl substituent (**5** and **7**, IC_{50}= 84 and 54 mM, respectively). When a methoxy group replaced the hydroxyl in position 3 on R1, the activity is completely lost (compounds **2**, **4**, **6** and **8**). Going from two hydroxyls in R1 (**7**) to compounds with three hydroxyls at varying positions in R1 (i.e. compounds **9, 10** and **11**) the activity is unaffected, with IC_{50} values ranging from 45 to 75 mM. Similar to what was described above, the 2-hydroxyphenyl analogue (**11**) has comparable activity as the counterpart carrying R2=NH_2 (**27**). Within the series carrying a 2-hydroxyphenyl R2-group, the activity of **11** is particularly intriguing. This N-acylhydrazone does not have the possibility to chelate in a tridentate ONO fashion, which we assumed to be the better chelation mode to obtain activity; however, **11** can coordinate two cations by means of its three OH groups in R1 (Fig. 1.22).

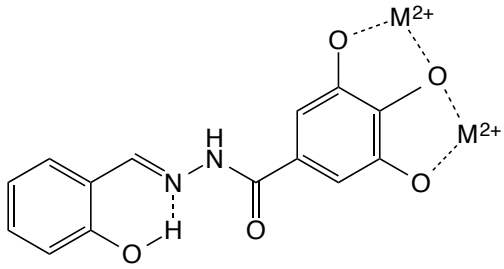

Fig. 1.22 Possible intramolecular hydrogen bonding and coordination mode. Example for compound **11** carrying a 2-hydroxyphenyl R1 group and its possible mechanism of coordination.

Note that a related chelating mode was observed in a crystal structure, solved by Cusack and coworkers[118], of PA-Nter endonuclease in complex with the inhibitor epigallocatechin-3-gallate (EGCG), showing that this ligand chelates the two manganese(II) cofactors through its gallic moiety.

The PA-Nter inhibitory activity strongly depends on the number and position of hydroxyl substituents in R1, and the same is true for R2. This is clearly highlighted by the data obtained with compounds **13-23**, in which R2 is a 3,4,5-trihydroxyphenyl (gallic) group, the most active scaffold in our series. The analogue carrying an unsubstituted aromatic ring as R1 (compound **13**) had moderate activity (IC_{50} = 69 mM). When one OH was added at position 2 of the R1 ring (**14**), the activity was lost. The introduction of a second OH substituent at position 5 resulted in strong activity (compound **15**, IC_{50} = 9 mM); a OH in position 3 gave rise to medium activity (**18**; IC_{50} = 83 μM), and low activity was seen when the second OH is at position 4 (**17**, $IC_{50} \geq$ 370 mM). The addition at any position of a 3-methoxy group (**19**) abolished the inhibitory activity. This cannot be related to variations in the chelating features displayed by the R1 moiety, since compounds **14-19** all have, in theory, the ability to chelate one metal ion through the ortho-OH and iminic nitrogen (mode A in

Fig. 1.13). Moreover, compound **18** can, in principle, chelate the two M^{2+} ions in the active site according to mode B (Fig. 1.13), yet **18** (IC_{50} = 83 mM) has nine-fold lower activity than **15**, that does not possess this two-metal chelating feature in R1. Therefore, it was hypothesised that the inhibitory activity of the series containing the gallic moiety is determined by (i) the ability of the R2 moiety to chelate the two metal ions in the active site according to mode C (Fig. 1.13), and (ii) the presence of one or more hydroxyl substituents in R1 in suitable positions to promote ligand-protein interactions (e.g. through hydrogen bonds). These assumptions were confirmed by molecular docking calculations and X-ray analysis of the compound **23** in complex with PA-Nter.

1.2.2.3.2 Inhibition of vRNP activity and virus replication in cells

Compound	Enzyme assay with PA--Nter	Virus Yield assay in Influenza virus infected MDCK cells			vRNP reconstitution assay in HEK293T cells	
		Antiviral activity		Cytotoxicity	Activity	Citotoxicity
	IC_{50}	EC_{99}	EC_{90}	EC_{90}	EC_{50}	CC_{50}
1	24	ND	ND	ND	107	>200
2	>500	ND	ND	ND	>100	>200
3	>500	ND	ND	>200	6.4	48
4	>500	ND	ND	>200	8.1	33
5	84	>25	>25	≥146	2.7	10
6	>500	>50	>50	>200	11	14
7	54	172	172	>200	2.2	9
8	>500	>12.5	>12.5	>200	2.2	15
9	75	16	5.3	>200	5.5	>200
10	68	14	8.5	111	0.4	132
11	45	30	12	>200	5.6	>200
12	>500	>12.5	>12.5	>200	21	39
13	69	71	34	>200	8.4	>200
14	>500	63	37	>200	2.2	>200
15	9	18	7.5	≥172	14	>200
16	454	67	28	>200	4.8	>200
17	≥370	21	8.1	>200	7.9	>200
18	83	6.2	2.2	>200	3.6	>200
19	>500	53	26	>200	7.1	>200
20	18	35	11	>200	2.2	>200
21	13	8.3	3.6	>200	2.5	>200
22	34	7.4	3.4	>200	0.42	>200
23	7	11	3.5	>200	3.1	>200
24	131	58	26	>200	29	>200
25	40	132	70	>200	3.7	>200
26	30	36	13	>200	23	>200
27	36	ND	ND	ND	21	>200
28	40	158	85	>200	7.2	>200
DPBA	5.5	ND	ND	ND	ND	ND
Ribavirin	ND	13	8.5	>200	9.3	>200

Table 1.3 Inhibitory activity of the N-acylhydrazones compounds 1-27 and hydrazide 28. Enzymatic assay with influenza virus PA-Nter endonuclease and in influenza virus assays. DPBA and Ribavirin were analysed as controls.

To determine the anti-influenza virus activity of compounds **1-28** in cell culture test on an influenza vRNP reconstitution assay in human Hembryonic Kidney 293 cells (HEK293T cells) was performed; furthermore the active compounds (i.e. EC_{50} < 100 μM) were subjected to a virus yield assay in influenza virus-infected Madin-Darby canine kidney (MDCK cells) (Table 1.2 and Table 1.3).
For some N-acylhydrazone compounds, we observed quite potent and selective activity in the vRNP reconstitution assay. This indicated that they are able to

inhibit viral RNA synthesis and suggested that they could be classified as original PA inhibitors. Values of EC_{50} (vRNP) or EC_{90} (virus yield) in the range of 0.4-18 μM were obtained for compounds **15** and **20-23**, which all carry a 3,4,5-trihydroxyphenyl as R2, and possess either two (**15**) or three (**20-23**) hydroxyl substituents in the R1 moiety. As in the enzymatic PA-Nter assays, the compounds having a gallic moiety as R2 showed slightly higher activity than the compounds carrying a 2-hydroxyl R2 group (Table 1.3: compare **9**, **10** and **11** to **21**, **22** and **23**, respectively). The strong activity of **15** was completely lost in its 3,4,5-trimethoxy analogue **12,** consistent with the crucial role of the R2 gallic moiety in metal chelation. On the other hand, compounds with a gallic moiety in R2 displayed moderate activity (IC_{50} values around 40 μM) when the hydroxy-derived phenyl ring on R1 was substituted with a different functional group as NH_2 (i.e. the 3,4,5-trihydroxybenzohydrazide **28**, Fig. 1.12), an extended ring system (**26**) or a pyrrole ring (**25**). Still lower activity was seen with the pyrimidine analogue **24**. The data put in evidence that the 3,4,5-trihydroxybenzyl moiety at R2 is fundamental but not sufficient to ensure potent PA-Nter endonuclease inhibition: hydrogen interactions, established with the amino acid side chains of the protein by the R1 moiety, appeared crucial in modulating the antiviral activity.

A second factor that greatly affects the activity is the position of the OH groups in R1. In particular, all compounds with a trihydroxylated phenyl group as R1 (i.e. **20**, **21**, **22** and **23**) were able to inhibit PA-Nter quite potently. The lowest IC_{50} values were obtained for **21** and **23** (IC_{50} = 13 and 7 μM, respectively), which both have one of their three hydroxyl groups at position 5. The most active compound of this series was **23**, which lacks the hydroxyl group at position 2 of R1, further confirming that this function is undesirable or even

detrimental for inhibitory activity against PA-Nter, as already noticed above for compound **14**.

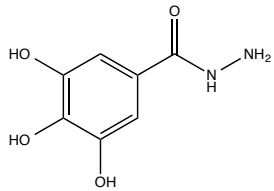

Fig. 1.23 Chemical structure of the N-acylhydrazone precursor 28.

Interestingly, the hydrazide **28** (Fig. 1.23) displayed weak (virus yield) to strong (vRNP reconstitution) activity, albeit less than the most active molecules in the 3,4,5-trihydroxyphenyl series (i.e. **18** and **21-23**). The activity observed with **28** raised the concern that, for some N-acylhydrazones, the antiviral activity in cell culture may be related to their intracellular hydrolysis into **28**. However, we can exclude this possibility: the antiviral potency showed large differences (i.e. EC_{50} values between 0.42 and 29 μM) for compounds with the same R2 but different R1 groups, this means that R1 does play a crucial role in modulating the antiviral effect. It is worth noting that substitution of the 5-hydroxyl in **15** by a methoxy group (**16**), causes a dramatic drop in activity (IC_{50} = 9 and 454 mM for **15** and **16**, respectively), confirming the importance of the interactions with the protein side chain by the R1 moiety.

Some N-acylhydrazone compounds were devoid of activity in the enzymatic assay, otherwise they showed good to moderate efficacy in cell culture (e.g. **14** and **19**, having EC_{50} values of 2.2 and 7.1 μM, respectively). Their antiviral mode of action appeared to be unrelated to PA, but rather associated with an early (virus entry) or late (maturation or release) event in the viral life cycle. To achieve a complete insight into the antiviral profile of the N-acylhydrazones, specific mechanistic experiments are in course.

1.2.2.4 Crystal structure of the ligand **23** with PA-protein

To obtain more information regards the mechanism of action of this class of molecules, several efforts were made in order to obtain the crystal structure of the compounds in the active site pocket of the PA-Nter terminal domain.

Attempts were made to co-crystallise PA-Nter with compound **15**, **20**, **21** and **23** in one to four molar excess. While crystals appeared and diffracted well, upon data processing, no or very little electron density for the inhibitors was observed. Attempts to soak apo crystals in crystallization solution containing 5 mM inhibitor overnight, also did not result in substantial electron density for the inhibitor. As a last resort, dry powder of the inhibitor was sprinkled over the crystallization drop containing apo crystals and left over night. This experiment was successful for compound **23**, and diffraction data was collected.

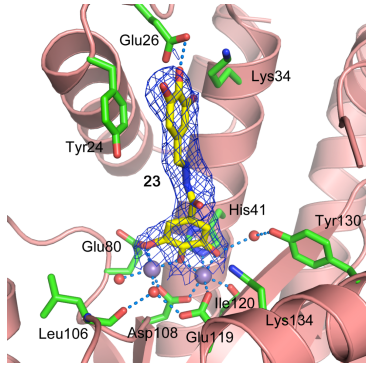

Fig. 1.24 Crystal structure of $PA_N^{\Delta Loop}$ in complex with compound 23. Active site residues are shown in sticks with green carbons, manganese atoms are shown as purple spheres and water molecules as red spheres. Compound **23** is shown in sticks with yellow carbons. Protein secondary structure is shown as ribbons in salmon color. *2Fo-Fc* electron density map contoured at 1σ is shown as blue mesh.

PDB code	5EGA
Data collection	
Space group	$P6_422$
a, b, c (Å)	73.99, 73.99, 128.55
α, β, γ (°)	90.0, 90.0, 120.0
Resolution (Å)*	50.0-2.15 (2.23-2.15)
R_{meas}*	7.3 (96.2)
$I/\sigma I$*	42.8 (3.0)
Completeness (%)	99.4
Redundancy	16.7
Refinement	
Resolution*	50.0-2.15 (2.21-2.15)
No. of reflections	11252
R_{work}/R_{free}	20.7/23.4
No. of atoms	
Protein	1405
Mn	2
Ligand	23
Water	32
B-factor (Å^2)	
Protein	64.11
Metal	57.25
Ligand	89.26
Water	56.31

Table 1.4 Crystallographic data collection and refinement statistics for the $PA_N^{\Delta Loop}$ - compound 23 complex.

The refined structure shows unambiguous electron density for the inhibitor (Table 1.4 and Fig. 1.24). The complex structure confirms one of the two binding modes predicted by the docking simulations (Fig. 1.20, panel B). The galloyl moiety chelates the manganese ions while the trihydroxyphenyl group stacks against the Tyr24 side chain. It is interesting to note that two of these hydroxyl groups are in position to form hydrogen bonds with Glu26 and Lys34 (Fig. 1.24). These interactions suggest that other functional groups, e.g. halogens, could be used in place of the hydroxyl for better interactions with Glu26 and Lys34 and the inhibitory potency of these compounds could be further improved.

1.2.3 Metal complexes

1.2.3.1 Mg^{2+}complex of **19**

The metal binding behaviour of some hydroxybenzamides has been previously investigated by computational docking studies to elucidate their interactions with the active site, but nothing is known about the complex formation of this class of ligands with magnesium. This information is essential in order to rationalise their inhibitory activity and the mechanism of action, since the inhibitory activity of the N-acylhydrazones was assumed to be related to the chelation of the divalent metal cofactor(s) in the influenza PA-Nter active site. We investigated the coordination properties of two model ligands, **19** and **23**, which can interact with metal ions through different chelating modes.

19 effectively formed the corresponding magnesium complex after reaction with magnesium acetate in the presence of triethylamine. The use of a base was necessary in order to force deprotonation of the ligand. The ligand can behave as bi, tri or tetradentate depending on the position of O and N donor atoms to coordinate one or several metal centres. In order to explore the coordination versatility towards the metal ion, different reaction conditions were used for the complexation reaction: 1:1 and 1:2 metal to ligand *ratio* (up to 4 equivalents of base) were explored but in any case the same chemical species was recovered (Fig. 1.25), as confirmed by experimental data.

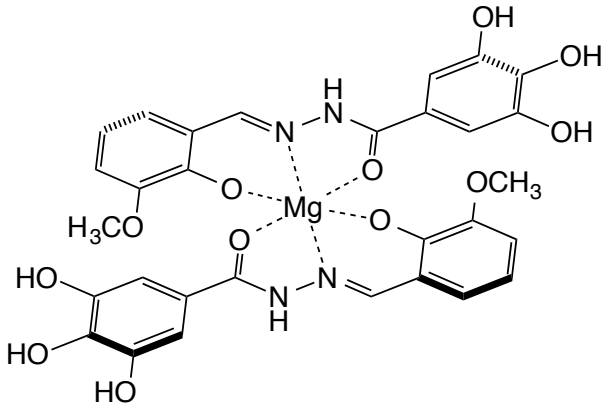

Fig. 1.25 Chemical structure of the magnesium complex with ligand 19.

The IR spectrum of the complex was analysed in comparison with the one of the free ligand H_2L. The spectrum of the magnesium compound displayed bands in the range of 3185-3260 cm^{-1} which are related to the stretching of the NH is not deprotonated upon complexation; so the ligand is monoanionic because of the OH deprotonation. The C=O band shifts from 1663 cm^{-1} in the free ligand to 1643 cm^{-1} when involved in magnesium coordination

The ^{1}H-NMR spectrum of the magnesium complex recorded in DMSO-d_6 evidenced the presence of two sets of signals: one set correspond to the free ligand, while the second one, with a shift in the signals of about 0.1-0.2 ppm, is related to the desired metal complex. The ^{1}H-NMR spectrum was also recorded using a non-coordinating solvent such as MeOD-d_4 and the spectrum showed only one set of signals attributable to the complex. The use of a strong coordinating solvent, therefore, caused the partial decoordination of the ligand. The ^{13}C-NMR spectrum evidenced that the signal of the quaternary C=O carbon is not shifted in the complex, thus suggesting that the C=O group is weakly involved in the coordination to the metal ion. ESI-mass spectra and elemental analysis confirmed the presence of a mononuclear specie of the type

$Mg(HL)_2 \cdot 4H_2O$. So, it is possible to suggest the formation of a bischelated compound where the ligand is monodeprotonated and coordinated to the metal by means of the phenolic oxygen, the iminic nitrogen and the carboxylic oxygen.

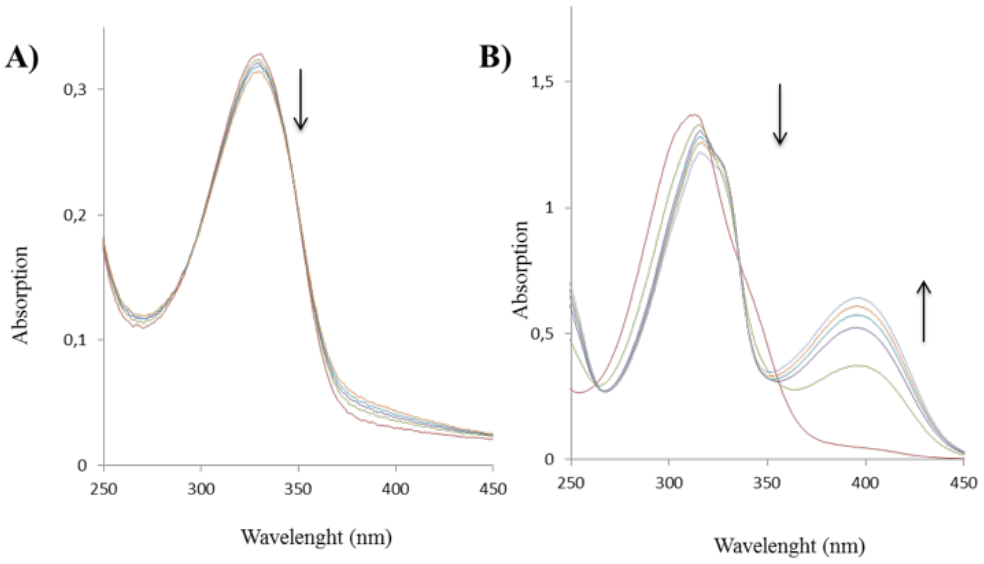

Fig. 1.26 UV-visible titration of ligands 23 (A) and 19 (B) with increasing amount of $Mg(CH_3COO)_2$.

The interaction between the N-acylhydrazone ligand and the magnesium cation was investigated also by means of UV-Vis experiments, considering the interaction of two ligands with different coordination properties. Increasing equivalents of $Mg(CH_3COO)_2$ were added to a methanolic solution of **19** and the resulting UV-visible spectra are shown in Fig. 1.26 (A). The spectrum of **19** includes a band, at 313 nm, assignable to n-π* transitions of the C=N and C=O groups. The absorption around 400 nm increases according to increase amount of metal concentration, and a new band appears with a maximum at 397 nm.

The opposite trend is observed in the range 300–350 nm, where an isosbestic point is present close to 335 nm. We were interested in studying the different coordinating features of the most active PA-Nter inhibitors, such as **23**, compared to the non-active **19**. When the same UV-visible experiment was performed with **23**, a different behaviour was observed. Increasing concentration of Mg^{2+} caused a decrease in the maximum absorption; an isosbestic point is visible at about 345 nm, but a new band at 400 nm does not appear. Ligands **19** and **23** coordinate the Mg^{2+} ions in different ways: **19** chelates the metal ion by using the deprotonated salicyl oxygen and iminic nitrogen; otherwise in **23** the gallic moiety is involved in the coordination leading to different, less extensive modifications of the UV spectrum (Fig. 1.13, A or B versus C). These results underline, again, the importance of the chelating mode toward biological activity: chelation itself is not sufficient to ensure activity, but a synergy is necessary among chelation, molecule orientation within the active site and interaction with the protein side chain.

1.2.3.2 Metal complexes of **8**

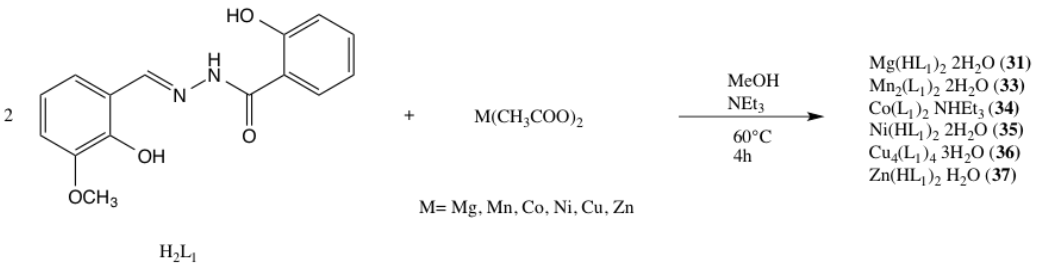

Fig. 1.27 Scheme of the syntheses of metal complexes of H_2L_1.

Within our panel, ligand **8** (**H_2L_1**) offers additional chelating possibilities, thanks to the presence of a salicylic moiety on both its aromatic rings (Fig. 1.27).

To explore its various coordination possibilities, H_2L_1 was reacted with the acetates of different divalent metal ions (Mg, Mn, Co, Ni, Cu and Zn) in presence of a base (NEt_3), yielding to the corresponding metal complexes **31-37**. The syntheses of the desired complexes were firstly confirmed through IR spectroscopy: spectra of the complexes were analyzed in comparison with that of the corresponding free ligand. In the IR spectra of the magnesium, nickel and zinc complexes (**31, 35** and **36)** the absorptions associated to the NH group (2993-3211 cm^{-1} in the free ligand) are still visible; this means that the NH is not deprotonated upon complexation. Different situation can be seen for the manganese, cobalt and copper compounds **33**, **34** and **36**: no bands associated to the stretching of the NH can be seen in the spectra confirming that the coordinated ligands are bi-deprotonated both on the OH and NH moieties. More difficult was the rationalization of the behavior of the C=O absorption band upon complexation. This is a strong band around 1605 cm^{-1} in H_2L_1; it is not

significantly shifted in **33** and **37**, while there is an upper shift of about 20 cm^{-1} in the other metal complexes. On the contrary, the C=O band in acylhydrazones usually undergoes a downshift upon complexation, as shown in the previous paragraph for complex **30**. Anyway, it has to be taken into account that, in H_2L_1, the C=O moiety is probably involved in an intramolecular hydrogen bond, as confirmed by the ^{1}H-NMR recorded in CH_3OD-d_4, and this results in abnormally lower IR values ($n_{C=O}$ = 1605 cm^{-1} in H_2L_1 and about 1650 cm^{-1}, normally, in acylhydrazones)[119, 120, 121]. The shift of the band induced by coordination to the metal ion could be comparable to the lowering induced by intramolecular hydrogen interaction (about 30-50 cm^{-1}) and therefore it is reasonable to consider, in **33** and **37**, the carbonyl oxygen coordinated to the metal. X-ray diffraction analysis has confirmed this hypothesis also in **34** and **36** and has confirmed that the ligand coordinates the metal in the keto form.

For the complexes **31**, **35** and **37** it was possible to suggest the formation of a bis-chelated compound $M(HL_1)_2$, where the ligand is monodeprotonated and coordinates to the metal by means of the phenolic oxygen, the iminic nitrogen and the carbonylic oxygen. ESI-MS and elemental analysis supported such hypothesis. The potentiometric measurements discussed later in this paragraph indicated, for magnesium complex, the presence in solution of another species with a Mg^{2+}: ligand 1:1 *ratio*. To isolate this specie, magnesium acetate was reacted with H_2L_1 in presence of 2.5 equivalents of NaOH (pH 8-9) in a 1:1 metal to ligand *ratio*: in these conditions the new complex **32** was isolated. In **32** the ligand is bi-deprotonated and the NH absorption band, at 3267 cm^{-1}, could be seen in the IR spectrum, band that was absent in the spectrum of **31**. On the basis of ESI-MS and of examples in the literature[122], the formation of a dinuclear coordination compound $Mg_2(L_1)_2$ is proposed (Fig. 1.28).

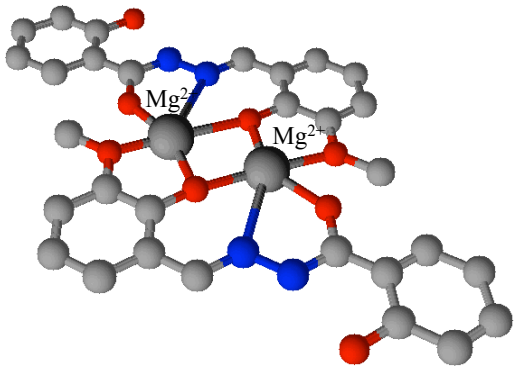

Fig. 1.28 Proposed coordinating mode of H_2L_1 in the complex 32.

Registration of ^{1}H-NMR spectrum in DMSO-d_6 of both **31** and **32** evidenced the presence of two sets of signals: one set corresponds to the free ligand, while the second one to the metal complex. The use of a coordinating solvent, therefore, caused the partial decoordination of the ligand. On the contrary, in the spectra of **31** and **32** in MeOD-d_4 there is a unique set of signals. In the ^{1}H-NMR spectrum of **31** a sharp set of signals can be observed, with only a 0.01-0.02 ppm shift compared to the free ligand; in the spectrum of **32**, instead, the signals are very broad and the chemical shifts are slightly different. In particular, both the aromatic proton in *ortho* to the methoxy group and the methoxy protons themselves are shifted downfield of 0.4 and 0.7 ppm respectively, thus suggesting the involvement of the methoxy moiety in coordination.

ESI-MS data and solution studies suggested that the manganese complex **33** was also synthesized as a dinuclear species $Mn_2(L_1)_2$, with the ligand bi-deprotonated (as shown in Fig. 1.20). In literature there are some examples of dinuclear and multinuclear clusters of manganese with (2-hydroxy-3-methoxy)benzoylhydrazone [123] or (2-hydroxy-3methoxy)benzylidene

acetohydrazide[122] and, even when a mononuclear stoichiometry is isolated at the solid state, multinuclear systems are proposed in solution[124].

Various examples have been published of cobalt complexes with hydrazonic ligands where the formation of both mononuclear and polynuclear metal complexes have been confirmed by experimental data[125, 126]. During the synthesis of **34**, in presence of NEt_3, Co(II) is oxidized to Co(III) and the ionic complexes $[Co(L_1)_2](NHEt_3)$ was isolated. The presence of a diamagnetic compound was confirmed by ^{1}H-NMR spectrum recorded in DMSO-d_6, where it is possible to observe the signals related to the triethylammonium counterion and to the bideprotonated ligand. Compared to the free ligand, the aromatic protons undergo a shift to higher fields of about 0.3-0.4 ppm and to lower fields of about 0.35 ppm for the iminic proton. MS-ESI(-) spectrum evidenced the signal of the $[Co(L_1)_2]^-$ specie and elemental analysis confirmed the stoichiometry of $[Co(L_1)_2](NHEt_3)$. Diffraction analysis on a single crystal of **34** confirmed definitively the formation of a bis-chelated ionic coordination compound.

As recently established by literature examples, acylhydrazones could be ligands for the synthesis of multinuclear copper complexes[127, 128]. The reaction of copper(II) acetate with H_2L_1 afforded the green tetranuclear complex $Cu_4(L_1)_4 \cdot 3H_2O$ (**36**) as confirmed by X-ray diffraction structure; the ESI-MS analysis confirmed the presence of the Cu_4L_4 specie also in solution. In the Cu(II) complex the ligand is bi-deprotonated, as demonstrated also by IR data, and is coordinated to the metal in a ONO fashion through the deprotonated phenolic oxygen, the iminic nitrogen and the carbonyl oxygen. It is well known[129] that acylhydrazones exhibit keto–enol tautomerism in solution: the enol form is stabilised once the ligand is coordinated to the metal as it is in its

deprotonated form. In the case of **36**, instead, the ligand is coordinated to the metal centre in the keto form (see crystal structure analysis).

Acylhydrazones represent an interesting class of polydentate, chelating agents with a great variety of modes derived from the possibility of a keto-enol tautomerization and to the presence of several potential donor sites. These peculiarities make the study of their speciation in solution very attractive but, at the same time, quite complicated to unravel; however this information is essential to understand their biological activity and mechanism of action.[130]

Potentiometric studies (Fig. 1.29) were carried out to examine the coordinating behavior of H_2L_1 in solution with a variety of divalent metal ions (Mg^{2+}, Mn^{2+}, Zn^{2+}, Ni^{2+}, Cu^{2+}) in mixed solvent methanol/water = 9/1 v/v, in which the ligand and almost all the complexes are soluble. The ionic strength was adjusted to 0.1 M KCl.

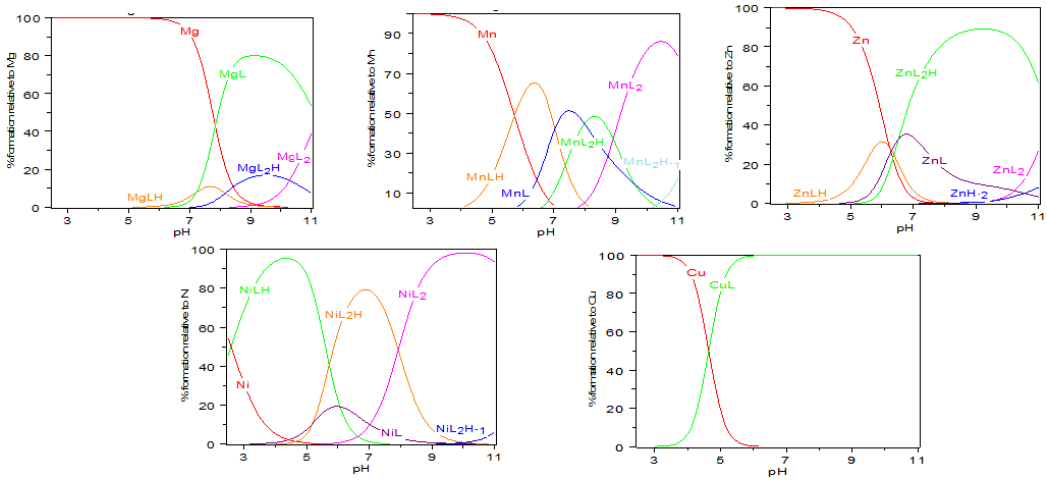

Fig. 1.29 Distribution diagrams for the systems under investigation at M/L=1/2 (methanol/water = 9:1 v/v, I = 0.1 M KCl).

H_2L_1 is a diprotic acid with pK_{a1}=8.43 (±0.01) and pK_{a2}=12.11 (±0.01); the more acidic group is probably the OH of the *o*-vanillin moiety, and pK_{a2} should be attributed to the dissociation of the salicylic OH.

For Mg^{2+}, Mn^{2+}, Zn^{2+} and Ni^{2+} were found in solution species with different stoichiometry ML_1H, $M(L_1)_2H$, ML_1, and $M(L_1)_2$ (charges are omitted for simplicity).

The experimental conditions led to the isolation of a solid powder related to complexes of Mg, Ni and Zn with stoichiometry $M(L_1)_2H_2$; it was also possible to obtain the species with 1:1 metal to ligand stoichiometry $Mg_2(L_1)_2$ (**32**) by simply changing the reaction conditions. $Zn(L_1)_2H_2$ can be found but in low quantities and with a high standard deviation, so it was excluded for statistical reasons. Bimetallic species, such as $M_2(L_1)H$ and M_2L_1, were also taken into account; for sure, we can exclude them for Zn^{2+}. To obtain a good fit between experimental and computed titration curves, it is necessary to add oxydrilated species to the model of that species which were obtained using a base in the experimental conditions. Working at high pH values, species of the type $Mg(OH)_2$ and $Zn(OH)_2$ (in our notation MH_{-2}) where found for Mg and Zn; different situation was obtained for Mn^{2+} and Ni^{2+} where the dissociation of a water molecules in the coordination sphere of the metal is suggested and led to the production of the species ML_1H_{-1} and $M(L_1)_2H_{-1}$. Oxydrilated species can be disregarded at L/M *ratio* higher than 1 and at pH values lower than 10.

Different is the behavior of the ligand with Cu^{2+} ion. CuL_1 is the only specie that was found in solution: as confirmed by the X-ray structure, the copper(II) ion greatly increases the acidity of the amidic hydrogen and induces bi-deprotonation of the ligand. Note that species of general formula M_nL_n cannot be excluded: the mathematical processing cannot distinguish between the different n values as the correlation between the species does not allow the

convergence of the iterative calculation. The presence of the tetranuclear specie Cu_4L_4 in solution was confirmed by mass spectrometry and, at the solid state, by single crystal XRD structure. The same argument is valid also for other cations under study: compounds **32** and **33** were isolated, at the solid state, as two dimeric species ($Mg_2(L_1)_2{\cdot}4H_2O$) and ($Mn_2(L_1)_2{\cdot}2H_2O$); but it cannot be excluded the formation of dimeric species of the type $M_2(L_1)_2$ and/or M_nL_n also in solution.

The values of the formation constants of the various species greatly differ (Table 1.5).

p	q	r	Mg(II)	Mn(II)	Zn(II)	Ni(II)	Cu(II)
			Log $ß_{pqr}$	Log $ß_{pqr}$	Log $ß_{pqr}$	Log $ß_{pqr}$	Log $ß_{pqr}$
1	1	1	14.87 (0.17)	17.45 (0.05)	17.04 (0.13)	20.58 (0.02)	
1	2	1	22.04 (0.13)	26.23 (0.17)	27.64 (0.14)	32.72 (0.36)	
1	2	0	11.76 (0.07)	17.32 (0.19)	16.28 (0.19)	24.8 (0.59)	
1	1	0	7.64 (0.02)	10.41 (0.04)	10.74 (0.06)	14.51 (0.05)	14.12 (0.01)
1	0	-2	-21.42 (0.09)		-15.52 (0.18)		
1	1	-1		-1.61 (0.05)		3.78 (0.06)	
1	2	-1		5.67 (0.2)		12.62 (0.59)	
0	1	1	L + H = LH	Log $ß_{011}$ = 8.43 (0.01)			
0	1	2	L + 2H = LH_2	Log $ß_{012}$ = 12.11 (0.01)			

Table 1.5 Logarithms of formation constants ($\beta_{pqr} = [M_pL_qH_r]/[M]^p[L]^q[H]^r$). Methanol/water = 9:1 v/v, I =0.1 M KCl at 25°C for the ligand under study with Mg^{2+}, Mn^{2+}, Zn^{2+}, Ni^{2+}, and Cu^{2+}. SDs are given in parentheses.

In particular, as expected, the stability constant for the complexes of Mg^{2+} are the lowest, whereas Ni^{2+} shows the highest affinities. In Fig. 1.29 the distribution diagrams of the systems formed by the different divalent metal ion and the ligand under investigation at M/L=1/2 are compared. The complexation reaction starts at acidic values of pH for all the metal ions under analysis. Exception was represented by Mg^{2+}: coordination takes place in basic conditions, as at physiological pH is almost present as aqua ion.

1.2.3.3 Biological activity of the metal complexes **31-37**

None of the tested compounds showed activity against influenza virus: the compounds were tested in both enzymatic and in virus yield assays in MDCK cells to compare the data with the ones of the free ligands (see Table 1.5).

A possible explanation for the inactivity of copper and cobalt complexes (**36** and **34**) can be found looking at the chemical structure. While Mg, Mn, Ni and Zn complexes **31**, **33**, **35**, **37** are in the neutral form of the type $M(HL)_2$ or M_2L_2, the copper complex **36** is a tetranuclear cluster Cu_4L_4 stable also in solution, as evidenced by mass and solution studies. Completely different is the case for compound **34**, that is a Co(III) complex with a ionic nature $[CoL_2](NHEt_3)$. Therefore, for copper and cobalt coordination compounds a very different structural situation can be observed and their inactivity could be explained, for example, considering their difficulty to pass the cell membrane. The biological inactivity of these compounds can be considered a proof of the stability of the complexes in the condition of the assay.

Compounds were also tested against other virus such as herpes virus (HSV, HSV-1, HSV-2), vaccinia virus (VV), vesicular stomatitis (VSV) and adenovirus (Ad-2). Results are reported in Table 1.6.

Compound	Antiviral activity (EC_{50} in uM)						Cytotoxicity
	HSV-1	HSV-1/TK	HSV-2	VV	VSV	Ad-2	MCC in uM
H_2L_1	1.6	2.6	2.2	1.3	>100	>100	60
31	1.3	0.8	1.1	0.6	>100	>100	>20
33	1.1	1.6	0.6	0.5	>100	>100	>20
34	>100	>100	>100	>100	>100	>100	20
35	1.8	1.8	4.3	2.9	>100	>100	100
36	>100	>100	>100	>100	>100	>100	0.8
37	1.1	0.8	0.8	0.4	>100	>100	>20
Brivudin	0.05	30	173	17	>250	ND	>250
Acyclovir	0.25	10	0.09	>250	>250	ND	>250
Ganciclovir	0.025	0.5	0.025	>100	>100	ND	>100
Cidofovir	0.95	1.1	0.65	16	>250	7.9	>250
Zalcitabine	ND	ND	ND	ND	ND	7.5	>250
Alovudine	ND	ND	ND	ND	ND	16	>250

Table 1.6 Antiviral activity and cytotoxicity of H_2L_1 and its metal complexes in culture of human embryonic lung fibroblast cell.

1.2.3.4 Crystal structures of complexes **34** and **36**

Compound **34** has been obtained as extremely twinned and weakly diffracting crystals, which nevertheless allowed unambiguous determination of the structure of the salt $[Co(L_1)_2(NHEt_3)]$ (Fig. 1.30).

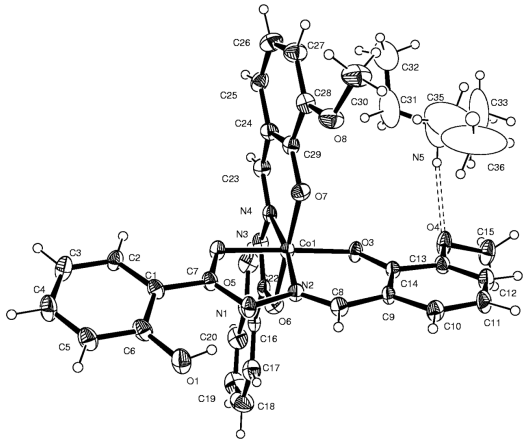

Fig. 1.30 Crystal structure and labelling of compound 34. Thermal ellipsoids at the 50% probability level. Hydrogens are drawn as fixed-size spheres of 0.11 Å of radius.

In the octahedral anionic bischelated complex, the two deprotonated ligands are coordinated by the same tridentate ONO chelation mode, as observed in the copper tetranuclear complex, forming a six-membered and one five-membered chelate ring with bite angles of 95° and 83°, respectively, for both ligands. The structure of the complex unit is stabilised by an intramolecular OH···N hydrogen bond where the nitrogen atom of the amide group acts as the hydrogen bond acceptor. (O5-H···N3= 2.56(1)Å, 148(1)°; O1-H···N1= 2.58(1)Å, 145(1)°). The $NHEt_3^+$ cation forms a hydrogen bond to the methoxy group of one of the two coordinated ligands (N5-H···O4=3.19(2)Å, 170(1)°).

Single crystals of $Cu_4L_4{\cdot}4CH_3CN$ were obtained by slow evaporation of a saturated solution of the compound in acetonitrile. Table 1.7 reports crystal data and structure analysis.

	$Cu_4L_4.4CH_3CN$
Empirical formula	$(C_{15}H_{12}CuN_2O_4)_4{\cdot}4CH_3CN$
Formula weight	1555.44
Temperature/K	293(2)
Crystal system	tetragonal
Space group	$I4_1/a$
a/Å	13.470(1)
b/Å	13.47
c/Å	38.680(4)
α/°	90
β/°	90
γ/°	90
Volume/$Å^3$	7018.6(16)
Z	16
ρ_{calc} g/cm^3	1.472
μ/mm^{-1}	1.271
F(000)	3184
Radiation	MoKα (λ = 0.71073)
2Θ range /°	3.202 to 48.052
Reflections collected	34451
Independent reflections	2760
Data/restraints/parameters	2760/0/231
Goodness-of-fit on F^2	1.024
Final R indexes [I>=2σ (I)]	R1 = 0.0379, wR2 = 0.0844
Final R indexes [all data]	R1 = 0.0678, wR2 = 0.0965
Largest ΔF max/min /e $Å^{-3}$	0.34/-0.21

Table 1.7 Crystal data and structure refinement for $Cu_4L_4{\cdot}4CH_3CN$.

A molecule of acetonitrile solvent is found in the crystal structure packing, together with the tetranuclear complex. $Cu_4L_4{\cdot}4CH_3CN$ crystallizes in the tetragonal space group $I4_1/a$, and the molecular structure of the complex is shown in Fig. 1.31.

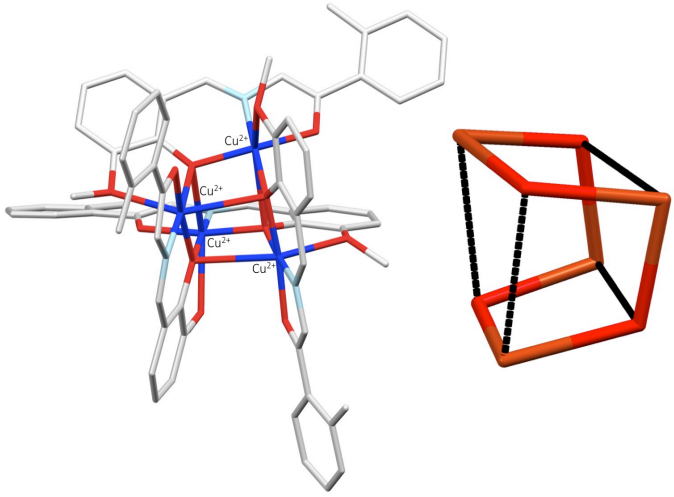

Fig. 1.31 Cu_4O_4 molecular core of the complex $Cu_4L_4{\cdot}4CH_3CN$. The elongation of the dotted bonds is due to the repulsion between ligand as evidenced in the image on the right.

The Cu_4L_4 neutral molecule is based on the monomeric unit shown in Fig. 1.31: the copper(II) ion is coordinated by a bideprotonated ligand in a tridentate O-N-O chelation mode, generating a five-membered and one six-membered chelation rings with bite angles of 82(1)° and 93(1)°, respectively. The unit is almost planar (rms deviation from planarity 0.18Å) as the rotatable terminal 2-hydroxy-phenyl ring is blocked, in the plane, thanks to an intramolecular hydrogen bond to the amidic nitrogen (O4-H…N1=2.593(6)Å, 128(6)°). That intramolecular hydrogen bond has been observed in analogous coordination compounds with acylhydrazonic ligands similar to H_2L_1: interestingly, it is responsible for the stabilization of the keto form in the keto-enol tautomerism of the ligand. The tetranuclear neutral complex is generated by a fourfold rotoinversion axis. The hydrazonic carbonyl O3 bridges three copper ions: the first through a short bond (1.957(3)Å, belonging to the O-N-O chelation), the second to the metal in the position (1/4-y, x-3/4,1/4-z) by a slightly longer bond

(1.991 Å) and the third at (1-x, -1/2-y, z) through a much longer contact (2.612(3)Å). The methoxy oxygen O2 is also involved in the coordination of a second copper ion, generating a five-membered chelation ring, in which both O2 and O3 are involved; the system is slightly distorted in the envelope conformation with the metal, with a deviation of 0.45 Å form the plane defined by the chelated system. The copper ion shows a distorted square planar coordination and the two apical positions are involved in longer contacts, completing a potential octahedral geometry. The resulting complex shows a Cu_4L_4 core with eight short (1.957 and 1.991 Å) and four long (2.612Å) Cu-O distances. The elongation of these contacts, that hinders the completion of the octahedral coordination, is due to the repulsion between the ligand skeletons that face each other and whose average plane diverge towards the outer part of the complex. The same complex has been previously described as the DMF solvate[131]: it is characterized by the same arrangement and the same space group but has a different cell and a different crystal packing; the crystal packing of $Cu_4L_4 \cdot 4CH_3CN$ is shown in Fig. 1.32.

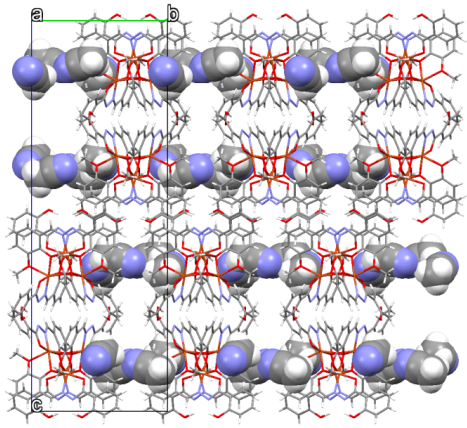

Fig. 1.32 Crystal packing of $Cu_4L_4 \cdot 4CH_3CN$. The solvent acetonitrile is highlighted in spacefilling representation.

1.3 CONCLUSIONS

A class of N-acylhydrazones were synthetized and completely characterised before be tested against influenza virus endonuclease. Biological analyses evidenced that the most successful scaffold is the group of compounds where R2 is a 3,4,5-trihydroxyphenyl. Docking studies confirmed that this activity is related to the interaction of the ligand with metal ions in the active site of the enzyme; this was further confirmed by the crystallographic structure of the ligand within the protein. The SAR analysis provided a relevant starting point for design of more potent and selective endonuclease inhibitors.

Metal complexes of the two prototype ligands **19** and **8** were synthesised and characterised with the common spectroscopic and spectrometric analyses. Metal complexes of ligand **8** showed potent antiviral activity in a broad-spectrum antiviral screening, with a promising activity in particular on HSV and vaccinia virus.

1.4 EXPERIMENTAL SECTION

1.4.1 Materials and methods.

1.4.1.1 Chemistry

All reagents of commercial quality were purchased from Sigma-Aldrich and used without further purification. The purity of the compounds was determined by elemental analysis and verified to be ≥ 95% for all synthesized molecules.

NMR spectroscopy. ^{1}H-NMR spectra were obtained in a 5 mm NMR precision tube at 298 K on a Bruker Avance 400 FT spectrophotometer. ^{1}H-NMR chemical shift were internally referenced to $(CHD_2)(CD_3)SO$ (2.50 ppm) for DMSO-d_6 and CD_3OD (3.31 ppm) for d_4-methanol-d_4. Data was processed using MestReNova 9.0.1 Mac version.

IR spectroscopy. The ATR-IR spectra were recorded by means of a Nicolet-Nexus (Thermo Fisher) spectrophotometer by using a diamond crystal plate in the range of 4000-400 cm^{-1}. Data was processed using the program OMNIC.

Elemental Analysis. Elemental analyses were performed by using a FlashEA 1112 series CHNS/O analyzer (Thermo Fisher) with gas-chromatographic separation.

Mass spectrometry. Electrospray mass spectral analyses (ESI-MS) were performed with an electrospray ionization (ESI) time-of-flight Micromass 4LCZ spectrometer. Samples were prepared in methanol.

Electronic impact mass spectra (EI-MS) were acquired in positive EI mode by means of a DEP-probe (Direct Exposure Probe) mounting on the tip of a Re-filament with a DSQII Thermo Fisher apparatus, equipped with a single quadrupole analyzer. Samples were prepared in methanol.

Elemental Analysis. Elemental analyses were performed by using a FlashEA 1112 series CHNS/O analyzer (Thermo Fisher) with gas-chromatographic separation.

UV-Vis spectroscopy. UV–Vis spectra were recorded on an Evolution 260 Bio Thermo spectrophotometer by using cells of 1 cm path length (600 μL). Spectra were recorded in the range 200-600 nm. UV-vis absorption spectra of **19** and **23** were registered using a ca. 10^{-5} M solution in methanol. Each metal/ligand system was studied by titrating a 2.8 ml sample of the ligand solution with a methanol solution of $Mg(CH_3COO)_2$; 8–12 spectra of samples with M:L molar *ratio* ranging from 0 to 6 were measured. Data was processed with Microsoft Excel 14.3.6 Mac version.

Computational Studies. The crystal structure of PA-Nter endonuclease in complex with epigallocatechin-3-gallate was retrieved from the RCSB Protein Data Bank (entry code 4AWM). The ligand and water molecules were discarded and the hydrogens were added to the protein by Discovery Studio 2.5. The charge on the metal ions was set as +2. The epigallocatechin-3-gallate, L-742,001, and 2-(4-(1*H*-tetrazol-5-yl)phenyl)-5-hydroxypyrimidin-4(3*H*)-one structures were extracted from their X-ray complexes (PDB IDs 4AWM, 4W9S and 4E5H respectively). The other ligand structures were constructed using Discovery Studio 2.5.5 (Accelrys, Discovery Studio) and energy minimized using the Smart Minimizer protocol (1000 steps), which combines the Steepest Descent and the Conjugate Gradient methods.

The minimized ligands were docked in their corresponding proteins by means of GOLD Suite 5.0.1[132]. The region of interest used by the GOLD program was defined in order to contain the residues within 15 Å from the original position of the ligand in the X-ray structure. The side-chain of residue Tyr24 was allowed to rotate according to the internal rotamer libraries in GOLD Suite

5.0.1. GoldScore was chosen as fitness function. The standard default settings were used in all calculations and the ligands were submitted to 100 genetic algorithm runs. The "allow early termination" command was deactivated. Results differing by less than 0.75 Å in ligand-all atom rmsd, were clustered together. The best GOLD-calculated conformation was used both for analysis and representation.

Potentiometric analyses. The metals stock solutions were prepared from $MgCl_2 \cdot 6H_2O$ (Aldrich), $MnCl_2 \cdot 4H_2O$ (Janssen), $CuCl_2 \cdot 2H_2O$ (Merck), $ZnCl_2$ (Anlyticals Carlo Erba) and $NiCl_2 \cdot 6H_2O$ (Merck). Their concentrations were determined by using EDTA as a titrant. Mn(II), Mg(II) and Zn(II), were titrated at pH=10 (ammonia/ammonium chloride as buffer; indicator: sodium salt of Eriochrome Black T). Mn(II) was titrated in the presence of triethanolamine and hydroxylamine chloride. For Ni(II) was used Muresside in potassium nitrate as an indicator. For Cu(II), the titrations were performed in the presence of concentrate ammonia using Fast Sulfon Black as indicator. Equilibrium constants at 25 ± 0.1 °C for protonation and complexation reactions were determined by means of potentiometric measurements in methanol/water = 9:1 v/v solution at ionic strength 0.1 M KCl, carried out under nitrogen in the pH range 2.5−11. Potentiometric titrations were carried out by a fully automated apparatus equipped with a CRISON GLP 21−22 digital voltmeter (resolution, 0.1 mV) and a 5 mL Metrohm Dosimat 655 autoburet, both controlled by a homemade software in BASIC, working on an IBM computer. Temperature was controlled to ±0.1 °C by using a thermostated circulating water bath (ISCO GTR 2000 IIx). Appropriate aliquots of ligand H_2L solution, prepared by weight, were titrated with standard KOH (methanol/water = 9:1 v/v, I = 0.1 M KCl) with and without metal ions, applying constant speed magnetic stirring. Freshly boiled methanol and double-distilled water, kept under nitrogen, were

used throughout. The experimental procedure to reach high accuracy in the determination of the equilibrium constants in this mixed solvent has been described in detail elsewhere[133]. The protonation constants of H_2L were obtained by titrating 20 mL of samples of the ligand (5×10^{-3} M). The speciation was defined by performing the titrations at different ligand/metal ratios (1 up to 4) and using a halved concentration of the ligand, to avoid solubility problems. At least two measurements (about 60 experimental points each) were performed for each system. The electrodic chain (Crison 5250 glass electrode and 0.1 M KCl in methanol/water = 9/1 v/v calomel electrode, Radiometer 401) was calibrated in terms of $[H^+]$ by means of a strong acid−strong base titration by Gran's method[134] allowing the determination of the standard potential, $E°$ (371.5 ± 0.4 mV), and of the ionic product of water, K_w (pK_w=14.40 ± 0.05) in the experimental conditions used. The software HYPERQUAD[135] was used to obtain the speciation and the logarithm of the stability constants ($\log \beta_{pqr}$) from titration data. $\beta_{pqr} = [M_pL_qH_r]/[M]^p\,[L]^q\,[H]^r$ is the equilibrium constant for the reaction $pM + qL + rH = M_pL_qH_r$, in which M indicates the metal, L the completely deprotonated ligand, H the proton and charges are omitted for simplicity.

X-Ray spectroscopy. A PA_N construct ($PA_N^{\Delta Loop}$) with a loop (residues 51-72) deleted and replaced with GGS from A/California/04/2009 H1N1 strain was used for the crystallographic studies. The details of cloning, over-expression and purification are described elsewhere[19, 136]. Briefly, the gene was cloned into pET52b vector and transformed into BL21 (DE3) cells, and the protein was expressed in LB medium overnight at 18 °C after induction at an OD_{600} ~0.8 with 0.2 mM isopropyl-β-thiogalactopyranoside (IPTG). The protein was purified from cell lysates by HisTrap affinity chromatography and the 10xHis tag was removed by digestion with thrombin. The protein was further purified

by gel filtration using a Superdex 75 size-exclusion chromatography column in 20 mM Tris pH 8.0, 150 mM NaCl and 1 mM TCEP. The protein was concentrated to 10-12 mg/ml for crystallization. Crystals were grown in 0.2 M $MgCl_2$, 2mM $MnCl_2$, 0.1 M Tris pH 8.5, 30% (w/v) PEG 4000 using the hanging drop method. For determination of the protein-inhibitor complex structure, the powder of the inhibitor was sprinkled on a 2 µl drop of a 1:1 ratio mixture of protein solution and well solution, on a cover slide hanging over 500 µl well solution, and left overnight. Next day, the crystals were cryo-protected using well solution supplemented with 25% ethylene glycol and flash frozen in liquid nitrogen. The data were collected at the 22-ID beam line maintained by SERCAT (Southeast Regional Collaborative Access Team) at the Advanced Photon Source, Argonne National Laboratory. The data were indexed, integrated and scaled using the HKL2000 suite of programs [137]. Phase determination, structure refinement and model building were completed using Phaser, Refmac and Coot (part of the CCP4 package)[138]. The apo structure of $PA_N^{\Delta Loop}$ (PDB ID: 5DES) was used as starting model for molecular replacement.

Single crystals of $Cu_4L_4 \cdot 4CH_3CN$ were selected and mounted on glass fibers to collect data on a SMART Breeze diffractometer. The crystals were kept at 293 K during data collection. Using Olex2[139], the structure was solved with the SIR2004[140] structure solution program using Direct Methods and refined with the ShelXL refinement package [141] using Least Squares minimization. Anisotropic displacement parameters were refined for all non-hydrogen atoms. Hydrogen atoms were partly introduced in calculated positions riding on their carrier atoms.

1.4.1.2 Biological tests

Biological assay. Both cells lines were cultivated in Dulbecco's modified Eagle medium (DMEM) supplemented with 10% fetal calf serum FCS), 1 mM sodium pyruvate, and 0.075% sodium bicarbonate. During virus experiments, the MDCK cells were maintained in MDCK infection medium, consisting of Ultra MDCK medium supplemented with 0.0225% sodium bicarbonate, 2 mM L-glutamine and 2 µg/ml tosylphenylalanylchloromethylketone (TPCK)-treated trypsin. The cells were incubated in a humidified atmosphere containing 5% of CO_2. The enzymatic endonuclease activity assay was performed according to a previous published method[142] with minor modifications. One microgram of recombinant PA-Nter was incubated with 1 µg of single stranded circular DNA plasmid in the presence of the test compounds and at the final volume of 25 µL. The assay buffer contained 50 mM tris-HCl pH=8, 100 mM NaCl, 10 mM β-mercaptoethanol and 1 mM $MnCl_2$. The reaction was incubated at 37°C for 2h and then stopped by heat inactivation (80°C, 20 min). The endonucleolytic digestion of the plasmid was visualized by gel electrophoresis on a 1% agarose gel with ethidium bromide staining. The amount of remaining intact plasmid was quantified by ImageQant TL software. The percentage inhibition of PA endonuclease activity was plotted against the compound concentration of semi-logarithmic plot, using GraphPad Prism software. Values were the mean ± SEM of three independent experiments. The 50% inhibitory concentrations (IC_{50}) were obtained by nonlinear least-squares regression analysis. To determine anti-influenza virus activity in infected cell cultures, we performed a virus yield assay as described in Meneghesso et al.[143] with minor modifications. One day prior to infection, MDCK cells were seeded into 96-well plates at 25.000 cells per well. At day 0, serial dilutions of the test compounds were added, after 16 h. of incubation at 35°C, the cells were infected with influenza A/PR/8/34 virus

and the compounds were added, immediately followed by infection. After 24 h. of incubation at 35°C, the supernatants were collected and stored at -80°C. The virus amount in these samples was estimated by determining the viral genome copy number in a one-step quantitative real-time reverse transcription (qRT)-PCR assay with influenza virus M1-specific primers and probe. Absolute quantification of vRNA copies was performed by including an M1-plasmid standard. The EC_{99} and EC_{90} values were calculated by interpolation from data of at least three experiments and defined as the compound concentration causing respectively a 2-$\log_{10}$ and 1-$\log_{10}$ reduction in viral RNA copy number, as compared to the virus control receiving no compound. In parallel, the CC_{50} values after 24 h. of incubation with compounds were determined in uninfected MDCK cells, using the MTS cell viability assay. Ribavirin was included as the reference compound.

1.4.2 Ligands syntheses

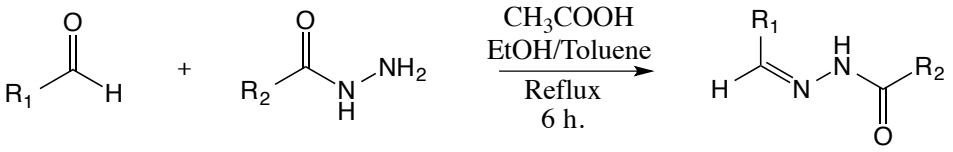

Scheme 1.1 General synthesis for N-acylhydrazones 1-27.

All the N-acylhydrazones were prepared following a reported procedure (Scheme 1.1) [144]. To a solution of the proper aldehyde in absolute ethanol, or toluene, an equimolar amount of the proper hydrazide, dissolved in the same solvent, was added. The mixture has been refluxed for 6 hours, cooled at room temperature and concentrated in vacuum. The resulting precipitate was filtered off, washed with cold ethanol and dried under vacuum.

N'-(2,3-dihydroxybenzylidene)-semicarbazide ***(1)***. Pink powder. Yield=54%. ^{1}H-NMR (DMSO-d_6, 25°C), δ: 6.36 (s, 2H, NH_2); 6.64 (t, 1H, J=8 Hz, CH_{Ar}); 6.76 (d, 1H, J=8 Hz, CH_{Ar}); 7.17 (d, 1H, J=8 Hz, CH_{Ar}); 8.14 (s, 1H, CH=N); 9.21 (s, 1H, OH); 9.39 (s, 1H, OH); 10.18 (s, 1H, NH). EI-MS ($C_8H_9N_3O_3$, CH_3OH): m/z=195.2 $[M]^+$. IR (cm^{-1}): ν_{NH}=3455, ν_{OH}=3166, $\nu_{C=O}$=1694, $\nu_{C=N}$=1592. Anal. Calcd for $C_8H_9N_3O_3$: C=49.23, H=4.65, N=21.53. Found: C=49.64, H=4.71, N=21.71.

N'-(2-hydroxy-3-methoxybenzylidene)-semicarbazide ***(2)***. Pink powder. Yield=81%. ^{1}H-NMR (DMSO-d_6, 25°C), δ: 3.84 (s, 3H, OCH_3); 6.39 (s, 2H, NH_2); 6.76 (t, 1H, J=8 Hz, CH_{Ar}); 6.92 (d, 1H, J=8 Hz, CH_{Ar}); 7.37 (d, 1H, J=8 Hz, CH_{Ar}); 8.17 (s, 1H, CH=N); 9.20 (s, 1H, OH); 10.20 (s, 1H NH). EI-MS ($C_9H_{11}N_3O_3$, CH_3OH): m/z=209.2 $[M]^+$. IR (cm^{-1}): ν_{NH}=3466, ν_{OH}=3170-3280

(br), $\nu_{C=O}$=1672, $\nu_{C=N}$=1586. Anal. Calcd for $C_9H_{11}N_3O_3 \cdot 1/4H_2O$: C=50.58, H=5.42, N=19.66. Found: C=50.67, H=5.37, N=19.44.

*N'-(2,3-dihydroxybenzylidene)heptylhydrazide (**3**)*. White powder. Yield=95%. ^{1}H-NMR (DMSO-d_6, 25°C), δ (overlapping isomer, 33%): 0.83-0.86 (m, CH_3); 1.16-1.26 (m, CH_2); 1.54-1.59 (m, CH_2); 2.17-2.29 (m, CH_2); 2.53-2.59 (m, 6.64-6.73, CH_2); 6.81-6.84 (m, overlapping isomers, CH_{Ar}); **6.92**, 7.03 (d, 1H, CH_{Ar}); **8.23**, 8.28 (s, 1H, CH=N); 9.21 (s, 1H, OH); 9.49 (s, 1H, OH); 11.06, 11.20, 11.59 (3s, 2H+1H, NH+OH). ESI-MS ($C_{15}H_{22}N_2O_3$, CH_3OH): m/z=301 $[M+Na]^+$. IR (cm^{-1}): ν_{NH}=3490, ν_{OH}=2922-2941, $\nu_{C=O}$=1663. Anal. Calcd for $C_{15}H_{22}N_2O_3 \cdot 1/2H_2O$: C=62.70; H=8.07; N=9.75. Found: C=62.84; H=7.97; N=9.88.

*N'-(2-hydroxy-3-methoxybenzylidene)heptylhydrazide (**4**)*. White powder. Yield=41%. ^{1}H-NMR (DMSO-d_6, 25°C), δ (overlapping isomers, 37.5%): 0.83-0.86 (m, CH_3); 1.26-1.27 (m, CH_2); 1.55-1.59 (m, CH_2); 2.18-2.23 (m, CH_2); 2.52-2.57 (m, CH_2); 3.79 (s, OCH_3); 6.80-6.86 (m, CH_{Ar}); 6.94-7.01 (m, CH_{Ar}); **7.08**, 7.20 (d, 1H, CH_{Ar}); **8.27**, 8.34 (s, 1H, CH=N); 9.54 (s, 1H, OH); 10.96, 11.25, 11.57 (3s, 1H+2H, NH+OH). EI-MS ($C_{16}H_{24}N_2O_3$, CH_3OH): m/z=292 $[M]^+$. IR (cm^{-1}): ν_{NH}=3182; ν_{OH}=3072, 2917; $\nu_{C=O}$=1663. Anal. Calcd for $C_{16}H_{24}N_2O_3$: C=65.73; H=8.27; N=9.58. Found: C=65.76; H=8.42; N=9.45.

*N'-(2,3-dihydroxybenzylidene)benzoylhydrazide (**5**)*. Yellow powder. Yield=32%. ^{1}H-NMR (DMSO-d_6, 25°C), δ: 6.74 (t, 1H, J=8 Hz, CH_{Ar}); 6.86 (d, 1H, J=7 Hz, CH_{Ar}); 6.97 (d, 1H, J=7 Hz, CH_{Ar}); 7.52-7.61 (m, 3H, CH_{Ar}); 7.94 (d, 2H, J=7 Hz, CH_{Ar}); 8.59 (s, 1H, CH=N); 9.28 (s, 1H, OH); 11.16 (s, 1H, NH); 12.14 (s, 1H, OH). EI-MS ($C_{14}H_{12}N_2O_3$, CH_3OH): m/z= 256.2 $[M]^+$. IR

(cm^{-1}): ν_{NH}=3280; ν_{OH}=3047; $\nu_{C=O}$=1658; $\nu_{C=N}$=1527. Anal. Calcd for $C_{14}H_{12}N_2O_3 \cdot 1/4H_2O$: C=64.48; H=4.83; N=10.74. Found: C=64.64; H=4.71; N=10.71.

*N'-(2-hydroxy-3-methoxybenzylidene)benzoylhydrazide (**6**)*. White powder. Yield=89%. ^{1}H-NMR (DMSO-d_6, 25°C), δ: 3.81 (s, 3H, OCH_3); 6.87 (t, 1H, J=8 Hz, CH_{Ar}); 7.04 (d, 1H, J=7 Hz, CH_{Ar}); 7.15 (d, 1H, J=7 Hz, CH_{Ar}); 7.52-7.64 (m, 3H, CH_{Ar}); 7.94 (d, 2H, J=7 Hz, CH_{Ar}); 8.65 (s, 1H, CH=N); 11.01 (s, 1H, NH); 12.05 (s, 1H, OH). EI-MS ($C_{15}H_{14}N_2O_3$, CH_3OH): m/z=270.1 $[M]^+$. IR (cm^{-1}): ν_{NH+OH}=2830-3072 (br); $\nu_{C=O}$=1657; ν_{OCH3}=1249, 1076. Anal. Calcd for $C_{15}H_{14}N_2O_3 \cdot H_2O$: C=62.49; H=5.59; N=9.72. Found: C=62.88; H=5.59; N=9.94.

*N'-(2,3-dihydroxybenzylidene)-2-hydroxybenzoylhydrazide (**7**)*. Brown powder. Yield=30%. ^{1}H-NMR (DMSO-d_6, 25°C), δ: 6.75 (t, 1H, J=8 Hz, CH_{Ar}); 6.87 (d, 1H, J=7 Hz, CH_{Ar}); 6.94-7.00 (m, 3H, CH_{Ar}); 7.43 (t, 1H, J=8 Hz, CH_{Ar}); 7.88 (d, 2H, J=7 Hz, CH_{Ar}); 8.64 (s, 1H, CH=N); 9.32 (s, 1H, OH); 11.03 (s, 1H, NH); 12.05 (s, 2H, OH). EI-MS ($C_{14}H_{12}N_2O_4$, CH_3OH): m/z=272.1 $[M]^+$. IR (cm^{-1}): ν_{NH+OH}=2980-3256 (br); $\nu_{C=O}$=1635. Anal. Calcd for $C_{14}H_{12}N_2O_4$·: C=61.76; H=4.44; N=10.29. Found: C=61.97; H=4.43; N=10.20.

*N'-(2-hydroxy-3-methoxybenzylidene)-2-hydroxybenzoylhydrazide (**8**)*. Yellow powder. Yield=89%. ^{1}H-NMR (DMSO-d_6, 25°C), δ: 3.82 (s, 3H, OCH_3); 6.85-7.06 (m, 4H, CH_{Ar}); 7.17 (d, 1H, J=7.5 Hz, CH_{Ar}); 7.45 (t, 1H, J=7.5 Hz, CH_{Ar}); 7.89 (d, 2H, J=7.5 Hz, CH_{Ar}); 8.69 (s, 1H, CH=N); 10.87 (s, 1H, NH); 11.99 (s, 2H, OH). EI-MS ($C_{15}H_{14}N_2O_4$, CH_3OH): m/z= 286.0 $[M]^+$. IR (cm^{-1}): ν_{NH+OH}=2993-3211 (br); $\nu_{C=O}$=1606; $\nu_{C=N}$=1560; ν_{OCH3}=1256, 1079. Anal.

Calcd for $C_{15}H_{14}N_2O_4 \cdot 1/2H_2O$: C=61.01; H=5.12; N=9.49. Found: C=61.20; H=4.89; N=9.58.

N'-(2,4,5-trihydroxyphenyl)-2-hydroxybenzoylhydrazide ***(9)***. Yellow powder. Yield=84%. ^{1}H-NMR (DMSO-d_6, 25°C), δ: 6.35 (s, 1H, CH_{Ar}); 6.93-6.98 (m, 3H, CH_{Ar}); 7.44 (t, 1H, J=7 Hz, CH_{Ar}); 7.89 (d, 1H, J=7 Hz, CH_{Ar}); 8.50 (s, 1H; CH=N); 8.62 (s, 1H, OH); 9.61 (s, 1H, OH); 10.50 (s, 1H, NH); 11.81, 12.00 (s, 1H, OH). EI-MS ($C_{14}H_{12}N_2O_5$, CH_3OH): m/z=288.1 $[M]^+$. IR (cm^{-1}): ν_{NH+OH}=3274-3420 (br); $\nu_{C=O}$=1634. Anal. Calcd for $C_{14}H_{12}N_2O_5 \cdot H_2O$: C=54.90; H=4.61; N=9.15. Found: C=54.65; H=4.72; N=9.29.

N'-(2,4,6-trihydroxyphenyl)-2-hydroxybenzoylhydrazide ***(10)***. Red powder. Yield = 65%. ^{1}H-NMR (DMSO-d_6, 25°C), δ: 5.86 (s, 2H, CH_{Ar}); 6.93-6.98 (m, 2H, CH_{Ar}); 7.45 (t, 1H, J=7 Hz, CH_{Ar}); 7.88 (d, 1H, J=7 Hz, CH_{Ar}); 8.83 (s, 1H, CH=N); 9.89 (s, 1H, OH); 11.09 (s, 1H, NH); 11.95, 11.97 (s, 1H, OH). EI-MS ($C_{14}H_{12}N_2O_5$, CH_3OH): m/z=288.1 $[M]^+$. IR (cm^{-1}): ν_{NH+OH}=3100-3360 (br); $\nu_{C=O}$= 631. Anal. Calcd for $C_{14}H_{12}N_2O_5 \cdot H_2O$: C=54.90; H=4.61; N=9.15. Found: C=54.82; H=4.52; N=9.42.

N'-(3,4,5-trihydroxyphenyl)-2-hydroxybenzoylhydrazide ***(11)***. White powder. Yield=76 %. ^{1}H-NMR (DMSO-d_6, 25°C), δ: 6.72 (s, 2H, CH_{Ar}); 6.92-6.97 (m, 2H, CH_{Ar}); 7.43 (t, 1H, J=7 Hz, CH_{Ar}); 7.88 (d, 1H, J=7 Hz, CH_{Ar}); 8.19 (s, 1H, CH=N); 8.67 (s, 1H, OH); 9.18 (s, 2H, OH); 11.67 (s, 2H, NH); 12.03 (s, 1H, OH). EI-MS ($C_{14}H_{12}N_2O_5$, CH_3OH): m/z=287.9 $[M]^+$. IR (cm^{-1}): ν_{NH+OH}=3280-3321 (br); $\nu_{C=O}$=1637. Anal. Calcd for $C_{14}H_{12}N_2O_5$: C=58.33; H=4.20; N=9.72. Found: C=58.19; H=4.03; N=9.54.

N'-(2,5-dihydroxybenzylidene)-3,4,5-trimethoxybenzoylhydrazone ***(12)***. White powder. Yield=90%. ^{1}H-NMR (DMSO-d_6, 25°C), δ: 3.74 (s, 3H, OCH_3); 3.87 (s, 6H, OCH_3); 6.74 (m, 2H, CH_{Ar}); 7.00 (s, 1H, CH_{Ar}); 7.27 (s, 2H, CH_{Ar}); 8.59 (s, 1H, CH=N); 8.98 (s, 1H, OH); 10.34 (s, 1H, NH); 11.83 (s, 1H, OH). EI-MS ($C_{17}H_{18}N_2O_6$, CH_3OH): m/z=346.3 $[M]^+$. IR (cm^{-1}): ν_{NH}=3274, ν_{OH}=3090-3160 (br); $\nu_{C=O}$=1654. Anal. Calcd for $C_{17}H_{18}N_2O_6$: C=58.96; H=5.24; N=8.09. Found: C=58.82; H=5.52; N=8.15.

N'-phenyl-3,4,5-trihydroxybenzoylhydrazide ***(13)***. Brown powder. Yield=70%. ^{1}H-NMR (DMSO-d_6, 25°C), δ: 6.93 (s, 2H, CH_{Ar}); 7.44 (m, 3H, CH_{Ar}); 7.68 (d, 2H, J=8 Hz, CH_{Ar}); 8.41 (s, 1H, CH=N); 8.84 (s, 1H, OH); 9.15 (s, 2H, OH); 11.54 (s, 1H, NH). EI-MS ($C_{14}H_{12}N_2O_4$, CH_3OH): m/z=272.1 $[M]^+$. IR (cm^{-1}): ν_{OH}=3534, ν_{NH+OH}=3226-3327, (br); $\nu_{C=O}$=1590. Anal. Calcd for $C_{14}H_{12}N_2O_4$·: C=61.76; H=4.44; N=10.29. Found: C=61.55; H=4.67; N=10.04.

N'-(2-hydroxy-benzylidene)-3,4,5-trihydroxybenzoylhydrazone ***(14)***. Brown powder. Yield=79%. ^{1}H-NMR (DMSO-d_6, 25°C), δ: 6.90-6.95 (m, 4H, CH_{Ar}); 7.29 (t, 1H, J=8 Hz, CH_{Ar}); 7.47 (d, 2H, J=8 Hz, CH_{Ar}); 8.58 (s, 1H, CH=N); 8.89 (s, 1H, OH); 9.20 (s, 2H, OH); 11.49 (s, 1H, OH); 11.84 (s, 1H, NH). EI-MS ($C_{14}H_{12}N_2O_5$, CH_3OH): m/z=288.1 $[M]^+$. IR (cm^{-1}): ν_{OH}=3534, ν_{NH+OH}=3226-3327, (br); $\nu_{C=O}$=1590. Anal. Calcd for $C_{14}H_{12}N_2O_5$·: C=58.33; H=4.20; N=9.72. Found: C=58.67; H=4.25; N=9.80.

N'-(2,5-dihydroxybenzylidene)-3,4,5-trihydroxybenzoylhydrazide ***(15)***. Yellow powder. Yield=59%. ^{1}H-NMR (DMSO-d_6, 25°C), δ: 6.74 (m, 2H, CH_{Ar}); 6.89 (s, 1H, CH_{Ar}); 6.94 (s, 2H, CH_{Ar}); 8.50 (s, 1H, CH=N); 8.89, 9.00 (s, 2H, OH); 9.22 (s, 1H, OH); 10.60 (s, 1H, NH); 11.74 (s, 1H, OH). EI-MS ($C_{14}H_{12}N_2O_6$,

CH_3OH): m/z=304.1 $[M]^+$. IR (cm^{-1}): ν_{OH}=3403 (br); ν_{NH+OH}=3215 (br); $\nu_{C=O}$=1592. Anal. Calcd for $C_{14}H_{12}N_2O_6 \cdot H_2O$: C=52.18; H=4.38; N=8.69. Found: C=52.44; H=4.44; N=8.58.

N'-(2-hydroxy-5-methoxybenzylidene)-3,4,5-trihydroxybenzoylhydrazide ***(16)***. Yellow powder. Yield=92%. ^{1}H-NMR (DMSO-d_6, 25°C), δ: 3.73 (s, 3H, OCH_3); 6.84-6.91 (m, 2H, CH_{Ar}); 6.94 (s, 1H, CH_{Ar}); 7.06 (s, 1H, CH_{Ar}); 8.56 (s, 1H, CH=N); 8.97 (s, 3H, OH); 10.89 (s, 1H, NH); 11.83 (s, 1H, OH). EI-MS ($C_{15}H_{14}N_2O_6$, CH_3OH): m/z=318.3 $[M]^+$. IR (cm^{-1}): ν_{OH} =3496, ν_{NH+OH}=3178 (br); $\nu_{C=O}$=1654. Anal. Calcd for $C_{15}H_{14}N_2O_6$: C=56.60; H=4.43; N=8.80. Found: C=56.89; H=4.32; N=8.96.

N'-(2,4-dihydroxybenzylidene)-3,4,5-trihydroxybenzoylhydrazide ***(17)***. Brown powder. Yield=43%. ^{1}H-NMR (DMSO-d_6, 25°C), δ: 6.31 (s, 1H, CH_{Ar}); 6.36 (d, 1H, J=8 Hz, CH_{Ar}); 6.92 (s, 2H, CH_{Ar}); 7.24 (d, 1H, J=8 Hz, CH_{Ar}); 8.45 (s, 1H, CH=N); 9.18 (s, 2H, OH); 9.93 (s, 1H, OH); 11.63 (m, 1H+1H, NH+OH). EI-MS ($C_{14}H_{12}N_2O_6$, CH_3OH): m/z=304.1 $[M]^+$. IR (cm^{-1}): ν_{OH}=3552; ν_{NH+OH}=3261-3320 (br); $\nu_{C=O}$=1630; $\nu_{C=N}$= 565. Anal. Calcd for $C_{14}H_{12}N_2O_6$·: C=55.27; H=3.98; N=9.21. Found: C=55.02; H=3.88; N=9.20.

N'-(2,3-dihydroxybenzylidene)-3,4,5-trihydroxybenzoylhydrazide ***(18)***. Yellow powder. Yield=83%. ^{1}H-NMR (DMSO-d_6, 25°C), δ: 6.73 (t, 1H, J=8 Hz, CH_{Ar}); 6.84 (d, 1H, J=7 Hz, CH_{Ar}); 6.90 (d, 1H, CH_{Ar}); 6.95 (s, 2H, CH_{Ar}); 8.53 (s, 1H, CH=N); 8.89 (s, 1H, OH); 9.12 (s, 1H, OH); 9.21 (s, 2H, OH); 11.41 (s, 1H, NH); 11.83 (s, 1H, OH). EI-MS ($C_{14}H_{12}N_2O_6$, CH_3OH): m/z=304.0 $[M]^+$. IR (cm^{-1}): ν_{NH+OH}=3255 (br); $\nu_{C=O}$=1654. Anal. Calcd for $C_{14}H_{12}N_2O_6$·: C=55.27; H=3.98; N=9.21. Found: C=55.04; H=4.12; N=9.15.

N'-(2-hydroxy-3-methoxybenzylidene)-3,4,5-trihydroxybenzoylhydrazide ***(19, H_2L)***. Yellow powder. Yield=61%. ^{1}H-NMR (DMSO-d_6, 25°C), δ: 3.81 (s, 3H, OCH_3); 6.85 (t, 1H, J=8 Hz, CH_{Ar}); 6.94 (s, 2H, CH_{Ar}); 7.03 (d, 1H, J=8 Hz, CH_{Ar}); 7.08 (d, 1H, J=8 Hz, CH_{Ar}); 8.58 (s, 1H, CH=N); 8.90 (s, 1H, OH); 9.19 (s, 2H, OH); 11.25 (s, 1H, NH); 11.80 (s, 2H, OH). ^{1}H-NMR (MeOD-d_4, 25°C), δ: 3.91 (s, 3H, OCH_3); 6.91 (t, 1H, J=8 Hz, CH_{Ar}); 7.03-7.07 (m, 3H, CH_{Ar}); 7.23 (d, 1H, J=7.5 Hz, CH_{Ar}); 8.57 (s, 1H, CH=N). ^{13}C-NMR (MeOD-d_4, 25°C), δ: 55.43; 107.11; 113.72; 118.87; 119.10; 121.39; 122.90; 137.54; 145.61; 147.48; 148.17; 148.54; 164.75. EI-MS ($C_{15}H_{14}N_2O_6$, CH_3OH): m/z=318.0 $[M]^+$. IR (cm^{-1}): ν_{OH}=3418; ν_{NH+OH}=3222 (br); $\nu_{C=O}$=1664; $\nu_{C=N}$=1598; ν_{OCH3}=1252, 1033. Anal. Calcd for $C_{15}H_{14}N_2O_6 \cdot H_2O$: C=53.57; H=4.80; N=8.33. Found: C=53.50; H=4.88; N=7.92.

N'-(2,3,4-trihydroxyphenyl)-3,4,5-trihydroxybenzoylhydrazide ***(20)***. White powder. Yield=25%. ^{1}H-NMR (DMSO-d_6, 25°C), δ: 6.38 (d, 1H, J=9 Hz, CH_{Ar}); 6.72 (d, 1H, J=9 Hz, CH_{Ar}); 6.92 (s, 2H, CH_{Ar}); 8.41 (s, 1H, CH=N); 8.44 (s, 1H, OH); 8.86 (s, 1H, OH); 9.19 (s, 2H, OH); 9.40 (s, 1H, OH); 11.66 (s, 1H, NH); 11.72 (s, 1H, OH). EI-MS ($C_{14}H_{12}N_2O_7$, CH_3OH): m/z=319.9 $[M]^+$. IR (cm^{-1}): ν_{NH+OH}=3298-3420 (br); $\nu_{C=O}$=1608. Anal. Calcd for $C_{14}H_{12}N_2O_7$.: C=52.51; H=3.78; N=8.75. Found: C=52.42; H=3.88; N=8.56.

N'-(2,4,5-trihydroxyphenyl)-3,4,5-trihydroxybenzoylhydrazide ***(21)***. Yellow powder. Yield=83%. ^{1}H-NMR (DMSO-d_6, 25°C), δ: 6.32 (s, 1H, CH_{Ar}); 6.79 (s, 1H, CH_{Ar}); 6.91 (s, 2H, CH_{Ar}); 8.38 (s, 1H, CH=N); 8.53 (s, 1H OH); 8.83 (s, 1H, OH); 9.16 (s, 2H, OH); 9.52 (s, 1H, OH); 10.83 (s, 1H, NH); 11.52 (s, 1H, OH). EI-MS ($C_{14}H_{12}N_2O_7$, CH_3OH): m/z=320.1 $[M]^+$. IR (cm^{-1}):

ν_{NH+OH}=3250-3300 (br); $\nu_{C=O}$=1635. Anal. Calcd for $C_{14}H_{12}N_2O_7$·: C=52.51; H=3.78; N=8.75. Found: C=52.35; H=4.02; N=8.67.

N'-(2,4,6-trihydroxyphenyl)-3,4,5-trihydroxybenzoylhydrazide ***(22)***. Red powder. Yield=72%. ^{1}H-NMR (DMSO-d_6, 25°C), δ: 5.83 (s, 2H, CH_{Ar}); 6.90 (s, 2H, CH_{Ar}), 8.75 (s, 1H, CH=N); 8.85 (s, 1H, OH); 9.18 (s, 2H, OH); 9.77 (s, 1H, OH); 11.12 (2s, 1H+1H, NH+OH); 11.60 (s, 1H, OH). EI-MS ($C_{14}H_{12}N_2O_7$, CH_3OH): m/z=320.2 $[M]^+$. IR (cm^{-1}): ν_{NH+OH}=3298-3420 (br); $\nu_{C=O}$=1608. Anal. Calcd for $C_{14}H_{12}N_2O_7$·: C=52.51; H=3.78; N=8.75. Found: C=52.74; H=3.51; N=8.53.

N'-(3,4,5-trihydroxyphenyl)-3,4,5-trihydroxybenzoylhydrazide ***(23)***. White powder. Yield=73%. ^{1}H-NMR (DMSO-d_6, 25°C), δ: 6.65 (s, 2H, CH_{Ar}); 6.89 (s, 2H, CH_{Ar}); 8.12 (s, 1H, CH=N), 8.55 (s, 1H, OH); 8.80 (s, 1H, OH); 9.11-9.14 (m, 4H, NH+OH); 11.26 (s, 1H, OH). EI-MS ($C_{14}H_{12}N_2O_7$, CH_3OH): m/z=320.2 $[M]^+$. IR (cm^{-1}): ν_{NH+OH}=3244-3343 (br); $\nu_{C=O}$=1620. Anal. Calcd for $C_{14}H_{12}N_2O_7$·: C=52.51; H=3.78; N=8.75. Found: C=52.55; H=3.92; N=8.73.

N'-(2-pyridyl)-3,4,5-trihydroxybenzoylhydrazide ***(24)***. Brown powder. Yield=55%. ^{1}H-NMR (DMSO-d_6, 25°C), δ: 6.97 (s, 2H, CH_{Ar}); 7.67 (m, 1H, CH_{Ar}); 8.12-8.22 (m, 2H, CH_{Ar}); 8.58 (s, 1H, CH=N); 8.71 (d, 1H, CH_{Ar}). EI-MS ($C_{13}H_{11}N_3O_4$, CH_3OH): m/z=273.1 $[M]^+$. IR (cm^{-1}): ν_{OH}=3531; ν_{NH+OH}=3216-3297 (br); $\nu_{C=O}$=1598. Anal. Calcd for $C_{13}H_{11}N_3O_4$·: C=57.14; H=4.06; N=15.38. Found: C=57.35; H=4.10; N=15.43

N'-(2-pyrrolidyl)-3,4,5-trihydroxybenzoylhydrazide ***(25)***. Yellow powder. Yield=25%. ^{1}H-NMR (DMSO-d_6, 25°C), δ: 6.12 (s, 1H, CH_{Ar}); 6.43 (s, 1H,

CH_{Ar}); 6.89 (s, 3H, CH_{Ar}); 8.24 (s, 1H, HC=N); 8.75, 9.10 (s, 3H, OH); 11.20 (s, 1H, NH); 11.44 (s, 1H, OH). EI-MS ($C_{12}H_{11}N_3O_4$, CH_3OH): m/z=261.0 $[M]^+$. IR (cm^{-1}): ν_{NH+OH}=3215 (br); $\nu_{C=O}$=1600. Anal. Calcd for $C_{12}H_{11}N_3O_4$·: C=55.17; H=4.24; N=16.09. Found: C=55.22; H=4.43; N=15.79.

N'-(3-(1,1'-biphenyl)-4-carboxylicacid)-3,4,5-trihydroxybenzoylhydrazide ***(26)***. White powder. Yield=51%. ^{1}H-NMR (DMSO-d_6, 25°C), δ: 6.95 (s, 2H, CH_{Ar}); 7.59 (t, 1H, J= 7.5 Hz, CH_{Ar}); 7.77 (m, 2H, CH_{Ar}); 7.86 (d, 2H, J=8 Hz, CH_{Ar}); 8.02 (s, 1H, CH_{Ar}); 8.07 (d, 2H, J=8 Hz, CH_{Ar}); 8.50 (s, 1H, CH=N); 8.86 (s, 1H, OH); 9.18 (s, 2H, OH); 11.65 (s, 1H, NH); 12.98 (s, 1H, COOH). ESI-MS ($C_{21}H_{16}N_2O_6$, CH_3OH): m/z=415 $[M+Na]^+$. IR (cm^{-1}): $\nu_{C=O}$=1676 (br), $\nu_{C=N}$=1599. Anal. Calcd for $C_{21}H_{16}N_2O_6 \cdot 2.5H_2O$: C=57.67; H=4.84; N=6.40. Found: C=57.11; H=4.84; N=6.40.

N'-(3,4,5-trihydroxybenzylidene)-semicarbazide ***(27)***. White powder. Yield=62%. ^{1}H-NMR (DMSO-d_6, 25°C), δ: 6.27 (s, 2H, NH_2); 6.81 (s, 2H, CH_{Ar}); 7.61 (s, 1H, CH=N); 8.57-8.96 (m, 3H, OH); 9.98 (s, 1H, NH). EI-MS ($C_8H_9N_3O_4$, CH_3OH): m/z=211.1 $[M]^+$. IR (cm^{-1}): ν_{NH}=3460; ν_{OH}=3170-3186; $\nu_{C=O}$=1690; $\nu_{C=N}$=1594. Anal. Calcd for $C_8H_9N_3O_4$: C=45.50; H=4.30; N=19.90. Found: C=45.62; H=4.41; N=20.05.

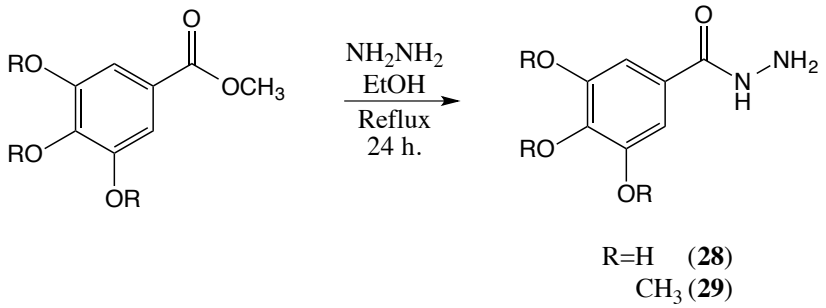

Scheme 1.2 General synthesis for hydrazides 28 and 29.

3,4,5-trihydroxybenzohydrazide (**28**) and 3,4,5-trimethoxybenzohydrazide (**29**) were obtained by reaction (Scheme 1.2) of the corresponding methyl esters with hydrazine monohydrate[145]. Hydrazine was added to an ethanol suspension of the ester and stirred at room temperature until the solute completely dissolved. Reaction mixture has then been refluxed overnight. On concentrating the solution, a precipitate was observed, which was filtered and washed with cold ethanol.

*3,4,5-trihydroxybenzohydrazide (**28**)*. Light brown powder. Yield=70%. ^{1}H-NMR (DMSO-d_6, 25°C), δ: 4.36 (s, 2H, NH_2); 6.79 (s, 2H, CH_{Ar}); 9.24 (s, 1H, NH). IR (cm^{-1}): ν_{NH}=3424, 3390, 3296; $\nu_{C=O}$=1600.

*3,4,5-trimethoxybenzohydrazide (**29**)*. White powder. Yield=63%. ^{1}H-NMR (DMSO-d_6, 25°C), δ: 3.69 (s, 3H, OCH_3); 3.81 (s, 6H, OCH_3); 4.47 (s, 2H, NH_2); 7.16 (s, 2H, CH_{Ar}); 9.72 (s, 1H, NH). IR (cm^{-1}): ν_{NH}=3455; $\nu_{C=O}$=1697; $\nu_{C=N}$=1596.

1.4.3 Metal complexes syntheses

1.4.3.1 Synthesis of the magnesium complex of ligand **19**

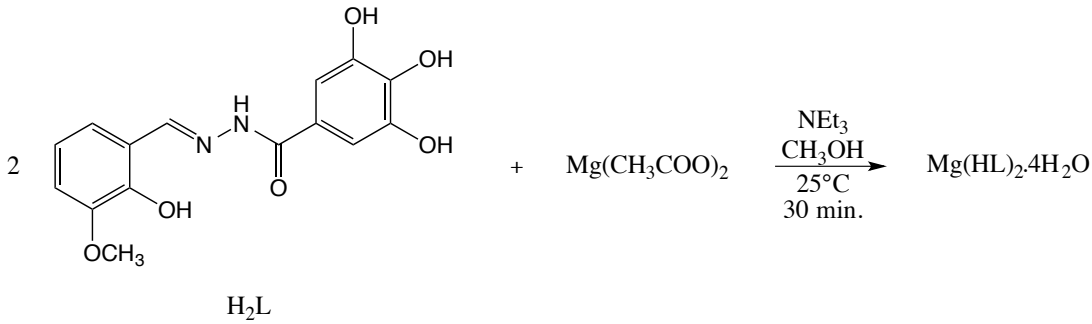

Scheme 1.3 Synthesis of the magnesium complex of 19.

*$Mg(HL)_2 \cdot 4H_2O$ **(30)***. (Scheme 1.3) 100 mg (0.37 mmol) of 19 (H_2L) were dissolved in 30 ml of methanol and 1 eq. of NEt_3 was added to the solution. The mixture turned yellow and it has been stirred at room temperature for 30 minutes. Upon addition of 0.5 eq. of $Mg(CH_3COO)_2 \cdot 4H_2O$ (40 mg), a light yellow precipitate was formed, which was has been stirred at room temperature for 3 hours. The reaction mixture was cooled overnight and the precipitate was filtered off and washed with water.

Light yellow powder. Yield=58%. ^{1}H-NMR (MeOD, 25°C), δ: 3.89 (s, 3H, OCH_3); 6.89 (t, 1H, J=8 Hz, CH_{Ar}); 6.99-7.04 (m, 3H, CH_{Ar}); 7.13 (d, 1H, J=8 Hz, CH_{Ar}); 8.51 (s, 1H, CH=N). ^{13}C-NMR (MeOD, 25°C), δ: 55.26; 106.89; 113.60; 118.69; 118.96; 121.35; 122.70; 137.56; 145.46; 147.44; 148.07; 148.65; 165.26. ESI-MS ($C_{30}H_{26}N_4O_{12}Mg$, CH_3OH): m/z= 659 $[M+H]^+$. IR (cm^{-1}): ν_{NH+OH}=3476, 3322 (br); $\nu_{C=O}$=1643. Anal. Calcd for $C_{30}H_{26}N_4O_{12}Mg \cdot 4H_2O$: C=49.30, H=4.69, N=7.67. Found: C=49.54, H=4.87, N=7.59.

1.4.3.2 Syntheses of metal complexes of ligand **8**

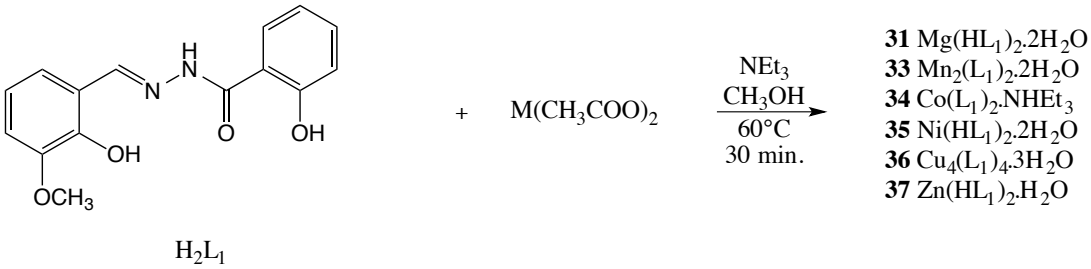

H_2L_1

Scheme 1.4 Synthesis of the metal complexes of 8.

The ligand **8** (H_2L_1) (0.5 mmol) was dissolved in 30 ml of methanol and 1 eq. of NEt_3 was added. The yellow solution has been stirred at 60°C for 30 minutes. 0.5 eq. of acetate of the metal were added and then the reaction mixture has been stirred at reflux for 4 hours, concentrated in vacuum and cooled overnight. The precipitate was filtered off, washed with water and dried under vacuum (Scheme 1.4).

$Mg(HL_1)_2\ 2H_2O$ (**31**). Light yellow powder. Yield=70%. ^{1}H-NMR (MeOD, 25°C), δ: 3.91 (s, 3H, OCH_3); 6.88-7.07 (m, 4H, CH_{Ar}); 7.20 (d, 1H, J=7.5 Hz, CH_{Ar}); 7.46 (t, 1H, J=8 Hz, CH_{Ar}); 7.92 (d, 1H, J=8 Hz, CH_{Ar}); 8.60 (s, 1H, CH=N). ESI-MS ($C_{30}H_{26}N_4O_8Mg$, CH_3OH): m/z= 595 $[M+H]^+$; m/z=617 $[M+Na]^+$. IR (cm^{-1}): ν_{NH} = 3267 (br); $\nu_{C=O}$ = 1627, 1609; ν_{OCH3} = 1211, 1082. Anal. Calcd. for $C_{30}H_{26}N_4O_8Mg\ 2H_2O$: C=57.11, H=4.79, N=8.88. Found: C=57.33, H=4.33, N=9.00.

$Mg_2(L_1)_2\ 4H_2O$ (**32**). 0.5 mmol of *H_2L_1* were dissolved in 30 ml of methanol and 2.5 eq. of NaOH 4M were added. The yellow solution has been stirred at 65°C for 30 minutes. 1 eq. of magnesium acetate was added and the reaction

mixture has been stirred at reflux for 4 hours, concentrated in vacuum and cooled overnight. The precipitate was filtered off and washed with water. Intense yellow powder. Yield=64%. ^{1}H-NMR (MeOD, 25°C), δ: 3.84 (s, 3H, OCH_3); 6.45 (s, 1H, CH_{Ar}), 6.68-6.82 (m, 5H, CH_{Ar}); 7.20 (s, 1H, CH_{Ar}); 7.90 (s, 1H, CH_{Ar}); 8.24 (s, 1H, CH=N). ESI-MS ($C_{30}H_{24}N_4O_8Mg_2$, CH_3OH): m/z= 309 $[MgL]^+$; m/z=617 $[Mg_2L_2]^+$; m/z=640 $[Mg_2L_2+Na]^+$. IR (cm^{-1}): ν_{OH}=3420-3500 (br); $\nu_{C=O}$=1609; ν_{OCH3}=1211, 1082. Anal. Calcd. for $C_{30}H_{24}N_4O_8Mg_2$ $4H_2O$: C=52.28, H=4.68, N=8.13. Found: C=52.67, H=4.63, N=8.03.

$Mn_2(L_1)_2$ $2H_2O$ ***(33)***. Brown powder. Yield=70%. ESI-MS ($C_{30}H_{24}N_4O_8Mn_2$, CH_3OH): m/z(-)= 624 $[Mn(HL)_2]^-$; m/z(-)=677 $[Mn_2L_2]^-$. IR (cm^{-1}): ν_{NH}=3267 (br); $\nu_{C=O}$=1607; ν_{OCH3}=1208. Anal. Calcd. for $C_{30}H_{24}N_4O_8Mn_2$ $2H_2O$: C=50.43, H=3.95, N=7.84. Found: C=50.68, H=4.27, N=7.87.

$[Co(L_1)_2](NHEt_3)$ ***(34)***. Brown powder. Yield=64%. ^{1}H-NMR (DMSO-d_6, 25°C), δ: 0.99 (t, 9H, CH_3, NEt_3); 2.50 (overlapping with solvent signal, CH_2, NEt_3); 3.36 (s, 3H, OCH_3); 6.41 (t, 1H; J=7.5 Hz, CH_{Ar}); 6.51 (d, 1H, J=7.5 Hz, CH_{Ar}); 6.67 (t, 1H, J=8 Hz, CH_{Ar}); 7.22 (m, 2H, CH_{Ar}); 7.47 (d, 1H, J=8 Hz, CH_{Ar}); 7.70 (d, 1H, J=8 Hz, CH_{Ar}); 8.93 (s, 1H, CH=N); 12.64 (s, 1H, $NHEt_3$). ESI-MS ($C_{36}H_{40}N_5O_8Co$, CH_3OH): m/z (-)=627 $[Co(L_1)_2]^-$. IR (cm^{-1}): ν_{NH}=3206 (br); $\nu_{C=O}$=1624; $\nu_{C=N}$=1598. Anal. Calcd. for $C_{36}H_{40}N_5O_8Co$: C=59.26, H=5.53, N=9.60. Found: C=59.55, H=5.48, N=9.41. Crystals suitable for X-ray diffraction analysis were obtained by slow evaporation of a methanol solution of the complex.

$Ni(HL_1)_2{\cdot}2H_2O$ ***(35)***. Green powder. Yield=87%. ESI-MS ($C_{30}H_{26}N_4O_8Ni$, CH_3OH): m/z=629 $[Ni(HL_1)_2]^+$; m/z=652 $[Ni(HL_1)_2+Na]^+$. IR (cm^{-1}):

ν_{NH+OH}=3150-3200 (br); $\nu_{C=O}$=1629; ν_{OCH3}=1201. Anal. Calcd. for $C_{30}H_{26}N_4O_8Ni$ $2H_2O$: C=54.16, H=4.55, N=8.42. Found: C=54.51, H=4.84, N=8.34.

*$Cu_4(L_1)_4 \cdot 3H_2O$ (**36**)*. Green powder. Yield=46%. ESI-MS ($C_{60}H_{48}N_8O_{16}Cu_4$, CH_3OH): m/z=348 $[CuL_1]^+$; m/z=717 $[Cu_2(L_1)_2+Na]^+$; m/z=1392 $[Cu_4(L_1)_4+H]^+$. IR (cm^{-1}): ν_{NH+OH}=3150-3200 (br); $\nu_{C=O}$=1629; ν_{OCH3}=1201. Anal. Calcd. for $C_{60}H_{48}N_8O_{16}Cu_4$ $3H_2O$: C=49.86, H=3.77, N=7.75. Found: C=50.00, H=3.42, N=7.60. Crystals of $Cu_4(L_1)_4 \cdot 4CH_3CN$ suitable for X-ray diffraction analysis were obtained by recrystallization from acetonitrile.

*$Zn(HL_1)_2 \cdot H_2O$ (**37**)*. Yellow powder. Yield=86%. ESI-MS ($C_{30}H_{26}N_4O_8Zn$, CH_3OH): m/z(-)=635 $[Zn(HL_1)_2]^-$. IR (cm^{-1}): ν_{NH}=3170 (br); $\nu_{C=O}$=1611; $\nu_{C=N}$=1534. Anal. Calcd. for $C_{30}H_{26}N_4O_8Zn$ H_2O: C=55.10, H=4.32, N=8.57. Found: C=55.10, H=4.00, N=8.52.

1.5 WORK CONTRIBUTIONS

Docking studies were performed by the group of Professor Laura de Luca; University of Messina (Italy), Department of chemical, biology, pharmaceutical and environmental science.

Biological analyses were performed by the group of Professor Lieve Naesens; University of Luven (Belgium), Department of Microbiology and Immunology.

Protein crystallographic studies were performed by the group of Professor Stephen W. White; St. Jude Children's Research Hospital, Memphis (USA); Department of Structural Biology.

1.6 BIBLIOGRAPHY

[1] A.R. Lamb, et al.; *Lippincott Williams & Wilkins: Philadelphia*; **2001**; 1487-1531.

[2] World Health Organization; *Bull. World Health Organ.*; **1980**; 58; 585-591.

[3] N. Salez, et al.; *J. Infect.*; **2014**; 69; 182-189.

[4] World Health Organization. Influenza (seasonal) - Fact sheet N°211. http://www.who.int/mediacentre/factsheets/fs211/en/ (accessed 19-1-2015).

[5] J.K. Taubenberger, D.M. Morens; *Emerg. Infect. Dis.;* **2006**; 12; 15-22.

[6] R.J. Garten, et al.; *Science*; **2009**; 325; 197–201.

[7] C. Chu, I.M. Dawson, W.J. Elford; *Lancet*; **1949**; 1; 602.

[8] G.B. Karlsson Hedestam, et al.; *Nat. Rev. Microbiol.*; **2008**; 6; 143-155.

[9] T. Sakaguchi, et al.; *Proc. Natl. Acad. Sci. U.S.A.*; **1997**; 94; 5000-5005.

[10] S.L. Zebedee, R.A. Lamb; *Proc. Natl. Acad. Sci. U.S.A.*; **1989**; 86; 1061-1065.

[11] J. Yasuda, et al.; *Virology*; **1993**; 196; 249-255.

[12] L. Ronconi, P.J. Sadler; *Coord. Chem. Rev.*; **2007**; 251; 1633-1648.

[13] T.A. Steitz; *Nature*; **1998**; 391; 231-232.

[14] A. Pingoud, et al.; *Cell. Mol. Life Sci.*; **2005**; 62; 685-707.

[15] A.J. Elsfeld, G. Neumann,Y. Kawaoka; *Nat. Rev. Micro.*; **2015**; 13; 28-41.

[16] W. Chen, et al.; *Nat. Med.*; **2001**; 7; 1306-1312.

[17] K. Das, et al.; *Nat. Struct. Mol. Biol.*; **2010**; 5; 530-538.

[18] A.J. Eisfeld, G. Neumann, Y. Kawaoka; *Nat. Rev. Microbiol.*; **2015**; 13; 28-41.

[19] S. Boulo, et al.; *Virus Res.*; **2007**; 124(1-2); 12-21.

[20] G.E. Mark, et al.; *J. Virol.*; **1979**; 29; 744-752.

[21] M. Bouloy, et al.; *Proc. Natl Acad. Sci. USA*; **1978**; 75; 4886-4890.

[22] S.J. Plotch, et al.; *Proc. Natl Acad. Sci. USA*; **1979**; 76; 1618-1622.

[23] S.J. Plotch, et al.; *Cell*; **1981**; 23; 847-858.

[24] M.E. Nemeroff, et al.; *Mol. Cell*; **1998**; 1; 991-1000.

[25] K. Shimizu, et al.; *Virology*; **1999**; 254; 213-219.

[26] E. Fodor; *Acta Virol.*; **2013**; 57; 113-12.

[27] E. Yanguez, A. Nieto; *Virus Res.*; **2011**; 156; 1-12.

[28] S. Zhang, et al.; *J. Biol. Chem.*; **2010**; 285; 41194-41201.

[29] L. Simonsen, et al.; *Lancet. Infect. Dis.*; **2007**; 7; 658-666.

[30] S.A. Madhi, et al.; *N. Engl. J. Med.*; **2014**; 371; 918-931.

[31] J.C. De Jong, et al.; *J. Med. Virol.*; **2000**; 61; 94-99.

[32] T. Sakaguchi, et al.; *Proc. Natl. Acad. Sci. U.S.A.*; **1997**; 94; 5000-5005.

[33] A. Helenius; *Cell*; **1992**; 69; 577-578.

[34] L.H. Pinto, L.J. Holsinger, R.A. Lamb; *Cell;* **1992**; 69; 517-528.

[35] F. Ciampor, et al.; *Virology*; **1992**; 69; 517-528.

[36] A. Stouffer, et al.; Nature; **2008**; 451; 596-599.

[37] R.M. Pielak, K. Oxenoid, J.J. Chou; *Structures*; **2011**; 19; 1655-1663.

[38] V.M. Deyde, et al.; *J. Infect. Dis.*; **2007**; 196; 249-257.

[39] A. Moscona; *N. Engl. J. Med.*; **2009**; 360; 953-956.

[40] M.J. Memoli, et al.; *J. Infect Dis.*; **2011**; 203; 348−357.

[41] A.J. Hay, et al.; *J. Antimicrob. Chemother.*; **1986**; 18 Suppl B; 19-29.

[42] R.B. Belshe, et al.; *J. Virol.*; **1988**; 62; 1508-1512.

[43] P. Palese, et al.; *Virology*; **1974**; 61; 397-410.

[44] M. Cohen, et al.; *Virol. J.*; **2013**; 10:321.

[45] M.N. Matrosovich, et al.; *J. Virol.*; **2004**; 78; 12665-12667.

[46] B. Su, et al.; *PLoS One*; **2009**; 4; e8495.

[47] M. Von Itzstein, et al.; *Nature*; **1993**; 363; 418-423.

[48] W. Li, et al.; *Antimicrob. Agents Chemother.*; **1998**; 42; 647-653.

[49] C.U. Kim, et al.; *J. Am. Chem. Soc.*; **1997**; 119; 681-690.

[50] Y.S. Babu, et al.; *J. Med. Chem.*; **2000**; 43; 3482-3486.

[51] M. Yamashita, et al.; *Antimicrob. Agents Chemother.*; **2009**; 53; 186-192.

[52] H.T. Nguyen, et al.; *Antimicrob. Agents Chemother.*; **2010**; 54; 3671-3677.

[53] A. Pflug, et al.; *Nature*; **2014**; 516; 355-360.

[54] S. Boivin, et al.; *J. Biol. Chem.*; **2010**; 285; 28411-28417.

[55] J. Rocha-Pereira, et al.; *Biochem. Biophys. Res. Commun.*; **2012**; 424; 777-780.

[56] X. He, et al.; *Nature*; **2008**; 454; 1123-1126.

[57] R.W. Sidwell, et al.; *Science*; **1972**; 177; 705-706.

[58] P.P Chegun, et al.; *Nat. Commun.*; **2014**; 5:4794.

[59] NIH, National Library Of Medicine, US. Hazardous Substances Databank Number: 6513. http://toxnet.nlm.nih.gov/).

[60] M. Tisdale, et al.; *Antimicrob. Agents Chemother.*; **1995**; 39; 2454-2458.

[61] H. Sangawa, et al.; *Antimicrob. Agents Chemother.*; **2013**; 57; 5202-5208.

[62] T. Baranovich, et al.; *J. Virol.*; **2013**; 87; 3741-3751.

[63] Z. Jin, et al.; *PLoS One*; **2013**; 8; e68347.

[64] Y. Furuta, et al.; *Antimicrob. Agents Chemother.*; **2002**; 46; 977-981.

[65] M. Kiso, et al.; *Proc. Natl. Acad. Sci. U.S.A.*; **2010**; 107; 882-887.

[66] R. Cao, et al.; *Antiviral Chem. Chemother.*; **2013**; 23(6); 237-240.

[67] K. Sleeman, et al.; *Antimicrob. Agents Chemother.*; **2010**; 54; 2517-2524.

[68] Y. Furuta, et al.; *Antimicrob. Agents Chemother.*; **2002**; 46; 977-981.

[69] L. Ostereich, et al.; *Antiviral. Res.*; **2014**; 105; 71-21.

[70] S.J. Smither, et al.; *Antiviral. Res.*; **2014**; 104; 153-155.

[71] B.B. Gowen, et al.; *Antimicrob. Agents Chemother.*; **2007**; 51; 3168-3176.

[72] B.B. Gowen, et al.; *PLoS One*; **2008**; 3; e2614.

[73] J.G. Julander, et al.; *Antimicrob. Agents Chemother.*; **2009**; 53; 202-209.

[74] J.G. Julander, et al.; *Antiviral. Res.*; **2009**; 82; 169-171.

[75] Y. Furuta, et al.; *Antimicrob. Agents Chemother.*; **2002**; 46; 977-981.

[76] R.M. Krug, J.M. Aramini; *Trends Pharmacol. Sci.*; **2009**; 30; 269-277.

[77] E. De Clercq; *Nature Rev.*; **2006**; 5; 1015-1025.

[78] E. De Clercq, J. Neyts; *Trends Pharmacol. Sci.*; **2007**; 28; 280-285.

[79] K. Klumpp; *Expert Opin. Ther. Pat.*; **2004**; 14(8); 1153-1168.

[80] K.E.B Parkers, et al.; *J. Med. Chem.*; **2003**; 46; 1153-1164.

[81] P. Yuan, et al.; *Nature*; **2009**; 458; 909-913.

[82] C. Zao, et al.; *J. Virol.*; **2009**; 83; 9024-9030.

[83] B. Tefsen, et al.; *J. Virol.*; **2014**; 88; 1935-1941.

[84] A. Dias, et al.; *Nature*; **2009**; 458; 914-918.

[85] T. Crépin, et al.; *J. Virol.*; **2010**; 84; 9096-9104.

[86] M.M. Harding, et al.; *Crystallogr. Rev.*; **2010**; 16; 247-302.

[87] T.Y. Yang, et al.; *J. Am. Chem. Soc.*; **2003**; 125; 3168-3180.

[88] C.W. Bock, et al.; *J. Am. Chem. Soc.*; **1999**; 121; 7360-7372.

[89] D. Sikora, et al.; *Sci. Rep.*; **2014**; 4:6181.

[90] M. Hagen, et al.; *J. Gen. Virol.*; **1995**; 76; 603-611.

[91] C. Geerts-Dimitriadou, et al.; *Virology*; **2011**; 409; 17-26.

[92] P. Rao, et al.; *EMBO J.*; **2003**; 22; 1188-1198.

[93] J. Hastings, et al.; *Antimicrob. Agents Chemother.*, **1996**, 40, 1304-1307.

[94] A. Stevaert, et al.; *Mol. Pharma.*; **2015**; 87; 323-337.

[95] J.E. Tomassini, et al.; *Antimicrob. Agents Chemother.*; **1996**; 40; 1189-1193.

[96] M. Carcelli, et al.; *Mol. Pharmaceutics*; **2014**; 11; 304-316.

[97] K.E. Parkes, et al.; *J. Med. Chem.*; **2003**; 46; 1153-1164.

[98] H.Y. Sagong, et al.; *J. Med. Chem.*; **2014**; 57; 8086-8098.

[99] Y. Iwai, et al.; *PLoS One*; **2011**; 6; e19825.

[100] T. Kuzuhara, et al.; *PLoS Curr.*; **2009**; 1; RRN1052.

[101] J.M.Song, et al.; *Antiviral Res.*; **2005**; 68; 66−74.

[102] D. Rogolino, et al.; *Coord. Chem. Rev.*; **2012**; 256; 3063-3086.

[103] K.E. Parkes, et al.; *J. Med. Chem.*; **2003**; 46; 1153-1164.

[104] M. Sechi, et al.; *J. Med. Chem.*; **2006**; 49; 4248-4260.

[105] A. Steavaert, et al.; *J. Virol.*; **2013**; 87; 10524-10539.

[106] D. Rogolino, et al.; *Eur. J. Med. Chem.*; **2014**; 78; 425-430.

[107] M. Carcelli, et al.; *Eur. J. Med. Chem.*; **2014**; 83; 594-600.

[108] N. Pala, et al.; *ACS Med. Chem. Lett.;* **2015**; 6; 866-871.

[109] D. Rogolino, et al.; *J. Biolo. Inorg. Chem.*; **2015**; 20; 1109-1121.

[110] M. Carcelli, et al.; *Scientific Reports*; **2016**; 6; 31500.

[111] S. Rollas, S.G. Küçükgüzel; *Molecules*; **2007**; 12; 1910-1939.

[112] Q. Gong, et al.; *Chem. Biol. Drug Des.*; **2011**; 77; 39-47.

[113] S.G. Sarafianos, et al.; *J. Mol. Biol.*; **2009**; 385; 693-713.

[114] S. N. Podyachev, et al.; *Spectrochimica Acta*; **2007**; 66; 250-261.

[115] D. Sarigol, et al.; *J. Mol. Struct.*; **2015**; 1086; 146-152.

[116] G. Jones, et al.; *Journal of Molecular Biology*; **1997**; 267; 727-748.

[117] A. Stevaert, et al.; *Mol. Pharmacol.*; **2015**; 87; 323-337.

[118] E. Kowalinski, et al.; *PLoS Pathog.*; **2012**; 8; e1002831.

[119] B.D. Wang, et al.; *Bioorg. Med. Chem.*; **2006**; 14; 1880-1888.

[120] Y.H. Li, Z.Y. Yang, B.D. Wang; *Transition Met. Chem.* **2006**; 31; 598-602.

[121] Q. Wang, Y. Wang, Z.Y. Yang; *Chem. Pharm. Bull.*; **2008**; 56; 1018-1021.

[122] A. Ray, et al.; *J. Inorg. Chem.*; **2009**; 48; 2915-2928.

[123] O. Pouralimardan, et al.; *Inorg. Chim. Acta;* **2007**; 360; 1599-1608.

[124] G.M. Yo, et al.; *J. Mol. Struct.*; **2010**; 982; 139-144.

[125] M. Nardelli; *J. Appl. Crystallogr.*; **1983**; 16; 146-153.

[126] F.H. Allen, O. Kennard, R Taylor; **2002**; 58 B; 389-397.

[127] M. Sutradhar, et al.; *Dalton Trans.*; **2013**; 42; 16578-16587.

[128] H.H. Monfared, et al.; *Inorg. Chimica Acta*; **2009**; 362; 3791-3795.

[129] B.D. Wang, et al.; *Bioorg. Med. Chem.;* **2006**; 14; 1880-1888.

[130] Z.A. Siddiqui, et al.; *Dalton Trans.*; **2013**; 42; 9513-9522.

[131] M.L. Liu, et al.; *J. Mol. Struct.*; **2012**; 1011; 140-144.

[132] G. Jones, et al.; *J. Mol. Bio.*; **1997**; 267; 727-748.

[133] E. Fisicaro, A. Braibanti; *Talanta;* **1988**; 10; 769-774.

[134] G. Gran; *Analyst*; **1952**; 77; 661-671.

[135] P. Gans, A. Sabatini, A. Vacca; *Talanta*; **1996**; 43; 1739-1753.

[136] M.S. Song, et al.; *PNAS*; **2016**; 113; 3669-3674.

[137] Z. Otwinowski, W. Minor; *Methods in Enzymology*; **1997**; 276; 307-326.

[138] M.D. Winn, et al.; *Acta Crystallogr. D Biol. Crystallogr.*; **2011**; 67; 235-42.

[139] O.V. Dolomanov, et al.; *J. Appl. Cryst.*; **2009**; 42; 339-341.

[140] M.C. Burla, et al.; *J. Appl. Cryst.*; **2007**; 40; 609-613.

[141] G.M. Sheldrick; *Acta Cryst.*; **2008**; A64; 112-122.

[142] M. Carcelli, et al.; *Mol. Pharma.*; **2014**; 11; 304-316.

[143] S. Meneghesso, et al.; *Antiviral Res.*; **2012**; 94; 35-43.

[144] S. Xiao, et al; *J. Phys. Chem. B*; **2014**; 118; 873–889.

[145] N.S. Gwaram, et al.; *Molecules*; **2012**; 17; 2408-2427.

2 *ORGANOMETALLIC OSMIUM AND RUTHENIUM COMPLEXES WITH ANTITUMORAL ACTIVITY*

ABBREVIATIONS

CCD Charge Coupled Device

CFA Colony Formation Assay

DNA Deoxyribonucleic acid

DMEM Dulbecco's Modified Eagle Medium

DPBS Dulbecco's Phosphate Buffered Saline

EDTA Ethylenediaminetetraacetic acid

ECACC European Collection of Cell Cultures

ESI-MS Electron Spray Ionization Mass Spectrometry

FT Fourier Transform

IC_{50} Compound concentration to obtain 50% inhibition of cleavage

MTT 3-(4,5-dimethylthiazol-2-yl)-2,5-diphenyltetrazolium bromide

NMP Nuclear Matrix Protein

NMR Nuclear Magnetic Resonnce

NOESY Nuclear Overhauser Effect Spectroscopy

OD Optical Density

PBS Phosphate Buffered saline

PML Promyeelocytic Leukaemia

RF Resistant Factor

RR Ribonucleotide Reductase

SD Standard Deviation

SRB Sulfate Reducing Bacteria

Tf Transferrine

TSC Thiosemicarbazone

WHO World Health Organization

2.1 INTRODUCTION

2.1.1 General Introduction

Cancer (other used definitions are “malignant tumor” or “neoplasm”) is one of the most serious health problems worldwide that affects individuals of different ages, sexes and races. It is the generic term used to define a large group of diseases characterized by uncontrolled cellular growth that can lead to frequent cells invasion to different part of the body[1]. Generally, the type of cells, or organs, from which they originate classifies tumors: cancer is a heterogeneous illness which can originate from many different organs of the human body. Compared to normal cells, one important difference is that cancer cells are less specialized: whereas normal cells mature into very distinct types with specific functions, cancer cells do not. This leads to a faster growth and diffusion in the organism. However, the most frequent cancer types in the world are lung, prostate, stomach, colorectal and esophagus in man and breast, lung, stomach, colorectal and cervical in woman[2].

The World Health Organization (WHO) names cancer as a leading cause of death worldwide accounting for 8.2 million deaths in 2012 (around 13% of all deaths), that are projected to rise above 13.1 million in 2030.

2.1.2 The tumor cell

In cancer cells there are morphological alterations of nuclear structure compared to the one of normal cells (Fig 2.1): these include changes in nuclear size and shape, in numbers and size of nucleoli and in chromatin texture. These modifications can be so characteristic of a given tumor type and stage that they are used in cancer diagnosis.

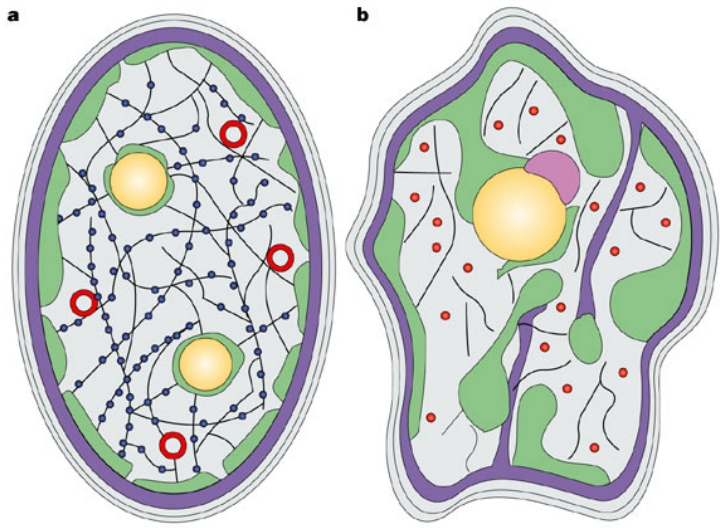

Fig. 2.1 Nuclear structure in normal and cancer cells.

a | Normal nucleus. The nucleus is bounded by the nuclear lamina (purple); in most cell types the lamina-associated chromatin domains correspond to heterochromatin (green). Another key site of heterochromatin formation is at the surface of the nucleoli (yellow). The nuclear matrix (black internal network; nuclear matrix proteins indicated by small blue circles) is the non-chromatin nuclear scaffolding that participates in the spatial organization of chromatin and the positioning of nuclear molecules and substructures. One such substructure is the promyelocytic leukaemia (PML) body (red). **b** | Some examples of nuclear changes that are observed in tumour cells. Nuclei can become irregular and begin to fold, and coarse heterochromatin aggregates are frequently observed. Nucleoli can be enlarged and PML bodies can mislocalize in microspeckles. Furthermore, appearance of the perinucleolar compartment (pink) is observed in tumour cells. [Taken from D. Zink et al.[3]]

Cancer research has generated a rich and complex body of knowledge. Cancer is a disease that involves dynamic changes in the genome as well as in the cell structure. Tumorigenesis is a multistep process, caused by genetic

alterations, that drives the progressive transformation of normal cells into highly malignant derivatives. These transformations lead to cancer cells have defects in regulatory circuits that govern normal cells proliferation and homeostasis: several studies have been set in the discovery of those specific mutations responsible of oncogenes[4].

There are more than 100 types of cancer and the vast catalogue of tumor cells genotypes is a manifestation of six essential alterations, in cell physiology, which collectively dictated malignant growth:

a- Self-sufficiency in growth signals. Normal tissues carefully control the production and release of growth-promoting signals that instruct entry into and progression through the cell growth-and-division cycle, thereby ensuring a homeostasis of cell number and thus maintenance of normal tissue architecture and function. Cancer cells, by deregulating these signals, become masters of their own destinies[5, 6].

b- Insensitivity to growth-inhibitory (antigrowth) signals. Ever-increasing expression of growth suppressor genes and the signals manifested in their protein products would result in increased cancer cell proliferation and, thus, tumor growth[7, 8].

c- Evasion of programmed cell death (apoptosis). Research has demonstrated that the cell-to-cell contacts, formed by dense populations of normal cells, operate to suppress further cell proliferation. Important, such “contact inhibition” is abolished in various types of cancer cells in culture[9, 10].

d- Limitless replicative potential. It was widely accepted that cancer cells require unlimited replicative potential in order to generate macroscopic tumors. This ability stands in marked contrast to the behaviour of the cells in most normal cell lineages in the body, which

are able to pass through only a limited number of successive cell growth-and-division cycles[11, 12].

e- Sustained angiogenesis. The multistep processes of invasion and metastasis have been schematised as a sequence of discrete steps, often termed as the invasion-metastasis cascade[13,14]: it begins with local invasion and then intravasation by cancer cells into nearby blood and lymphatic vessels, transit of cancer cells through the lymphatic and hematogenous systems followed by escape of cancer cells from the lumina of such vessels into the parenchyma of distant tissues (extravasation), the formation of small nodules of cancer cells (micrometastases) and finally the growth of micrometastatic lesions into macroscopic tumors.

Each of these physiological changes represents the successful breaching of an anticancer defence mechanism hardwired into cells and tissues[15].

2.1.3 Cancer cells proliferation

Many cancers arise from just one single cell (or from a small number of cells)[16] and, to become cancerous, these cells must acquire several changes in oncogenes or tumor suppression genes, that will make that cells capable of proliferating well beyond their normal limit.

At the cellular level, the development of cancer is viewed as a multistep process that involves mutation and selection for cells with progressively increasing ability for proliferation, survival, invasion and metastasis (Fig. 2.2)[17].

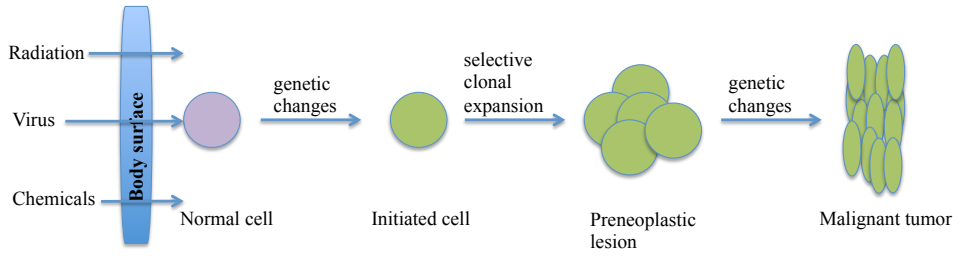

Fig. 2.2 Initiation, promotion and progression steps of carcinogenesis.

2.1.3.1 Initiation

The carcinogenic factors, responsible for cancer development, are classified as exogenous or endogenous[18]. The exogenous ones include agents associated with food preservation and preparation, socio-economic status, lifestyle, ionizing and non-ionizing radiation, natural and synthetic chemical compounds and xenobiotics including *Helicobacter pylori*, Epsteine-Barr virus, human T-lymphtropic virus, human papilloma virus, hepatitis B and C virus and certain parasites[19], alcohol consumption, and tobacco smoking; intake of certain foods, contaminated by mycotoxins, are also responsible for

causing certain types of neoplasms[20].

Hormones, age and genetic heritage, instead, are endogenous factors that can be related to cancer development. It is thought that all this exogenous and endogenous elements are responsible for genetic alterations in the DNA sequence that lead to abnormal proliferation of a single cell[21].

In describing the detailed mechanism that governs cancer initiation, genetic and epigenetic changes have to be considered together as two sides of the same coin. The term "epigenetic" refers to the study of heritable changes in gene expression without the change in gene sequence. These heritable factors are propagated as covalent changes to the cytosine bases and are referred to as DNA methylation[22]. The maintenance of these epigenetic signals through cell division ensures appropriate regulation of gene activation and repression[23].

Moreover, cancer develops as a result of cellular acquisition of specific growth advantages through the stepwise accumulation of chromosomal and genetic changes. Cancer genome can be highly unstable and typically exhibits extensive genomic changes, ranging from intragenic mutations to gross gain and losses of chromosomal material[24, 25, 26]. This ability of cancer cells to accumulate mutations is critical for the development of cancer as well as for the rapid development of resistance to cytotoxic cancer treatments[27]. Several databases are available that compile mutations in cancer genes reported in literature. The most extensive of these databases is the COSMIC database maintained at the Sanger Institute, Hinxton, UK (//www.sanger.ac.uk/genetics/CGP/cosmic/)[28]. It contains the description of over 40,000 individual mutations occurring in a set of 291 genes that have been identified as mutated and causally implicated in cancer development[29].

2.1.3.2 Promotion

Once a cell has been mutated by an initiator, it can remain harmless unless and until it is stimulated to undergo further proliferation, upsetting the cellular balance. Tumor promotion comprises the selective clonal expansion of initiated cells, and because the accumulation rate of mutations is proportional to the rate of cell division or, at least, the rate at which stem cells are replaced, clonal expansion of initiated cells produces a large population of cells that are at risk of further genetic changes and malignant conversion[30, 31]. From this point of view, the immediate effect of the promoter is apparently to stimulate cell division (or to cause cells, that would normally undergo terminal differentiation, to continue dividing)[32].

These promoter agents are characterised by their ability to reduce the latency period for tumor formation, after exposure of a tissue to an initiator, or to increase the number of cancer cells formed in that tissue; in addition, they induce tumor formation in conjunction with a dose of an initiator that is too low to be carcinogenic alone.

How promoters work is not certain, and different tumor promoters are likely to work in different ways. One possibility is that they simply induce expression of growth-controlling genes that had been mutated before the promoter was applied: a mutation that makes a gene product hyperactive will not show its effects until the gene is expressed. Another possibility is that the promoter temporarily releases the cell from an inhibitory influence that normally overrides the proliferation-inducing effect of the mutation; as a result, the cell is enabled to divide and grow into a large cluster of cells. Unlike initiators, promoters do not covalently bind to DNA or to macromolecules within the cell. Many promoters bind to receptors on the cell surface in order to affect intracellular pathways that lead to increase cell

proliferation[33]. There are two general categories of promoters: specific promoters, which interact with receptors on or in target cells of defined tissues; nonspecific promoters, which alter gene expression without the presence of a known receptor. Promoters are often specific for a particular tissue or specie due to their interaction with specific receptors that are present in different amounts in different tissue types. While the risk of tumor growth with promoter application is dose-dependent, there is both a threshold and a maximum effect of promoters. Very low doses of promoters will not lead to tumor development and extremely high doses will not produce more risk than moderate levels of exposure[19]. The phorbol esters, that stimulate cell proliferation by activating protein kinase C, are classic examples of promoters. Hormones, particularly estrogens, are important as tumor promoters in the development of some human cancers. In addition to chemicals and radiation, some viruses induce cancer both in experimental animals and in humans[17].

2.1.3.3 Propagation

Propagation is the final stage of cancer transformation, where successive changes in the neoplasm give rise to increasing malignant sub-populations. Such alterations, in the structure of the genome of the neoplastic cells during this stage, are directly related to the increased growth rate, invasiveness, metastatic capability and biochemical changes in the malignant cells[34]. The irreversibility of this stage is assumed because of obvious alterations in the cell genome that accompany this stage, distinguishing progression from the reversible preceding stage of promotion. During this process, further genetic and epigenetic changes can occur again, including the activation of proto-oncogenes and the functional loss of tumor suppressor genes[35]. Oncogenes is

a gene whose function is activated in cancer and it drives abnormal cell proliferation as a consequence of genetic alterations, that either increase gene expression or lead to uncontrolled activity of the oncogene-encoded proteins. These malfunctioning genes produce protein products that normally enhance cell division or inhibit normal cell death. Activation of cellular oncogenes represents only one of two distinct types of genetic alterations involved in tumor development; the other one is the inactivation of tumor suppressor genes. They represent the opposite side of cell growth control, normally acting to inhibit cell proliferation and cancer development. In many tumors, these genes are lost or inactivated, thereby removing negative regulators of cell proliferation and contributing to the abnormal proliferation of tumor cells[17].

2.1.4 Anticancer therapies

Chemotherapy involves the use of low-molecular weight drugs to selectively destroy cancer cells or at least limit their proliferation.

The use of chemotherapy began in 1940 with nitrogen mustards, which are extremely powerful alkylating agents, and antimetabolites. Since the early success of these initial treatments, a large number of additional anticancer drugs have been developed[36]. In particular, anticancer drugs can be classified, according to their mechanism of action, as DNA-interactive agents, antimetabolites, antitubulin agents, molecular targeting agents, hormones, monoclonal antibodies and other biological agents[37].

Antimetabolites are one of the oldest families of anticancer drugs whose mechanism of action is based on the interaction with essential biosynthesis pathways. Structural analogues of pyrimidine or purine are incorporated into cell components to disrupt the synthesis of nucleic acids. 5-Fluorouracil and mercaptopurine (Fig. 2.3) are typical pyrimidine and purine analogues, respectively. Other antimetabolites, such as methotrexate (Fig. 2.3), interfere with essential enzymatic processes of metabolism.

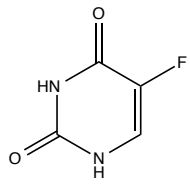

5-Fluorouacil

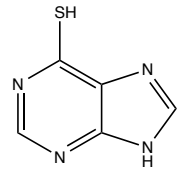

Mercaptopurine

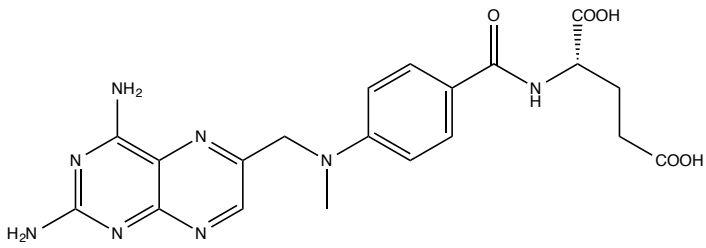

Methotrexate

Fig. 2.3 Chemical structures of antimetabolites with tested anticancer activity.

DNA interactive agents constitute one of the largest and most important anticancer drug families, acting through a variety of mechanisms:

–alkylating agents lead to the alkylation of DNA bases, in either the minor or major grooves. For example: dacarbazine (Fig. 2.4), procarbazine and temozolomide;

–cross-linking agents act by binding to DNA, resulting to an intra-strand or inter-strand cross-linking of DNA. Nitrogen mustards compounds (e.g., cyclophosphamide, ifosfamide, Fig. 2.4) are the main group of this anticancer drug sub-family. Nitrosourea compounds, busulfan and thiotepa are also cross-linking agents;

–intercalating agents act by binding between base pairs. The family include anthracyclines (e.g., epirubicin, doxorubicin, Fig. 2.4), mitoxantrone and actinomycin-D;

–topoisomerase inhibitors include irinotecan (Fig. 2.4) and etoposide compounds. These drugs inhibit the enzymes responsible for the cleavage, annealing, and topological state of DNA.

–DNA-cleaving agents such as bleomycin interact with DNA and cause strand scission at the binding site.

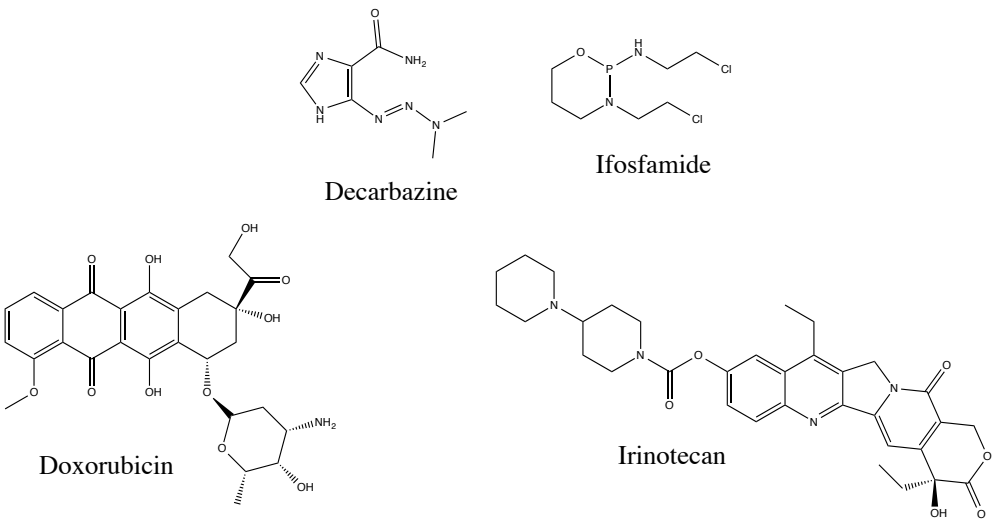

Fig. 2.4 Chemical structures of some examples of DNA-interactive compounds.

Antitubulin agents interfere with microtubule dynamics (i.e., spindle formation or disassembly), block division of the nucleus and lead to cell death. The main members of this family include taxanes and vinca alkaloids[36].

2.1.5 Metal-based anticancer therapies

Medicinal inorganic chemistry is a field of increasing prominence as metal-based compounds offer possibilities, for the design of new therapeutic agents, which are not readily available with organic molecules.

It is known that numerous metal ions play a vital role in biological systems and currently many metal-based drugs are routinely administrated to patients for therapeutic and diagnostic benefits. For that reason there is a growing interest in the development of new metal containing drug; from this point of view, medicinal inorganic chemistry, covering applications of metals in therapeutics and diagnostics, is a field of increasing prominence[38, 39, 40, 41, 42, 43].

Metal-containing molecules offer many advantages over carbon-based compounds in the development of new drugs: these advantages are related to the ability to coordinate ligands in a three dimensional configuration, thus allowing functionalization with specific groups that can be tailored to defined molecular target [44, 45]. Metal-based complexes offer a rich environment to build upon a variety of distinct molecular structures that confer a wide spectrum of coordination numbers and geometries, as well as kinetic properties that cannot be realised with conventional carbon-based compounds[46, 47, 48]. The partially filled d-orbitals, in transition metals, impart interesting electronic properties as the final compounds can act as suitable probes in the design of anticancer agents[49]. The oxidation state of the metal is also an important factor to take into consideration: it can allow the participation of the metal in biological redox chemistry and it can play an influential role in the optimal dose response and bioavailability of the administrated agent[50, 51]. Furthermore, the ability to undergo ligand exchange reactions offers a myriad of opportunities, for metals, to interact and

coordinate to biological molecules, as demonstrated by the widely used drug cisplatin[44]. Furthermore, the design of new metal-based therapeutics should not be limited to that metals already available in biochemistry, but further advantages can be achieve by the use of different metals that are commonly used in the diagnosis of cancer and in other medicinal applications[52].

Despite the relatively small number of metal-based drugs, which are currently used in clinic, some have proven to be invaluable.

2.1.5.1 Platinum-based compounds

Research in anticancer has been stimulated by the accidental discovery of cisplatin, *cis*-[$Pt^{II}(NH_3)_2Cl_2$] (Fig. 2.5). This compound has been widely employed to treat a variety of tumors including ovarian, cervical, head and neck, non-cell lung carcinoma and testicular cancer. Its mode of action involves distortion of the DNA helix: its chloride ions are replaced with water molecules before reacting with DNA[53]. However, its clinical use is quite restricted due to dose dependent toxicity and resistance, coupled with a narrow spectrum of activity[54, 55]. The first purpose of metal-drug research was to discover a less-toxic platinum analogue that retains anticancer activity. Carboplatin (Fig. 2.5) was synthesised considering the hypothesis that a leaving group, more stable than chloride, might lower toxicity without affecting antitumor efficacy[56]: the replacement of the chloride group of cispaltin by cyclobutanedicarboxylate ligand in carboplatin confers good aqueous solubility and greater stability due to the formation of a six-membered ring[57]. Studies indicate that the interaction with the DNA helix proceeds via ring opening and subsequently binding to DNA bases[58, 59].

Carboplatin is essentially devoid of nephrotoxicity and is less toxic to gastrointestinal track as well as less neurotoxic; however, it appears to have

a similar spectrum of activity as cisplatin as the mechanism of action is similar and, thus, problems persist when used against many cisplatin-resistant tumors[44]. To circumventing platinum drug resistance mechanism, a new platinum-drug was discovered. Oxaliplatinum (1R,2R-diaminocyclohexane oxalatoplatinum(II)) (Fig. 2.5) is soluble in aqueous solvents and it has undergone phase I and phase II clinical trials[60]: it possess a wide spectrum of activity toward cisplatin resistant cancer cell lines[61].

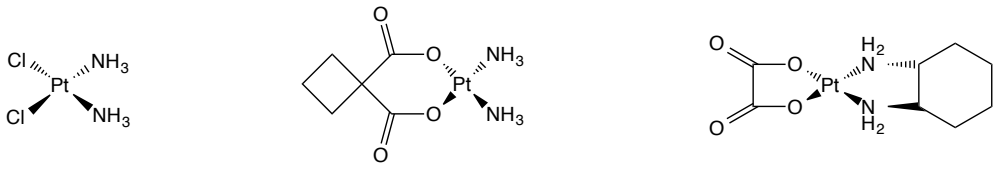

Cisplatin Carboplatin Oxaliplatin

Fig. 2.5 Chemical structures of platinum-based drugs. Cisplatin, carboplatin and oxaliplatin.

2.1.5.2 Ruthenium-based compounds

Platinum based drug are widely used to treat cancer[62, 63], but their therapeutic uses can be altered by intrinsic or acquired resistance and the occurrence of numerous side effects[64, 65].

These limiting issues have led to an intense effort to design new transition metal-based compounds potentially able to overcoming problems related to cisplatin but maintaining the same level of activity and therapeutic effects. Ruthenium, a second row transition metal, continues to attract much attention[66, 67] as complexes of this metal have long been known to be well suited for biological applications[68, 69]. Ruthenium has several oxidation states (Ru^{II}, Ru^{III} and Ru^{IV}) which can be tuneable under physiological conditions.

In aqueous media ruthenium complexes have the same kinetic of ligands substitution as Pt^{II} complexes, therefore they are a suitable alternative to Pt^{II} anticancer drugs. In the past few decades, several ruthenium (Ru^{II} and Ru^{III}) complexes were developed and studied for their antiproliferative activity against various tumor models, but a real breakthrough came from the development of NAMI-A and KP1019 ruthenium(III) compounds (Fig. 2.6)[70].

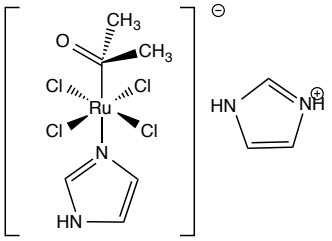

NAMI-A

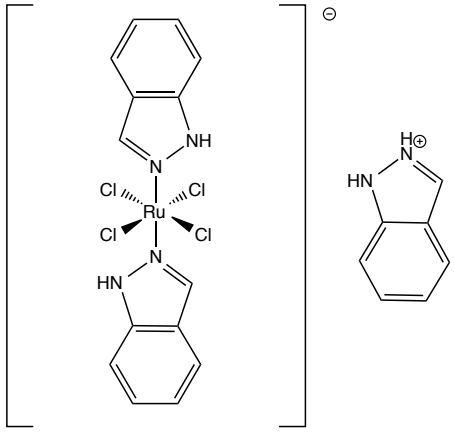

KP1019

Fig. 2.6 Chemical structure of NAMI-A and KP1019.

These complexes are particularly useful for the treatment of metastatic tumors and cisplatin resistant ones.

Sadler, Dyson and co-workers have developed a series of Ru^{II}-arene based antitumor active complexes[71,72]. A typical structure of a half-sandwich "piano-stool" complex of the type [(η^6-arene)Ru(X)(Y)(Z)] is shown in Fig. 2.7: the arene forms the seat of the piano stool and the ligands resemble the legs. The use of a chelating ligand (YZ) can help to modulate the stability and ligand-exchange kinetics of these complexes: on of the three legs is

usually a chloride ion, as it is quite active toward ligand substitution and of primary importance to control the timing of activation of these complexes.

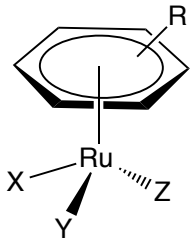

Fig. 2.7 Chemical structure of Ru(II) half-sandwich complexes.

These organometallic compounds are remarkably stable in biological media and can be recognised by various bio-targets. They often have amphiphilic properties and are very active toward a variety of tumor models[73, 74, 75]. Ru^{II}-arene system offers a rich platform for incorporation of a variety of functional groups at either the metal centre or arene moiety[76].

2.1.6 Objective of the research: development of novel half-sandwich metal-based compounds

Development of more efficient anticancer drugs with better selectivity and less toxic side effects is currently an area of intense research in bioinorganic chemistry[77]. Owing to the limited activity of platinum based drugs and the broad spectrum of human malignancies, acquired resistance and side effects non-platinum metal-based complexes have received significant attention as anticancer agents[78].

The traditional platinum-based therapeutics and the organometallics compounds, discussed in the previous section, owe their anticancer activity to their non-reparable interaction with DNA: one strategy, in the development of more potent drugs, involves the design of compounds that can undergo a transformation *in vivo*, releasing the active species with improved physiochemical, biopharmaceutical and pharmacokinetic properties. For metal-based therapeutics, this activation might be realised through photochemical activation[79], by oxidation-reduction of the metal or of the ligand, or by ligand substitution. This requires extensive knowledge of ligand substitution rates, redox potentials, photochemistry and choice of the metal and, in addition, the effect of the other coordinated ligands in the complex.

The organometallic Ru^{II} complexes with the half-sandwich type structure have demonstrated their anti-proliferative potential increasingly[75]. Their coordination site can be filled with various ligands, which offer numerous possibilities to modulate biological and pharmacological properties by proper ligand selection[48, 80]. In particular the presence of a chelating ligand, in these piano-stool complexes, offers structural stability and the opportunity to "tune" the electronics of the metal centre[81]. If the chelating ligand is itself

biologically active its release inside tumor cells must enhance the activity of the complexes.

The design of new Ru-arene complexes [(η^6-arene)Ru(X)(Y)(Z)] with biologically active organic ligands, has been emerged as a promising method in the exploration of anticancer organometallic drugs with a different mechanism compared to that of cisplatin.

2.1.6.1 Thiosemicarbazones as chelating ligands

Thiosemicarbazones (TSC) (Fig. 2.8) are Schiff-base type ligands that have been extensively investigated in recent years[5]. There are emerging studies reporting on the wide spectrum of biological activities of this class of compounds[82, 83].

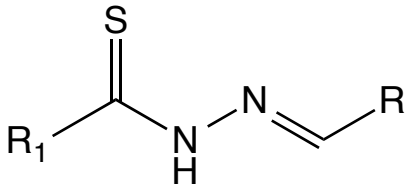

Fig. 2.8 General structure of the thiosemicarbazones.

Substituted thiosemicarbazone compounds and their metal complexes have shown a wide variety of biological properties such as cytotoxicity, antitumor, antibacterial and antiviral propertie[84, 85, 86]. Different mechanisms of activation have been reported, that are often related to metal ions coordination[80]: inhibition of iron cellular uptake from transferrin (Tf),[8788,89] mobilization of iron from cells[82, 83, 84], inhibition of Ribonucleotide Reductase (RR) activity[90, 91, 92], up regulation of the metastasis suppressor protein[93, 94], and formation of redox active metal complexes that produce reactive oxygen species[88, 95, 96, 97]. The nature of the R substituent influences

the biological activity: in particular, heterocyclic thiosemicarbazones are able to interact with the hydrophobic cavities of proteins leading to a higher anticancer activity[98]. The acidic character of the NH allows the ligand to be anionic and conjugation to be extended to include the thiosemicarbazone moiety; it has been proposed that this conjugation enhances the antitumor activity[99]. Moreover, different studies[100] have demonstrated that biological properties of TSC ligands can be modified and improved by the binding to transition metal ions[84, 101].

2.1.6.2 Half-sandwich complexes: ruthenium and osmium as metals.

Metal coordination complexes offer biological and chemical diversities that are different from the organic drugs[102]; firstly the lipophilicity, which controls the rate of entry into the cell, is modified upon complexation[103].

Osmium containing compounds are relatively unexplored, perhaps because of the reputation of osmium as being highly toxic or substitution-inert[104]. Nevertheless, several half sandwich "piano stool" osmium(II) complexes have exhibited promising *in vitro* activity and no cisplatin cross-resistance[105, 106, 107], with cancer cell cytotoxicity comparable to that of the clinical drugs cisplatin and carboplatin[108, 109]. This was achieved by systematically varying the nature of the chelating ligand to fine-tune both the kinetic and thermodynamic properties of the osmium compounds in aqueous solution[110, 111]. From this point of view, organometallic chemistry offers a potentially rich field for biological and medicinal applications[112]. However, lack of understanding of the aqueous chemistry of the organometallic complexes has emerged as a major obstacle for further development. This is particularly true for osmium(II)-arene complexes[113]. Third row transition metals are more inert than those of the first and second raw, probably due to the

lanthanide contraction: for example, substitution reactions are slower for platinum(II) compared to the lighter congener palladium(II) and, similarly, Os^{II} is generally found to be more inert than its lighter congener Ru^{II} [114, 115, 116]. However, reports on ruthenium arene complexes show that aqueous reactivity is highly dependent on the nature of the ligand XY and of the monodentate ligand Z, as well as on the arene rather than the type of metal[117, 118].

2.1.6.3 Aim of the work

In the laboratory where the present work has been conducted, a series of differently substituted tridentate thiosemicarbazone ligands were previously synthesised and tested on Mia-Paca 2 cells; the two most active compounds were chosen for the synthesis of the metal complexes: N-(2-hydroxy)-3-metoxybenxylidenethiosemicarbazide and N-(2,3-dihydroxybenxylidene)-3-phenylthiosemicarbazide. The aim of the present study was to increase the anticancer activity of the TSC compounds by synthesising two osmium and two ruthenium metal complexes of the type $[(\eta^6\text{-p-cymene})M(L)Cl]Cl$ where M = Ru(II) or Os(II) and L = N-(2-hydroxy)-3-metoxybenxylidenethiosemicarbazide or N-(2,3-dihydroxybenxylidene)-3-phenylthiosemicarbazide.

The chemical reactivity and in solution stability of all the synthesised compounds were analysed before submitting the samples to biological tests.

2.2 RESULTS AND DISCUSSION

2.2.1 Preliminary studies

2.2.1.1 Thiosemicarbazone ligands syntheses

Condensation reactions between the proper aldehyde (Fig. 2.9, A) and the proper thiosemicarbazide (Fig. 2.9, B) were carried out in ethanol at 80°C and led to the synthesis of the differently substituted thiosemicarbazones **L_1-L_{13}** (Table 2.1). The synthesised molecules were completely characterised with the common spectroscopic and spectrometric analyses. They are stable at room temperature and soluble in DMF and DMSO, but insoluble in methanol and ethanol as well as in chlorinated solvents.

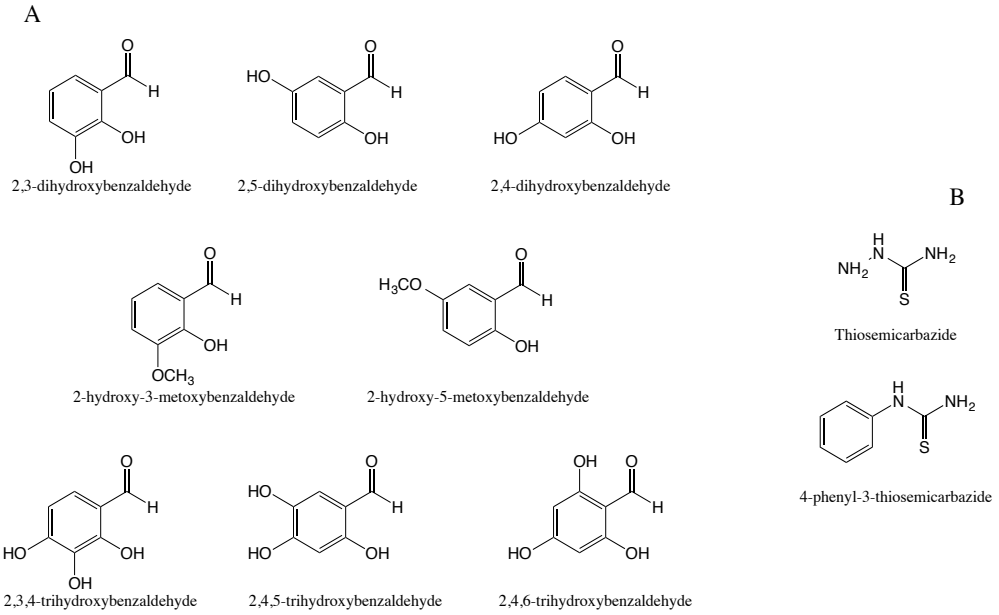

Fig. 2.9 Chemical structure of aldehydes (panel A) and thiosemicarbazides (panel B) used for the syntheses of the thiosemicarbazone ligands.

The ^{1}H-NMR spectra were recorded in DMSO-d_6 and confirmed the identity of the synthesised compounds: a sharped singlet attributable to the iminic proton CH=N, characteristic of the final product, can be seen around 8 ppm. Moreover, the NMR spectra confirmed that all compounds adopt a E conformation in solution, as evidenced by the chemical shift values of the CH=N and NH proton around 8.40 and 11.50 ppm respectively.

The anticancer activity of all the synthesised compounds was tested against pancreatic MIA PaCa-2 cancer cells line (from American Type Culture Collection, Manassas, VA, USA).

2.2.1.2 Biological results

The ability of the thiosemicarbazones **L_1-L_{13}** to induce cytotoxicity and inhibit cell proliferation of MIA PaCa-2 pancreatic cancer cell lines was tested. Cells were treated with compounds at a concentration of 30 μM for 72 hours. MTT assay was performed to measure the activity of these compounds. Inhibition of cells proliferation was calculated by the following formula

$$\text{Inhibition} = 1-(OD_{treated}/OD_{control}) \times 100\%$$

Values represent a mean from four independent experiments.

Compound	Inhibition	Compound	Inhibition
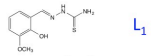 L_1	78.7%	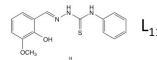 L_{11}	21.7%
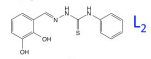 L_2	61.8%	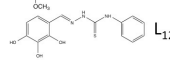 L_{12}	17.4%
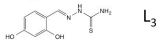 L_3	22.2%	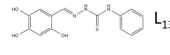 L_{13}	14.4%
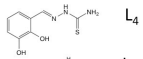 L_4	13.0%	DMSO	0.3%
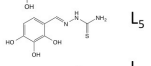 L_5	28.4%	Gemcitabine	78.4%
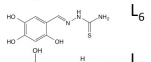 L_6	37.2%	Doxorubicin	90.2%
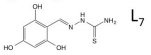 L_7	13.2%		
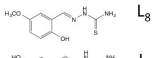 L_8	18.8%		
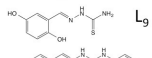 L_9	20.8%		
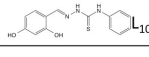 L_{10}	31.9%		

Table 2.2 Cytotoxicity of the tested compounds at 30 µM in MIA PaCa-2 cancer cells.

The results (Table 2.2) revealed that **L_1** and **L_2** are highly cytotoxic, with percentage inhibition values, in the tested cell lines, of 78.7% and 61.8 %, respectively. MIA PaCa-2 cancer cells were treated for 72 hours with decrease concentration, ranging from 30 to 0.1 µM, of the two most active ligands **L_1** and **L_2** in order to obtain a proper dose-response curve (Fig. 2.10).

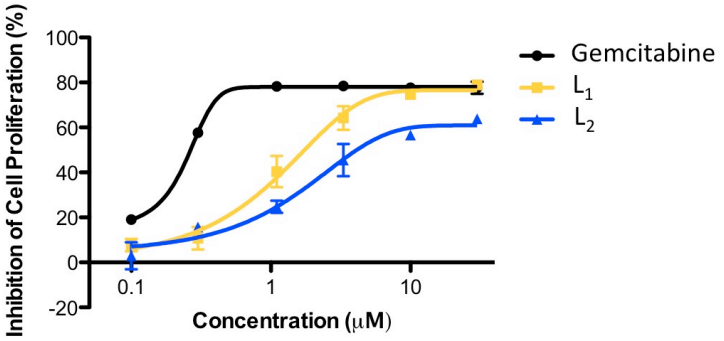

Fig. 2.10 Representative dose response curves for L_1 and L_2. Values indicate mean±SD of three independent MTT experiments.

In primary screening both **L_1** and **L_2** have demonstrated to be highly cytotoxicity in MTT assay, with an IC_{50} value comparable with that of Gemictabine (Table 2.3).

	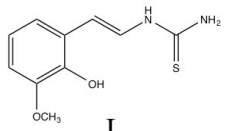 L_1	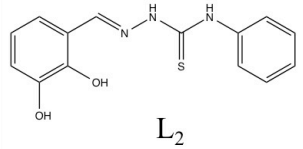 L_2	Gemcitabine
Inhibition	78.70%	61.80%	78.40%
IC_{50}	1.8±0.4	4±1	0.23±0.01

Table 2.3 IC_{50} values of active compounds tested on MIA PaCa-2 cells.

The CFA (colony formation assay) was, then, performed in order to obtain information toward the inhibition of cancer proliferation. MIA PaCa-2 cells were treated with **L_1** and **L_2** at a concentration of 30 μM for 24 hours and left in culture in fresh media until colonies were observed in controls (Fig. 2.11). Cells were then stained with crystal violet and imaged.

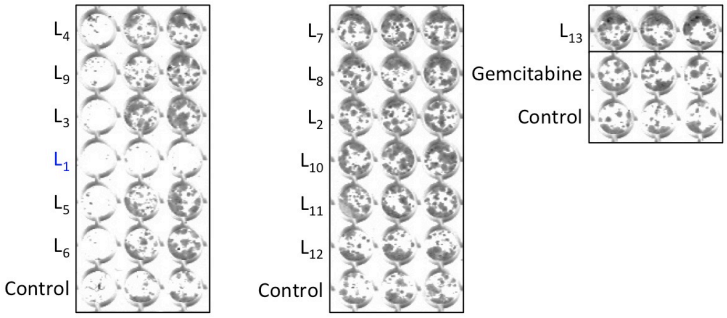

Fig. 2.11 Colony inhibitory activity of the tested compounds at 30 µM in MIA PaCa-2 cancer cells.

To further characterise the cytotoxic activity of the most active compounds, cells were incubated with decrease concentration of ligand ranging from 30 to 0.3 µM (Fig. 2.12). MIA PaCa-2 were treated for 24 hours and left in culture in fresh media until colonies were observed in controls. Cells were stained with crystal violet and imaged.

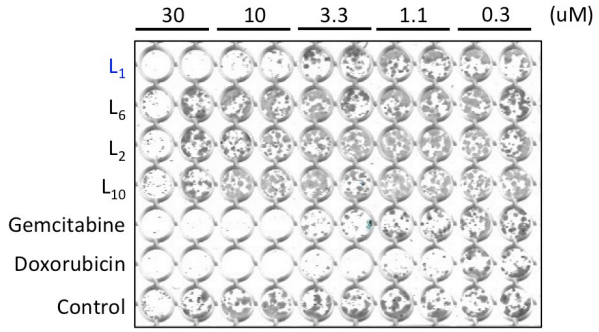

Fig. 2.12 Colony formation assay for potential active compounds.

Data confirms **L_1** be the most active compounds with an IC_{50} value of 1.8 µM in MTT assay, and of 3.3 µM in colony formation assay. **L_2** has an IC_{50} value of 3.8 µM in MTT assay, however, it does not show any cytotoxicity in colony formation assay.

2.2.2 Syntheses and characterization of the metal complexes in solution

The reactions between $[(\eta^6\text{-p-cymene})MCl_2]_2$ (where M=Os, Ru) and the proper thiosemicarbazone ligand were carried out in a mixture of dry CH_3OH and CH_2Cl_2 at ambient temperature and led to the isolation of the pseudo octahedral complexes **1-4,** of the general formula $[(\eta^6\text{-p-cymene})M(L)Cl]Cl$, in good yield where L = N-(2-hydroxy-)-3-metoxybenzylidenethiosemicarbazide (**L_1**) or N-(2,3-dihydroxybenzylidene)-3-phenylthiosemicarbazide (**L_2**). In all cases the metal coordinates a chloride ion, a η^6 coordinated p-cymene ring and a N,S bidentate thiosemicarbazone ligand (Fig. 2.13).

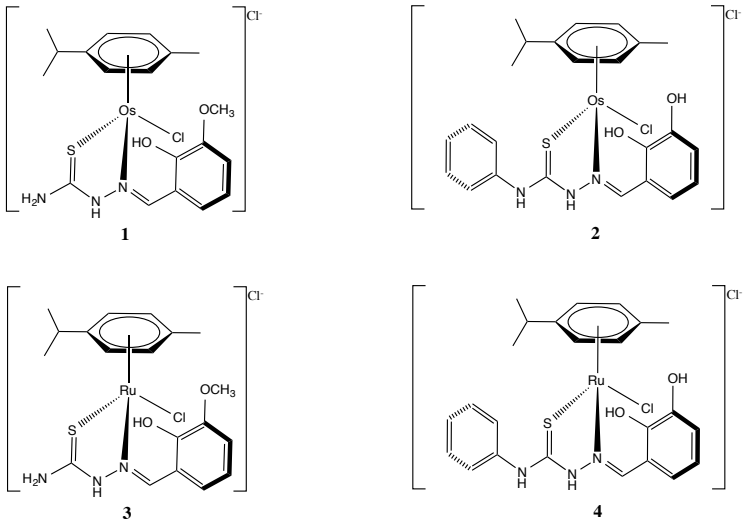

Fig. 2.13 General scheme of the pseudo-octahedral complexes 1-4 containing the proper thiosemicarbazone (L_1 or L_2) ligand.

The identity of the complexes was verified by using ^{1}H-NMR spectroscopy, ESI-MS spectrometry and confirmed by single crystal X-Ray crystallography.

Firstly, the ^{1}H-NMR spectra of the complexes were recorded in MeOD-d_4, due to their low solubility in chlorinated solvents such as chloroform or dichloromethane. The aromatic protons of the thiosemicarbazone ligands are displayed between 6.5 and 8.2 ppm, and the hydrazinic protons between 8.7 and 8.9 ppm. The coordination with a thiosemicarbazone ligand leads to the loss of the two-fold symmetry of the p-cymene ring: this is evidenced by the appearance of four sets of doublets between 4.90 and 5.90 ppm. The methyl groups of the isopropyl moiety are observed as two doublets at 1.1 and 1.2 ppm.

To evaluate the stability of the compounds in coordinating solvents, ^{1}H-NMR studies were carried out in acetone. The behavior in DMSO solution was also took in consideration in order to mimic the biological tests conditions (biological tests are performed using stock solution of the compound in DMSO).

2.2.2.1 In methanol studies

The proton ^{1}H-NMR spectra of the free ligands were recorded in DMSO-d_6, due to the low solubility in protic solvents: a single set of signal is displayed consistent with the E isomer. One single set of signals was obtained also in the ^{1}H-NMR of the metal complexes recorded in MeOD-d_4: peaks are related to the complexes with the ligand in the E form, and this is the predominant specie found in solution at time zero (100%) (Fig. 2.14, *a* set). However, just after 24 hours, a new set of signals can be seen in the spectrum, related to the presence of the Z (Fig. 2.14, *b* set) isomers in solution.

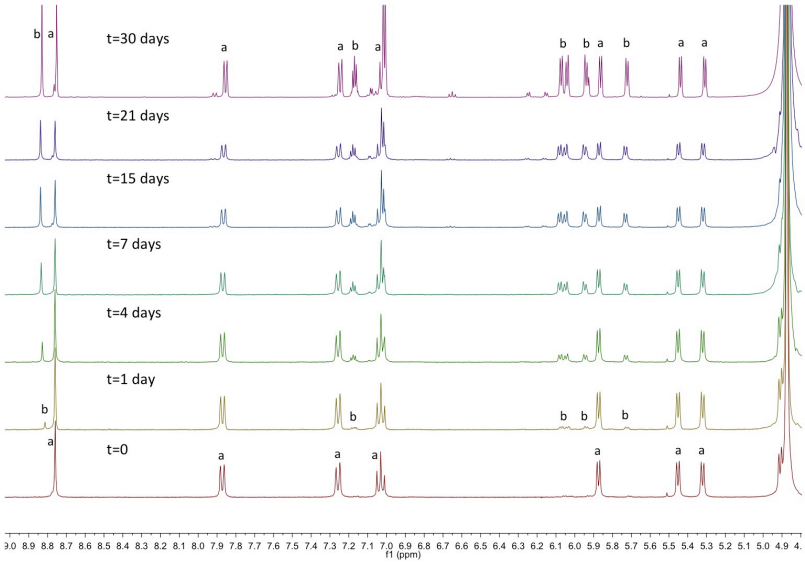

Fig. 2.14 ^{1}H-NMR aromatic region expansion of the spectrum of complex 1 in methanol. Increase in the percentage of the Z isomer with time. The set of signals marked with letter *a* is related to the E isomer. The set of signals marked with letter *b* is related to the Z isomer.

The ligand is subjected to isomerization around the C=N bond and this leads to an E-Z interconversion: at the beginning the E form is predominant (100% at time zero). This is confirmed by the shift of the iminic proton to lower field due to its close proximity to the NH proton. Moreover, one of the four proton resonances of the p-cymene ring is shifted to high field, in the range of 4.90 ppm for osmium compounds and 4.87 for ruthenium ones, whereas the other doublets are at lower field. This is the consequence of the interaction between the aromatic p-cymene protons and the aromatic ring, interaction that is only possible with the E conformation (see X-ray crystallography discussion). In the NOESY spectrum of **1** (Fig. 2.15), recorded at t=30 days in DMSO-d_6, an interaction between the iminic hydrogen of the ligand and the aromatic proton of the p-cymene is displayed

just for the set of signals related to the Z conformation (Fig. 2.16, structure on the right). On the contrary, this interaction is absent for the set of signals related to the E isomer: this is in accordance with what just said, because the interaction of the iminic proton with the p-cymene moiety is possible just with a Z conformation and not with the E one.

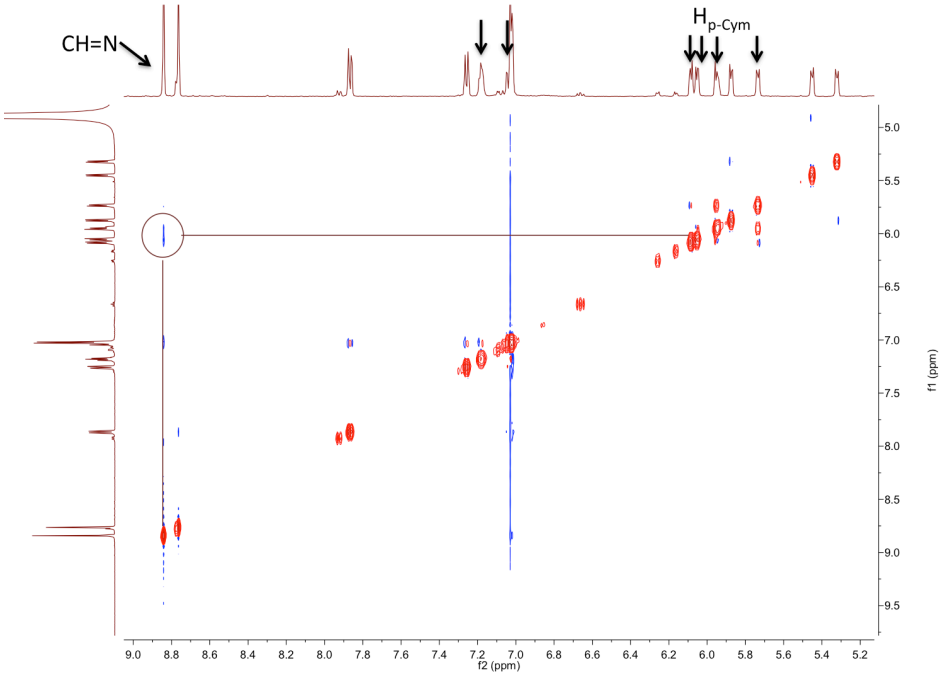

Fig. 2.15 NOESY spectrum. Interaction between the iminic and the aromatic p-cymene protons in the Z conformation (black arrows).

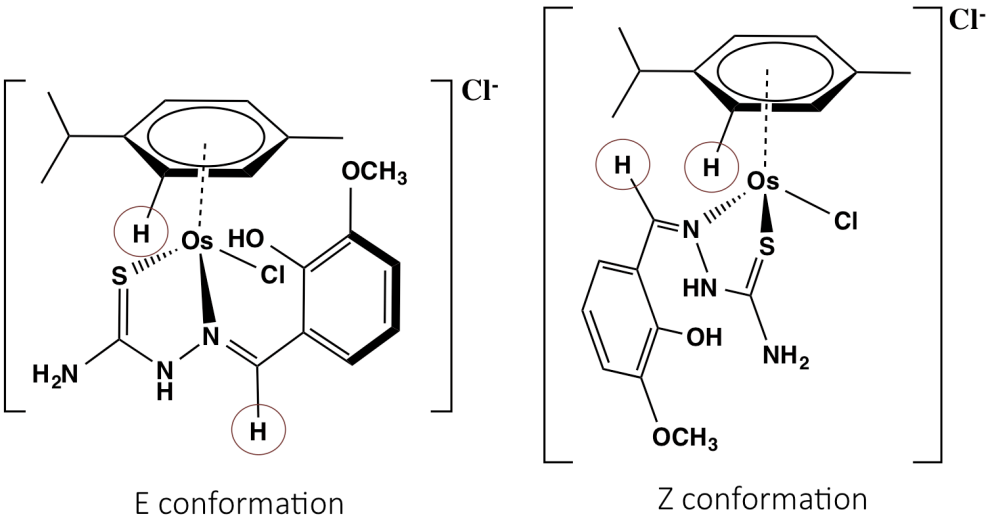

Fig. 2.16 Chemical structures of the E and Z isomers. In circles the two protons involved in the interaction in the NOESY spectrum.

The ^{1}H-NMR spectra were recorded both at 25°C and at variable temperature, reaching the maximum value of 50°C in two hours. The *ratio* of the two isomers does not change drastically, suggesting that the process requires more than two hours to detect visible variations. The percentage of the Z isomer did not increase when the analysis was recorded at 50°C and a spectrum identical to the one carried out at ambient temperature was obtained. Different situation was observed when the process has been monitored every day over a four weeks period (Fig. 2.14): the percentage of the Z isomer drastically increased, reaching an equimolar *ratio* of the two E/Z isomers after 21 days.

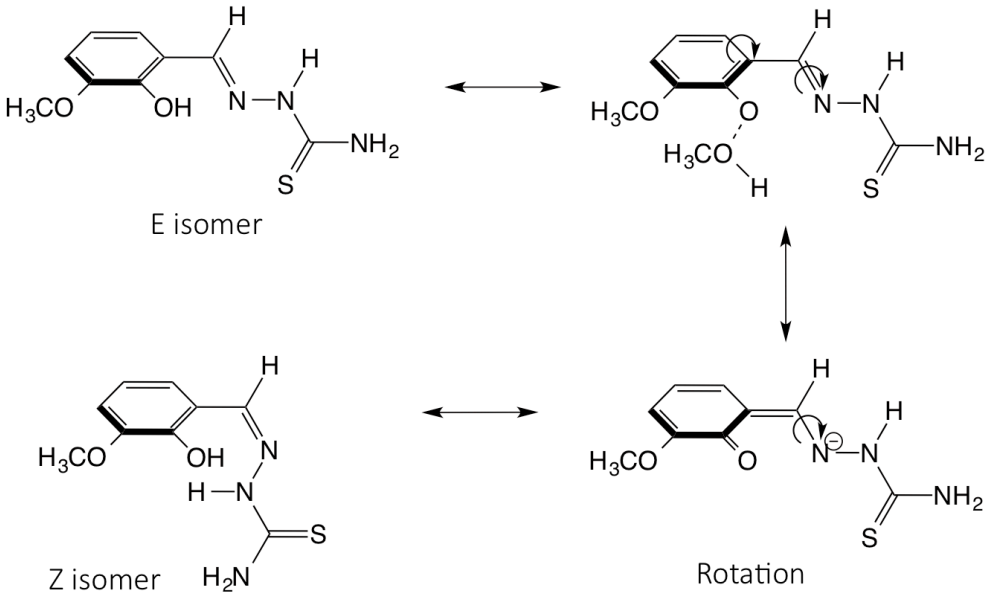

Scheme 2.1 Scheme for the E-Z interconversion process of the ligand in complexes 1 and 3 in methanol.

The increase in the area of the peaks related to the Z isomer suggests that the presence of a protic solvent could lead to the formation of a negative charge on the iminic nitrogen and to the rotation of the C-N single bond, which results in the isomerization and the formation of the Z isomer (Scheme 2.1). A further confirmation that the solvent plays a crucial role in the isomerization process was obtained by the ^{1}H-NMR spectrum of the crystals in methanol solution. In the X-ray crystal structures of the complexes **1** and **3**, obtained from slow evaporation of a methanol solution of the two compounds, the ligand is in the E conformation. The ^{1}H-NMR spectra of these crystals dissolved in d^{4}-methanol showed the presence of both isomers of the ligands, thus confirming that the solvent plays a crucial role in the isomerization.

Moreover, the analysis provides evidence that the interconversion is faster for the ruthenium compounds: the Z isomer takes two weeks to be predominant over the E one (the area of the peaks related to the Z isomer is 20% higher than that of the signals related to the E isomer); whereas more than four weeks are required for the osmium complexes to reach the same *ratio*.

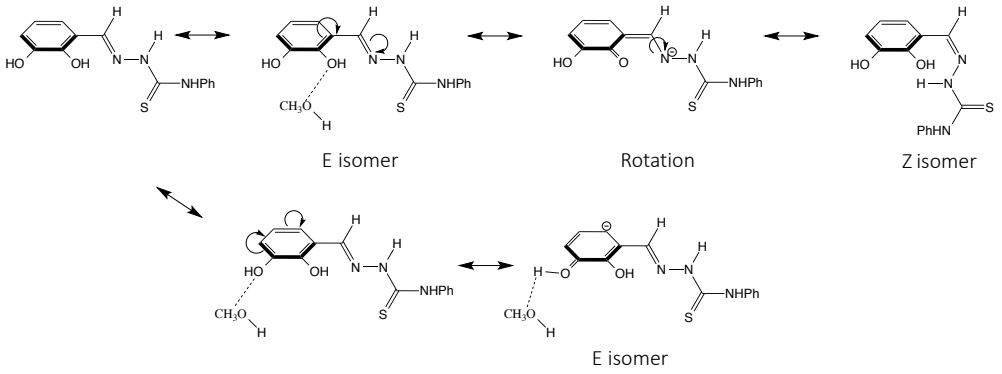

Scheme 2.2 General scheme for the E-Z interconversion of the ligands in the complexes 2 and 4 in methanol.

The situation is slightly different for the complexes **2** and **4**. The presence of two hydroxyl groups, which can both interact with the solvent, leads to a faster interconversion (Scheme 2.2). This is confirmed by the presence of a single resonance for both the isomers in the aromatic region and of a doublet in the aliphatic region of the p-cymene: the interaction of the solvent with the hydroxyl group in position 2 is not so strong as for **1** and **3** due to the presence of a second hydroxyl group, and this leads to an equilibrium of the two species.

Complexes **2** and **4**, in which the ligand $\mathbf{L_2}$ displayed a catechol moiety in the structure, can be subjected to oxidation. Actually, the UV-Vis spectra of a methanol solution of **2** did not change after three days at the air. Ultraviolet

visible spectroscopy was performed in order to verify whether the catechol moiety of **2** is involved in oxidation processes in methanol solution. The process was followed by the development of a stable and strong absorption band around 337 nm.

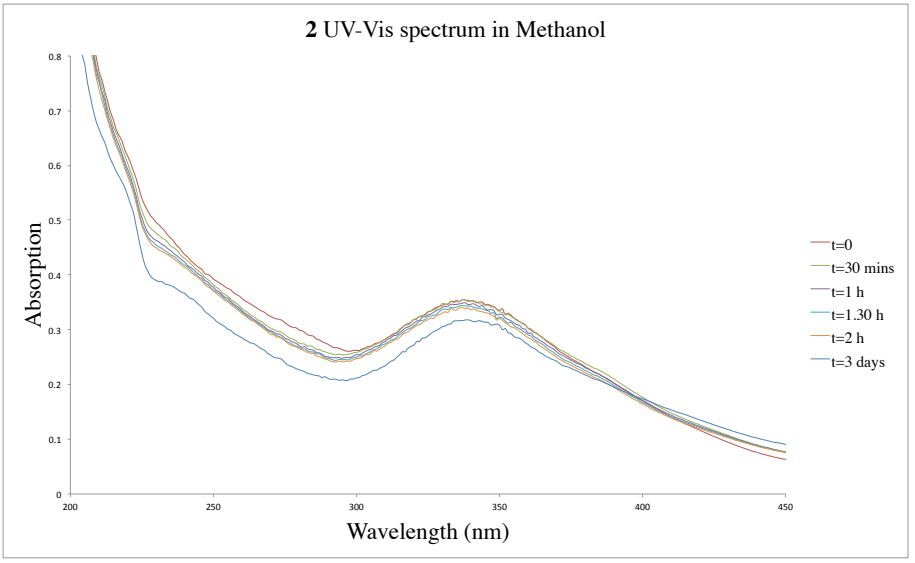

Fig. 2.17 Absorption profiles of the UV-Vis solution of 2 in methanol.

Data (Fig. 2.17) has been initially collected every 30 minutes for two hours: a maximum absorption at 337 nm, related to π-π^* transition of the catechol aromatic ring, was observed. The methanol solution of **2** was then left in a dark ambient, under air exposure for three days: the final solution displayed an absorption spectrum similar to that obtained from the starting one, with the same maximum absorption band at 337 nm. This confirms that no oxidation processes had occurred in methanol solution; the same analysis was carried out under the light and the same UV spectrum profile was obtained.

2.2.2.2 In acetone studies

A different picture of the dynamic process emerged when the complexes had been dissolved in the non-protic coordinating acetone-d_6. The fact that two different resonance profiles are observed, when the complexes are dissolved either in methanol or acetone, could be explained by the role that the solvents play in promoting ligand dissociation. The isomerization process can occur only in protic solvent, as it is mainly due to the interactions of the hydroxyl groups with the solvent through hydrogen bond.

In the spectrum of **1** in acetone there are two different sets of signals that can be related to the presence of both the starting chloride complex and an acetone adduct, obtained by displacement of the chloride ion, in a *ratio* of 1:1.20. After four days, just a single set of signals appears, corresponding to the acetone adduct. In order to confirm this assertion, the same analysis was carried out after four days: just a single set of signals appears in the spectrum corresponding to the acetone adduct.

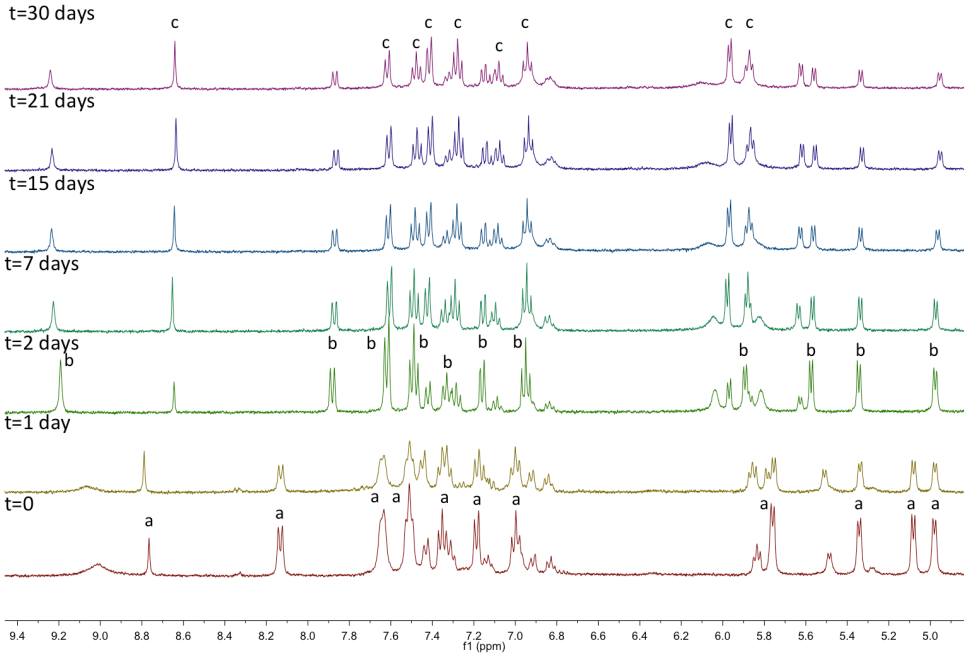

Fig. 2.18 ^{1}H-NMR aromatic region expansion of 2 in acetone-d$_6$. The set of signals marked with letter *a* is related to complex **2**. The set marked with letter *b* is related to the complex with one molecule of coordinated solvent. The set of signals marked with *c* is related to the complex coordinated by two molecules of solvent.

In the case of complex **2** (Fig. 2.18), in which the steric hindrance of the ligand probably decreases the rate of solvent coordination, the initial spectrum shows just one set of signals related to the starting complex. However, a new set of signals attributable to the solvated species becomes predominant after two days. The same analyses were carried out both for the osmium and ruthenium compounds and confirmed that the solvation process is faster for the ruthenium ones

2.2.2.3 Stability in DMSO

Due to the usual limited aqueous solubility of metal complexes, *in vitro* biological activity determinations are carried out preparing stock solutions of the compound in DMSO followed by dilution in water (the final concentration of DMSO must be at maximum 0.5%). Thus the study of the behavior of the complexes in DMSO is of great interest to have indications of the stability of the pro-drug under the biological testing conditions. In the ^{1}H-NMR spectra of **1** and **3** recorded in DMSO-d_6 (Fig. 2.19), signals related to both [Os(η^6-p-cymene)(**L$_1$**)Cl]Cl, [Os(η^6-p-cymene)(DMSO)$_2$Cl]Cl and the free ligand (**L$_1$**) are displayed. The hydrazinic proton of the complexes can be found at 8.40 ppm as singlet, but a new peak appears at 8.80 ppm, related to the hydrazinic proton of the free ligand. The presence of two doublets in the p-cymene region at 5.99 and 6.07 ppm are ascribable to a solvated metal species of the type [Os(η^6-p-cymene)(DMSO)$_2$Cl]Cl.

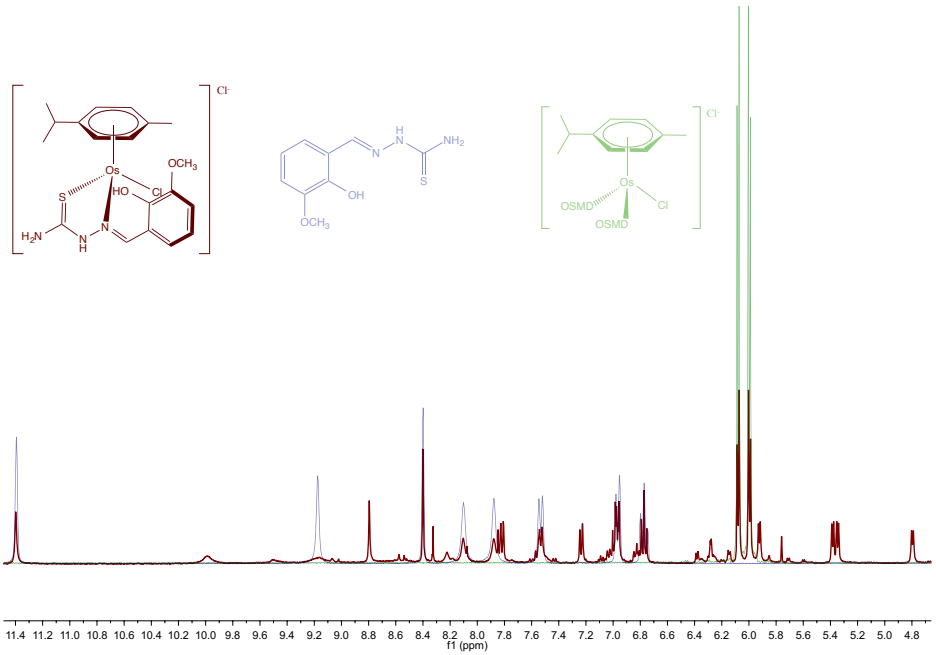

Fig. 2.19 ^{1}H-NMR aromatic region expansion of complex 1 in DMSO-d$_6$ (red spectrum). Overload of the ^{1}H-NMR of the free ligand **L$_1$** (blu), and of the solvated specie (green).

If the individual ^{1}H-NMR spectra of the three species are overlaid together, it can be seen that the final spectrum is exactly the one of [Os(η^6-p-cymene)(**L$_1$**)Cl]Cl, **L$_1$** and [Os(η^6-p-cymene)(DMSO)Cl$_2$] in equimolar ratio (Fig. 2.19).

Immediate dissociation of the ligand, however, is not guaranteed for complexes **2** and **4**. The presence of a phenyl ring on the amidic NH (NH-Ph compared to the NH_2) is probably crucial for obtaining a more stable structure.

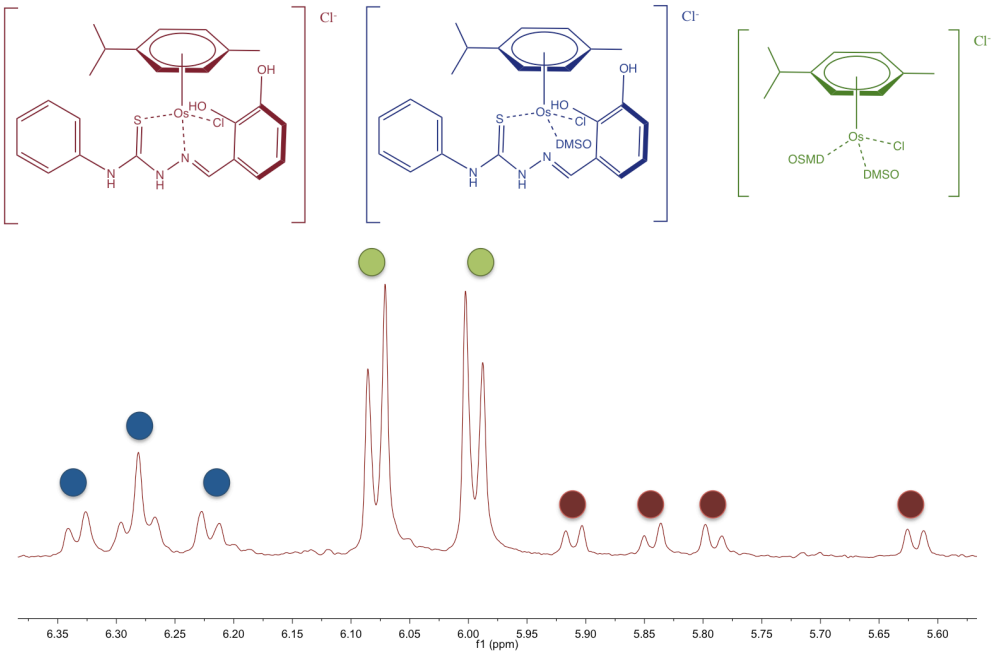

Fig. 2.20 ^{1}H-NMR p-cymene region expansion of complex 2 in DMSO-d$_6$. The spectrum displayed sets of signals related to the complex (red dots), the mono solvated specie (blu) and a bi-solvated one (green), that is predominant in solution.

The DMSO-mediated ligand dissociation takes place, but the process is slower for complex **2**, as it takes more than three days to be completed. Focusing the attention on the p-cymene region, it can be seen that the four doublets between 4.5 and 5.7 ppm, attributable to the complex, were substituted by two new sets of signals (Fig. 2.20): two doublets at 5.99 and 6.07 ppm are related to the solvated specie [Os(η^6-p-cymene)(DMSO)$_2$Cl]Cl, and another set of signals between 6.20 and 6.35 ppm is related to the formation of a mono-solvated specie [Os(η^6-p-cymene)(DMSO)LCl]Cl in solution.

Ligand dissociation can also be confirmed visually: addition of DMSO to the orange powder of **1** leads to an orange solution that tends to become green when the dissociation process starts to take place.

To confirm that the degradation process is correlated to the concentration of DMSO, the same analysis was carried out using a solution of D_2O-(10%) DMSO. The solutions have been monitored for 24 hours to mimic the biological test conditions: spectra of all the complexes displayed broad signals with complicated splitting patterns.

2.2.3 Biological analyses

The anti-proliferative activity of the two ligands **L_1** and **L_2** and of the related osmium (**1** and **2)** and ruthenium (**3** and **4)** complexes was investigated towards a variety of human cancer cells lines (lung, ovarian, colon and prostate cell lines) and compared to that of cisplatin, which was used as positive control.

All compounds were dissolved in DMF: ^{1}H-NMR experiments demonstrated that all compounds were stable within 24 hours as no ligand dissociation took place.

The efficacy of the drugs under analysis was first tested in cell culture by performing dose-response studies (Fig. 2.21): cell lines were treated with stock solution of drugs and concentrations were varied from 100 to 0.01 mM. The drug exposure was of 24 hours, after that period of time the percentage of cell survival was quantified by fluorescence measurements.

Such data is conventionally analysed from the prospective of IC_{50} values, which are descriptive of the dose-response curve in the mid-point. IC_{50} values (concentrations which caused 50% of cell growth inhibition) (Table 2.4), were determined as duplicates of triplicates in two independent sets of experiments and their standard deviations were calculated. Untreated solution was taken as negative control. Cytotoxicity of the tested compounds was compared to that of cisplatin, which was taken as positive control.

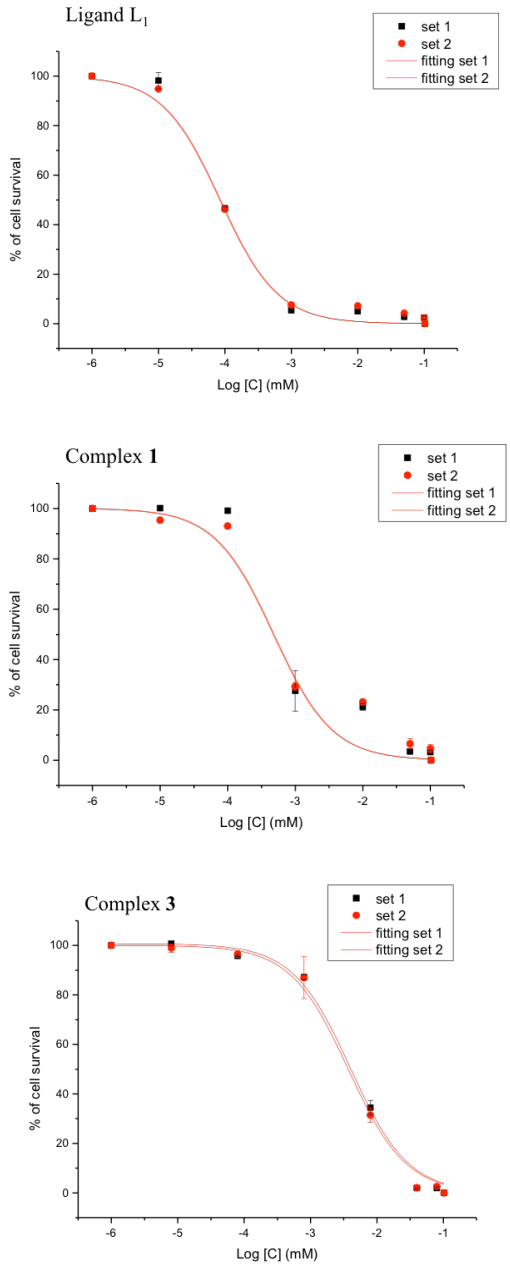

Fig. 2.21 Example of dose response curve of ligand L_1 and the osmium (1) and ruthenium (3) complexes in A2780 cancer cell line. Vertical bars represent the standard deviation. Black dots are referred to the first replicate data. Red dots are referred to the second replicate data.

Compound	A2780 (ovarian)	A 2780cis	A 549 (lung)	HCT 116 (prostate)	PC3 (colon)
L_1	0.085±0.03	0.12±0.02	42±2	30.6±0.5	6.1±0.1
L_2	0.27±0.02	1.23±0.08	23±1	33±5	4.6±0.2
1	1.60±0.02	6.6±0.9	2.4±0.2	24±2	21±1
2	0.75±0.08	7.2±0.1	17±1	2.7±0.2	1.60±0.08
3	4.2±0.3	5.6±0.8		10.5±0.3	19±1
4	0.36±0.03	1.25±0.06		1.64±0.08	1.38±0.04

Table 2.4 IC_{50} values of TSCs (L_1 and L_2) and of related metal complexes (1-4) towards ovarian (A2780) and ovarian cisplatin-resistant (A2780cis), lung (A549), prostate (HCT116) and colon (PC3) cancer cell lines. Values are express in micromolar.

In A2780 human ovarian cell line there is an order of magnitude difference in potency compared to the other cancer cell lines: IC_{50} values are in the micromolar range. Interestingly, all the tested compounds did not lose activity in the cisplatin resistant cell line A2780cis as the IC_{50} values are still in the micromolar range. In particular, the resistant factor (RF) of only 1.3 (calculated as the ratio between the IC_{50} values in the resistant and in the parental line) is particularly intriguing in the case of **L_1** and the related ruthenium complexes **3**. It has been proposed that the underlying resistance associated with A2780cis involves a two-fold more efficient efflux and a consequent reduction in cellular accumulation as compared to the parental A2780, as well as an increase in DNA-repair mechanism. The mechanism of action of that compounds must, therefore, differ from that of cisplatin as they demonstrate low micromolar cytotoxicity in both the cisplatin-sensitive and –resistant A2780 cell lines.

Another striking results were obtained for HCT116 colon cancer cell line where both the osmium (**2**) and the ruthenium (**4**) complexes resulted more cytotoxic than the organic ligands alone. This indicates that the mechanism of action is metal dependent and that the incorporation of a phenyl ring, at

the N terminal domain of the thiosemicarbazone ligand, actively enhances the potency of that compounds: the activity of the metal complexes derived from the unique properties of the complexes themselves and not the individual components, this explain why the ligands showed less activity.

Different situation can be seen for the A549 lung cancer and PC3 prostate cancer cell lines. In this case the ligands and the related metal complexes showed similar activity indicating that the mechanism of action is not influenced by the presence of the metal moiety in the structure.

2.2.4 X-Ray crystallography

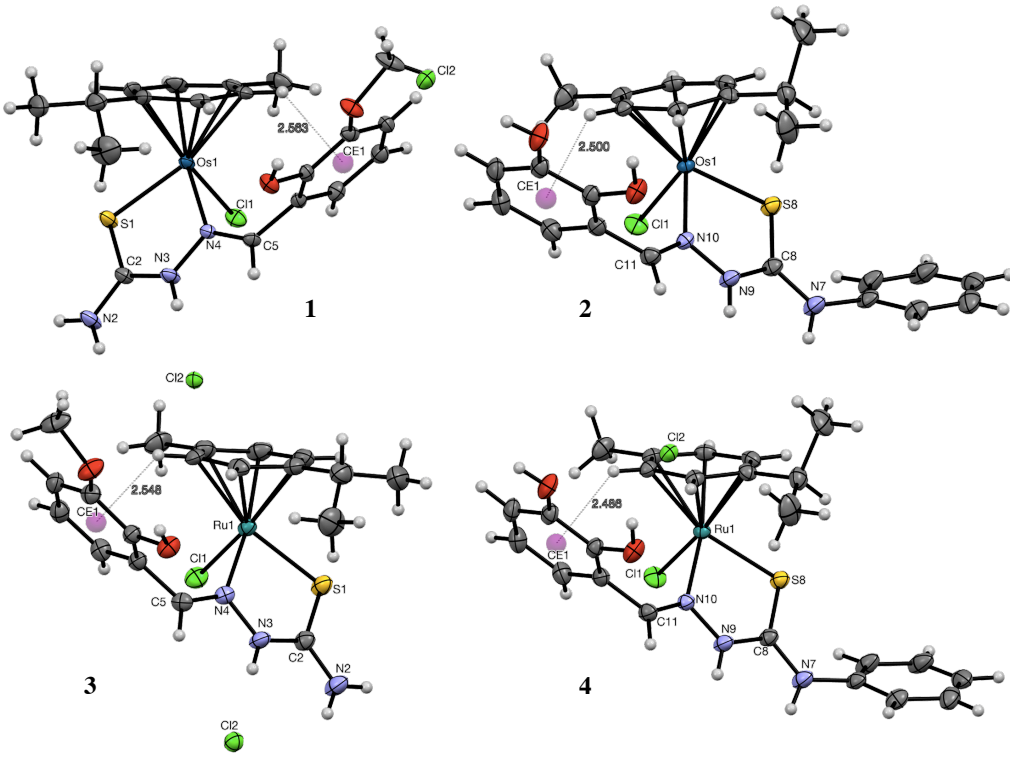

Fig. 2.22 X-Ray crystal structure for 1-4. Thermal ellipsoids are drawn at 50% of probability. Hydrogens are drawn as fixed-size spheres of 0.11 Å of radius and solvent molecules have been omitted for clarity.

Distance (Å)	Complex 1
Os1-Cl1	2.4113(12)
Os1-S1	2.3551(13)
Os1-N4	2.118(4)
S1-C2	1.695(5)
H14-CE1	2.563
Angle(°)	
S1-Os1-Cl1	86.52(4)
N4-Os1-Cl1	81.63(10)
N4-Os1-S1	81.63(11)

Distance (Å)	Complex 2
Os1-Cl1	2.4030(5)
Os1-S8	2.3527(5)
Os1-N10	2.1227(17)
S8-C8	1.693(2)
N21-CE1	2.5
Angle(°)	
S8-Os1-Cl1	87.81(2)
N10-Os1-Cl1	83.44(59
N10-Os1-S8	81.79(5)

Distance (Å)	Complex 3
Ru1-Cl1	2.4046(11)
Ru1-S1	2.3501(10)
Ru1-N4	2.125(3)
S1-C2	1.695(4)
H14-CE1	2.548
Angle(°)	
S1-Ru1-Cl1	86.90(4)
N4-Ru1-Cl1	83.06(9)
N4-Ru1-S1	81.95(10)

Distance(Å)	Complex 4
Ru1-Cl1	2.3993(3)
Ru1-S8	2.3508(3)
Ru1-N10	2.1256(9)
S8-C8	1.6923(12)
H21-CE1	2.486
Angle(°)	
S8-Ru1-Cl1	88.338(11)
N4-Ru1-Cl1	84.77(3)
N4-Ru1-S1	81.94(3)

Table 2.5 Selected bond lengths (Å) and angles (°) for 1-4 with estimated standard deviation in parenthesis.

The X-ray crystal structures of [(p-cymene)Os(L_1)Cl]Cl, [(p-cymene)Os(L_2)Cl]Cl, [(p-cymene)Ru(L_1)Cl]Cl, [(p-cymene)Ru(L_2)Cl]Cl were determined (Fig. 2.22). Selected bond lengths and angles are listed in Table 2.5. Complexes 1 and 3 crystallise in an orthorhombic system with the achiral space group $P2_12_12_1$. Complexes 2 and 4 crystallise in a triclinic system with centrosymmetric space group P_{-1}.

The complexes adopted the expected half-sandwich pseudo-octahedral "three legs piano stool" geometry: the metal centre is bound to η^6-p-cymene ligand that occupies three coordination sites, a chelating ligand covers two coordination positions of the legs and the structure is completed with a chloride ion. In complexes **1** and **3** the chloride anion is linked to the iminic nitrogen through hydrogen bond NH···Cl of 2.16Å; in complex **2** and **4** the

same interaction is displayed with the hydroxyl group in position three of the aromatic ring with a bond distance OH···Cl of 2.24Å. The thiosemicarbazone ligands bind the metal centre through the imine nitrogen and the thione sulphur, forming a five member chelate ring with an angle of 82° for N-Ru-S, indicating a distortion from regular octahedron (90°). The bond lengths are 2.12 for Ru-N, 2.35 for Ru-S and 1.69 for Ru-Cl. Ru(II) ion is therefore sitting in a SNCl (η^6-p-cymene) coordination environment which is pseudo-octahedral in nature, as reflected in all the bond parameters of Ru(II) ion. The bond length for S-C of 1.69 Å confirms the double character of the bond. The dihedral angles between the aromatic ring plane and the thiosemicarbazones are around 70° in complex **1** and **3** and around 78° in complex **2** and **4**. The repulsive interactions between the iminic hydrogen and the protons of the aromatic moiety prevent the ring from becoming coplanar with the thiosemicarbazones. In all the crystal structures of **1-4** the same T-shaped stacking edge to face π interactions, between the aromatic hydrogen of the σ framework of the p-cymene ring and π electron density of the aromatic ring of the thiosemicarbazones ligands, are identified with regarded to non-bonding interaction between the aromatic ring (distances from 2.50 to 2.86Å). The stability of this interaction is probably due to the presence of two OR electron donors group in the aromatic ring. This is supported by the high field shift of two of the aromatic protons (in E conformation) in the ^{1}H-NMR spectra, which is likely to be due to the close proximity of the phenyl group of the coordinated ligand.

XRD structures of this type of ruthenium arene complexes have already been known by literature[118, 119, 120]; on the contrary no structures with the osmium counterpart seem to be already published.

2.3 CONCLUSIONS

In this work two osmium(II) and two ruthenium(II) half-sandwich complexes of the type [(η^6-p-cymene)M(L)Cl]Cl were synthesised and characterized with ^{1}H-NMR and UV-Vis spectroscopy, ESI-MS spectrometry and single crystal X-Ray crystallography. Two differently substituted thiosemicarbazones were chosen as coordinating ligands.

Single crystal XRD analyses demonstrated that the complexes are structurally very similar: they are characterized by a distorted octahedral geometry in which the chelating ligand is in E conformation.

In protic solvents, such as methanol, an interconversion mechanism takes place that leads to the presence of both E and Z isomers. Signals related to both isomers can be found in the ^{1}H-NMR spectra: the isomerization process is promoted by the interaction of the solvent with the acidic OH proton of the aromatic ring.

A different picture emerged when the complexes had been dissolved in the non-protic, coordinated acetone: the solvation process seems to be favored in the aprotic coordinated solvent, whereas the catalytic tautomerization is likely to be the most relevant mechanism in protic and acidic conditions, due to the retarding effect of the solvent and the reverse effect of tautomerization.

As none of the studied compounds is water soluble, they were dissolved in dimetyl sulfoxide, in order to mimic the biological test conditions, and the stability was monitored by ^{1}H-NMR. Signals related to both the complex and the free ligand can be displayed in the spectrum: the complete displacement of the ligand, substituted by the solvent molecules, is complete within 24 hours. Different situation was obtained using DMF: no ligand dissociation can be seen within 24 hours.

All compounds were dissolved in DMF and tested against different cancer cell lines. Promising results were obtained toward ovarian cancer cell lines as they demonstrate low micromolar cytotoxicity in both the cisplatin-sensitive and –resistant A2780 cell lines.

2.4 EXPERIMENTAL SECTION

2.4.1 Materials and Methods.

2.4.1.1 Chemistry

All reagents were purchased from Sigma-Aldrich and used as received. All reactions were performed under inert atmosphere of nitrogen using standard schlenk line techniques and all glassware was oven-dried (120°C) overnight. Dry solvents were purchased by Sigma-Aldrich and stored under nitrogen. $[(\eta^6\text{-p-cymene})OsCl_2]_2$ and $[(\eta^6\text{-p-cymene})RuCl_2]_2$[49] were synthesised according to a literature procedure.

NMR spectroscopy. ^{1}H-NMR spectra were obtained in 5 mm NMR precision tube at 298 K on either Bruker DPX-300 and DPX-400 NMR spectrometer. ^{1}HNMR chemical shifts were internally referenced to $(CHD_2)(CD_3)SO$ (2.50 ppm) for DMSO-d_6, CD_3OD (3.31 ppm) for methanol-d_4, D_2O (4.79 ppm) for water-d_2, $(CD_3)CO$ (2.05 ppm) for acetone-d_6. ^{1}H-NMR spectra at variable temperature were obtained in 5 mm NMR precision tube on Bruker AV-III 400 NMR spectrometer. ^{1}H-NMR chemical shifts were internally referenced to CD_3OD (3.31 ppm) for methanol-d_4. NOESY spectra were obtained in 5 mm NMR precision tube at 298 K on Bruker DPX-500 NMR spectrometer. ^{1}HNMR spectra were internally referenced CD_3OD (3.31 ppm) for methanol-d_4 and $C_4D_8O_2$ (3.66 ppm) for 1,4-Dioxane-d_8. Data was processed using MestReNova 9.0.1.

Mass Spectrometry. Electrospray ionization mass spectra (ESI-MS) were obtained using a Bruker Esquire 2000 ion trap spectrometer. Samples were prepared in methanol. The mass spectra were recorded with a scan range of m/z 50-500 for positive ions for **L_1-L_2** and m/z 400-1000 for positive ions for the complexes **1-4**.

UV-Vis spectroscopy. UV-Vis absorption spectra were recorded on a Cary 300 spectrometer using quartz cuvettes of 1 cm path-length (600 µL). The temperature was adjusted to 298 K by PTP1 Peltier temperature controller. Samples were prepared in methanol. Spectra were recorded in the range between 200 and 600 nm. Data was processed with Microsoft Excel 14.3.6 Mac version.

X-Ray Crystallography. Diffraction data was obtained on an Xcalibur Gemini diffractometer four-circles system with a Ruby CCD area detector using Mo Kα radiation. Absorption corrections were applied using ABSPACK[50]. The crystals were mounted on a glass fiber with Fromblin oil and kept at 150(2) K during data collection. Using Olex2[50], the structures were solved with the ShelXT[51] structure solution program using Direct Methods and refined with the ShelXL[52] refinement package using Least Squares minimisation.

2.4.1.2 Biological tests for ligands

2.4.1.2.1 Cell culture

Pancreatic cancer cell lines (MIA PaCa) were purchased from the American Type Culture Collection (Manassas, VA, USA). Human foreskin fibroblast cell lines (HFF-1) were kindly provided by Dr. Carla Grandori (Fred Hutchinson Cancer Research Center, Seattle, WA, USA). Resistant cell lines, MIA PaCa-2-GR (gemcitabine resistant) and MIA PaCa-2-GTR (gemcitabine and erlotinb resistant) were kindly provided by Dr. Sarkar (Department of Pathology, Wayne State University School of Medicine, Detroit, MI, USA). All cell lines were maintained in culture under 35 (10 for HFF-1) passages and tested regularly for Mycoplasma contamination using Plasmo Test™ (InvivoGen, San Diego, CA, USA). Cell lines were

maintained in the appropriate growth media [DMEM (Cellgro, Mediatech, Manassas, VA, USA) for PANC-1, MIA PaCa-2, and RPMI-1640 (Cellgro) for ASPC-1, BxPC-3 and HFF-1] containing 10% heat-inactivated FBS (Gemini-Bioproducts, West Sacramento, CA, USA) at 37°C in a humidified atmosphere of 5% CO_2. MIA PaCa-2-GR and MIA PaCa-2-GTR were maintained in DMEM (with 10% FBS) supplemented with 200 nM gemcitabine, and 200 nM gemcitabine and 2 μM erlotinib (every other week), respectively. For subculture and experiments, cells were washed with 1 × Dulbecco's PBS (DPBS, Cellgro), detached using 0.025% trypsin-EDTA (Cellgro), collected in growth media and centrifuged. All experiments were performed in growth media using sub-confluent cells in the exponential growth phase.

2.4.1.2.2 Cytotoxicity assay

The cytotoxicity was assessed by 3-(4,5-dimethylthiazol-2-yl)-2,5-diphenyltetrazolium bromide MTT assay and colony formation assay in Mia Paca-2 pancreatic cancer cell line.

All compounds were stored as concentrated DMSO stock frozen at -20°C. Dilutions were prepared in DPBS without calcium and magnesium and re-used for a maximum of 3 freeze-thaw cycles.

2.4.1.2.3 Colony formation assay

Cells were seeded in 6-well plates (1000 cells per well) and allowed overnight to adhere. The next day, drugs were added to the wells for 72 h following which media was replaced with drug free media.

Treated cells were collected via brief trypsinization and stained using trypan blue 0.4% solution (Lonza Group Ltd) according to manufacturer's recommendation. Cells were counted using a hemacytometer.

Cells were handled identical to MTT assay. At the end of treatment, alamar blue (AbD Serotec©) was added to wells according to manufacturer's recommendation. Fluorescence was detected at 560/590 ex/em wavelengths.

2.4.1.3 Biological tests for metal complexes

2.4.1.3.1 Cell Culture

Cell lines used in this work include: A2780 human ovarian carcinoma and its cisplatin resistant variant A2780cis, A549 human caucasian lung carcinoma, HCT116 human colon carcinoma, and PC3 human prostate carcinoma. They were all obtained from the European Collection of Cell Cultures (ECACC), used between passages 5 and 18 and were grown in Roswell Park Memorial Institute medium (RPMI-1640) supplemented with 10% of fetal calf serum, 1% of 2 mM glutamine and 1% penicillin/streptomycin. They were grown as adherent monolayers at 310 K in a 5% CO_2 humidified atmosphere and passaged at approximately 70-80% confluence.

2.4.1.3.2 *In vitro* growth inhibition assay

Briefly, 5000 cells were seeded per well in 96-well plates. The cells were pre-incubated in drug-free media at 310 K for 48 h. before adding different concentrations of the compounds to be tested. A stock solution of the metal complex was firstly prepared in 5% DMF (v/v) and a mixture 0.9% saline and medium (1:1) (v/v) following serial dilutions in RPMI-1640. The drug exposure period was 24 h. After this, supernatants were removed by suction and each well was washed with PBS. A further 72 h. was allowed for the cells to recover in drug-free medium at 310 K. The SRB assay was used to determine cell viability. Absorbance measurements of the solubilised dye (on a BioRad iMark microplate reader using a 470 nm filter) allowed the

determination of viable treated cells compared to untreated controls. IC_{50} values (concentrations which caused 50% of cell growth inhibition) were determined as duplicates of triplicates in two independent sets of experiments and their standard deviations were calculated.

2.4.2 General procedure for the syntheses of thiosemicarbazone ligands (L_1-L_2).

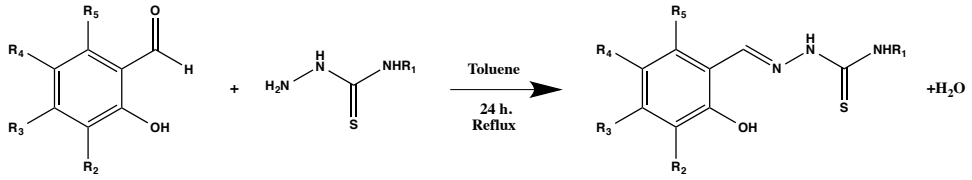

L_1 R_1=H, R_2=OCH_3, R_3=H, R_4=H, R_5=H
L_2 R_1=Ph, R_2=OH, R_3=H, R_4=H, R_5=H
L_3 R_1=H, R_2=H, R_3=OH, R_4=H, R_5=H
L_4 R_1=Ph, R_2=OH, R_3=H, R_4=H, R_5=H
L_5 R_1=H, R_2=OH, R_3=OH, R_4=H, R_5=H
L_6 R_1=H, R_2=H, R_3=OH, R_4=OH, R_5=H
L_7 R_1=H, R_2=H, R_3=OH, R_4=H, R_5=OH
L_8 R_1=H, R_2=OH, R_3=H, R_4=OCH_3, R_5=H
L_9 R_1=H, R_2=OH, R_3=H, R_4=OH, R_5=H
L_{10} R_1=Ph, R_2=H, R_3=OH, R_4=H, R_5=H
L_{11} R_1=Ph, R_2=OCH_3, R_3=H, R_4=H, R_5=H
L_{12} R_1=Ph, R_2=OH, R_3=OH, R_4=H, R_5=H
L_{13} R_1=Ph, R_2=H, R_3=OH, R_4=OH, R_5=H

Scheme 2.3 General synthesis for L_1 and L_2.

The synthesis of **L_1** and **L_2** (Scheme 2.3) were performed using the following adapted literature procedure[51]. The appropriate aldehyde (1 mol. equiv.) was dissolved in hot toluene and few drops of glacial acetic acid were added to the solution. An equimolar amount of the corresponding thiosemicarbazide (1 mol. equiv.) was added to the solution and the reaction has been heated under reflux for 8 h. The solution was cooled to ambient temperature and the TSC ligands were obtained as precipitate. After filtration the solid was washed several times with toluene and ether and dried under vacuum.

*N-(2-hydroxy-)-3-metoxybenxylidenethiosemicarbazone (**L_1**).* White powder. Yield=87%. ^{1}H-NMR (DMSO-d_6, 25°C), δ: 11.39 (s, 1H, NH), 9.17 (s, 1H, OH), 8.40 (s, 1H, CH=N), 8.10-7.88 (2s, 1H+1H, NH_2), 7.52 (d, 1H, J= 7.5 Hz, CH_{Ar}), 6.95 (d, 1H, J=7.5 Hz, CH_{Ar}), 6.75 (t, 1H, J=7.5 Hz, CH_{Ar}), 3.81 (s, 3H, OCH_3). MS ($C_9H_{11}N_3SO_2$, CH_3OH): m/z=225.0 $[M+H]^+$. Anal.

Calcd. for $C_9H_{11}N_3SO_2$: C 48.01, H 4.92, N 19.66. Found: C 48.01, H 4.83, N 19.57.

*N-(2,3-dihydroxybenxylidene)-phenylthiosemicarbazone (**L_2**)*. White powder. Yield=81%. ^{1}H-NMR (DMSO-d_6, 25°C), δ: 11.76 (s, 1H, NH), 10.01-9.54 (2s, 1H+1H, OH), 9.01 (s, 1H, NH), 8.49 (s, 1H, CH=N), 7.56 (d, 2H, J=7.5 Hz, CH_{Ar}), 7.49 (d, 2H, J=8 Hz, CH_{Ar}), 7.34 (t, 2H, J=7.5 Hz, CH_{Ar}), 7.17 (t, 1H, J=7.5 Hz, CH_{Ar}), 6.81 (d, 1H, J=8 Hz, CH_{Ar}), 6.64 (t, J=8 Hz, CH_{Ar}). MS ($C_{14}H_{13}N_3SO_2$, CH_3OH): m/z=287.0 $[M+H]^+$. Anal. Calcd. for $C_{14}H_{13}N_3SO_2$ +1/4 H_2O: C 57.64, H 4.66, N 15.40. Found: C 57.92, H 4.09, N 15.34.

*N-(2,4-dihydroxybenxylidene)-thiosemicarbazone (**L_3**)*. Pink powder. Yield=68%. ^{1}H-NMR (DMSO-d_6, 25°C), δ: 11.18 (s, 1H, NNH); 9.75 (s, 2H, OH); 8.25 (s, 1H, CH_{Ar}); 7.95, 7.75 (2s, 1H+1H, NH_2); 7.66 (d, 1H, J=8.5 Hz, CH_{Ar}); 6.29 (d, 1H, J=2.5 Hz, CH=N); 6.24 (dd, 1H, J=8.5 Hz, J=2.5 Hz, CH_{Ar}). MS ($C_8H_9N_3SO_2$, CH_3OH): m/z=211.0 $[M+H]^+$. Anal. Calcd. for $C_8H_9N_3SO_2$: C 45.51, H 4.30, N 20.90. Found: C 45.06, H 4.28, N 21.00.

*N-(2,3-dihydroxybenxylidene)-thiosemicarbazone (**L_4**)*. White powder. Yield=59%. ^{1}H-NMR (DMSO-d_6, 25°C), δ: 11.37 (s, 1H, NNH); 9.51, 8.92 (2s, 1H+1H, OH); 8.37 (s, 1H, CH=N); 8.08, 7.85 (2s, 1H+1H, NH_2); 7.33 (d, 1H, J=8 Hz, CH_{Ar}); 6.78 (dd, 1H, J=8 Hz, J'=1.5 Hz, CH_{Ar}); 6.61 (t, J=8 Hz, CH_{Ar}). MS ($C_8H_9N_3SO_2$, CH_3OH): m/z=211.0 $[M+H]^+$. Anal. Calcd. for $C_8H_9N_3SO_2$: C 43.65, H 4.58, N 20.08. Found: C 43.64, H 4.61, N 20.27.

N-(2,3,4-trihydroxybenxylidene)-thiosemicarbazone ***(L5)***. White powder. Yield=40%. ^{1}H-NMR (DMSO-d_6, 25°C), δ: 11.22 (s, 1H, NNH); 9.54, 8.98, 8.46 (3s, 1H+1H+1H, OH); 8.24 (s, 1H, CH=N); 7.98, 7.76 (2s, 1H+1H, NH_2); 7.12 (d, 1H, J=9 Hz, CH_{Ar}); 6.32 (d, 1H, J=9 Hz, CH_{Ar}). MS (CH_3OH, $C_8H_9N_3SO_3$): m/z=227.0 $[M+H]^+$. Anal. Calcd. for $C_8H_9N_3SO_2$: C 42.31, H 3.99, N 19.50. Found: C 41.98, H 4.05, N 19.71.

N-(2,4,5-trihydroxybenxylidene)-thiosemicarbazone ***(L6)***. White powder. Yield=64%. ^{1}H-NMR (DMSO-d_6, 25°C), δ: 11.16 (s, 1H, NNH); 9.51, 9.15, 8.27 (3s, 1H+1H+1H, OH); 8.21 (s, 1H, CH=N); 7.95, 7.64 (2s, 1H+1H, NH_2); 7.15 (s, 1H, CH_{Ar}); 6.32 (s, 1H, CH_{Ar}). MS ($C_8H_9N_3SO_3$, CH_3OH): m/z=227.0 $[M+H]^+$. Anal. Calcd. for $C_8H_9N_3SO_2$ +1/4 H_2O: C 41.48, H 4.13, N 18.14. Found: C 41.83, H 3.75, N 19.02.

N-(2,4,6-trihydroxybenxylidene)-thiosemicarbazone ***(L7)***. White powder. Yield=40%. ^{1}H-NMR (DMSO-d_6, 25°C), δ: 11.17 (s, 1H, NNH); 9.98, 9.83 (2s, 1H+1H+1H, OH); 8.48 (s, 1H, CH=N); 7.94, 7.74 (2s, 1H+1H, NH_2); 5.82 (s, 2H, CH_{Ar}). MS ($C_8H_9N_3SO_3$, CH_3OH): m/z=227.0 $[M+H]^+$. Anal. Calcd. for $C_8H_9N_3SO_2$ +1/4 H_2O: C 41.48, H 4.13, N 18.14. Found: C 41.14, H 4.23, N 18.92.

N-(2-hydroxy)-5-metoxy-thiosemicarbazone ***(L8)***. White powder. Yield=56%. ^{1}H-NMR (DMSO-d_6, 25°C), δ: 11.34 (s, 1H, NNH); 9.44 (s, 1H, OH); 8.35 (s, 1H, CH=N); 8.13, 8.01 (2s, 1H+1H, NH_2); 7.48 (d, 1H, J=2 Hz, CH_{Ar}); 6.76 (m, 2H, CH_{Ar}); 3.72 (s, 3H, OCH_3). MS ($C_9H_{11}N_3SO_2$, CH_3OH): m/z=225.0 $[M+H]^+$. Anal. Calcd. for $C_9H_{11}N_3SO_2$ +1/2 H_2O: C 46.14, H 5.17, N 17.95. Found: C 46.00, H 5.35, N 18.09.

N-(2,5-dihydroxybenxylidene)-thiosemicarbazone (***L*$_9$**). White powder. Yield=69%. ^{1}H-NMR (DMSO-d$_6$, 25°C), δ: 11.34 (s, 1H, NNH); 9.18, 8.79 (2s, 1H+1H, OH); 8.30 (s, 1H, CH=N); 8.08, 7.79 (2s, 1H+1H, NH_2); 7.23 (s, 1H, CH_{Ar}); 6.68 (2s, H+H, CH_{Ar}). MS ($C_8H_9N_3SO_2$, CH_3OH): m/z=211.0 $[M+H]^+$. Anal. Calcd. for $C_8H_9N_3SO_2$ +1/2 Et_2O: C 46.16, H 45.16, N 17.94. Found: C 46.55, H 4.56, N 21.21.

N-(2,4-dihydroxybenxylidene)-phenylthiosemicarbazone (***L*$_{10}$**). White powder. Yield=21%. ^{1}H-NMR (DMSO-d$_6$, 25°C), δ: 11.58 (s, 1H, NH); 9.92 (1s, 1H, OH); 9.85 (s, 1H, NH); 9.79 (s, 1H, OH), 8.37 (s, 1H, CH=N); 7.86 (d, 1H, J=8.5 Hz, CH_{Ar}); 7.58 (d, 2H, J=7.5 Hz, CH_{Ar}); 7.34 (t, 2H, J=8 Hz, CH_{Ar}); 7.16 (t, 1H, J=7.5 Hz, CH=N); 6.33 (s, 1H, CH_{Ar}); 6.28 (d, 1H, J=8.5 Hz, CH_{Ar}). MS ($C_{14}H_{13}N_3SO_2$, CH_3OH): m/z=255.0 $[M+H]^+$.

N-(2-hydroxy-3-metoxybenxylidene)-phenylthiosemicarbazone (***L*$_{11}$**). Pale yellow powder. Yield=76%. ^{1}H-NMR (DMSO-d$_6$, 25°C), δ: 11.80, 10.04 (2s, 1H+1H, NH); 9.27 (s, 1H, OH); 8.52 (s, 1H, CH=N); 7.70 (d, 1H, J=7.5 Hz, CH_{Ar}); 7.56 (dd, 2H, J=7.5 Hz, J'=1 Hz, CH_{Ar}); 7.34 (tt, 2H, J=7.5 Hz, J'=2 Hz, CH_{Ar}); 7.17 (tt, 1H, J=8 Hz, J'=1 Hz, CH_{Ar}); 6.98 (dd, 1H, J=8 Hz, J'=1 Hz CH_{Ar}); 6.77 (t, 1H, J=8 Hz, CH_{Ar}); 3.83 (s, 3H, OCH_3). MS ($C_{15}H_{15}N_3SO_2$, CH_3OH): m/z=287.0 $[M+H]^+$. Anal. Calcd. for $C_{15}H_{15}N_3SO_2$ +1/4 H_2O: C 58.92, H 5.11, N 14.74. Found: C 59.16, H 4.93, N 14.81.

N-(2,3,4-trihydroxybenxylidene)-phenylthiosemicarbazone (***L*$_{12}$**). White powder. Yield=68%. ^{1}H-NMR (DMSO-d$_6$, 25°C), δ: 11.60 (s, 1H, NH); 9.92, 9.56 (2s, 1H+1H, OH); 9.03 (s, 1H, NH); 8.47 (s, 1H, OH); 8.36 (s, 1H, CH=N); 7.58 (d, 2H, J=7.5 Hz, CH_{Ar}); 7.33 (t, 2H, J=8 Hz, CH_{Ar}); 7.16

(t, 1H, J=7 Hz, CH_{Ar}); 6.36 (d, 1H, J=8 Hz, CH_{Ar}). MS ($C_{14}H_{13}N_3SO_3$, CH_3OH): m/z=303.0 $[M+H]^+$.

N-(2,4,5-trihydroxybenxylidene)-phenylthiosemicarbazone ***(L_{13})***. White powder. Yield=41%. ^{1}H-NMR (DMSO-d_6, 25°C), δ: 11.50 (s, 1H, NH); 10.07, 9.93, 9.834 (3s, 1H+1H+1H, OH); 8.58 (s, 1H, CH=N); 7.49 (dd, 2H, J=8 Hz, J'=1, CH_{Ar}); 7.31 (tt, 2H, J=8 Hz, J'=1 Hz, CH_{Ar}); 7.13 (tt, 1H, J=8 Hz, J'=1 Hz, CH_{Ar}); 5.84 (s, 2H, CH_{Ar}). MS ($C_{14}H_{13}N_3SO_3$, CH_3OH): m/z=303.0 $[M+H]^+$.

2.4.3 General procedure for the syntheses of metal complexes (1-4).

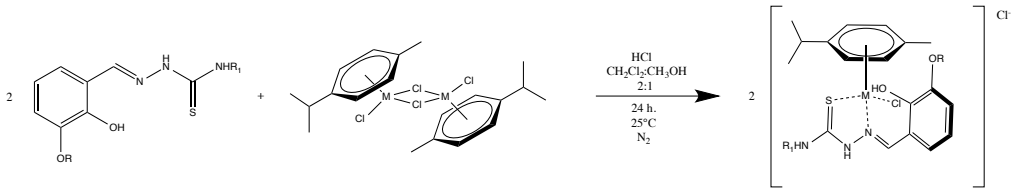

1 M=Os, R=CH_3, R_1=H
2 M=Os, R=H, R_1=Ph
3 M=Ru, R=CH_3, R_1=H
4 M=Ru, R=H, R_1=Ph

Scheme 2.4 General synthesis for metal complexes. Osmium and ruthenium complexes of the L_1 and L_2 thiosemicarbazones.

The proper TSC ligand (2 mol. equiv.) was dissolved in dry methanol and the solution was acidified with the addition of one drop of HCl 96%. The dimer $[(\eta^6$-p-cymene$)MCl_2]_2$ (1 mol. equiv.) was dissolved in 10 mL of dry dichloromethane and the solution was added to the previous one. The reaction mixture has been maintained under stirring at room temperature under nitrogen for 24 h. (Scheme 2.4). The solution was than reduced to half

the volume by rotary evaporator, and diethyl ether was added until the precipitation of a solid. The product was than filtered and dried under vacuum.

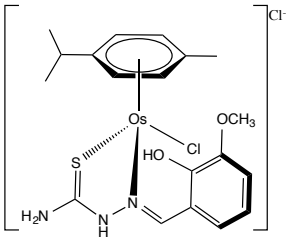

[Os(η^6-p-cymene)Cl(L^1)]Cl ***(1)***. Orange powder. Yield=98%. ^{1}H-NMR (MeOD-d_4, 25°C), δ: 8.76 (s, 1H, CH=N); 7.86 (d, 1H, J=8 Hz, CH_{Ar}); 7.25 (d, 1H, J=8 Hz, CH_{Ar}); 7.01 (t, 1H, J=8 Hz, CH_{Ar}); 5.87 (d, 1H, J=5.5 Hz, $CH_{p\text{-}cym}$); 5.44 (d, 1H, J=5.5 Hz, $CH_{p\text{-}cym}$); 5.31 (d, 1H, J=5.5 Hz, $CH_{p\text{-}cym}$); 4.90 (d, 1H, J=5.5 Hz, $CH_{p\text{-}cym}$); 3.99 (s, 3H, OCH_3); 2.54 (m, 1H, J=7 Hz, $CH_{i\text{-}prop}$); 2.16 (s, 3H, CH_3); 1.20-1.11 (2d, 3H+3H, J=7 Hz, $CH_{3i\text{-}prop}$). ESI-MS ($C_{20}H_{27}ClN_3O_2OsS$, MeOH): m/z= 609 $[M+Na]^+$, 580 $[M\text{-}Cl+CH_3OH]^+$, 572 $[M\text{-}Cl+Na]^+$, 550 $[M\text{-}Cl]^+$.

Crystals suitable for X-Ray analysis were obtained by vapour diffusion of ether in saturated methanol solution of the compound.

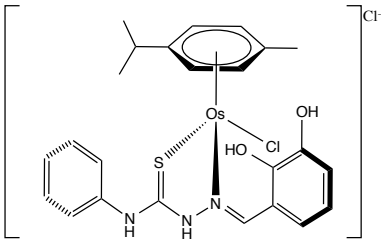

[Os(η^6-p-cymene)Cl(L^2)]Cl ***(2)***. Orange powder. Yield=72%. ^{1}H-NMR (MeOD-d_4, 25°C), δ: 8.87 (s, 1H, CH=N); 7.75 (d, 1H, J=7 Hz, CH_{Ar}); 7.48 (t, 2H, J=7 Hz, CH_{Ar}); 7.43 (d, 2H, J=7 Hz, CH_{Ar}); 7.35 (t, 1H, J=7 Hz, CH_{Ar}); 7.08 (dd, 1H, J=8 Hz, CH_{Ar}); 6.88 (t, 1H, J=8 Hz, CH_{Ar}); 5.86 (d, 1H, J=5.5 Hz, $CH_{p\text{-}cym}$); 5.49 (d, 1H, J=5.5 Hz, $CH_{p\text{-}cym}$); 5.31 (d, 1H, J=5.5 Hz, $CH_{p\text{-}cym}$); 4.93 (d, 1H, J=5.5 Hz, $CH_{p\text{-}cym}$); 2.55 (m, 1H, J=7 Hz, $CH_{i\text{-}prop}$); 1.21-1.13 (2d, 3H+3H, J=7 Hz, $CH_{3i\text{-}prop}$). ESI-MS ($C_{25}H_{29}ClN_3O_2OsS$, CH_3OH): m/z=634 $[M\text{-}Cl+Na]^+$, m/z= 612 $[M\text{-}Cl]^+$.

Crystals suitable for X-Ray analysis were obtained by slow evaporation of a saturated acetone solution of the compound.

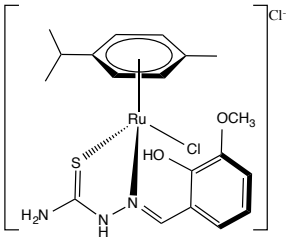

[Ru(η^6-p-cymene)Cl(L^1)]Cl ***(3)***. Red powder. Yield=78%. ^{1}H-NMR (MeOD-d_4, 25°C), δ: 8.79 (s, 1H, CH=N); 8.06 (d, 1H, J=8 Hz, CH_{Ar}); 7.28 (d, 1H, J=8 Hz, CH_{Ar}); 7.07 (t, 1H, J=8 Hz, CH_{Ar}); 5.71 (d, 1H, J=6 Hz, $CH_{p\text{-}cym}$); 5.17 (d, 1H, J=6 Hz, $CH_{p\text{-}cym}$); 5.04 (d, 1H, J=6 Hz, $CH_{p\text{-}cym}$); 4.00 (s, 3H, OCH_3); 2.64 (m, 1H, J=7 Hz, $CH_{i\text{-}prop}$); 2.10 (s, 3H, CH_3), 1.20-1.14 (2d, 3H+3H, J=7 Hz, $CH_{3i\text{-}prop}$). ESI-MS ($C_{20}H_{27}ClN_3O_2RuS$, CH_3OH): m/z= 482 $[M\text{-}Cl+Na]^+$, m/z= 460 $[M\text{-}Cl]^+$.

Crystals suitable for X-Ray analysis were obtained by vapour diffusion of ether in saturated methanol solution of the compound.

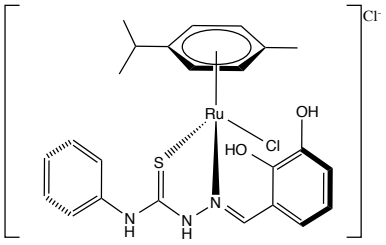

*[Ru(η^6-p-cymene)Cl(L^2)]Cl (**4**).* Red powder. Yield=87%. ^{1}H-NMR (MeOD-d_4, 25°C), δ: 8.90 (s, 1H, CH=N); 7.95 (dd, 1H, J=8 Hz, J'=1 Hz, CH_{Ar}); 7.48 (t, 2H, J=7.5 Hz, CH_{Ar}); 7.41 (d, 2H, J=7.5 Hz, CH_{Ar}); 7.37 (d, 1H, J=7.5 Hz, CH_{Ar}); 7.09 (td, 1H, J=7.5 Hz, J'=1 Hz, CH_{Ar}); 6.94 (t, 1H, J=7.5 Hz, CH_{Ar}); 5.86 (d, 1H, J=5.5 Hz, $CH_{p\text{-}cym}$); 5.49 (d, 1H, J=5.5 Hz, $CH_{p\text{-}cym}$); 5.31 (d, 1H, J=5.5 Hz, $CH_{p\text{-}cym}$); 4.93 (d, 1H, J=5.5 Hz, $CH_{p\text{-}cym}$); 2.55 (m, 1H, J=7 Hz, $CH_{i\text{-}prop}$); 1.21-1.13 (2d, 3H+3H, J=7 Hz, $CH_{3i\text{-}prop}$). ESI-MS ($C_{25}H_{29}ClN_3O_2RuS$, CH_3OH): m/z= 544 $[M\text{-}Cl+Na]^+$, m/z= 522 $[M\text{-}Cl]^+$.

Crystals suitable for X-Ray analysis were obtained by slow evaporation of an unsaturated acetone solution of the compound.

2.5 WORK CONTRIBUTIONS

This work is the result of a collaboration with professor Peter J. Sadler, University of Warwick (Coventry, UK), Department of Chemistry.
Biological analyses were performed by Dr. Isolda Canelon Romero, University of Warwick (Coventry, UK), Department of Chemistry.
XRD analyses and structures resolutions were performed by professor Guy J. Clarkson, University of Warwick (Coventry, UK), Department of Chemistry.

Preliminary biological analyses were performed by the group of Professor Nouri Neamati; University of Michigan (U.S.A.), Department of Pharmacology and Pharmaceutical Science.

2.6 BIBLIOGRAPHY

[1] World Health Organization. *Cancer*; Fact sheet No.297; WHO Press: Geneva, 2013.

[2] T. Tanaka, et al.; *J. Exp. Clin. Med.*; **2013**; 5; 203–209.

[3] D. Zink, A.H. Fischer, J.A. Nickerson; *Nat. Rev. Cancer*; **2004**; 4; 677-687.

[4] J.M. Bishop, R.A. Weinberg; *Molecular Oncology*; **1996**; New York.

[5] M.A. Lemmon, J. Schlssinger; *Cell*; **2010**; 141; 1117-1134.

[6] E. Witsch, M. Sela, Y. Yarden; *Physiology*; **2010**; 25; 85-101.

[7] M. Collado, M. Serrano; *Nat. Rev. Cancer*; **2010**; 10; 51-57.

[8] G.I. Evan, F. D'Adda; *Curr. Opin. Genet. Dev.*; **2009**; 19; 25-31.

[9] M. Curto, et al.; *J. Cell Biol.*; **2007**; 177; 893-903.

[10] T. Okada, M. Lopez-Lago, F.G. Giancotti; *J. Cell Biol.*; **2005**; 171; 361-371.

[11] M.A. Blasco; *Nat. Rev. Genet.*; **2005**; 6; 611-622.

[12] J.W. Shay, W.E. Wright; *Nat. Rev. Mol. Cell Biol.*; **2000**; 1; 72-76.

[13] J.E. Talmadge, I.J. Fidler; *Cancer Res.*; **2010**; 70; 5649-5669.

[14] I.J. Fidler; *Nat. Rev. Cancer*; **2003**; 3; 453-458.

[15] D. Hanan, R.A. Weinberg; *Cell*; **2000**; 100; 57-70.

[16] P.C. Nowell; *Science*; **1976**; 194; 23-28.

[17] G.M. Cooper; *The Cell: A molecular approach.*; 2000; 2nd edition.

[18] T. Tanaka; *Crit. Rev. Oncol. Hematol.*; **1997**; 25; 73-95.

[19] H.C. Pitot, Y.P. Dracan; *FASEB J.*; **1991**; 5; 2280-2286.

[20] J.H. Weisburger; *Mutat. Res.*; **1999**; 437; 105-112.

[21] Z. Herceg, P. Hainaut; *Molecular Oncology*; **2007**; 1; 26-41.

[22] B.E. Bernstein, A. Meissner, E.S. Lander; *Cell*; **2007**; 17; 5-18.

[23] P.A. Jones, S.B. Baylin; *Nat. Rev. Genet.*; **2002**; 3; 415-428.

[24] L.A. Loeb, J.H. Bielas, R.A Beckman; *Cancer Res.*; **2008**; 68; 3551-3557.

[25] P. Hainaut, M. Hollstein; *Adv. Cancer Res.*; **2000**; 77; 81-137.

[26] IARC TP53 Mutation Database, R13; **2008**; available from http://www-p53.iarc.fr.

[27] J.H. Bielas, et al.; *Proc. Natl. Acad. Sci. USA*; **2006**; 103; 18238-18242.

[28] S. Forbes et al.; *British Journal of Cancer*; **2006**; 94; 318-322.

[29] P.A. Futreal, et al.; *Nature Reviews in Cancer*; **2006**; 4; 77-183.

[30] J. Carins; *Nature*; **1975**; 255; 197-200.

[31] A.K. Verma, R.K. Boutwell; *Carcinogenesis*; **1980**; 1; 271-276.

[32] H.C. Pitot, T. Goldsworthy, S. Moran; *J. Supramol. Struct. Cell. Biochem. Suppl.*; **2004**; 17(2); 133-146.

[33] W. Troll, R. Wiesner; *Annu. Rev. Pharmacol. Toxicol.;* **1985**; 25; 509-528.

[34] H.C. Pitot; *Symp. Fund. Cancer Res.*; **1987**; 39; 187-196.

[35] S. Rodenhuis; *Semin. Cancer Biolo.*; **1992**; 3; 241-247.

[36] D.S. Shewach, R.D. Kuchta; *Chem. Rev.*; **2009**; 109; 2859-2861.

[37] D.E. Thurston; *Chemistry and Pharmacology of Anticancer Drugs*; **2007**; 97; 1713.

[38] T. Storr, K.H. Thompson, C. Orgiv; *Chem. Soc. Rev.*; **2006**; 35; 534-544.

[39] Z.J. Guo, P.J. Sadler; *Angew. Chem. Int. Ed.*; **1999**; 38; 1513-1531.

[40] K.H. Thompson, C. Orgiv; *Science*; **2003**; 300; 936-939.

[41] A. Casini; *J. Inorg. Biochem.*; **2012**; 109; 97-106.

[42] G. Ludwig, et al.; *J. Inorg. Biochem.*; **2012**; 113; 77-82.

[43] S.M. Choen; *Curr. Opin. Chem. Biol.*; **2007**; 11; 115-120.

[44] S.P. Fricker; *Dalton Trans.*; **2007**; 4903-4917.

[45] E. Meggers; *Chem. Commun.*; **2009**; 1001-1010.

[46] S.M. Cohen; *Curr. Opin. Chem. Biol.*; **2007**; 11; 115-120.

[47] I. Ott, R. Gust; *Arch. Pharm.*; **2007**; 340; 117-126.

[48] Y.K. Yan, et al.; *Chem. Commun.*; **2005**; 4764-4776.

[49] T.W. Hambley; *Dalton Trans.*; **2007**; 4929-4937.

[50] C. Orgiv, M.J. Abrams; *Chem. Rev.*; **1999**; 99; 2201-2204.

[51] K.H. Thompson, C. Orgiv; *Science*; **2003**; 300; 936-939.

[52] K.L. Haas; *Chem. Rev.*; **2009**; 109; 4921-4960.

[53] E.R. Jamieson, S.J. Lippard; *Chem. Rev.;* **1999**; 99; 2467-2498.

[54] R.B. Weiss, M.C. Christian; *A Review. Drugs.*; **1993**; 46; 360-377.

[55] J.J. Criado, J.L. Manzano, E. Rodriguez-Fernandez; *J. Inorg. Biochem.*; **2003**; 96; 311-320.

[56] K. Aabo, et al.; *Br. J. Cancer*; **1998**; 78; 1479-1487.

[57] E. Wong, C.M. Giandomenico; *Chem. Rev.*; **1999**; 99; 2451-2466.

[58] I. Kostova; *Recent Pat. Anticancer Drug Discov.*; **2006**; 1; 1-22.

[59] M.A. Jakupec, M. Galanski, B.K. Keppler; *Rev. Physiol. Biochem. Pharacol.*; **2003**; 146; 1-54.

[60] F. Levi et al.; *Cancer*; **1992**; 69; 893-900.

[61] L. Pendyala, P.J. Creaven; *Cancer Res.*; **1993**; 53; 5970-5976.

[62] M. Adams, et al.; *Dalt. Trans.*; **2015**; 44; 2456–2468.

[63] S. Dilruba, G.V. Kalayda; *Cancer Chemother. Pharmacol.*; **2016**; doi:10.1007/s00280-016-2976-z.

[64] C.M. Clavel, et al.; *J. Med. Chem.*; **2014**; 57; 3546-3558.

[65] E. Wong, M. Giandomenico; *Chem. Rev.*; **1999**; 99; 2451-2466.

[66] C.G. Hartinger, et al.; *Chemistry and Biodiversity*; **2008**; 5; 2140-2155.

[67] D.S. Perekalin, et al.; *Inorg. Chim. Acta*; **2014**; 409; 390-393.

[68] W.H. Ang, et al.; *Inorg. Chem.*; **2006**; 45; 9006-9013.

[69] M.J. Clarke, F. Zhu, D.R. Frasca; *Chem. Rev.*; **1999**; 99; 2511-2533.

[70] G. Sava, A. Bergamo, P.J. Dyson; *Dalton Trans.*; **2011**; 40; 9069-9075.

[71] W.H. Ang, et al.; *J. Organomet. Chem.*; **2011**; 696; 989-998.

[72] G. Suss-Fink; *Dalton Trans.*; **2010**; 39; 1673-1688.

[73] K.J. Kilping, et al.; *Dalton Trans.*; **2013**; 42; 2008-2014.

[74] F.A. Khan, et al.; *J. Organomet. Chem.*; **2013**; 730; 49-56.

[75] I. Romero-Canelon, L. Salassa, P.J. Sadler; *J. Med. Chem.*; **2013**; 56; 1291-1300.

[76] N.P. Barry, P.J. Sadler; *Chem. Soc. Rev.*; **2012**; 41; 3264-3279.

[77] M. Algesan, et al.; *Dalton Trans.*; **2014**; 43; 15829-15840.

[78] I. Kostova; *Curr. Med. Chem.*; **2006**; 13; 1085-1107.

[79] N.J. Farrer, P.J. Sadler; *Aust. J. Chem.*; **2008**; 61; 669-674.

[80] S. Thota, et al.; *Chinese Chem. Lett.*; **2015**; 26; 721-726.

[81] M.P. Chelopo, et al.; *Eur. J. Med. Chem.*; **2013**; 66; 407-414.

[82] F.A. Beckford, et al.; *Inorg. Chem. Commun.*; **2009**; 12; 1094-1098.

[83] W. Su, et al.; *Appl. Organomet. Chem.*; **2013**; 27; 307-312.

[84] P. Chellan, et al.; *Organometallics*; **2012**; 31; 5791-5799.

[85] A. Mrozek, et al.; *Plos One*; **2014**; 9; 1-15.

[86] A.Y. Lukmantara, et al.; *Bioorg. Met. Chem. Lett.*; **2013**; 23; 967-974.

[87] C. Stefani, et al.; *J. Med. Chem.*; **2013**; 56; 357-370.

[88] K.C. Agrawal, et al.; *J. Med. Chem.*; **1972**; 15; 1154-1158.

[89] J. Shao, et al.; *Mol. Cancer Ther.*; **2006**; 5; 586-593.

[90] L. Zhu, et al.; *Biochemical Pharmacology*; **2009**; 78; 1178-1185.

[91] Z. Kovacevic, et al.; *Mol. Pharmacol.*; **2011**; 80; 598-609.

[92] Z. Kovacevic, et al.; *Carcinogenesis*; **2011**; 32; 732-740.

[93] P.V. Bernhardt, et al.; *J. Med. Chem.*; **2009**; 52; 407-415.

[94] D.R. Richardson, et al.; *J. Med. Chem.*; **2006**; 49; 6510-6521.

[95] D.B. Lovejoy, et al.; *Cancer Res.*; **2011**; 71; 5871-5881.

[96] S. Wei, et al.; *Inorg. Chem.*; **2013**; 52; 12440-12449.

[97] B.M. Zeglis, V.J. Divilov; *J. Med. Chem.*; **2011**; 54; 2391-2398.

[98] H. Zhang, et al.; *J. Biol. Inorg. Chem.*; **2008**; 13; 47-55.

[99] S. Arora, S. Agarwal, S. Singhal; *Int. J. Pharm. Pharm. Sci.;* **2014**; 6; 34-41.

[100] S.H. Van Rijt, P.J. Sadler; *Drug Discovery Today*; **2009**; 14; 1089-1097.

[101] N.P.E. Barry, P.J. Sadler; *ACS Nano*; **2013**; 7; 5654-5659.

[102] H. Beraldo, D. Gambino; *Mini Review in Medicinal Chemistry*; **2004**; 4; 31-39.

[103] S. Dilruba, G.V. Kalayda; *Cancer Chemother. Pharmacol.*; **2016**; 77; 1103-1124.

[104] Y. Fu, et al.; *J. Med. Chem.*; **2010**; 53; 8192-8196.

[105] S.D. Shnyder, et al.; *J. Med. Chem. Commun.*; **2011**; 2; 666-668.

[106] R.H. Fish, G. Jaouen; *Organometallics*; **2003**; 22; 2166-2177.

[107] Y. Hung, W. Kung, H. Taube; *Inorg. Chem.;* **1981**; 20; 457-463.

[108] A.F.A. Peacock, P.J. Sadler; *Chem. Asian J.*; **2008**; 3; 1890-1899.

[109] S.H. van Rijt, P.J. Sadler; *Inorg. Chem.*; **2009**; 48; 1753-1762.

[110] A.F.A. Peacock, et al.; *J. Am. Chem. Soc.*; **2006**; 128; 1739-1748.

[111] A.F.A. Peacock, et al.; *J. Am. Chem. Soc.*; **2007**; 129; 3348-3357.

[112] A.F.A. Peacock, et al.; *J. Am. Chem. Soc.*; **2006**; 1; 79-87.

[113] M. Stebler-Rothlisberger, et al.; *Inorg. Chem.*; **1988**; 27; 1358-1363.

[114] H.D. Mui, et al.; *Organometallics*; **1999**; 18; 3264-3272.

[115] F. Wang, et al.; *J. Chem. Eur. J.*; **2003**; 9; 5810-5820.

[116] H. Chen, et al.; *PNAS*; **2003**; 100; 14623-14628.

[117] M.A. Bennett, et al.; *Inorganic Synthesis.*; **1982**; 21; 74-78.

[118] F. Beckford, et al.; *J. Inorg. Biochem.*; **2011**; 105; 1019-1029.

[119] M.U Raja, E. Sindhuja, R. Ramesh; *Inorg. Chem. Comm.*; **2010**; 13; 1321-324.

[120] T. Stringer, et al.; *Inorg. Chem. Comm.;* **2011**; 14; 956-960.

3 *THIOSEMICARBAZONES COPPER COMPLEXES AS POTENTIAL ANTIFUNGAL AGENTS*

ABBREVIATIONS

4-ABOA 4-acetyl-benzoxazolin-2-one

A. flavus *Aspergillus flavus*

A. parasiticus *Aspergillus parasiticus*

Adha Alcohol Dehydrogenase

AF Aflatoxin

AFBO Aflatoxin B(1)-8,9-epoxide

aldA Aldehyde Dehydrogenase

AsA Aflastatin A

AvnA Monoxygenase

BcA Blasticidin A

CCM Coconut milk-derived medium

CoA Coenzyme A

DEP Direct Exposure Probe

DNA Deoxyribonucleic Acid

Dot A Dioctatin A

EI-MS Electron Ionization mass spectrometry

ESI-MS Electron Spray Ionization Mass Spectrometry

EstA Esterase

facA AcetylCoA Synthetase

FAD Flavin Adenine Dinucleotide

FAO Food and Agricultural Organization

FDA Food and Drug Administration

ICP-AES Inductively Coupled Plasma Atomic Emission Spectroscopy

IR Infrared Spectroscopy

LOX Lipoxigenase

MBOA 6-metoxy- benzoxazolin-2-one

MIC Minimum Inhibitory Concentration

NA Norsolonic Acid

NMR Nuclear Magnetic Resonance

NNA Norsolonic Acid Anthrtone

Nor-1 Oxydoreductase

OD Optical Density

OrdA Cytochrome p450 monoxygenase gene

OTA Ochratoxin A

ROS Reactive Oxygen Species

pksA Polyketide Synthases

ST Sterigmatocystin

TFP Trifluoroperazine

TSC Thiosemicarbazone

VA Vescicolorin A

Vbs Versicolorin B synthase

Ver B Vescicolorin B Desaturase

3.1 INTRODUCTION

3.1.1 General Introduction

Plant diseases are probably the greatest obstacle to the increase of global crop production and also one of the major factors limiting agricultural quality. Crop protection plays a key role in ensuring food security and, in turn, is directly related to food preservation, a key step in increasing both food supply and safety. About 40% of the food produced worldwide is lost or spoiled[1]; this not only reduces its availability, but has also an impact on global climate change by causing excess consumption of fresh water and fossil fuels.

One of the major causes of food spoilage is the presence of microorganisms, in particular fungi. Among known species, many fungi are producers of beneficial metabolites such as antibiotics and other pharmaceuticals[2], but others produce many secondary metabolites[3, 4] that are not always beneficial, and some of them are even toxic and carcinogenic. It is believed that fungi evolve these metabolites as means of protecting their food supply by preventing other organisms from eating it[5, 6]. These harmful metabolites are referred to as mycotoxins and are associated with various crop diseases that can lead not only to significant production losses, but can also be hazardous for human and animal health[7]. Mycotoxins are structurally very diverse chemical compounds with different toxic effects and a variety of biological activities[8]: they include nitrogen-free (such as terpens, polyketides, saponins and polyacetylenes) and nitrogen containing compounds (such as alkaloids, amines, cyanogenic glycoside, non-protein amino acids and glucosinolates)[9].

Aspergillus, Penicillium, Fusarium and *Alternaria* genera of fungi are the main producers of mycotoxins[10, 11, 12, 13]. While *Aspergillus* and *Pennicilium* species are generally found as contaminants in food during drying and storage,

Fusarium and *Alternaria* can produce mycotoxins before or immediately after harvesting[14]. The effects of poisoning by mycotoxins are referred to as mycotoxicoses: the knowledge that mycotoxicoses is the result of fungal action was a relatively recent discovery[15]. Until now, approximately 400 secondary metabolites have been reported by the Food and Agricultural Organisation (FAO), estimating that as much as 25% of the world's agricultural commodities are contaminated with mycotoxines[16, 17, 18, 19, 20], leading to significant economic losses[21, 20, 22]. Consumption of mycotoxin-contaminated food or feed leads to the induction of teratogenic, cancerogenic, neurotoxic and immunosuppressive effects in human and/or animals[22, 23].

In Fig. 3.1 are shown the chemical structures of the mycotoxins that are considered of worldwide importance[20, 22, 23, 24].

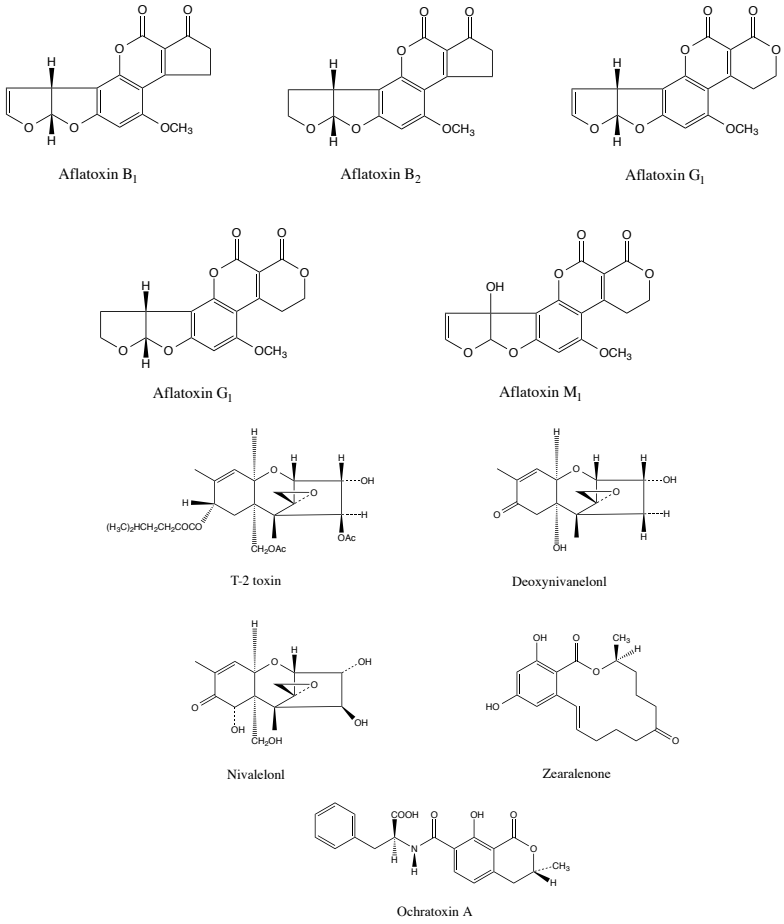

Fig. 3.1 Chemical structures of the most important mycotoxins.

3.1.2 *Aspergillus flavus* and aflatoxins

Aspergilli belong to the class of filamentous fungi. Among this category the genus *Aspergillus Flavus* is the most important, from an economic point of view, and the most notorious because it produces aflatoxins. *A. Flavus* is not a single specie, but a "species complex", made up of eleven species that are known to occur in many kinds of plant material, including store grains[25, 26]: it is a saprobe capable of surviving on many organic nutrients sources and with the ability to survive at temperatures ranging from 12 to 48°C, even if the optimal growth temperature ranges is between 28 and 37°C. Its ability to grow at relatively high temperatures contributes to its pathogenicity. For most of its lifecycle the fungus exists in the form of mycelium or asexual spores known as *conidia*; under adverse conditions, such as lack of adequate nutrients or water, the fungal mycelium will transform to resistant structures called *sclerotia*, which can survive in extremely harsh environmental conditions. When conditions become favourable, *sclerotia* germinates directly to produce new colonies of fungi[27, 28, 29].

Aflatoxins, the toxic and highly carcinogenic secondary metabolites of *Aspergillus flavus*, are the most widely investigated of all mycotoxins: they have had a central role in establishing the significance of mycotoxins in animal diseases and in the regulation of their presence in food[30, 31]. Most *A. flavus* produces afltatoxins B_1 and B_2 whereas *Aspergillus parasiticus* produces aflatoxins B_1, B_2, G_1 and G_2. These four major aflatoxins are named based on their blue (B) or green (G) fluorescence under ultraviolet light and their relative mobility by thin-layer cromatography on silica gel. Aflatoxin M_1 (Fig. 3.1) is a hydroxylated derivative that is metabolized from aflatoxin B_1 by cows and secreted in milk[32]. Aflatoxin B_1 (Fig. 3.1), among the four major types, is the most toxic and the most carcinogenic in both humans and animals. Early

research on aflatoxins determined that the conditions[33] favourable for the growth of the *A. flavus* and production of aflatoxin are narrow: in particular, *A. flavus* must grow alone and the grain cannot be, previously or simultaneously, invaded by other fungi[34, 35, 36].

Chronic exposure to aflatoxins can result in suppressed immune response, malnutrition, proliferation of the bile duct, cetrilobular necrosis and fatty infiltration of the liver, hepatic lesions and even hepatomas[37, 38, 39, 40].

Food and feed contamination by aflatoxins is a significant food safety issue in the developing countries because of lack of detection, monitoring and regulating measures to safe guard the food supply. It is estimated that approximately 4.5 billion people who lives in that countries have been chronically exposed to largely uncontrolled amounts of aflatoxins[41].

To minimise potential exposure, in many commodities maximum levels of aflatoxins have been set at levels below 20 ppb by most countries[32, 42, 43]. Regulatory guidelines of the U.S. Food and Drug Administration (FDA) specifically prevent the sale of commodities if contamination exceeds 20 ppb total for interstate commerce of food and feedstuff and 0.5 ppb aflatoxin M1 in milk.

Due to restrictions limiting the trade of contaminated crops, aflatoxin contamination of agricultural commodities is not only a serious food safety concern[44, 45, 46], but it has significant economic implications for the agricultural industry worldwide.

3.1.3 Aflatoxin biosynthesis

Aflatoxins are polyketide-derived difuranocumarins. The biosynthetic synthesis of these mycotoxins includes gene clusters, controlled by a complex regulatory network (Fig. 3.2), that involve multiple proteins and complexes that respond to various environmental stimuli. These stimuli include sources of carbon and nitrogen, temperature, light, pH, amino acids in the environment, reactive oxygen species, hypoxic conditions, biofilm formation, iron availability and stimuli derived from other organisms[47, 48, 49, 50].

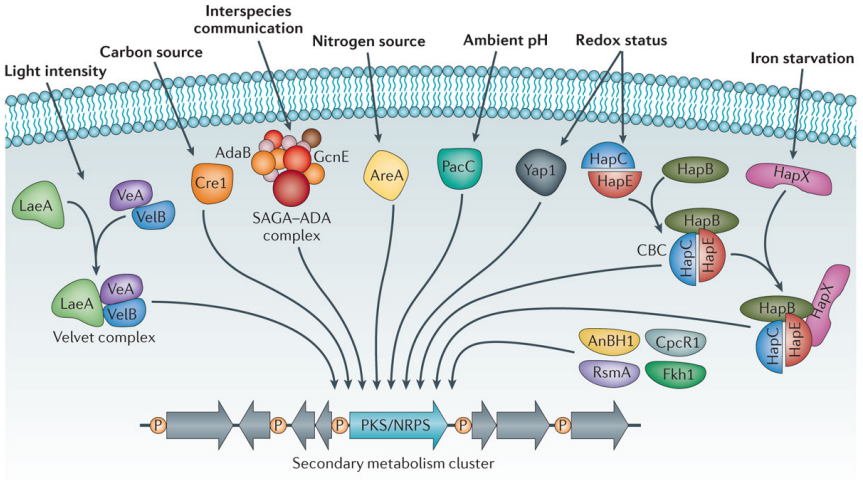

Fig. 3.2 Global regulatory proteins involved in the regulation of secondary metabolism gene clusters in various fungi. [Taken from A.A. Brachage[51]]

To understand better the biosynthetic pathway of aflatoxin, many genes encoding the enzymes and the transcription factors have been cloned and characterized: they are located within a huge gene cluster of about 70 kb in the genome of *A. parasiticus* and *A. flavus.*

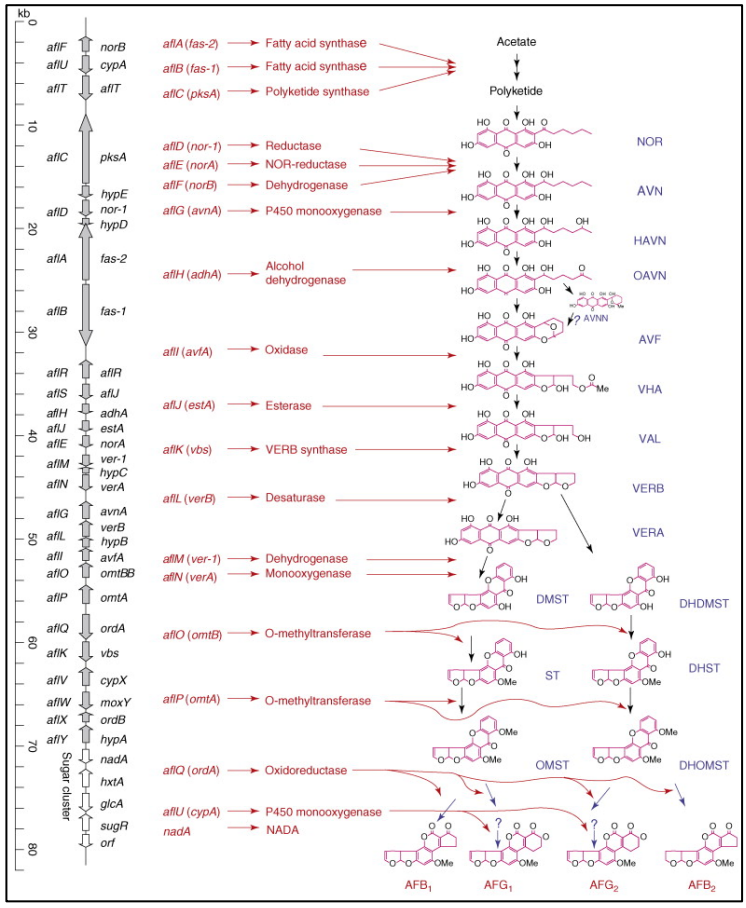

Fig. 3.3 Clustered genes and the aflatoxin biosynthetic pathway. The corresponding genes and their enzymes, involved in each bioconversion step, are shown on the left side. The vertical line represents the 82-kb aflatoxin biosynthetic pathway gene cluster and sugar utilisation gene cluster in *A. parasiticus* and *A. flavus*. The new gene names are given on the left of the vertical line and the old gene names are given on the right. Arrows along the vertical line indicate the direction of gene transcription. The ruler at far left indicates the relative sizes of these genes in kilobases. Red arrows indicate the connections from the genes to the enzymes they encode, from the enzymes to the bioconversion steps they are involved in, and from the intermediates to the products in the aflatoxin bioconversion steps. [Taken from T.E. Cleaveland et al.[52]]

18 enzyme steps are required for conversion of Acetil CoA into its final products AFB_1, AFB_2, AFG_1, AFG_2, as illustrated in Fig. 3.3. Aflatoxins are produced from acetate and malonyl precursors thanks to two fatty acid synthase genes (fas-1 and fas-2) and a polyketide synthase gene (pksA) that are involved in the synthesis of the decaketide, the starting material for the aflatoxin synthesis from malonyl CoA. Once formed, the decaketide is, then, used by the iterative type I polyketide synthase pksA, in extension and condensation reaction, to produce norsolonic acid anthrtone (NAA). This intermediate is oxidised by the enzymatic HypC to form the anthraquinone norsolonic acid (NA), the first stable intermediate in the aflatoxin biosynthesis[53]. The enzyme Nor-1 (oxidoreductase), AvnA (monoxygenase), Adha (dehydrogenase), FAD (flavin adenine dinucleotide)-containing monooxygenase, EstA (esterase) and Vbs (versicolorin B synthase) act in sequence to produce versicolorin B. This intermediate is a common precursor for divergent biosynthetic branches yielding aflatoxin[54]. Following the aflatoxin B_1 branch, VerB (vescicolorin B desaturase) produces vescicolorin A (VA), which contains the 2,3 double bond in the dihydrobisfuran ring. This double bond can be oxidized in the host organism and form highly reactive epoxide that mediates the mutagenicity, carcinogenicity and cytotoxicity of aflatoxin B_1. Several enzymatic reactions are involved in the conversion of VA to demethylsterigmatocystin and then to ST and O-methylsterigmatocystin; the cytochrome P450 monoxygenase OrdA catalyses the final reaction to generate aflatoxin B_1 from O-methylstergnatocystin.

3.1.4 Aflatoxin Inhibitors

For human and animal health biological effects of aflatoxins may be carcinogenic, mutagenic, teratogenic, hepatotoxic, and immunosuppressive, as already described previously in this chapter[55]. The International Agency for Research on Cancer classified B_1 and M_1 as group 1 human carcinogens, even though M_1 is about 10 times less carcinogenic then B_1. In particular, B_1 is metabolised in the liver by the cytochrome P450 system, generating its most carcinogenic metabolite AFB_1-8,9-epoxide (AFBO) or the less mutagenic forms such as M_1, Q_1 or P_1. AFBO can follow several pathways after it is metabolised, with one of them leading to cancer, another to toxicity and another one to excretion. AFBO exo-form easily binds to cell macromolecules, including genetic material such as DNA proteins, producing adducts. Formation of these DNA adducts leads to genetic mutations and cancer, and their excretion in the urine of infected people is not only a proof that in humans the biochemical pathways leads to carcinogenesis, but also offers a reliable biomarker for AFB exposure[56].

The use of pesticides is still the most efficient way to prevent food and feed contamination, but the use of potent fungicides can lead, in the medium and long terms, to the evolution of resistant pathogens. This is why it represents a serious concern for the environment[57, 58]. Moreover, new fungicides could have contradictory and unwanted effects on mycotoxin biosynthesis[59]. Concerns on food safety and environmental health, combined with the global issue of emerging resistant pest strains, make urgent to develop novel crop-protective agents.

Most inhibitors of AF biosynthesis act at one of these three levels: altering the physiological environment or other signal inputs perceived by the fungus, interfering with signal transduction and gene expression regulatory networks

upstream of AF biosynthesis, or blocking enzymatic activity of a biosynthetic enzyme (Fig. 3.4). In particular, many inhibitors possess antioxidant activity; in contrast, strong inducers of AF biosynthesis are oxidants[60]. What remains uncertain is the cause-effect relationship between AF biosynthesis, oxidative stress and the signaling pathways whereby these processes interact: the stimulation and suppression of AF biosynthesis, by oxidants and antioxidants respectively, indicate just that perturbations in the oxidative state of the fungal cell influence AF biosynthesis but there is no information regards the mechanism[61, 62, 63].

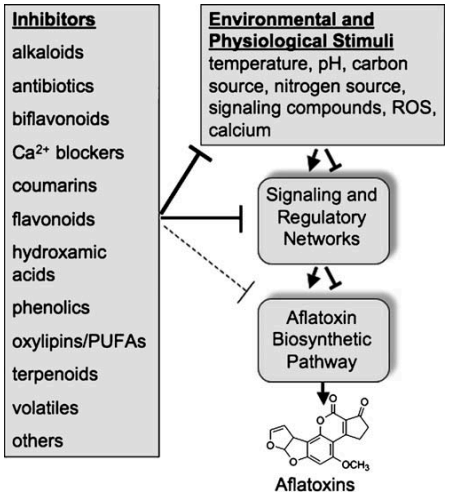

Fig. 3.4 Schematic representation of regulation and biosynthesis of AF with potential mode of action of major groups of inhibitors. Inhibitors of AF biosynthesis may act at three levels: (1) modulate environmental and physiological factors that affect aflatoxin biosynthesis, (2) inhibit signaling circuits upstream of the biosynthetic pathway, or (3) directly inhibit gene expression or enzyme activity in the pathway. [Taken from R.A. Holmes et al.[64]]

Here we present a brief overview of the most important classes of known AF inhibitors.

Phenylpropanoids

Previous studies have demonstrated that, in *Aspergillus,* oxidative stress and aflatoxin production are closely linked. Antioxidants can directly inhibit aflatoxin biosynthesis, as mentioned before[65]. Phenylpropanoids encompass a diverse assemblage of compounds, many with demonstrated antioxidant activity. This category includes simple phenolics and flavonoids such as flavones, coumarins, chromones and biflavonoids (Fig. 3.5).

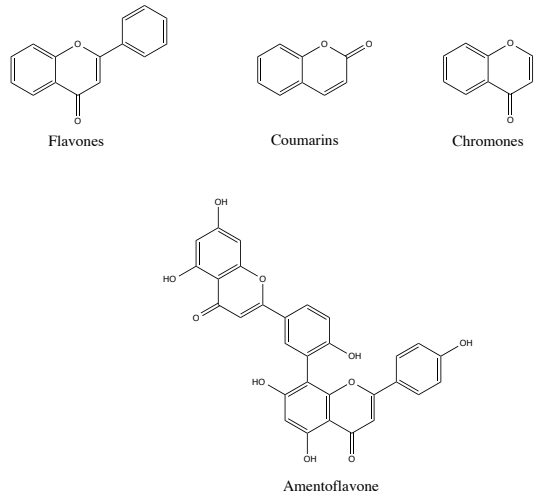

Fig. 3.5 Chemical structure of phenylpropanoids with antimycotic activity.

Most of these compounds have marked antioxidant activity but the strength of the oxygen quenching activity is not positively correlated with the inhibition of AF biosynthesis. Consequently, while antioxidant activity may be important for the mode of action of this group of compounds, it seems that additional factors may be required for inhibition. These may include bioavailability and uptake, intracellular mobility and interaction with specific enzymes, metabolite pools or signaling pathways.

Terepenoids

Terpenoids are a major class of natural products, synthesised in plants through the mevalonic acid pathway. With the exception of limonene, all the tested terpenoids were potent inhibitors of AF biosynthesis, with IC_{50} values less than 0.5 mM. Data indicates that inhibition may occur at the level of whole pathway intermediates. Among the terpenoids, lutein (Fig. 3.6) was the most potent inhibitor with an IC_{50} value of 1.1 μM[66].

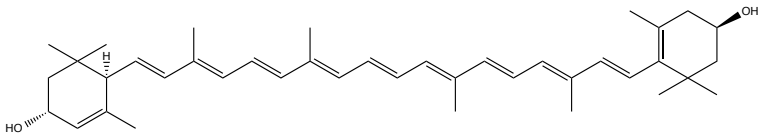

Fig. 3.6 Chemical structure of lutein.

Alkaloids

Caffeine (Fig. 3.7) is a well-studied inhibitor of AF production. The proposed mechanism of action is related to the interference with glucose uptake. As caffeine, pepper species have been shown to inhibit AF production even if the mechanism of action of these compounds, against AF production, is not known[67].

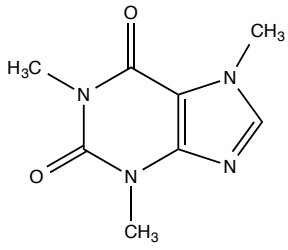

Fig. 3.7 Chemical structure of caffeine.

Plant signaling molecules

Lipoxygenase-generated signals. Plant lipoxygenases (LOX) have been hypothesised to play a regulatory role in response to many plant pathogens[68, 69] and in plant microbe interactions[69, 70, 71]. Increase in LOX activity has been observed in plant tissue and cells in response to bacterial, fungal and viral infections[72]. LOX metabolites must be acting directly on the pathogen, leading to development of resistance[73]. The function of LOX, in the defence against pests, seems to be related to the synthesis of a number of different compounds with signaling functions[74, 75, 76]: it provides building units of physical barriers against pathogens invasion, it regulates plant cell death and has a major role in the formation of phytohormones in senescence and inhibition of aflatoxin production[77] or development of the hypersensitive response[78].

Ethylene. The volatile compound ethylene is an important plant signaling hormone. Many fungi can produce or encounter ethylene in their environment[79]. A potential relationship between ethylene and AF production was noted after the observation that non-toxicogenic *A. flavus* and *A. oryzae* strains produce less ethylene than toxigenic *A. flavus* and *A. parasiticus* strains. More recently, Roze et al.[80] provided direct evidence that ethylene inhibits AF production in *A. parasiticus*, even if the mechanism of how ethylene inhibits AF production is still unclear.

Other plant-derived compounds

Phytic acid. Phytic acid (inositol hexakisphosphate) (Fig. 3.8) is an abundant component of seeds and a potent chelator of divalent cations, particularly zinc and iron.

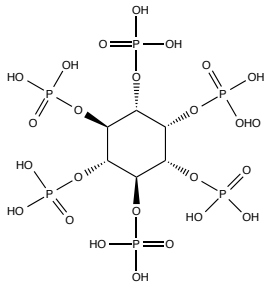

Fig. 3.8 Chemical structure of phytic acid.

Because of the antinutritive effects of phytic acid on humans and animals, cultivars with reduced phytic acid are highly desirable. The regulation of AF production by phytic acid is not only attributed to chelation of zinc and other polyvalent cations, but other properties can contribute to this activity. In particular, phytic acid is a natural antioxidant that can inhibit iron-catalysed free radical production and lipid peroxidation[81], and this antioxidant activity may contribute to its anti-toxigenic properties.

Hydroxamic acid. Two hydroxamic acids (Fig. 3.9), 4-acetyl-benzoxazolin-2-one (4-ABOA) and 6-metoxy-benzoxazolin-2-one (MBOA), are strong inhibitors of AF biosynthesis. MBOA is inhibitory toward growth at higher concentration, whereas 4-ABOA does not significantly reduce growth until concentration reached 50 mM. How hydroxamic acids inhibit AF biosynthesis is unclear, but perturbation of sugar utilization could conceivably interfere with aflatoxin production[82].

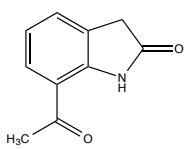

4-ABOA

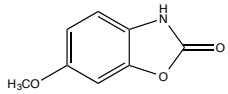

MBOA

Fig. 3.9 Chemical structure of 4-ABOA and MBOA.

Metabolites altering calcium signaling

There are multiple lines of evidence that support a role of calcium-dependent signaling in regulation of AF biosynthesis. Trifluoroperazine (TFP) (Fig. 3.10) is able to interact with Ca^{2+} ions blocking the activity of the protein calmodulin (protein involved in the life cycle of all eukaryotic cells)[83].

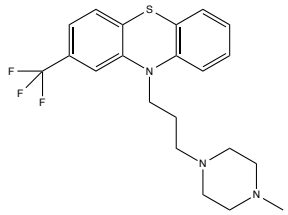

TFP

Fig. 3.10 Chemical structure of trifluoroperazine.

However, whether these proteins are specifically associated with regulation of AF biosynthesis or are a response to TFP-mediated growth inhibition remains an open question. Also, TFP can antagonize other Ca^{2+} binding proteins besides calmodulin, so it is also unclear if calmodulin is the TFP target associated with AF biosynthesis[84]. Another potential mode of action for TFP may be interference with acetyl-CoA carboxylase activity, one possible route for the production of malonyl-CoA precursors for AF biosynthesis[85]. Altered transport of calcium ions may also negatively affect AF production. Treatment of *A. parasiticus* with the calcium channel blockers verapamil and diltiazem strongly inhibited AF accumulation with only a negligible decrease in fungus growth[86].

Antibiotics and cyclic dipeptides

Bacteria are rich sources of fungistatic and anti-aflatoxigenic compounds, as evidenced by co-culturing experiments. Efforts in this area have yielded several

highly active inhibitors of AF production[87]. The bacterium *Achromobacter xylosoxidans* was found to inhibit accumulation of AF precursor (NOR and hydroxyversicolorone); the cyclic dipeptide Cyclo(l-leucyl-L-prolyl) was shown to be responsible for the observed inhibition. Aflastatin A (AsA) mode of action is not known but it enhances glucose utilization and accumulation of ethanol. Also transcriptase for aldehyde dehydrogenase (aldA) and acetyl CoA synthetase (facA), involved in ethanol utilization, were suppressed by AsA[88]. These observations suggest that inhibition is probably a result of perturbations in primary metabolism[89]. An elegant approach, allowing dissection of anti-toxigenic and antimicrobial activities, was used to investigate blasticidin A (BcA) (Fig. 3.11), an antibiotic that is structurally related to AsA. Like AsA, BcA suppresses AF biosynthetic pathway genes[90]. More recently, dioctatin A (DotA) (Fig. 3.11), an inhibitor of human dipeptidyl aminopeptidase II was shown to inhibit AF production: the treatment with DotA reduced expression of AflR and three AF biosynthetic genes[89, 91].

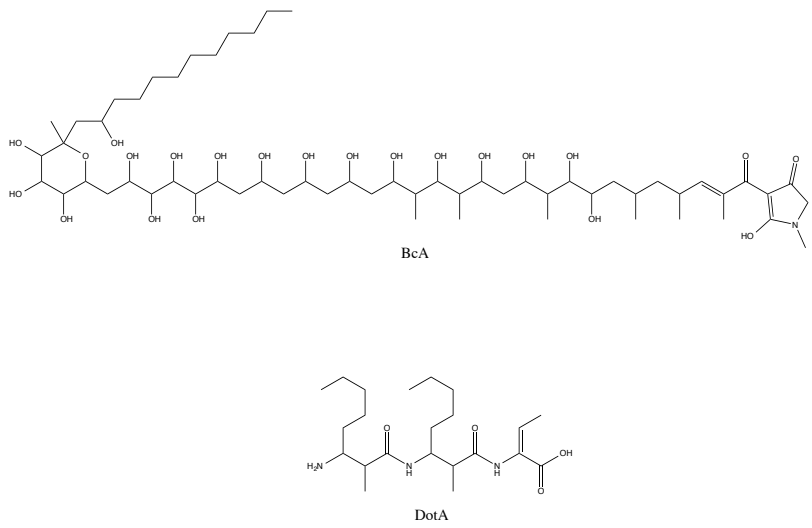

Fig. 3.11 Chemical structures of BcA and DotA antibiotics.

3.1.5 Thiosemicarbazones as aflatoxin inhibitors

Already in 1980s, when the correlation between oxidative stress and AF production was first demonstrated[92], the hypothesis was advanced that the role of toxins production could be to detoxify the cell from excessive accumulation of ROS (Reactive Oxygen Species): this is confirmed by the fact that at least six steps of AF biosynthesis involve oxidative processes[93]. This hypothesis has recently been strengthened by physiological and molecular studies. In a study regarding oxidant formation, development and AF biosynthesis during the fungal life cycle of *A. parasiticus,* Reverberi et al.[94] demonstrated a close relationship between endogenous oxidative state and AF biosynthesis. Besides the antioxidant cell response, they found that excess of unscavenged ROS also triggers the biosynthesis of the toxins. Jayashree and Subramanyam [95] demonstrated that oxidative stress is a "prerequisite" for AF production by studying the redox balance in toxigenic and non-toxigenic strains during the different growth phases. The biosynthesis of mycotoxins helps the cell to maintain the oxidative status at levels that are less harmful for the fungus, besides providing other ecological advantages. If control over mycotoxin has to be achieved, is essential to clarify how fungal strains manage to survive, grow and reproduce without mycotoxin synthesis, and why their metabolism produces lower oxidative burst without compromising their growth.

From this point of view, thiosemicarbazones have received great attention because of their chemical and biological activities on plant pathogens[96]. The mechanism of action of this class of compounds has to be elucidated: what is known is that thiosemicarbazones are an important class of sulphur-donor Schiff base ligands that are particularly useful for their interaction with transition metal ions. The chelation mechanism has been supported by the fact that semicarbazones are less active than the thiosemicarbazones counterpart:

this difference is attributed to the formation of metal complexes, which would occur readily with thiosemicarbazones. This interaction with metal ions could lead to the activation of the ligands as antioxidant, depending on the nature of the metal centre; moreover it could lead to the inactivation of metallo-enzymes, whose activity depends on the metal and that are involved in ROS production[97]. In particular, iron plays an essential role in many biological processes[98]: thiosemicarbazones inactivate the non-heme iron subunit of several iron-dependent enzymes, such as the ribonucleotide reductase, a key enzyme for fungal survival[99]. There is considerable experimental evidences to support the view that the formation of a toxic metal-organic complex is the possible mechanism of their fungicidal action.

Recently, data on the effects of some thiosemicrabazones and the related metal complexes on a subset of plant pathogens has been published; however the studies were mainly aimed at characterizing the coordination compounds and to investigate the influence of the metal on the features of the compound that a very limited part of the work was dedicated to mycological studies[100]. Some copper complexes of thiosemicarbazones are of great interest because they show higher biological activity than their corresponding free thiosemicarbazones[101]. The higher antimicrobial activity of the metal complexes is attributed to the increased lipophilicity in comparison with that of the free ligand[102].

In view of the above description it is highly desirable to further investigate thiosemicarbazones and related metal complexes as potential antimycotic. The structure of the thiosemicarbazone moiety confers to the molecule a good chelating ability, while substituents can be varied in order to modulate lipophilicity.

3.1.6 Aim of the work

The aim of this project is to develop new typologies of inhibitors of *Aspergillus* proliferation and, in particular, of aflatoxins production, harmless to the environmental and to human health. The research was focused on the synthesis of a panel of thiosemicarbazones ligands with different physico-chemical features to be screened for their antifungal and anti-aflatoxin activity. Starting from molecules of natural origin, with documented antimycotic activity, the organic scaffold was modified in the perspective to obtain more potent compounds. Metal complexes (in particular copper coordination compounds) were also synthesised with the aim to synergistically improve the capability of the free ligands to inhibit toxin production. Derivatives of some natural aldehydes with known antimycotic activity were taken into account, in particular vanillin and cinnamaldehyde (Fig 3.12).

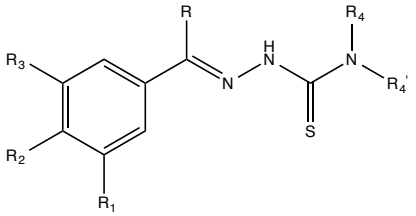

L_1 R=H, R_1=H, R_2=OH, R_3=OH, R_4=R_4'= H
L_2 R=H, R_1=OCH_3, R_2=OH, R_3=OCH_3, R_4=R_4'=H
L_3 R=H, R_1=OCH_3, R_2=OCH_3, R_3=H, R_4=R_4'=H
L_4 R=CH_3, R_1=H, R_2=OH, R_3=OCH_3, R_4=R_4'=H
L_5 R=CH_3, R_1=OCH_3, R_2=OH, R_3=OCH_3, R_4=R_4'=H
L_6 R=H, R_1=H, R_2=H, R_3=H, R_4=R_4'=CH_3
L_7 R=H, R_1=OCH_3, R_2=OCH_3, R_3=H, R_4=R_4'=CH_3

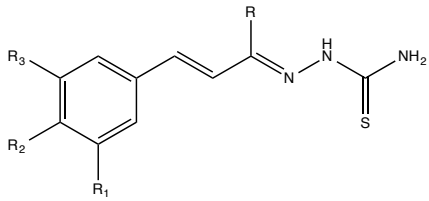

L_8 R=H, R_1=OCH_3, R_2=OH, R_3=H
L_9 R=H, R_1=OCH_3, R_2=OH, R_3=OCH_3
L_{10} R=H, R_1=H, R_2=$N(CH_3)_2$, R_3=H
L_{11} R=H, R_1=H, R_2=OH, R_3=OCH_3
L_{12} R=CH_3, R_1=OCH_3, R_2=OH, R_3=H

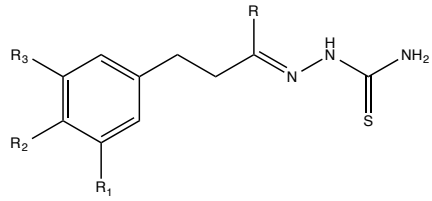

L_{13} R=H, R_1=H, R_2=H, R_3=H
L_{14} R=CH_3, R_1=OCH_3, R_2=OH, R_3=H

Fig. 3.12 Chemical structures of the thiosemicarbazone derivatives of the natural compounds vanillin (L_1-L_7) and cinnamaldehyde (L_8-L_{14}).

The effects of the synthesised molecules toward fungal growth and aflatoxin biosynthesis inhibition were determined. Moreover, cytotoxic tests were also performed in order to assess epi-genotoxic effects toward healthy human cells. Best hits were evaluated for their toxicological and genotoxicological assessment on bacteria and plants.

3.2 RESULTS AND DISCUSSION

Antifungal activity associated with thiosemicarbazones has already been described in literature[103]. However, in all previous reports, only minimum inhibitory concentration (MIC) value, against few fungal genera, was determined and no data was shown on the effects on mycotoxin production.

In this work, a panel of thiosemicarbazone ligands were synthesised and tested for their antifungal and antimycotoxigenic activities: in particular, the attention was focused on derivatives of the two natural aldehydes vanillin and cinnamaldehyde. The research was, then, extended to the evaluation of the antimicrobial activity of the related copper complexes: several studies have been reported that demonstrate the coordination compounds be more toxic than the organic counterparts. These observations suggested that complexation can be used as an interesting strategy of dose reduction.

3.2.1 Vanillin derivatives

3.2.1.1 Vanillin type thiosemicarbazone ligands

Seven TSC ligands were synthesised: substituents on the aromatic ring were varied in order to modulate the physical-chemical features of the ligand but not its chelating properties. No hydroxyl as well as methoxy groups were add in position 2 in order to avoid a possible tridentate O, N, S chelation.

Five different compounds (Fig. 3.13, $\mathbf{L_1}$-$\mathbf{L_5}$) were obtained by a condensation reaction between the proper aldehyde and thiosemicarbazide. To modulate the lipophilicity and hydrogen-bonding capabilities, 4,4-dimethyl-N-thiosemicarbazide was also used and ligands $\mathbf{L_6}$ and $\mathbf{L_7}$ were obtained (Fig. 3.13).

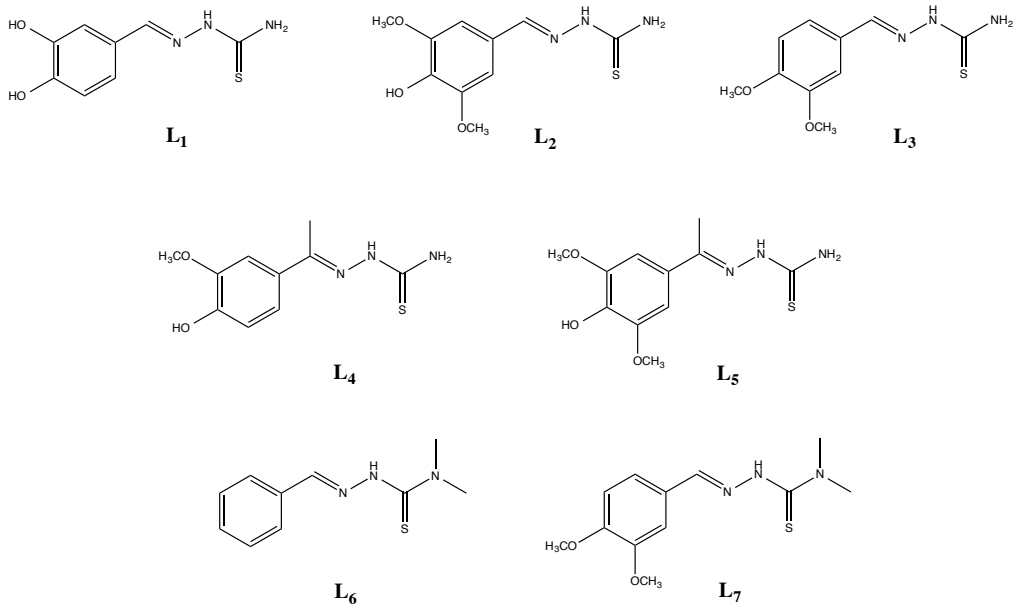

Fig. 3.13 Chemical structure of the thiosemicarbazone ligands (L_1-L_7).

The compounds were fully characterised by mean of the common spectroscopic and spectrometric analyses such as IR, ^{1}H-NMR, EI-MS and elemental analysis. The IR spectra of the ligands show two medium bands around 3100-3300 cm^{-1} attributable to NH and OH vibrational stretching. Strong bands are displayed in the range 820-831 cm^{-1} and 1540-1527 cm^{-1} assigned to C=S and C=N stretching vibrations, respectively. No band was observed near 2575 cm^{-1} suggesting that, at the solid state, the ligand is in its thione form[104].

In the ^{1}H-NMR spectra (for a representative spectrum, see Fig. 3.14) the resonance of the iminic proton, characteristic of the final product, can be observed in the expected spectral range, around 8 ppm; all the other signals are in agreement with the expected chemical shifts.

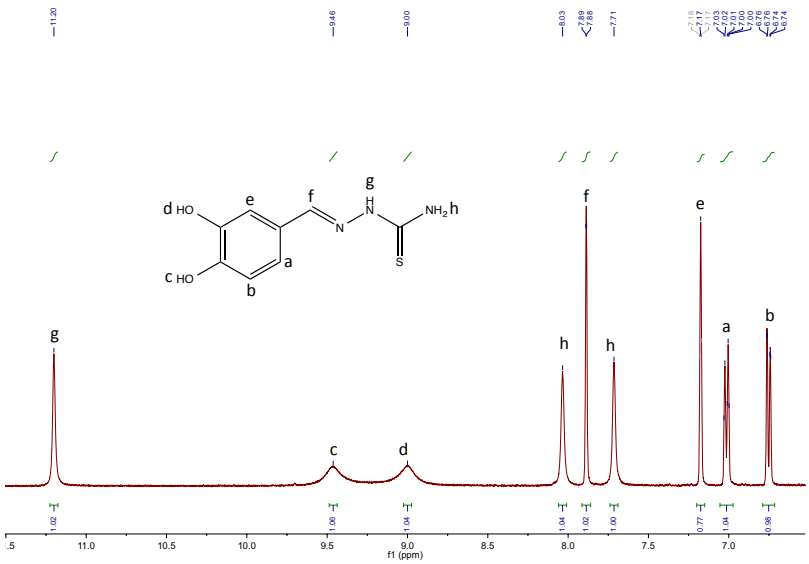

Fig. 3.14 ^{1}H-NMR of L_1 recorded in DMSO-d_6.

These type of ligand are characterized by the possibility of E/Z isomerisation around the C=N double bond. The ^{1}H-NMR spectra, of all the synthesised ligands, showed just one set of signals related to the E isomer. The predominance of this isomer is influenced by steric effects: in the Z conformation the position of the phenyl group (R_1), on the same side of the acidic NH proton, is disfavoured compared to the E conformation where two hydrogens are on the same side (Fig. 3.15).

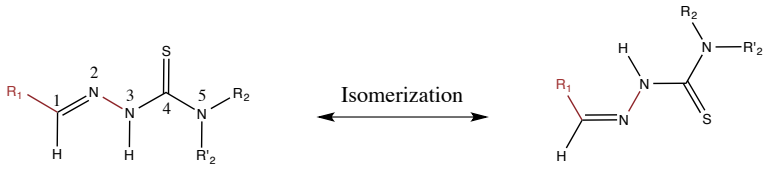

E form Z form

Fig. 3.15 E/Z isomers of N-acylhydrazones.

3.2.1.2 Vanillin type thiosemicarbazone copper complexes

3.2.1.2.1 Thiosemicarbazones containing NH_2 as terminal moiety

Copper is a bio-essential metal with two oxidation states, +1 and +2, both accessible in living organisms. Copper salts have been long used for their ability to inhibit the development of moulds and bacteria: the mechanism of action is usually explained in terms of interference with the respiration processes of the cells and growth of the microorganisms. The lipid membrane, that surrounds the cell, constitutes a barrier for metal ions diffusion but small hydrophobic molecules can easily diffuse through this barrier: from this point of view, lipophilicity is an important factor that should be considered for the synthesis of antimycotic compounds. Metal chelation could improve lipophilicity and facilitate the penetration of the complexes into lipid membranes, thus arrest the microorganisms proliferation.

Thiosemicarbazones are known to act as versatile metal chelators and, in many cases, their activity has been associated to their ability to sequester metal ions essential to life. Therefore, we used compounds **L_1-L_7** as chelating ligands towards copper(II) with the aim to improve the bioavailability and efficacy of these potential inhibitors.

The reaction of one equivalent of $CuCl_2$ with two equivalents of the thiosemicarbazone ligands **L_1-L_5** led to the isolation of the copper(I) complexes **1-5**, as inferred by experimental data (^{1}H-NMR, ESI-MS, elemental analysis, ICP). All the isolated copper compounds are stable at room temperature, non-hygroscopic and insoluble in water, as well as in the common organic solvents, but readily soluble in DMF and DMSO.

The formation of copper(I) complexes is not completely surprising since the versatility of thiosemicarbazone is very well-known, not only as far as from the coordinative point of view, but also because they can undergo intramolecular

oxidative cyclisation in presence of bases, oxidants or redox-active metals like Fe^{3+} or Cu^{2+}. In literature[105] there are examples of copper(I) complexes obtained by the reaction of a copper(II) salt with a thiosemicarbazone ligand; these reactions can also be accompanied by oxidation/cyclisation of the ligand. In our case, data put in evidence that copper reduction is a consequence of a mechanism in which the cyclisation of the thiosemicarbazone ligands is also involved. It is well known that semi- and thiosemicarbazones can be cyclised under the action of bases[106], acids[107], oxidants[108] or other cyclisation reagents[109], and they are useful and versatile precursors for the preparation of five- or six-membered heterocyclic compounds. The ring-closure process may be induced by metal ions such as Fe^{3+} or Cu^{2+}. The exact mechanism is still not well understood but it has been suggested that the influence of the metal ions is probably due to both inductive and stereochemical effects[110]. Cyclisation can yield to 1,2,4-triazole (A) or 1,3,4-thiadiazole (B) rings (Scheme 3.1), depending on the mechanism.

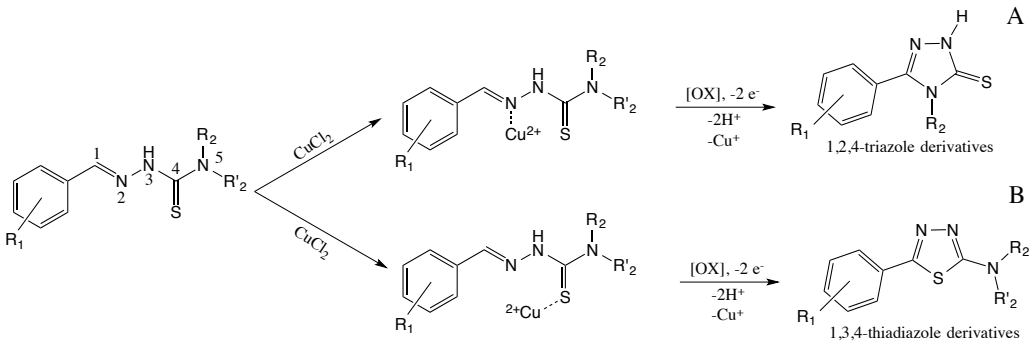

Scheme 3.1 Cyclisation mechanism for thiosemicarbazones.

Because thiosemicarbazones usually possess two nucleophilic centres (N(2) and S) and a C=N double bond, two mechanisms are possible that lead to different products: 1,2,4-triazolidine-3-thione, formed by intramolecular addition of N(5)

to C=N (Scheme 3.1, A) , and 1,3,4-thiadiazoline-2-amine, obtained by the addition of the sulphur atom to the iminic moiety (Scheme 3.1, B). Other oxidative cyclisation mechanisms are also possible: they lead to different heterocycles with or without the presence of the sulphur atom, as desulfurization processes can also occurr[111].

The ^{1}H-NMR spectra of the complexes **1-5**, recorded in DMSO-d_6, confirmed the copper(I) oxidation state: the metal has a d_{10} electronic configuration and its diamagnetic nature leads to sharp signals in the ^{1}H-NMR spectra. In the spectrum of **1** (as example, Figure 3.16) the NH proton is shifted to lower fields, compared to the free ligand, due to the coordination to the metal; the same trend is observed for the chemical shifts of the NH_2 and of the iminic protons. The presence of the hydrazonic NH proton, in all the recorded spectra, confirmed that the ligand interacts with the metal in its neutral form.

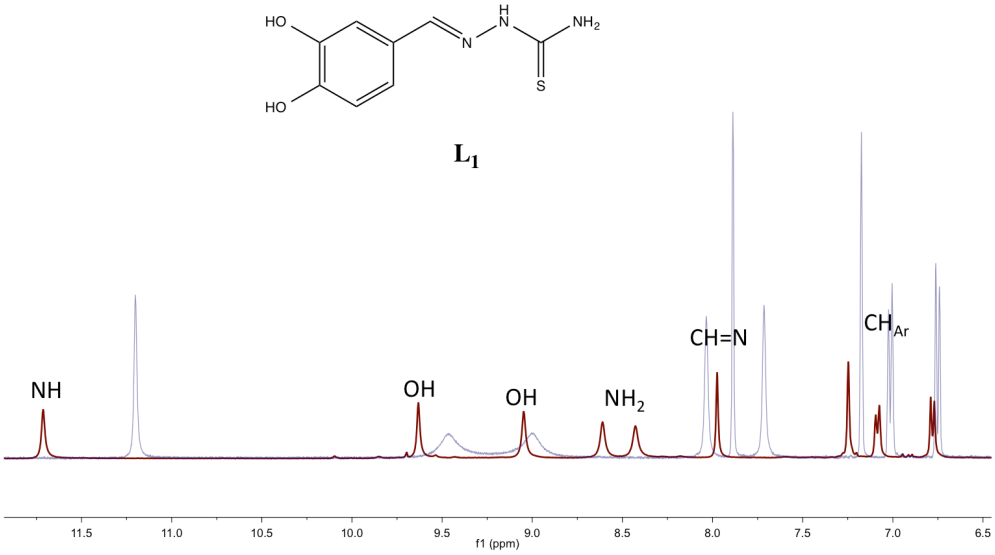

Fig. 3.16 Comparison of the ^{1}H-NMR spectrum of the ligand L_1 (violet) with that of the coordinated ligand in the complex 1(red).

The assignment of the IR bands was useful to determine the ligand mode of coordination. A strong band between 3500 and 3000 cm^{-1} is related to the symmetric and asymmetric stretching mode of NH_2, as well as the stretching of NH and OH groups: this data reinforced the idea that at least part of the ligand is in its neutral form. Comparison of the IR spectra of the copper complexes with that of the corresponding ligands results in a shift to slightly higher wavenumbers of the C=N stretching vibration, indicating the involvement of the iminic nitrogen in coordination. Moreover, the *ν*(C=S), around 830 cm^{-1} in free ligands, is shifted to lower frequencies in the spectra of metal complexes: this indicates that the binding of metal ion is *via* its thione sulphur. Therefore, it is possible to confirm a N, S bidentate coordination of the ligand to the metal centre.

It is interesting to note that in the ^{1}H-NMR spectra of all the synthesised complexes **1-5**, recorded in DMSO-d_6, just one single set of signals is displayed related to complexes of copper(I) with the proper thiosemicarbazone ligand: no signals attributable to the cyclized products could be seen in the spectra of the isolated powders. On the contrary, the signals related to the cyclized product can be found in ^{1}H-NMR spectra of the mother liquors (as example see Fig. 3.17): no signals related to the iminic proton can be found in the spectrum, as well as peaks attributable to the NH_2 protons.

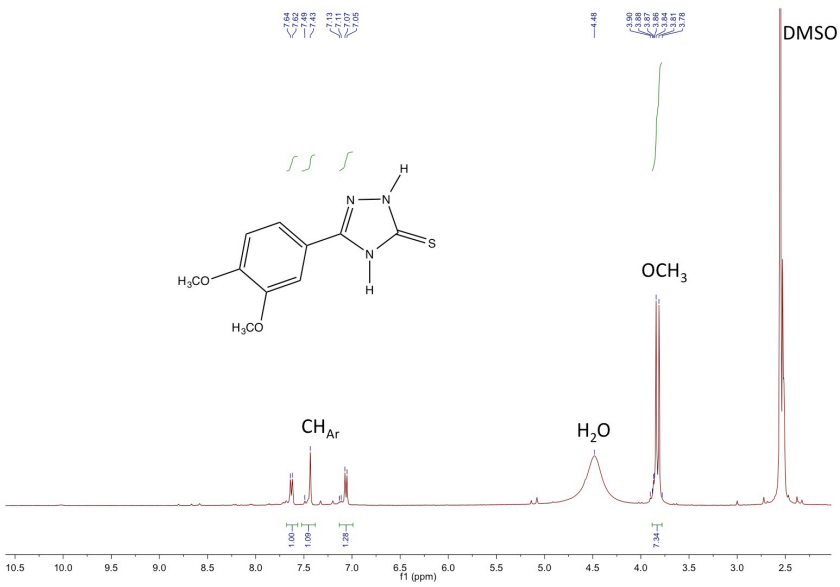

Fig. 3.17 ^{1}H-NMR spectrum of residues of the evaporation of the solution from which the complex 3 is precipitated.

ICP and elemental analyses, carried out on complexes **1-5,** are consistent with the isolation of multimetallic structures. The stoichiometric unit for the different compounds are proposed in Table 3.1.

Complex	Molecular formula	Mol. Wt.	Colour	Elemental analysis found (calcd.)			ICP found (calcd.)
				C	H	N	
1	$C_{16}H_{17}Cl_2Cu_3N_6O_4S_2$	682.8	orange	28.39 (28.15)	2.81 (2.51)	12.48 (12.31)	28.9% (27.8%)
2	$C_{20}H_{25}Cl_3Cu_3N_6O_6S_2+2H_2O$	806.91	yellow	29.45 (29.77)	3.49 (3.62)	10.47 (10.41)	21.8% (22%)
3	$C_{20}H_{25}Cl_2Cu_3N_6O_4S_2$	738.9	yellow	32.71 (32.51)	3.55 (3.41)	11.44 (11.44)	27.8% (28%)
4	$C_{10}H_{13}Cl_2Cu_2N_3O_2S+H_2O$	455.19	green	25.81 (26.39)	2.87 (3.32)	8.93 (9.23)	29.5% (28%)
5	$C_{11}H_{14}Cl_2Cu_3N_3O_3S+H_2O$	547.75	white	23.91 (24.12)	2.80 (2.94)	7.60 (7.67)	36.7% (34.7%)

Table 3.1 Physiochemical data for compounds 1-5.

As part of the ligand is involved in the reduction and cyclization processes, the initial 2:1 ligand to metal stoichiometry is lost: multimetallic structures could be obtained as a consequence of an excess of copper(I) ions in solution.

The formation of these structures could be possible since the thiosemicarbazone ligands possess various coordinative sites (Fig. 3.18). Ligands **L_1-L_5** can coordinate the metal ion in a N, S chelating mode both in their neutral form (structure I), or as anion (structure II). Moreover, the ligand can coordinate the metal as monodentate ligand (structure III) or can form bridged structures. The presence of additional donor atoms on the phenyl ring could give rise to additional coordination sites (structure IV).

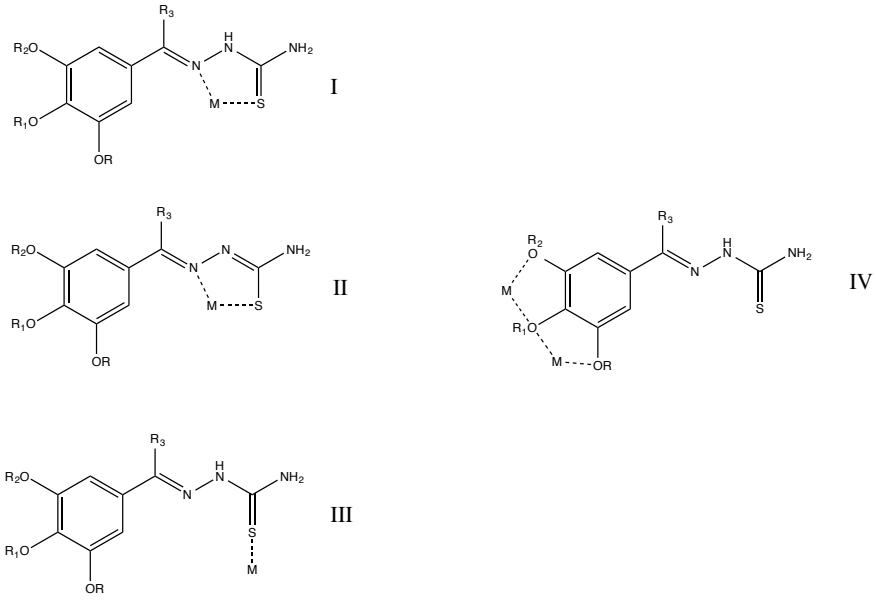

Fig. 3.18 Possible metal binding mode of thiosemicarbazone ligands.

In particular, data analysis led to the following proposed stoichiometric units: 3:2 metal to ligand for compounds 1-3, and 2:1 metal to ligand for complexes 4 and 5 (Fig. 3.19).

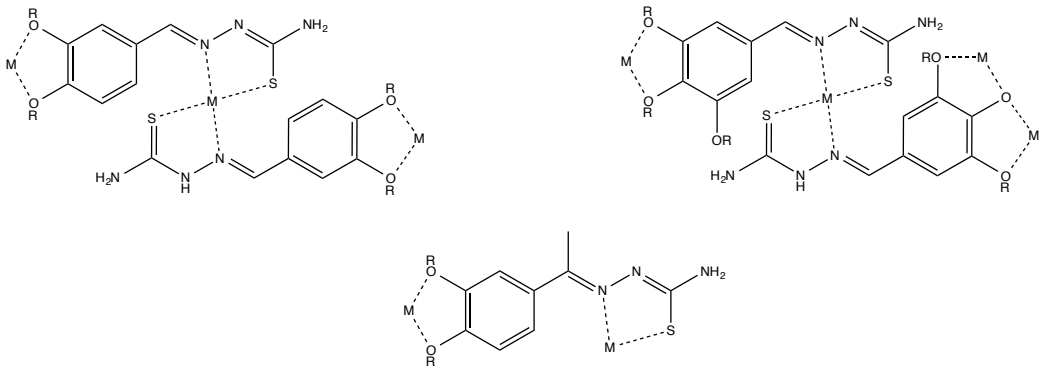

Fig. 3.19 Chemical structures of copper complexes 1-5.

In all the ESI-MS spectra the peak attributable to a 1:2 metal to ligand stoichiometry is predominant; peaks attributable to multinuclear structure can also be seen with lower intensity.

It seems reasonable to conclude that the reactions of $\mathbf{L_1}$-$\mathbf{L_5}$ with $CuCl_2$ led to the isolation of multinuclear copper(I) complexes **1-5**: hypotheses on the effective coordination structure of these complexes still remain speculative due to the absence of X-ray diffractometric data.

As all experimental data was in agreement with the isolation of diamagnetic copper(I) complexes, further analyses were performed in order to analyse the effects after exposure of a solution of copper(I) complex to the air (in order to simulate the biological test conditions). The ^{1}H-NMR spectrum of a solution of the complex **1** in DMSO-d_6 was recorded after 15 days of air exposure: the presence of broad signals confirmed the conversion to a paramagnetic specie (Fig. 3.20).

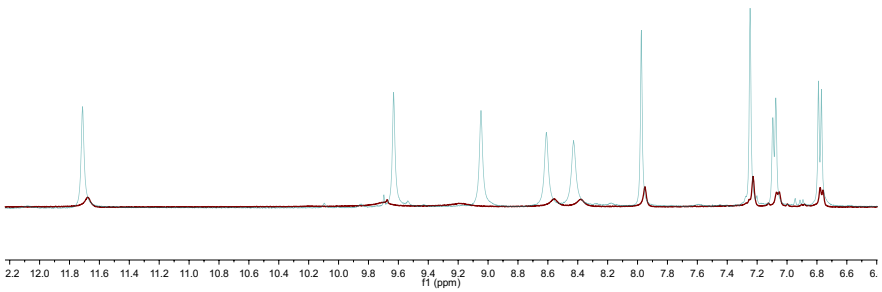

Fig. 3.20 ^{1}H-NMR spectra of the complex 1 recorded in DMSO-d_6. In light blue the spectrum recorded immediately after dissolution, in red the same spectrum recorded after 15 days.

Copper oxidation can be confirmed also visually: the colour of the solution changed from orange to brown when the oxidation had taken place. In particular, until the process was completed, two different situations could be seen in the NMR tube (Fig. 3.21): the upper part, which was directly in contact with the atmosphere, tended to become rapidly brown, while the lower part of the solution remained orange.

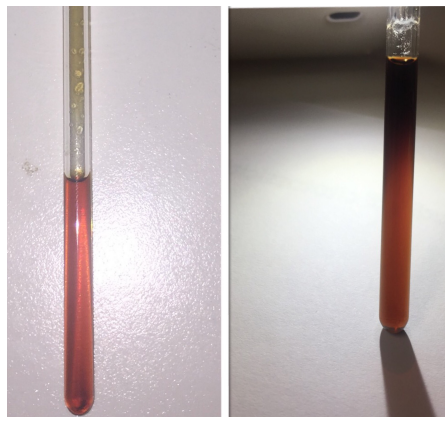

Fig. 3.21 Changing in colour of a DMSO-d_6 solution of complex 1 at t=0 (on the left) and after 7 days (on the right). After 7 days is visible the occurring of the oxidation process in the upper part of the NMR tube.

3.2.1.2.2 Thiosemicarbazones containing $N(CH_3)_2$ as terminal moiety

In the two ligands **L_6** and **L_7** (Fig. 3.13), the -NH_2 group is substituted by -$N(CH_3)_2$. The complexation reactions with $CuCl_2$ were carried out following the same experimental conditions used for complexes **1**-**5**, but results (complexes **6** and **7**) differed significantly from those obtained previously. Complete cyclisation of the ligand (Fig. 3.22) occurred as confirmed by the ^{1}H-NMR spectra.

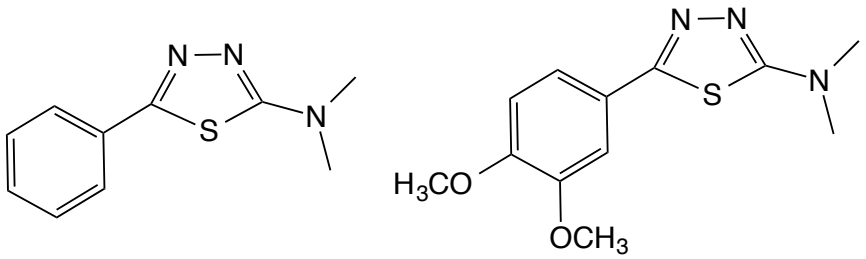

Fig. 3.22 Chemical structure of the products of the cyclisation of L_6 and L_7.

L_6 and **L_7** react with $CuCl_2$ giving the related complexes **6** and **7**. The ESI-MS spectra show peaks referred to both 2:1 and 1:1 ligand:copper complexes, with the ligand in its cycled form. ICP and elemental analysis confirmed the proposed structure Cu(I)($ligand_{cyclized}$)Cl. The higher grade of cyclisation of ligands **L_6** and **L_7**, towards **L_1**-**L_5**, highlights that the mechanism is influenced by the nature of the group bound to C4, as well as by the substituents on the phenyl ring. According to the proposed cyclisation mechanism (Scheme 3.2, mechanism B), the reaction is initiated by deprotonation, forming a radical at thiosemicarbazone N(5); after resonance of this radical, the thiol radical attacks azomethine carbon to form the ring and expulsion of another hydrogen radical.

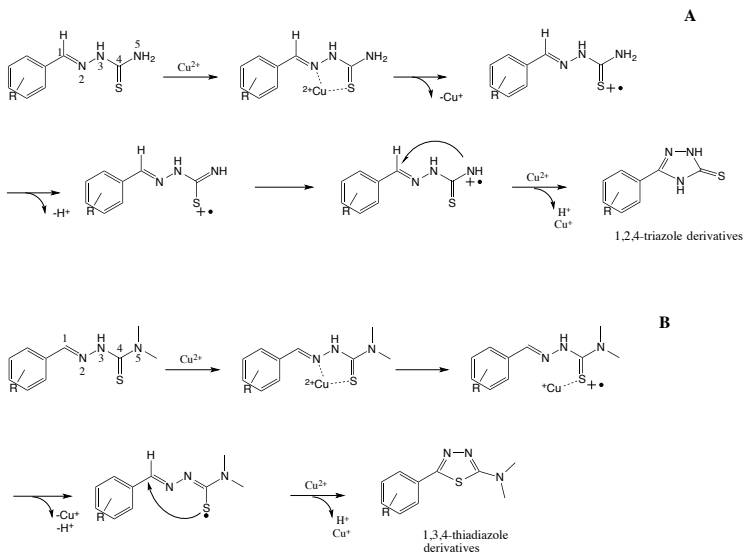

Scheme 3.2 Proposed cyclisation mechanism of ligand 1-5 (A) and 6-7 (B).

The mechanism of cyclisation, that leads to the cycled forms of the ligands $\mathbf{L_6}$ and $\mathbf{L_7}$, followed a different pathway: the two methyl groups, attached on the terminal N4, denied the hydrogen NH_2 elimination as the terminal step for ring closure. Moreover, the thione form is stabilised by the presence of the terminal dimethylamino group. This led to the synthesis of 1,3,4-thiadiazole derivatives as then confirmed by single crystal XRD analyses of the complexes **6** and **7**.

The isolation of copper(I) complexes **6** and **7** was confirmed by ^{1}H-NMR, recorded in DMSO-d_6: the aromatic region displayed sharp signals related to the phenyl ring of the coordinated cycled thiosemicarbazone. No other signals can be found around 8 ppm or 10 ppm, related respectively to iminic or NH protons. This data seems to confirm that the ligand cyclisation process was completed.

Recrystallization of **6** and **7** led to the isolation of the Cu(II) complexes **6'** and **7'**: the oxidation under air exposure led to the isolation of the 2:1 ligand to copper(II) complexes, whose structures were confirmed also by single crystal XRD analyses (see crystal structure discussion below).

3.2.2 Cinnamaldehyde type thiosemicarbazone compounds

3.2.2.1 Cinnamaldehyde type thiosemicarbazone ligands

Ligands **L_8-L_{12}** were prepared by reacting the proper unsaturated α,β-aldehyde (or ketone) with thiosemicarbazide at room temperature in ethanol solution. The resulted cinnamaldehyde thiosemicarbazone derivatives are shown in Scheme 3.3.

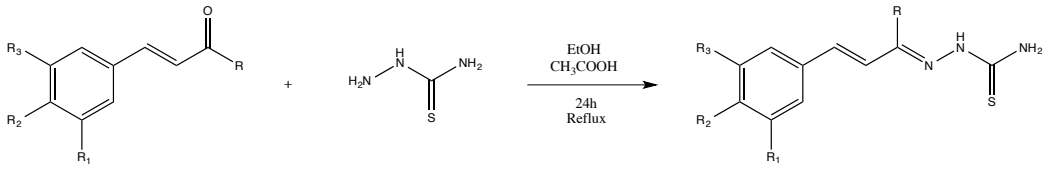

L_8 R=H, R_1=OCH_3, R_2=OH, R_3=H
L_9 R=H, R_1=OCH_3, R_2=OH, R_3=OCH_3
L_{10} R=H, R_1=H, R_2=$N(CH_3)_2$, R_3=H
L_{11} R=H, R_1=H, R_2=OH, R_3=OCH_3
L_{12} R=CH_3, R_1=OCH_3, R_2=OH, R_3=H

Scheme 3.3 General scheme for the syntheses of ligands L_8-L_{12}.

In compounds **L_{13}** and **L_{14}** (Scheme 3.4) a saturated C-C bond replaced the double C=C one.

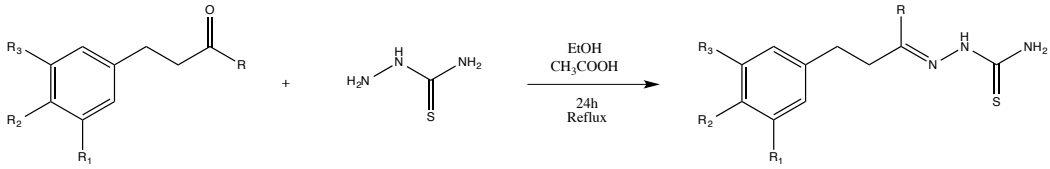

L_{13} R=H, R_1=H, R_2=H, R_3=H
L_{14} R=CH_3, R_1=OCH_3, R_2=OH, R_3=H

Scheme 3.4 General scheme for the syntheses of ligands L_{13} and L_{14}.

The chemical structure of compounds **L_8-L_{14}** was verified by ^{1}H-NMR and IR spectroscopy, EI-MS spectrometry and elemental analysis.

Briefly: the infrared spectra show a band in the range of 3100 and 3000 cm^{-1} related to the NH_2 and NH vibration modes; the presence of a medium stretching frequency for the C=S stretching, around 820 cm^{-1}, is characteristic of the free ligand; the strong band around 1543 cm^{-1} is assigned to the ν(C=N).

The ^{1}H-NMR spectra of the free ligands were recorded in DMSO-d_6 because of the low solubility in protic solvents such as methanol. The aromatic protons of the thiosemicarbazone ligands are displayed between 6.5 and 8.2 ppm and the hydrazinic protons, characteristic of the final products, between 8.7 and 8.9 ppm. The EI-MS spectra confirmed the identity of all the synthesised ligands: an intense peak related to the molecular ion $[L]^+$ could be seen for all the compounds.

The evaluation of the absolute configuration was necessary as compounds containing a C=N group can exist both as E and Z isomers; additionally, in compounds **L_8-L_{12}**, the presence of a C=C double bond gives rise to a further possible *cis*/*trans* configurations.

The unsaturated α,β-aldehyde were used as enantio pure reagents. In the spectra of all the synthesised ligands just one set of signals can be found. The calculation of the J coupling constants led to the hypothesis of an E conformation around the C=C bond (J_{HH}=16 Hz) and a Z conformation for the C=N bond (J_{HH}= 9 Hz): the final structure (Fig. 3.23) is stabilized by hydrogen interactions between H_A and the iminic nitrogen. The preferred E conformation of the C=C double bond probably arises because of steric constrains between the aryl ring and the thiosemihydrazones moiety (C=N-NH-C=S-NH_2).

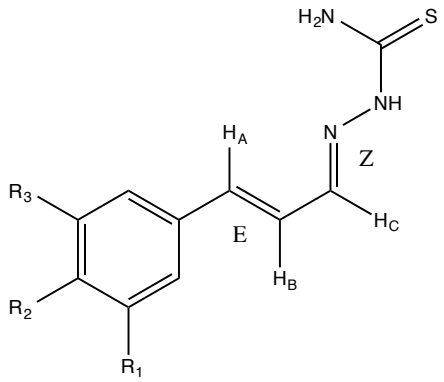

Fig. 3.23 Proposed configuration of ligands L_8-L_{11} and L_{13}.

Different situation was found for ligands **L_{12}** and **L_{14}**: the ^{1}H-NMR displayed two different sets of signals, confirming the coexistence of two isomers in equimolar ratio (50%). This is due to the effect of the methyl group, which replaces the iminic proton. In the Z configuration, around the C=N bond, the acidic N-H proton is in close proximity to the methyl group and this probably favours the E isomer of **L_{12}** and **L_{14}**.

3.2.2.2 Cinnamaldehyde type thiosemicarbazone copper complexes

Complexation reaction between two equivalents of the proper thiosemicarbazone ligand (**L_8-L_{14}**) with one equivalent of copper chloride $CuCl_2$ in a methanol solution led to the synthesis of complexes **8-14**. All the synthesised compounds were fully characterised with the common spectroscopic and spectrometric analyses: compounds of the general formula $Cu(L)_2$ were obtained, where L is the mono-deprotonated ligand.

In the IR spectra the signal of the iminic C=N, around 1630 cm^{-1} in the free ligand, is shifted to lower wavenumbers as a consequence of the coordination. A similar behaviour was seen for the C=S stretching band that is downshift of ca 20 cm^{-1} foreshadowing a significant bond elongation. The 2:1 ligand to metal

stoichiometry was confirmed by ESI-MS spectra in which the highest peak is always related to the molecular ion $[ML_2+H]^+$. ^{1}H-NMR spectra of the complexes **L_8-L_{14}**, recorded in DMSO-d_6, show broad signals that confirmed the paramagnetic nature of the copper ion involved in the coordination.

The final structures of the synthesised complexes are completely different from that of the vanillin thiosemicarbazones analogues. For compounds **8-12** this can be explained considering the amplified conjugated system, derived from the introduction of an additional C=C double bond in the free ligand. In this case the cyclisation mechanism is disfavoured due to an amplified delocalised electrons system (Fig. 3.23) that renders these compounds less active toward radical cyclisation.

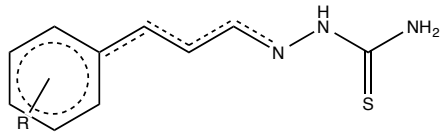

Fig. 3.24 Delocalised electron system in ligands with an additional C=C double bond (L_8-L_{12}).

The same structures were found also for complexes **13** and **14**. The ^{1}H-NMR recorded in DMSO-d_6 confirmed that the copper ion was still in its highest oxidation state and no cyclisation happened in solution. The presence of the unsaturated C-C single bond, in the structure of the free ligands, breaks the conjugated system of the iminic C=N bond with the phenyl ring: the uncoupled electron, derived from the radical mechanism, is not stable enough to induce the ring closure.

Two opposite situations lead to the same chemical structures where the central copper (II) ion is coordinated by two monodeprotonated thiosemicarbazone ligands, as confirmed by physiochemical data.

3.2.3 Biological analyses

Biological assays were performed to assess the relative effects of the different thiosemicarbazones and of the copper complexes on growth and mycotoxin accumulation of *Aspergillus flavus* (Fig. 3.25).

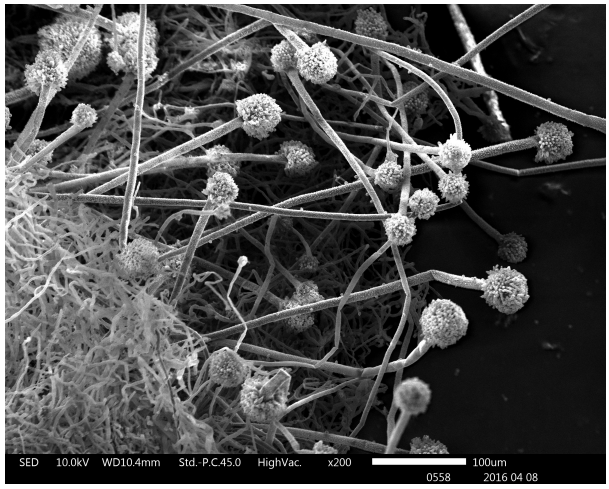

Fig. 3.25 *Aspergillu Flavus*. Microscpe SEM 200X image.

Compound	AF Inhibition (%)		Growth Inhibition (%)	
	50 µM	100 µM	50 µM	100 µM
L_1	5	0	ND	ND
L_3	26	25	20	3
L_4	26	12	48	50
L_6	76	90	22	44
L_7	42	40	5	22
1	0	6	/	/
2	29	61	48	61
3	62	80	41	51
4	52	72	61	72
6	35	67	0	0
7	34	59	0	5

Table 3.2 Aflatoxin inhibition and fungal growth inhibition percentages for L_1-L_7 ligands and for the related copper complexes.

Results on fungal growth inhibition and aflatoxin production inhibition are collected in Table 3.2. DMSO was used as control, at both 50 and 100 mM concentration. Looking at the results, it can be seen that free ligands $\mathbf{L_1}$-$\mathbf{L_4}$ do not show high inhibition percentage towards fungal growth as far as aflatoxin inhibition. The best activity was observed for $\mathbf{L_6}$: at 100 mM the percentage of aflatoxin production inhibition is higher than 90% and the activity remains interesting also at 50 mM (Fig. 3.26). Moreover, $\mathbf{L_6}$ displayed good values towards fungal growth inhibition. This is an important aspect to take into consideration: not only is important to block the synthesis of aflatoxin, but it is also important to preserve the fungal integrity for microbiota healthiness.

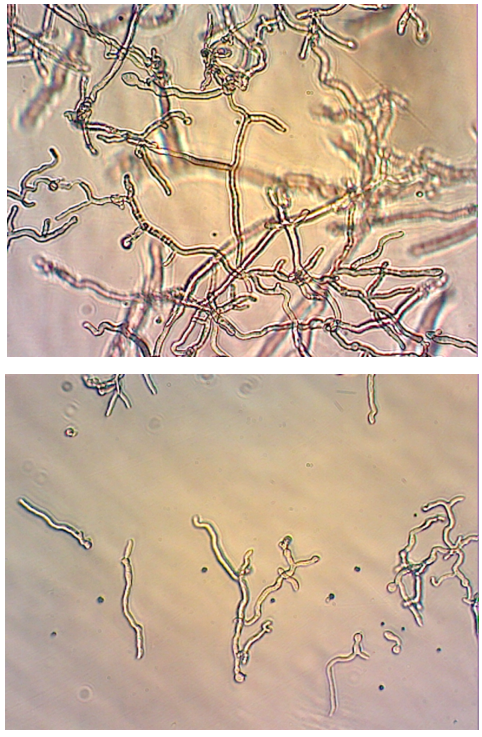

Fig. 3.26 Images at the optic reverse microscope of ife growth used for performing inhibition tests. The first image is referred to the control, the second one is after the treatment with $\mathbf{L_6}$.

Differences in activity on aflatoxin production and fungal growth inhibition can be analysed as a function of lipophilicity of the tested ligands, as it is generally correlated to the ability of the molecule to penetrate through the cell membrane. From this point of view, the low activity of **L_1-L_5** could be correlated to the fact that they were unable to efficiently penetrate the cell membrane due to their low values of lipophilicity.

In case of **L_6**, no hydroxyl or methoxy substituents are displayed on the aromatic ring (Fig. 3.13) and this gives rise to a more lipophilic system: this is confirmed by the calculated value of LogP (LogP = Log $[solute]_{oct}/[solute]_{water}$) of 2.50 that is the higher value found for the tested ligands (Table 3.3).

COMPOUND	LogP
L_1	0.91
L_3	1.53
L_4	1.14
L_6	2.5
L_7	2.15

Table 3.3 Calculated values of LogP for L_1-L_7.

The related copper complexes have shown a better activity in the aflatoxin inhibition: this suggested that the mechanism of action is not related to the complexation ability of the organic moiety, but that the activity could be affected by the increased ability of the metal complex to permeate the cell membrane.

Complexes **6** and **7** are particularly intriguing since they showed, respect to the corresponding free ligand, lower aflatoxin inhibition percentage. Data is in contrast with that of the complexes **1**-**5**, and this is accompanied by negligible fungal growth inhibition. This is probably the consequence of the different chemical structure that characterise these two complexes compared to the other

multinuclear copper(I) compounds. Further analyses are ongoing to better understand the mechanism of action of these molecules. Cinnamaldehyde derivatives couldn't be analysed with the same procedure as they showed a marked fluorescence, thus interfering with the assays. Alternative methods, aimed to evaluate the aflatoxin inhibition activity of these compounds, are ongoing.

L_6 and the related copper complex **6,** the two compounds with more interesting activity, were further tested for their cytotoxic effect on human cells. Four different normal cell lines were taken into consideration: colon (Crl1790), skin (Hs27), lung (HFL1) and pleura (U937) were chosen for tests as contamination primarily passes through the gastrointestinal track and the skin. Cell lines were treated with stock solutions of both **L_6** and **6** for 24 h and concentrations were varied from 100 to 0.5 μM. Data is calculated as a mean of three independent experiments.

COMPOUND	Crl1790	Hs27	HFL1	U937
L_6	>100	>100	>100	>100
6	2	3	1	5

Table 3.4 GI_{50} values (concentration which caused 50% of reduction in population growth) in μM for compounds L_6 and 6 towards four different normal cell lines.

Such data is conventionally analysed from the prospective of GI_{50} values (Table 3.4).

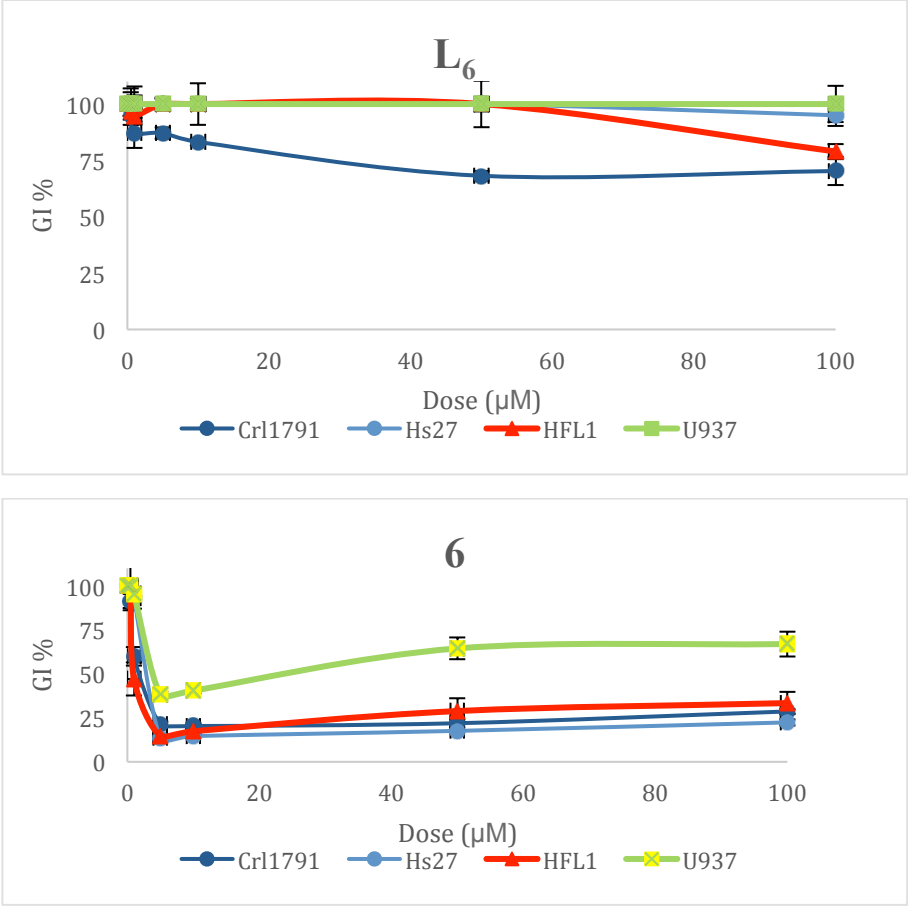

Fig. 3.27 Dose response curve for the ligand L_6 and its copper complex (6) in Crl1791, Hs27, HFL1 and U937 normal cell line. Vertical bars represent the standard deviations.

Data demonstrated metal complex **6** be highly toxic (Fig. 3.27). Different behaviour was observed for the related organic ligand: no growth inhibition was seen, indicating the compound $\mathbf{L_6}$ as not cytotoxic towards normal cells.

3.2.4 Single crystal XRD structures

3.2.4.1 Crystal structure of complex **6'**

Crystals of complex **6,** suitable for XRD analysis, were grown by vapour diffusion of ether into a saturated solution of DMF. Selected bond lengths and angles are listed in Table 3.5 and Table 3.6.

Number	Atom1	Atom2	Atom3	Angle	Number	Atom1	Atom2	Atom3	Angle
1	Cl1	Cu1	N2	89.96	48	H10A	C10	H10B	109.4
2	Cl1	Cu1	Cl1	180	49	H10A	C10	H10C	109.5
3	Cl1	Cu1	N2	90.04	50	H10B	C10	H10C	109.4
4	N2	Cu1	Cl1	90.04	51	C1	S1	C2	87.4(2)
5	N2	Cu1	N2	180	52	N2	N3	C2	112.0(3)
6	Cl1	Cu1	N2	89.96	53	Cu1	N2	N3	113.3
7	C1	S1	C2	87.4(2)	54	Cu1	N2	C1	131.7
8	N2	N3	C2	112.0(3)	55	N3	N2	C1	114.0(3)
9	Cu1	N2	N3	113.3	56	C1	N1	C9	120.9(4)
10	Cu1	N2	C1	131.7	57	C1	N1	C10	120.8(4)
11	N3	N2	C1	114.0(3)	58	C9	N1	C10	118.3(4)
12	C1	N1	C9	120.9(4)	59	C2	C3	C4	121.2(4)
13	C1	N1	C10	120.8(4)	60	C2	C3	C8	119.8(3)
14	C9	N1	C10	118.3(4)	61	C4	C3	C8	119.0(4)
15	C2	C3	C4	121.2(4)	62	S1	C1	N2	112.4(3)
16	C2	C3	C8	119.8(3)	63	S1	C1	N1	122.3(3)
17	C4	C3	C8	119.0(4)	64	N2	C1	N1	125.2(4)
18	S1	C1	N2	112.4(3)	65	S1	C2	N3	114.2(3)
19	S1	C1	N1	122.3(3)	66	S1	C2	C3	122.8(3)
20	N2	C1	N1	125.2(4)	67	N3	C2	C3	123.0(3)
21	S1	C2	N3	114.2(3)	68	C3	C4	H4	120.1
22	S1	C2	C3	122.8(3)	69	C3	C4	C5	119.8(4)
23	N3	C2	C3	123.0(3)	70	H4	C4	C5	120.1
24	C3	C4	H4	120.1	71	C3	C8	H8	119.7
25	C3	C4	C5	119.8(4)	72	C3	C8	C7	120.6(4)
26	H4	C4	C5	120.1	73	H8	C8	C7	119.7
27	C3	C8	H8	119.7	74	H6	C6	C5	120.1
28	C3	C8	C7	120.6(4)	75	H6	C6	C7	120.2
29	H8	C8	C7	119.7	76	C5	C6	C7	119.7(5)
30	H6	C6	C5	120.1	77	C4	C5	C6	120.8(4)
31	H6	C6	C7	120.2	78	C4	C5	H5	119.6
32	C5	C6	C7	119.7(5)	79	C6	C5	H5	119.5
33	C4	C5	C6	120.8(4)	80	C8	C7	C6	120.1(4)
34	C4	C5	H5	119.6	81	C8	C7	H7	120
35	C6	C5	H5	119.5	82	C6	C7	H7	119.9
36	C8	C7	C6	120.1(4)	83	N1	C9	H9A	109.5
37	C8	C7	H7	120	84	N1	C9	H9B	109.5
38	C6	C7	H7	119.9	85	N1	C9	H9C	109.5
39	N1	C9	H9A	109.5	86	H9A	C9	H9B	109.4
40	N1	C9	H9B	109.5	87	H9A	C9	H9C	109.5
41	N1	C9	H9C	109.5	88	H9B	C9	H9C	109.4
42	H9A	C9	H9B	109.4	89	N1	C10	H10A	109.5
43	H9A	C9	H9C	109.5	90	N1	C10	H10B	109.5
44	H9B	C9	H9C	109.4	91	N1	C10	H10C	109.5
45	N1	C10	H10A	109.5	92	H10A	C10	H10B	109.4
46	N1	C10	H10B	109.5	93	H10A	C10	H10C	109.5
47	N1	C10	H10C	109.5	94	H10B	C10	H10C	109.4

Table 3.5 List of the angles for complex 6.

Number	Atom1	Atom2	Length	Number	Atom1	Atom2
1	Cu1	Cl1	2.275	29	C10	H10B
2	Cu1	N2	1.985	30	C10	H10C
3	Cu1	Cl1	2.275	31	S1	C1
4	Cu1	N2	1.985	32	S1	C2
5	S1	C1	1.739(4)	33	N3	N2
6	S1	C2	1.745(3)	34	N3	C2
7	N3	N2	1.384(3)	35	N2	C1
8	N3	C2	1.299(5)	36	N1	C1
9	N2	C1	1.318(5)	37	N1	C9
10	N1	C1	1.336(4)	38	N1	C10
11	N1	C9	1.451(6)	39	C3	C2
12	N1	C10	1.446(6)	40	C3	C4
13	C3	C2	1.468(4)	41	C3	C8
14	C3	C4	1.403(6)	42	C4	H4
15	C3	C8	1.387(5)	43	C4	C5
16	C4	H4	0.93	44	C8	H8
17	C4	C5	1.386(5)	45	C8	C7
18	C8	H8	0.93	46	C6	H6
19	C8	C7	1.388(5)	47	C6	C5
20	C6	H6	0.93	48	C6	C7
21	C6	C5	1.377(6)	49	C5	H5
22	C6	C7	1.384(7)	50	C7	H7
23	C5	H5	0.93	51	C9	H9A
24	C7	H7	0.93	52	C9	H9B
25	C9	H9A	0.96	53	C9	H9C
26	C9	H9B	0.96	54	C10	H10A
27	C9	H9C	0.96	55	C10	H10B
28	C10	H10A	0.96	56	C10	H10C

Table 3.6 Bond length list of complex 6.

The compound crystallised in the centrosymmetric space group P_{-1}. In Fig. 3.28 the $[Cu(\mathbf{L})_2Cl_2]$ building block unit is shown.

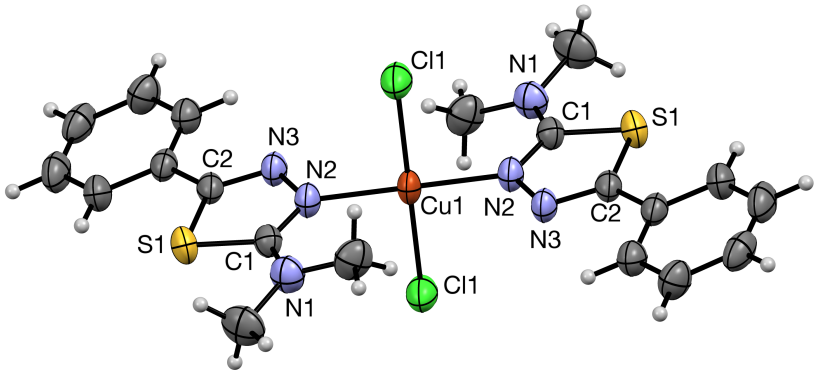

Fig. 3.28 X-Ray crystal structure for complex 6. Thermal ellipsoids are drawn at 50% of probability. Hydrogens are drawn as fixed-size spheres of 0.11 Å of radius and solvent molecules have been omitted for clarity.

The copper(II) ion adopts a square planar geometry with coordination angles of 90°: two positions are occupied by the N2 atoms of the ligands and two chloride ions complete the coordination geometry.

The structure determination showed that the ligand exists in the cyclised form. The C1···S1 distance of 1.739 Å is intermediate between those of a single and double bonds (1.82 and 1.56 Å respectively). The N2···N3 bond distance of 1.364 Å is shorter that 1.44 Å, accepted for a single N-N bond. The C2···N3 distance of 1.299 Å and the thioamide C1···N2 distance of 1.316 Å indicate an increased double bond character, in accordance with a five members thiadiaziole type ring. The formation of a five members ring leads to a wide planarity of the ligand, induced by an extended system of conjugated double bonds.

The solid state packing is characterised by a three-dimensional network of hydrogen bonds established by the two methyl group of $N(CH_3)_2$: in particular, H10 interacts with the chloride ion of a second molecule. Moreover a T-stack interaction between the H9 hydrogen and the aromatic ring of the thiosemicarbazone ligands can be displayed in the packing (Fig. 3.29 and Fig. 3.30).

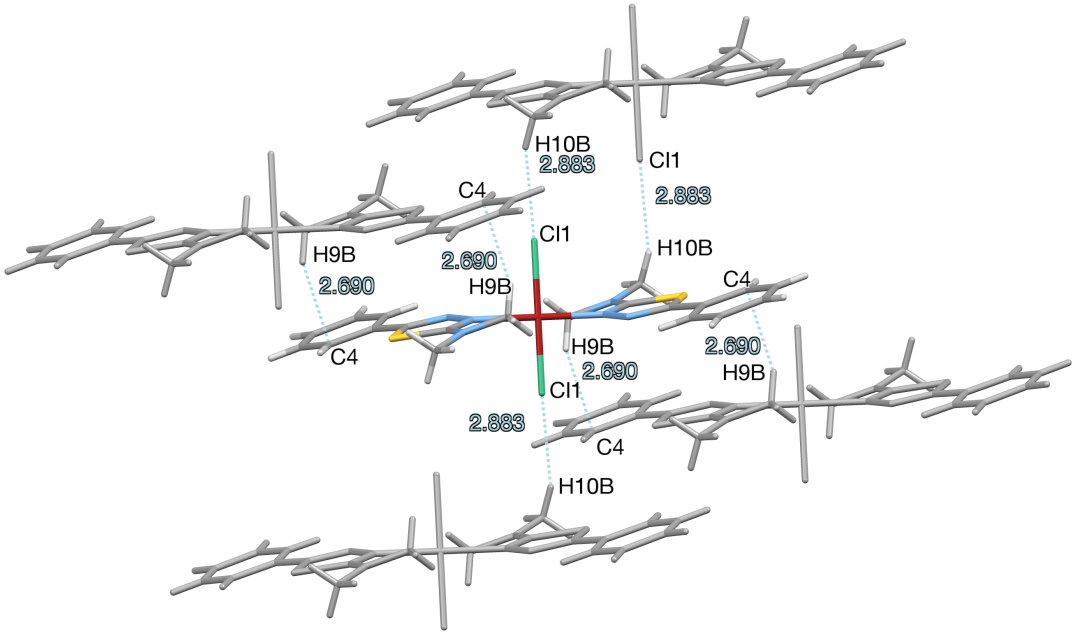

Fig. 3.29 Intramolecular hydrogen bond and T-stacking interactions involved in the crystal packing.

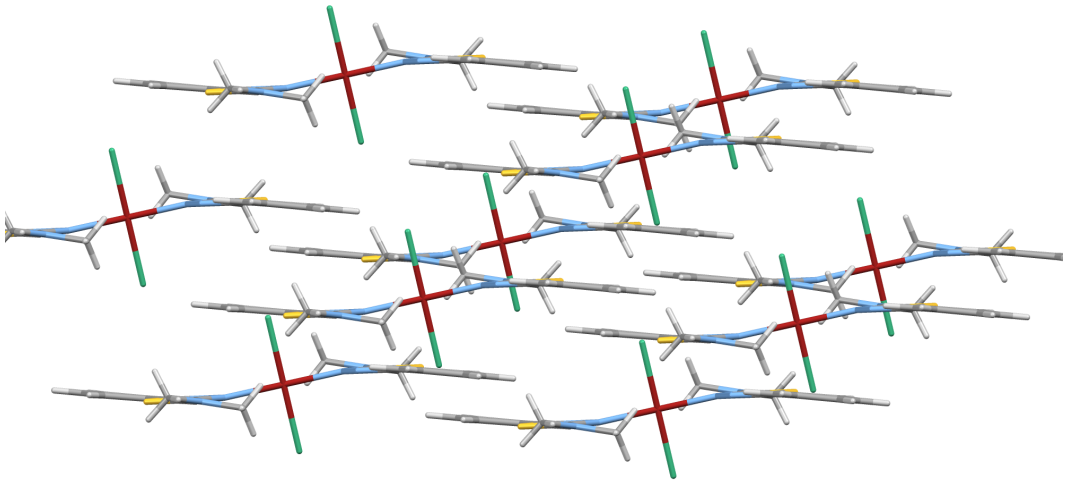

Fig. 3.30 Crystal packing of complex 6.

3.2.4.2 Crystal structure of complex **7'**

Crystals of complex **7,** suitable for synchrotron XRD analysis, were grown by vapour diffusion of ether into a saturated solution of DMF. Selected bond lengths and angles are listed in Table 3.7 and Table 3.8.

Number	Atom1	Atom2	Length	Number	Atom1	Atom2	Length
1	Cu1	Cl1	2.2673	37	C12	H12A	0.96
2	Cu1	N3	1.99	38	C12	H12C	0.96
3	Cu1	Cl1	2.2673	39	S1	C1	1.745(2)
4	Cu1	N3	1.99	40	S1	C2	1.730(2)
5	S1	C1	1.745(2)	41	O2	C6	1.356(2)
6	S1	C2	1.730(2)	42	O2	C12	1.431(3)
7	O2	C6	1.356(2)	43	O1	C5	1.363(2)
8	O2	C12	1.431(3)	44	O1	C11	1.435(3)
9	O1	C5	1.363(2)	45	N3	N2	1.380(2)
10	O1	C11	1.435(3)	46	N3	C2	1.310(3)
11	N3	N2	1.380(2)	47	N1	C1	1.340(2)
12	N3	C2	1.310(3)	48	N1	C9	1.452(3)
13	N1	C1	1.340(2)	49	N1	C10	1.456(3)
14	N1	C9	1.452(3)	50	N2	C1	1.327(3)
15	N1	C10	1.456(3)	51	C3	C2	1.462(3)
16	N2	C1	1.327(3)	52	C3	C8	1.388(3)
17	C3	C2	1.462(3)	53	C3	C4	1.414(2)
18	C3	C8	1.388(3)	54	C5	C6	1.416(3)
19	C3	C4	1.414(2)	55	C5	C4	1.385(3)
20	C5	C6	1.416(3)	56	C6	C7	1.386(2)
21	C5	C4	1.385(3)	57	C8	H8	0.93
22	C6	C7	1.386(2)	58	C8	C7	1.397(3)
23	C8	H8	0.93	59	C11	H11B	0.96
24	C8	C7	1.397(3)	60	C11	H11A	0.961
25	C11	H11B	0.96	61	C11	H11C	0.96
26	C11	H11A	0.961	62	C7	H7	0.93
27	C11	H11C	0.96	63	C4	H4	0.93
28	C7	H7	0.93	64	C9	H9B	0.96
29	C4	H4	0.93	65	C9	H9A	0.96
30	C9	H9B	0.96	66	C9	H9C	0.96
31	C9	H9A	0.96	67	C10	H10C	0.961
32	C9	H9C	0.96	68	C10	H10A	0.959
33	C10	H10C	0.961	69	C10	H10B	0.961
34	C10	H10A	0.959	70	C12	H12B	0.96
35	C10	H10B	0.961	71	C12	H12A	0.96
36	C12	H12B	0.96	72	C12	H12C	0.96

Table 3.7 Bond length list of complex 7.

Number	Atom1	Atom2	Atom3	Angle	Number	Atom1	Atom2	Atom3	Angle
1	Cl1	Cu1	N3	90.1	62	H12B	C12	H12A	109.5
2	Cl1	Cu1	Cl1	180	63	H12B	C12	H12C	109.5
3	Cl1	Cu1	N3	89.9	64	H12A	C12	H12C	109.5
4	N3	Cu1	Cl1	89.9	65	C1	S1	C2	87.38(9)
5	N3	Cu1	N3	180	66	C6	O2	C12	117.0(2)
6	Cl1	Cu1	N3	90.1	67	C5	O1	C11	116.3(2)
7	C1	S1	C2	87.38(9)	68	Cu1	N3	N2	113.3
8	C6	O2	C12	117.0(2)	69	Cu1	N3	C2	130.7
9	C5	O1	C11	116.3(2)	70	N2	N3	C2	115.6(2)
10	Cu1	N3	N2	113.3	71	C1	N1	C9	120.5(2)
11	Cu1	N3	C2	130.7	72	C1	N1	C10	120.3(2)
12	N2	N3	C2	115.6(2)	73	C9	N1	C10	119.1(2)
13	C1	N1	C9	120.5(2)	74	N3	N2	C1	110.0(2)
14	C1	N1	C10	120.3(2)	75	C2	C3	C8	121.0(2)
15	C9	N1	C10	119.1(2)	76	C2	C3	C4	119.6(2)
16	N3	N2	C1	110.0(2)	77	C8	C3	C4	119.4(2)
17	C2	C3	C8	121.0(2)	78	O1	C5	C6	116.0(2)
18	C2	C3	C4	119.6(2)	79	O1	C5	C4	123.9(2)
19	C8	C3	C4	119.4(2)	80	C6	C5	C4	120.1(2)
20	O1	C5	C6	116.0(2)	81	O2	C6	C5	115.2(2)
21	O1	C5	C4	123.9(2)	82	O2	C6	C7	125.4(2)
22	C6	C5	C4	120.1(2)	83	C5	C6	C7	119.3(2)
23	O2	C6	C5	115.2(2)	84	S1	C1	N1	121.4(2)
24	O2	C6	C7	125.4(2)	85	S1	C1	N2	114.5(1)
25	C5	C6	C7	119.3(2)	86	N1	C1	N2	124.1(2)
26	S1	C1	N1	121.4(2)	87	S1	C2	N3	112.5(1)
27	S1	C1	N2	114.5(1)	88	S1	C2	C3	122.1(1)
28	N1	C1	N2	124.1(2)	89	N3	C2	C3	125.3(2)
29	S1	C2	N3	112.5(1)	90	C3	C8	H8	119.8
30	S1	C2	C3	122.1(1)	91	C3	C8	C7	120.4(2)
31	N3	C2	C3	125.3(2)	92	H8	C8	C7	119.8
32	C3	C8	H8	119.8	93	O1	C11	H11B	109.4
33	C3	C8	C7	120.4(2)	94	O1	C11	H11A	109.4
34	H8	C8	C7	119.8	95	O1	C11	H11C	109.5
35	O1	C11	H11B	109.4	96	H11B	C11	H11A	109.5
36	O1	C11	H11A	109.4	97	H11B	C11	H11C	109.5
37	O1	C11	H11C	109.5	98	H11A	C11	H11C	109.5
38	H11B	C11	H11A	109.5	99	C6	C7	C8	120.6(2)
39	H11B	C11	H11C	109.5	100	C6	C7	H7	119.7
40	H11A	C11	H11C	109.5	101	C8	C7	H7	119.7
41	C6	C7	C8	120.6(2)	102	C3	C4	C5	120.1(2)
42	C6	C7	H7	119.7	103	C3	C4	H4	119.9
43	C8	C7	H7	119.7	104	C5	C4	H4	119.9
44	C3	C4	C5	120.1(2)	105	N1	C9	H9B	109.5
45	C3	C4	H4	119.9	106	N1	C9	H9A	109.5
46	C5	C4	H4	119.9	107	N1	C9	H9C	109.4
47	N1	C9	H9B	109.5	108	H9B	C9	H9A	109.5
48	N1	C9	H9A	109.5	109	H9B	C9	H9C	109.5
49	N1	C9	H9C	109.4	110	H9A	C9	H9C	109.5
50	H9B	C9	H9A	109.5	111	N1	C10	H10C	109.5
51	H9B	C9	H9C	109.5	112	N1	C10	H10A	109.5
52	H9A	C9	H9C	109.5	113	N1	C10	H10B	109.4
53	N1	C10	H10C	109.5	114	H10C	C10	H10A	109.4
54	N1	C10	H10A	109.5	115	H10C	C10	H10B	109.4
55	N1	C10	H10B	109.4	116	H10A	C10	H10B	109.5
56	H10C	C10	H10A	109.4	117	O2	C12	H12B	109.5
57	H10C	C10	H10B	109.4	118	O2	C12	H12A	109.4
58	H10A	C10	H10B	109.5	119	O2	C12	H12C	109.5
59	O2	C12	H12B	109.5	120	H12B	C12	H12A	109.5
60	O2	C12	H12A	109.4	121	H12B	C12	H12C	109.5
61	O2	C12	H12C	109.5	122	H12A	C12	H12C	109.5

Table 3.8 Angle list of complex 7.

The compound crystallised in the centrosymmetric space group $P2_1/n$. The $[Cu(ligand)_2Cl_2]$ building block unit is shown in Fig. 3.31.

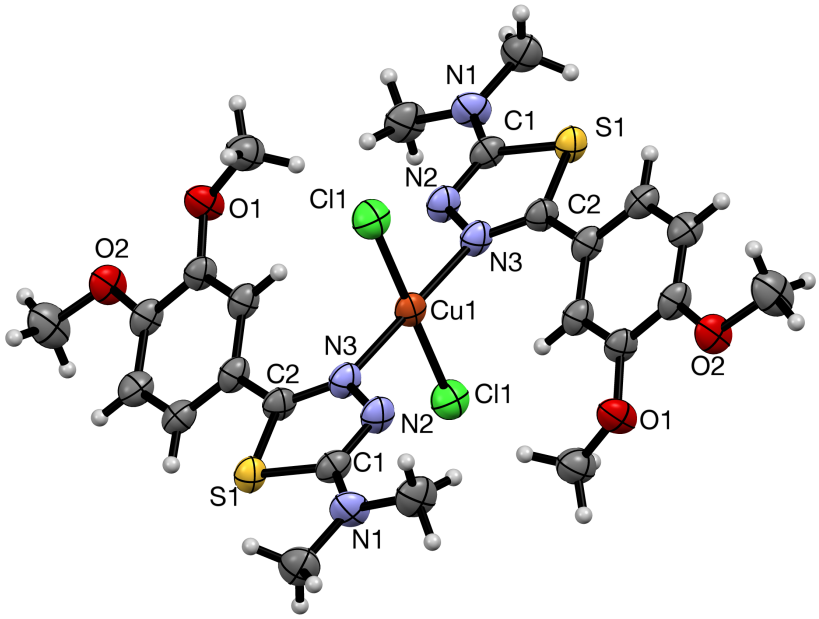

Fig. 3.31 X-Ray crystal structure for complex 7. Thermal ellipsoids are drawn at 50% of probability. Hydrogens are drawn as fixed-size spheres of 0.11 Å of radius and solvent molecules have been omitted for clarity.

The copper(II) ion adopts a square planar geometry with coordination angles of 90°: the two positions in the basal plane are occupied by the hydrazinic N3 atoms of two molecules of thiosemicarbazone ligands, two chloride ions complete the coordination geometry, occupying the two remaining axial positions.

The situation is slightly different from that obtained in complex **6,** where the copper ion is not coordinated by the hydrazinc nitrogen but through N2 one. This could be due to the electron donating effects of the two methoxy groups on the aromatic ring, which render N3 electron rich and more favourable for the coordination of copper ion.

The two bi-deprotonated thiosemicarbazone ligands are equivalent and are coordinated to the metal in a monodentate fashion via the hydrazinic nitrogen.

The structure determination showed that the ligand existed in the cycled form. The C2···S1 distance of 1.730 Å is intermediate between those of a single and double bonds (1.82 and 1.56 Å respectively). The N3···N2 bond distance of 1.360 Å is shorter that 1.44 Å, accepted for a single N-N bond. The C2···N3 distance of 1.327 Å and the thioamide C1···N2 distance of 1.310 Å indicate an increased double bond character, in accordance with a five members thiadiaziole type ring. The formation of a five members ring leads to a wide planarity of the ligand induced by an extended system of conjugated double bonds. The solid state packing (Fig. 3.32) is characterised by a three-dimensional network of weak interactions established by the two methyl of $N(CH_3)_2$ and the two metoxy groups: in particular the hydrogen atoms of the $N(CH_3)_2$ moiety are involved in T-stacking interactions with the phenyl ring of an adjacent molecule; moreover, the oxygen atoms of the two methoxy group on the phenyl ring interacts through hydrogen bond with the hydrogen atoms of the terminal $N(CH_3)_2$ moiety of a second molecule.

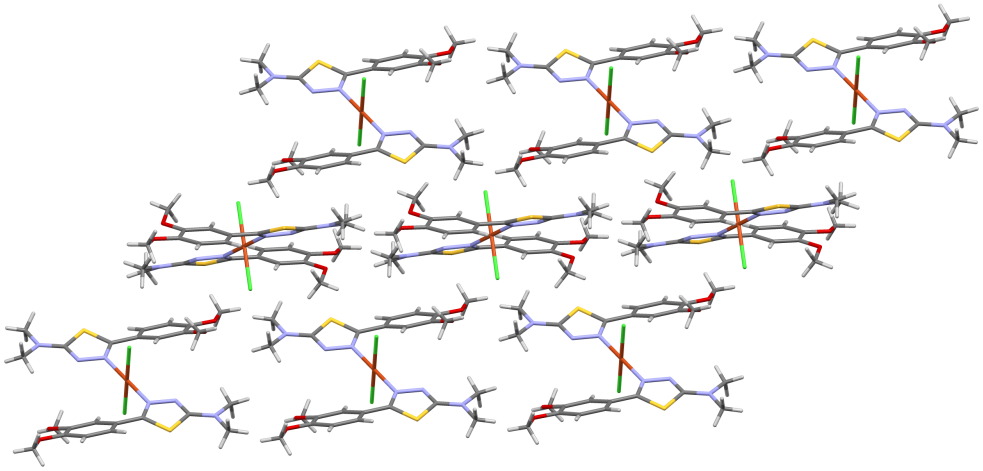

Fig. 3.32 Crystal packing of complex 7.

3.3 CONCLUSIONS

A class of differently substituted thiosemicarbzones were synthesised and completely characterised with the common spectroscopic and spectrometric analyses. Complexation reactions with $CuCl_2$ led to the isolation of different compounds, depending on the structure of the starting ligand.

Vannilin type thiosemicarbazone gave rise to multinuclear copper(I) complexes as confirmed by ^{1}H-NMR and ICP analyses. All NMR spectra displayed sharped signals attributable to diamagnetic species. Analysis of the data put in evidence that copper(II) reduction is a consequence of a mechanism in which the cyclisation of the thiosemicarbazone ligands is also involved: signals related to the cycled product can be found in the NMR spectrum of the mother liquor. Air exposure of a solution of copper(I) complexes gives rise to metal oxidtion.

Cinnamaldehyde type thiosemicarbazone led to the isolation of copper(II) complexes, as confirmed by NMR analyses. The amplified conjugated system stabilises the structure that is now less reactive toward cyclization.

Results about *Aspergillus flavus* growth inhibition and aflatoxin production inhibition evidenced that the activity is strictly related to the lipophilicity of the compound under analysis. Ligand $\mathbf{L_6}$ gave the best results as it showed good activity in aflatoxin inhibition but not toward normal cell lines.

3.4 EXPERIMENTAL SECTION

3.4.1 Materials and methods

3.4.1.1 Chemistry

All reagents of commercial quality were purchased from Sigma-Aldrich and used without further purification. The purity of the compounds was determined by elemental analysis and verified to be ≥ 95% for all synthesised molecules.

NMR spectroscopy. ^{1}H-NMR spectra were obtained in a 5 mm NMR precision tube at 298 K on a Bruker Avance 400 FT spectrophotometer. ^{1}H-NMR chemical shift were internally referenced to $(CHD_2)(CD_3)SO$ (2.50 ppm) for DMSO-d_6 and $(CD_3)_2CO$ (2.09 ppm) for acetone-d_6. All data was processed using MestReNova 9.0.1.

IR spectroscopy. The ATR-IR spectra were recorded by means of a Nicolet-Nexus (Thermo Fisher) spectrophotometer by using a diamond crystal plate in the range of 4000-400 cm^{-1}. All data was processed using OMNIC.

Mass spectrometry. Electrospray mass spectral analyses (ESI-MS) were performed with an electrospray ionization (ESI) time-of-flight Micromass 4LCZ spectrometer. Samples were prepared in methanol.

The EI-MS spectra were acquired in positive EI mode by means of a DEP-probe (Direct Exposure Probe) mounting on the tip of a Re-filament with a DSQII Thermo Fisher apparatus, equipped with a single quadrupole analyser. Samples were prepared in methanol.

Elemental Analysis. Elemental analyses were performed by using a FlashEA 1112 series CHNS/O analyzer (Thermo Fisher) with gas-chromatographic separation.

ICP-AES spectrometry. ULTIMA 2 instrument HORIBA (Jobin Yvon, Kyoto, Japan) in radial configuration, with a JY 2501 monochromator. The optical path

was continuously purged with nitrogen (2 l/min). Instrumental and optical parameters are listed below.

Monochromator	
Model	JY 2501
Focal distance	1 m
Grating	2400 grooves/mm
Entrance slit	10µm, 20µm
Resolution	5,00 pm
Nitrogen flow rate	2 l/min
ICP-source	
Nebulizer	Meinhard
Spray chamber	Cyclonic
Argon flow rate	12 l/min
Wavelength range	160-785 nm
Optical bench temperature	32°C

The quantitative analyses were acquired after calibration with a standard solution of 2% of HNO_3. Emission copper wavelength of 224.700. Samples concentration were of 100 mg/L in copper. Compounds were dissolved in 10 mL of CH_3OH (10% HNO_3). Data acquisition and processing were performed using the ICP JY v 5.2 software (Jobin Yvon).

3.4.1.2 Biology

3.4.1.2.1 *Aspergillus flavus*

Conidia suspensions were obtained from10-day YES-agar [2% (w⁄v) yeast extract (Difco, Detroit, MI), 5% (w⁄v) sucrose (Sigma, St Louis, MO), 2% (w⁄v) agar (Difco)] cultures incubated at 28 °C; conidia concentration (quantified by OD600) and viability (N90%) were determined according to Degola et al.[112]. Determination of *A. flavus* radial growth was performed in YES-agar amended with 100 µM of the proper compound: three single spots (5 µL of a 107 conidia/mL suspension each) of aflatoxigenic strain Fri2 were equidistant inoculated in 90-mm Petri dishes. Plates were incubated for 4 days at 25 °C and

the mycelial growth was evaluated daily by measuring the reverse of colonies along two orthogonal diameters. Radial growth was expressed as cm/day ± SD. Additionally, conidial germination rate and post-germination hyphal outgrowth were assessed by analysing changes in optical density of spore suspensions over time: in a 96 well microtiter plate (Sarstedt, Newton, NC, USA) 10^4 spores were inoculated in a final volume of 200 µL of YES liquid medium amended with the proper compound and incubated at 28 °C. The optical density at 620 nm (OD620) was recorded for each well every 120 min with a microplate reader (MULTISKAN EX, Thermo Electron Corporation, Vantaa, Finland) without shaking. Samples were inoculated in triplicate. Preliminary experiments indicated that OD values, recorded between 38 and 46 h after inoculum, could reliably be used to compare growth rate of the different samples. Results obtained according to radial growth and optical density determinations were comparable, as far as the inhibitory effect of the thiosemicarbazone compounds is concerned. Biomass variation was also determined in some experiments involving inoculation in CCM medium: fresh or dry mycelium weight was obtained, for each sample, withdrawing the mycelium from eight wells of the microplate and pooling them. The pooled mycelia were then blotted dry on clean paper and weighed (fresh weight determination) and then incubated at 80 °C for 48 h before dry weight determination. Samples were inoculated in triplicate.

3.4.1.2.2 Evaluation of the effects of molecules on mycotoxins production

A high throughput procedure performed in a multi-well plate was used to assess aflatoxin accumulation in a coconut milk-derived medium (CCM)[112]. Briefly: 400 mL of commercial coconut cream was diluted to the final volume of 1.2 L with bidistilled water, sterilized by autoclaving (10 min, 120 °C), cooled at 4 °C

overnight and clarified by centrifugation (15 min at 3200 g). The residual floating material and the pellet were discarded, and the intermediate phase was then recovered and used as culture medium in the aflatoxin inhibition assays. The effect on aflatoxin biosynthesis was assessed by the microplate fluorescence-based procedure described in Degola et al. (2012)[112]. Standard flat-bottom 96-well microplates (Sarstedt, Newton, NC, USA) were used. Suspensions of conidia were diluted to the appropriate concentrations and brought to the final concentration of 5 Å~ 102 conidia well; cultures were set in a final volume of 200 µL/well of CCM medium added with the proper compound. The plates were incubated in the dark under stationary conditions for up to 6 days at 25 °C. Aflatoxin accumulation was monitored by fluorescence emission determination: readings were performed directly from the bottom of wells of the culture plate with a microplate reader (TECAN SpectraFluor Plus, Männedorf, Switzerland) using the following parameters: λex = 360 nm; λem = 465 nm; manual gain = 83; lag time = 0 µs; number of flashes = 3; and integration time = 200 µs.

3.4.1.2.3 Toxicity of thiosemicarbazones on human cells

The growth inhibitory effect towards a human fetal lung fibroblast cell line was evaluated by the MTS assay (CellTiter96® AQ_{ueous} One Solution Cell Proliferation Assay, Promega Corporation, Madison, WI, USA).

Briefly, 5×10^3 cells/well were seeded in 96-well plates in 100 µL of DMEM medium supplemented with 1% glutamine, 0.5% penicillin/streptomycin and 5% fetal bovine serum and then incubated at 37 °C in a humidified (95%) CO_2 (5%) incubator. After seeding (24 h), cells were treated, in quadruplicate, with increasing concentrations of the compounds for 24 h. The cytotoxicity assay was performed by adding 20 µL of the CellTiter96® AQ_{ueous} One Solution Cell

Proliferation Assay directly to the culture wells, incubating for 4 h and then recording the absorbance at 450 nm with a 96-well plate reader (MULTISKAN EX, Thermo Electron Corporation, Vantaa, Finland).

3.4.2 Syntheses of the vanillin type compounds

3.4.2.1 Syntheses of the vanillin type ligands

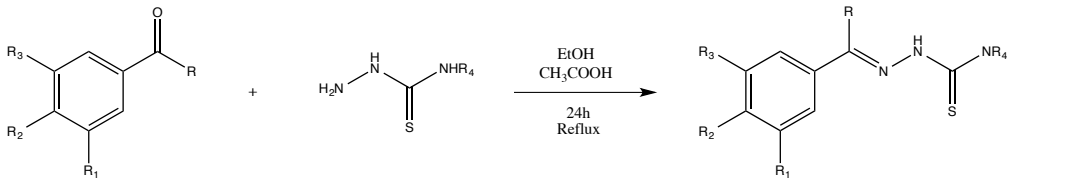

L_1 R=H, R_1=H, R_2=OH, R_3=OH, R_4=H_2
L_2 R=H, R_1=OCH_3, R_2=OH, R_3=OCH_3, R_4=H_2
L_3 R=H, R_1=OCH_3, R_2=OCH_3, R_3=H, R_4=H_2
L_4 R=CH_3, R_1=H, R_2=OH, R_3=OCH_3, R_4=H_2
L_5 R=CH_3, R_1=OCH_3, R_2=OH, R_3=OCH_3, R_4=H_2
L_6 R=H, R_1=H, R_2=H, R_3=H, R_4=$(CH_3)_2$
L_7 R=H, R_1=OCH_3, R_2=OCH_3, R_3=H, R_4=$(CH_3)_2$

Scheme 3.5 General scheme for the synthesis of thiosemicarbazone ligands.

The syntheses of the thiosemicarbazone ligands (Scheme 3.5) were performed using the following adapted literature procedure. The appropriate aldehyde (1 mol. equiv.) was dissolved in a hot ethanol solution and few drops of glacial acetic acid were added. An equimolar amount of the corresponding thiosemicarbazide (1 mol. equiv.) was added to the solution and the reaction has been heated under reflux for 24 h. The solution was cooled to ambient temperature and the TSC ligands were obtained as precipitate. After filtration, the solid was washed several times with toluene and ether and dried under vacuum.

N'-(3,4-dihydroxybenzylden)-thiosemicarbazone ***(L_1)***. Brown powder. Yield=81%. ^{1}H-NMR (DMSO-d_6, 25°C), ∂: 11.20 (s, 1H, NNH); 9.47, 9.01 (2s, 1H+1H, OH); 8.04, 7.71 (2s, 1H+1H, NH_2); 7.89 (s, 1H, CH=N); 7.17 (s, 1H, CH_{Ar}); 7.00 (d, 1H, J=8 Hz, CH_{Ar}); 6.74 (d, 1H, J=8 Hz, CH_{Ar}). EI-MS ($C_8H_9N_3SO_2$, CH_3OH): m/z=211.0 $[M+H]^+$.

*N'-(3,5-dimetoxy-4-hydroxybenzylden)-thiosemicarbazone (**L₂**)*. Brown powder. Yield=90%. ^{1}H-NMR (DMSO-d_6, 25°C), ∂: 11.32 (s, 1H, NNH); 8.80 (s, 1H, OH); 8.13, 7.99 (2s, 1H+1H, NH_2); 7.92 (s, 1H, CH=N); 7.05 (s, 1H, CH_{Ar}); 3.81 (s, 6H, OCH_3). EI-MS ($C_{10}H_{13}N_3SO_3$, CH_3OH): m/z=255.0 $[M+H]^+$.

*N'-(3,4-dimetoxybenzylden)-thiosemicarbazone (**L₃**)*. Pink powder. Yield=64%. ^{1}H-NMR (DMSO-d_6, 25°C), ∂: 11.18 (s, 1H, NNH); 9.48, 8.99 (2s, 1H+1H, OH); 8.30 (t_{broad}, 1H, NH_{Et}); 7.89 (s, 1H, CH=N); 7.21 (d, 1H, J=2 Hz, CH_{Ar}); 6.99 (dd, 1H, J=8 Hz, J'=2 Hz, CH_{Ar}); 6.75 (d, 1H, J=8 Hz, CH_{Ar}); 3.55 (m, 2H, J=7 Hz, CH_2); 1.12 (t, 3H, J=7 Hz, CH_3). EI-MS ($C_{10}H_{13}N_3SO_2$, CH_3OH): m/z=240.0 $[M+H]^+$.

*N'-(4-hydroxy-5-metoxyacetophenone)-thiosemicarbazone (**L₄**)*. Yellow powder. Yield=87%. ^{1}H-NMR (DMSO-d_6, 25°C), ∂: 10.03 (s, 1H, NNH); 9.34 (s, 1H, OH); 8.22, 7.87 (2s, 1H+1H, NH_2); 7.49 (d, 1H, J=2 Hz, CH_{Ar}); 7.26 (dd, 1H, J=8 Hz, J'=2 Hz, CH_{Ar}); 6.76 (d, 1H, J=8 Hz, CH_{Ar}); 3.84 (s, 3H, OCH_3); 2.25 (s, 3H, CH_3). EI-MS ($C_{10}H_{13}N_3SO_2$, CH_3OH): m/z=240.0 $[M+H]^+$.

*N'-(3,5-dimetoxy-4-hydroxyacetophenone)-thiosemicarbazone (**L₅**)*. White powder. Yield=71%. ^{1}H-NMR (DMSO-d_6, 25°C), ∂: 10.02 (s, 1H, NH); 8.70 (s, 1H, OH); 8.21, 7.87 (2s, 1H+1H, NH_2); 7.13 (s, 1H, CH=N); 3.82 (s, 6H, OCH_3); 2.27 (s, 3H, CH_3). EI-MS ($C_{11}H_{15}N_3SO_3$, CH_3OH): m/z=284.0 $[M+H]^+$.

*N'-(benzylden-3-dimethylthiosemicarbazone (**L₆**)*. Yellow powder. Yield=57%. ^{1}H-NMR (DMSO-d_6, 25°C), ∂: 10.95 (s, 1H, NNH); 8.20 (s, 1H, CH=N); 7.64 (d, 2H, J=7 Hz, CH_{Ar}); 7.38 (m, 3H, CH_{Ar}); 3.30 (s, 6H, NCH_3). EI-MS ($C_{10}H_{13}N_3S$, CH_3OH): m/z=207.0 $[M+H]^+$.

*N'-(3,4-dimetoxybenzylden)-dimethylthiosemicarbazone (**L**$_7$).* Red powder. Yield=61%. ^{1}H-NMR (DMSO-d$_6$, 25°C), ∂: 10.84 (s, 1H, NNH); 8.10 (s, 1H, CH=N); 7.25 (s, 1H, CH$_{Ar}$); 7.12 (d, 1H, J=8.4 Hz, CH$_{Ar}$); 6.99 (d, 1H, J=8.4 Hz, CH$_{Ar}$); 3.79 (s, 6H, NCH$_3$). EI-MS (C$_{12}$H$_{17}$N$_3$SO$_2$, CH$_3$OH): m/z=268.0 [M+H]$^+$.

3.4.2.2 Syntheses of the vanillin type copper complexes

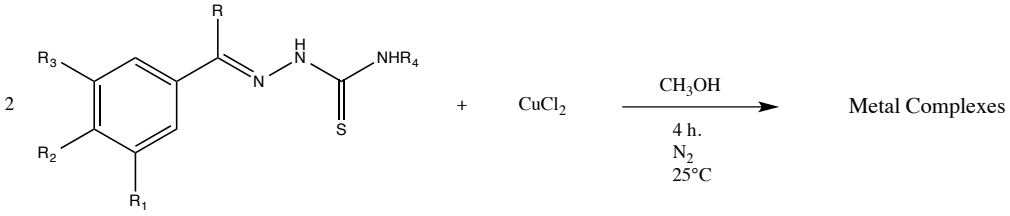

Scheme 3.6 General scheme for the synthesis of thiosemicarbazone complexes.

100 mg (2 eq.) of the proper thiosemicarbazone ligand (H$_2$L) were dissolved in 10 ml of degassed methanol. 1 eq. of CuCl$_2$·2H$_2$O was dissolved in 5 mL of degassed methanol and the solution was added to the previous one (Scheme 3.6). The mixture has been stirred at room temperature for 4 hours under N$_2$. The reaction mixture has been cooled overnight and then the precipitate was filtered off and washed with ether.

*Cu$_3$[N'-(3,4-dihydroxybenzylden)-thiosemicarbazone]$_2$Cl$_2$ (**1**).* Orange powder. Yield=25%. ^{1}H-NMR (DMSO-d$_6$, 25°C), ∂: 11.68 (s, 1H, NNH); 9.62, 9.04 (2s, 1H+1H, OH); 8.57, 8.37 (2s, 1H+1H, NH$_2$); 7.97 (s, 1H, CH=N); 7.24 (s, 1H, CH$_{Ar}$); 7.07 (d, 1H, J=9 Hz, CH$_{Ar}$); 6.74 (d, 1H, J=8.5 Hz, CH$_{Ar}$). ESI-MS

($C_8H_9N_3SO_2CuCl$, CH_3OH): m/z=485 $[ML_2\text{-}Cl]^+$, 332 $[MLCl+Na]^+$, 274 $[ML\text{-}Cl]^+$. ICP: found 28.9%, calcd 27.8%. Anal. Calcd. for $C_{16}H_{17}N_6S_2O_4Cu_3Cl_2$: C 28.39, H 2.81, N 12.48. Found: C 28.19, H 2.37, N 12.32.

Cu_3[N'-(3,5-dimetoxy-4-hydroxybenzylden)-thiosemicarbazone]$_2Cl_2$ ***(2)***. Yellow powder. Yield=37%. ^{1}H-NMR (DMSO-d_6, 25°C), ∂: 11.81 (s, 1H, NNH); 8.95 (s, 1H, OH); 8.70, 8.66 (2s, 1H+1H, NH_2); 8.01 (s, 1H, CH=N); 7.13 (s, 1H, CH_{Ar}). ESI-MS ($C_{10}H_{13}N_3SO_3Cu$, CH_3OH): m/z=573 $[ML_2\text{-}Cl]^+$, 318 $[ML\text{-}Cl]^+$. ICP: found 21.8%, calcd 22%. Anal. Calcd. for $C_{20}H_{25}N_6S_2O_6Cu_3Cl_2$ +2H_2O: C 29.45, H 3.49, N 10.47. Found: C 29.77, H 3.62, N 10.41.

Cu_3[N'-(3,4-dimetoxybenzylden)-thiosemicarbazone]$_2Cl_3$ ***(3)***. Yellow powder. Yield=28%. ^{1}H-NMR (DMSO-d_6, 25°C), ∂: 11.76 (s, 1H, NNH); 8.65, 8.58 (2s, 1H+1H, NH_2); 7.55 (s, 1H, CH_{Ar}); 8.05 (s, 1H, CH=N); 7.58 (s, 1H, CH_{Ar}); 7.21(d, 1H, J=8.5 Hz, CH_{Ar}); 6.98 (d, 1H, J=8.5 Hz, CH_{Ar}); 3.83, 3.80 (2s, 3H+3H, OCH_3). ESI-MS ($C_{10}H_{13}N_3SO_2CuCl$, CH_3OH): m/z=541 $[ML_2\text{-}Cl]^+$, 315 $[ML\text{-}Cl]^+$. ICP: found 27.8%, calcd. 28%. Anal. Calcd. for $C_{20}H_{25}N_6S_2O_4Cu_3Cl_2$: C 32.71, H 3.55, N 11.44. Found: C 32.51, H 3.41, N 11.37.

Cu_2[N'-(4-hydroxy-5-metoxyacetophenone)-thiosemicarbazone]Cl_2 ***(4)***. Green powder. Yield=28%. ^{1}H-NMR (DMSO-d_6, 25°C), ∂: 10.48 (s, 1H, NNH); 9.43 (s, 1H, OH); 8.79, 8.42 (2s, 1H+1H, NH_2); 7.55 (s, 1H, CH_{Ar}); 7.33 (d, 1H, J=8.5 Hz, CH_{Ar}); 6.78 (d, 1H, J=8.5 Hz, CH_{Ar}); 3.85 (s, 3H, OCH_3); 2.37 (s, 3H, CH_3). ESI-MS ($C_{10}H_{13}N_3SO_2CuCl$, CH_3OH): m/z=567 $[ML_2\text{-}Cl]^+$, 302

$[ML\text{-}Cl]^+$. ICP: found 33.5%, calcd 28%. Anal. Calcd. for $C_{10}H_{13}N_3SO_2Cu_2Cl_2$ +1.5H_2O: C 25.81, H 2.87, N 8.93. Found: C 26.39, H 3.32, N 9.23.

Cu_3[N'-(3,5-dimetoxy-4-hydroxyacetophenone)-thiosemicarbazone]$_2Cl_2$ ***(5)***. Pale yellow powder. Yield=55%. ^{1}H-NMR (DMSO-d_6, 25°C), ∂: 10.49 (s, 1H, NNH); 8.82 (s, 2H, NH_2); 7.19 (s, 2H, CH_{Ar}); 3.83 (s, 3H, OCH_3); 2.40 (s, 3H, CH_3). ESI-MS ($C_{11}H_{15}N_3SO_3CuCl$, CH_3OH): m/z=600 $[ML_2\text{-}Cl]^+$, 331 $[ML\text{-}Cl]^+$. ICP: found 36.7%, calcd. 34.7%. Anal. Calcd. for $C_{11}H_{14}N_3SO_3Cu_3Cl_2$ +2H_2O: C 24.12, H 2.94, N 7.67. Found: C 23.91, H 2.80, N 7.60.

Cu[benzylden-dimethylthiosemicarbazone]$_2Cl_2$ ***(6)***. Yellow powder. Yield=33%. ^{1}H-NMR (DMSO-d_6, 25°C), ∂: 7.78 (m, 2H, CH_{Ar}); 7.48 (m, 3H, CH_{Ar}). ESI-MS ($C_{10}H_{11}N_3SCuCl$, CH_3OH): m/z=476 $[ML_2\text{-}Cl]^+$, 270 $[ML\text{-}Cl]^+$.
Crystals suitable for X-Ray analysis were obtained by vapour diffusion of ether in saturated DMF solution of the compound.

Cu[N'-(3,4-dimetoxybenzylden)-dimethylthiosemicarbazone]Cl ***(7)***. Yellow powder. Yield=37%. ^{1}H-NMR (DMSO-d_6, 25°C), ∂: 11.28 (s, 1H, NNH); 7.34 (s, 1H, CH=N); 7.29 (d, 1H, J=8 Hz, CH_{Ar}); 7.06 (d, 1H, J=8 Hz, CH_{Ar}); 7.00 (s, 1H, CH_{Ar}); 4.16, 4.09 (2s, 3H+3H, OCH_3); 3.83, 3.80 (2s, 3H+3H, $N(CH_3)_2$). ESI-MS ($C_{12}H_{17}N_3SO_2CuCl$, CH_3OH): m/z=596 $[ML_2\text{-}Cl]^+$, 330 $[ML\text{-}Cl]^+$. ICP: found 16.0%, calcd 16.4%.

3.4.3 Syntheses of the cinnamaldehyde type compounds

3.4.3.1 Syntheses of the cinnamaldehyde type ligands

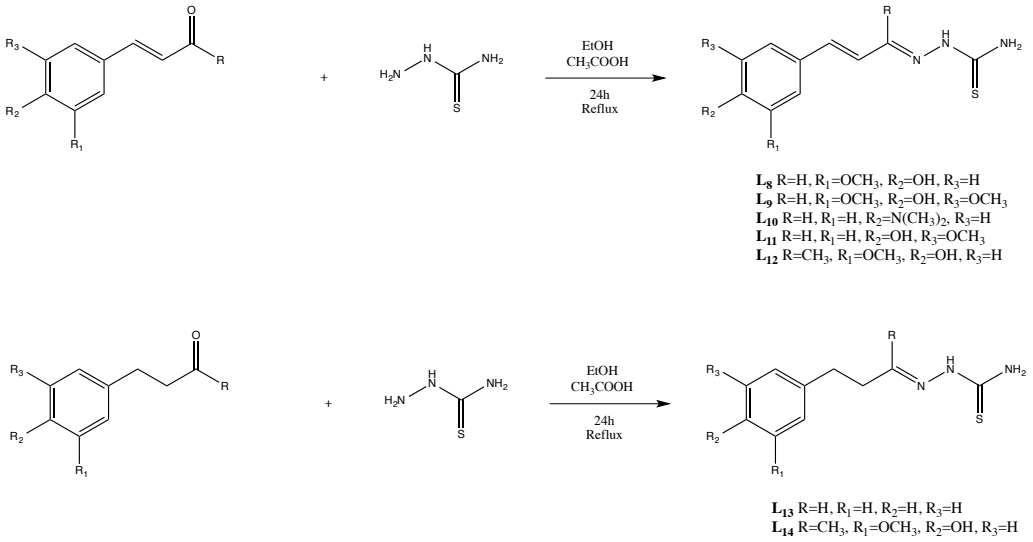

Scheme 3.7 General scheme for the synthesis of thiosemicarbazone ligands.

The syntheses of the thiosemicarbazone ligands (Scheme 3.7) were performed using the following adapted literature procedure. The appropriate aldehyde (1 mol. equiv.) was dissolved in hot ethanol and few drops of glacial acetic acid were then added to the mixture. An equimolar amount of the corresponding thiosemicarbazide (1 mol. equiv.) was added to the solution and the reaction has been heated under reflux for 24 h. The solution was cooled to ambient temperature and the TSC ligands were obtained as precipitate. After filtration the solid was washed several times with toluene and ether and dried under vacuum.

N'-(4-hydroxy-3-methoxycinnamaldehyde)thiosemicarbazone ***(L8)***. Yellow powder. Yield=75%. ^{1}H-NMR (DMSO-d$_6$, 25°C), overlapping isomer 5%, ∂:

11.30, 10.81 (s, 1H, NH); **9.38** (s, 1H, OH); 8.18, **8.10**, **7.50** (2s, 1H+1H, NH_2); 7.85, 7.79 (d, 1H, J=9 Hz, CH_{Ar}); 7.26, **7.15** (s, 1H, CH_{Ar}); 7.04, **6.96** (d, 1H, J=8 Hz, CH_{Ar}); **6.88** (d, 1H, J=16 Hz, CH); 6.76 (d, 1H, J=8 Hz, CH_{Ar}); **6.69** (dd, 1H, J=16 Hz, J'=8 Hz, CH); 3.84, **3.80** (s, 3H, OCH_3). EI-MS ($C_{11}H_{13}N_3SO_2$, CH_3OH): m/z=2501$[L]^+$.

*N'-(4-hydroxy-3,5-dimethoxycinnamaldehyde)thiosemicarbazone (**L₉**)*. Orange powder. Yield=93%. ^{1}H-NMR (DMSO-d_6, 25°C), ∂: **11.30** (s, 1H, NH); **8.75** (s, 1H, OH); **8.11, 7.48** (2s, 1H+1H, NH_2); **7.86** (d, 1H, J=9 Hz, CH=N); **6.88** (d, 1H, J=16 Hz, CH); **6.86** (s, 2H, CH_{Ar}); **6.74** (dd, 1H, J=16 Hz, J'=9 Hz, CH); **3.79** (s, 6H, OCH_3). EI-MS ($C_{12}H_{15}N_3SO_3$, CH_3OH): m/z=281 $[L]^+$.

*N'-(4-dimethylaminocinnamaldehyde)thiosemicarbazone (**L₁₀**)*. Orange powder. Yield=82%. ^{1}H-NMR (DMSO-d_6, 25°C), overlapping isomer 3%, ∂: **11.24**, 10.86 (s, 1H, NH); 8.11, **8.06**, 7.60, **7.49** (2s, 1H+1H, NH_2); 8.40, **7.84** (d, 1H, J=9.5 Hz, CH=N); **7.37**, 7.25 (d, 2H, J=8.5 Hz, CH_{Ar}); 7.02, **6.85** (d, 1H, J=16 Hz, CH); 6.74, **6.69** (d, 2H, J=9 Hz, CH_{Ar}); **6.58** (dd, 1H, J=16 Hz, J'=9 Hz); 2.97, **2.94** (s, 6H, $N(CH_3)_2$). EI-MS ($C_{12}H_{16}N_4S$, CH_3OH): m/z=248 $[L]^+$.

*N'-(3-methoxyphenyl-4-hydroxycinnamaldehyde)thiosemicarbazone (**L₁₁**)*. Brown powder. Yield=73%. ^{1}H-NMR (DMSO-d_6, 25°C), ∂: **11.30** (s, 1H, NH); **9.38** (s, 1H, OH); **8.10, 7.49** (2s, 1H+1H, NH_2); **7.86** (d, 1H, J=9 Hz, CH_{Ar}); **7.15** (s, 1H, CH_{Ar}); **6.96** (d, 1H, J=8.5 Hz, CH_{Ar}); **6.88** (d, 1H, J=16 Hz, CH); **6.76** (d, 1H, J=8.5 Hz, CH_{Ar}); **6.69** (dd, 1H, J=16 Hz, J'=9 Hz, CH); **3.81** (s, 3H, OCH_3). EI-MS ($C_{11}H_{13}N_3SO_2$, CH_3OH): m/z=251 $[L]^+$.

*N'-(Vanillyldenacetone)thiosemicarbazone (**L$_{12}$**)*. Yellow powder. Yield=51%. ^{1}H-NMR (DMSO-d$_6$, 25°C), overlapping isomer 6%, ∂: 10.80, **10.21** (s, 1H, NH); 9.43, **9.30** (s, 1H, OH); **8.21,** 8.10, **7.75**, 7.71 (2s, 1H+1H, NH_2); 7.30, **7.13** (d, 1H, J=2 Hz, CH_{Ar}); 7.44, **6.99** (d, 1H, J=16 Hz, CH); 7.19, **6.95** (dd, 1H, J=9 Hz, J'=2 Hz, CH_{Ar}); 6.81, **6.77** (d, 2H, J=8.5 Hz, CH_{Ar}); **6.72**, 6.66 (d, 1H, J=16.5 Hz, CH); 3.84, 3.81 (s, 3H, OCH_3); 2.14, 2.11 (s, 3H, CH_3). EI-MS ($C_{12}H_{15}N_3SO_2$, CH_3OH): m/z=265 $[L]^+$.

*N'-(Vanillylacetone)thiosemicarbazone (**L$_{13}$**)*. White powder. Yield=78%. ^{1}H-NMR (DMSO-d$_6$, 25°C), overlapping isomer 17%, ∂: 10.11, **9.93** (s, 1H, NH); 8.69, **8.65** (s, 1H, OH); **8.04**, 7.99, 7.53, **7.48** (2s, 1H+1H, NH_2); 6.84, **6.78** (d, 1H, J=2.5 Hz, CH_{Ar}); **6.43** (m, 1H, CH_{Ar}); 6.64, **6.58** (d, 1H, J=8 Hz, J'=2.5 Hz, CH_{Ar}); 3.76, **3.74** (s, 3H, OCH_3); **2.65** (m, 2H, CH_2), **2.46** (m, 2H, CH_2); **1.91**, 1.88 (s, 3H, CH_3). EI-MS ($C_{12}H_{17}N_3SO_2$, CH_3OH): m/z=267 $[L]^+$.

*(Hydrocinnamaldehyde)-thiosemicarbazone (**L$_{14}$**)*. White powder. Yield=50%. ^{1}H-NMR (acetone-d$_6$, 25°C), ∂: 10.61 (s, 1H, NH); 7.72, 7.67 (2s, 1H+1H, NH_2); 7.56 (t, 1H, J=5 Hz, CH=N); 7.33 (d, 2H, J=7.5 Hz, CH_{Ar}); 7.20 (d, 2H, J=7.5 Hz, CH_{Ar}); 7.21 (t, 1H, J=7.5 Hz, CH_{Ar}); 2.88 (t, 2H, J=7.5 Hz, CH_2); 2.58 (m, 2H, CH_2). EI-MS ($C_{10}H_{13}N_3S$, CH_3OH): m/z=207 $[L]^+$.

3.4.3.2 Syntheses of the cinnamaldehyde type copper complexes

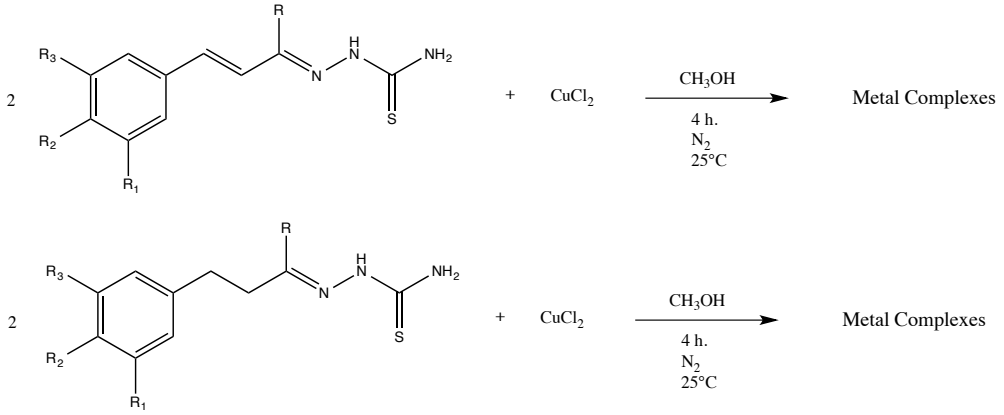

Scheme 3.8 General scheme for the synthesis of thiosemicarbazone copper complexes.

100 mg (2 eq.) of the proper thiosemicarbazone ligand (H_2L) were dissolved in 10 ml of degassed methanol. 1 eq. of $CuCl_2 \cdot 2H_2O$ was dissolved in 5 mL of degassed methanol and the solution was added to the previous one (Scheme 3.8). The mixture has been stirring at room temperature for 4 hours under N_2. After 30 minutes a precipitate was formed, which was stirred at room temperature for other 3 hours; the reaction mixture was cooled overnight and then the precipitate was filtered off and washed with ether.

Cu[N'-(4-hydroxy-3-methoxycinnamaldehyde)thiosemicarbazone]$_2Cl_2$ ***(8).*** Brown powder. Yield=97%. ESI-MS ($C_{11}H_{13}N_3SO_2CuCl$, CH_3OH): m/z=564 $[ML_2\text{-}Cl]^+$; m/z=316 $[ML\text{-}Cl]^+$.

Cu[N'-(4-hydroxy-3,5-dimethoxycinnamaldehyde)thiosemicarbazone]$_2Cl_2$ ***(9).*** Brown powder. Yield=13%. ESI-MS ($C_{12}H_{15}N_3SO_3CuCl$, CH_3OH): m/z=625 $[ML_2\text{-}Cl]^+$; m/z=344 $[ML\text{-}Cl]^+$.

Cu[N'-(4-dimethylaminocinnamaldehyde)thiosemicarbazone]$_2Cl_2$ ***(10)***. Brown powder. Yield=86%. [1]ESI-MS ($C_{12}H_{16}N_4SCuCl$, CH_3OH): m/z=558 $[ML_2]^+$; m/z=310 $[ML]^+$.

Cu[N'-(3-methoxyphenyl-4-hydroxycinnamaldehyde)thiosemicarbazone]$_2Cl_2$ ***(11)***. Brown powder. Yield=87%. ESI-MS ($C_{11}H_{13}N_3SO_2CuCl$, CH_3OH): m/z=565 $[ML_2\text{-}Cl]^+$; m/z=316 $[ML]^+$.

Cu[N'-(Vanillyldenacetone)thiosemicarbazone]$_2Cl_2$ ***(12)***. Orange powder. Yield=54%. ESI-MS ($C_{12}H_{15}N_3SO_3CuCl$, CH_3OH): m/z=593 $[ML_2\text{-}Cl]^+$; m/z=328 $[ML\text{-}Cl]^+$.

Cu[N'-(Vanillylacetone)thiosemicarbazone]$_2Cl_2$ ***(13)***. Green powder. Yield=14%. ESI-MS ($C_{10}H_{13}N_3SCuCl$, CH_3OH): m/z=270 $[ML]^+$.

Cu[(Hydrocinnamaldehyde)-thiosemicarbazone]$_2Cl_2$ ***(14)***. White powder. Yield=21%. ESI-MS ($C_{12}H_{17}N_3SO_2CuCl$, CH_3OH): m/z=595 $[ML_2]^+$; m/z=330 $[ML]^+$

3.5 WORK CONTRIBUTIONS

Biological analyses on *Aspergillus Flavus* were performed by the group of Professor Francesco Restivo; Università degli Studi di Parma (Italy), Department of Biology.

Cytotoxic analyses were performed by the group of Professor. Annamaria Buschini, Università degli Studi di Parma (Italy), Department of Biology.

The project has been founded by “cariplo Foundation” (Brescia, Italy). Grant number: 2014-0555.

3.6 BIBLIOGRAPHY

[1] E.C. Oerke, H.W. Dehne; *Crop. Prot.*; **2004**; 23; 275-285.

[2] A.A. Brakhage, et al.; *Prog. Drug. Res.*; **2008**; 66; 3-12.

[3] J.W. Bennet, R. Bentley; *Adv. Appl. Microbiol.*; **1989**; 34; 1-28.

[4] Ciba Foundation Symposium 171. *Secondary Metabolites: Their Function and Evolution* (John Wiley & Sons, Chicester, 1992).

[5] D. Garcia, et al.; *Reviews Food Microbiology*; **2009**; 26; 757-769.

[6] B. Kabak, A.D. Dobson; *J. Food Prot.*; **2009**; 72; 2006-2016.

[7] R. Goswam, H. Kistler; *Phytopathology*; **2005**; 95; 1397-1404.

[8] M.J. Sweeney, A.D.W. Dobson; *Int. J. Food Microbiol.*; **1998**; 43; 141-158.

[9] M. Wink; *Scheffield Academic Press*; **1999**; 1-14.

[10] M.O. Moss; *J. Appl. Bacteriol. Symp. Suppl.*; **1992**; 73; 80-88.

[11] M.J. Sweeney, A.D.W. Dobson; *Int. J. Food Microbiol.*; **1998**; 43; 141-148.

[12] C.M. Placinta, J.P.F. D'Mello, A.M.C. Macdonald; *Anim. Feed Sci.Technol.*; **1999**; 78; 21-37.

[13] D.P. Overy, et al.; *Int. J. Food Microbiol*; **2003**; 2737; 1-9.

[14] M.J. Sweeney, A.D.W. Dobson; *FEMS Microbiol. Lett.*; **1999**; 175; 149-163.

[15] G. Lackner, L.P. Partida-Martinez, C. Hertweck; *Trends in Microbiology*; **2009**; 17; 570-576.

[16] M. Mclean, M.F. Dutton; *Pharmac. Ther.*; **1995**; 65; 163-192.

[17] J. Wang, J.D. Groopman; *Mutat. Res.;* **1999**; 424; 167-181.

[18] M. Weidenbörner, et al.; *Food Microbiol.*; **2000**; 17; 103-107.

[19] D. Cazzaniga, et al.; *Lett. Appl. Microbiol.*; **2001**; 33; 144-147.

[20] F. Galvano, et al.; *J. Food. Prot.;* **2001**; 64; 120-131.

[21] N.H. Aziz, L.A.A Moussa; *Food Control.*; **2002***;* 13; 281-288.

[22] H.S. Hussein, J.M. Brasel; *Toxicol.*; **2001**; 167; 101-134.

[23] F. Atroschi, et al.; *Toxicol.*; **2002**; 180; 151-167.

[24] E. Papp, et al.; *Microchemical Rev.*; **2002**; 73; 39-46.

[25] C.M. Christensen; *Molds, Mushrooms, and Mycotoxins*; **1975**; University of Minnesota Press, Minneapolis, USA; 264.

[26] W.J. Meggs; *Toxicol of Industrial Health*; **2009**; 25; 571-576.

[27] J.W. Bennet, et al.; *Experientia*; **1986**; 42; 848-851.

[28] P. Cotty; *Pytopathol.*; **1988**; 78; 1250-1253.

[29] P.K. Chang, J.W. Bennet, P.J. Cotty; *Mycopathologia*; **2002**; 153; 41-4.

[30] R.T. Awuah, et al.; *Peanut Science*; **2009**; 36; 68-76.

[31] U.L. Diener, N.D. Davis; *J. Am. Oil Chem. Soc.*; **1967**; 44; 259EOF-63EOF.

[32] H.P. Van Egmond; *J. Food. Addit. Contam.*; **1989**; 6; 139-188.

[33] M.A. Klich; *Toxicol.*; **2009**; 25; 657-667.

[34] A. Lugauskas, J. Stakeniene; *Annals of Agriculture and Environmental Medicine*; **2002**; 9; 183-187.

[35] N. Magan, et al.; *Food Addit. Contam.*; **2010**; 27 Part A; 644-650.

[36] J. He, T. Zhou; *Microbiol.*; **2010**; 2; 96-104.

[37] D. Eaton, E. Gallagher; *Annu. Rev. Pharacol. Toxicol.;* **1994**; 34; 135-172.

[38] D.P.H. Hsieh; *Annu. Rev. Pharmacol.*; **1994**; 34; 135-172.

[39] A. Ngindu, et al.; *Lancet*; **1982**; 1; 1346-348.

[40] L. Lewis, et al.; *Environ. Health Prospect.*; **2005**; 113; 1763-1767.

[41] J.H. Williams; *Am. J. Clin. Nutr.*; **2004**; 80; 1106-1122.

[42] H.P. Van Egmond,R.C. Shothorost, M.A. Jonker; *Anal. Bioanal. Chem.*; **2007**; 389; 147-157.

[43] H.P. Van Egmond, M.A. Jonker; *Worldwide Regulations of Aflatoxin.*; **2005**; 77-93.

[44] J.L. Richard, G.A. Pyne; Council for Agricultural Science and Technology

(CAST): Ames, IA, USA, 2003.

[45] J.W. Bennet, M. Klich; *Clin. Microbiol. Rev.*; **2003**; 16; 497-516.

[46] J.W. Bennet; *Mycopathologia*; **1987**; 100; 3-5.

[47] A.A. Brakhage, et al.; *Phytochemistry*; **2009**; 70; 1801-1811.

[48] S. Bruns, et al.; *Proteomics*; **2010**; 10; 3097-3107.

[49] M. Vodisch, et al.; *J. Proteome Res.*; **2011**; 10; 2508-2524.

[50] W. Yin, N.P. Keller; *J. Microbiol.*, **2011**; 49; 329-339.

[51] A.A. Brakhage; *Nat. Rev. Microbiol.*; **2013**; 11; 21-32.

[52] T.E. Cleaveland, et al.; *Trends in Biotechnol.*; **2009**; 27; 151-157.

[53] K.C. Ehrlich, et al.; *Appl. Envirom. Microbiol.*; **2010**; 76; 3374-3377.

[54] K. Yabe, H. Nakajima; *Appl. Microbiol. Biothecnol.*; **2004**; 64; 745-755.

[55] M. Pierides, et al.; *Journal of Food Protection*; **2000**; 63; 645-650.

[56] P.A. Murphy, et al.; *Journal of Food Science*; **2006**; 71; 51-65.

[57] J.B. Anderson; *Nat. Rev. Microbiol.*; **2005**; 3; 547-556.

[58] Z. Ma, T. Michailides; *Crop. Prot.*; **2005**; 24; 853-863.

[59] M. Schmidt-Heydt, D. Stoll, R. Geisen; *Int. J. Food Microbiol.*; **2013**; 166; 407-412.

[60] C. De Luca, et al.; *Food Addit. Contam.*; **1995**; 12; 445-450.

[61] M.L. Ferrandiz, M.J. Alcaraz; *Inflamm. Res.*; **1991**; 32; 283-288.

[62] R.J. Nijveldt, et al.; *Am. J. Clin. Nutr.*; **2001**; 74; 418-425.

[63] H.P. Kim, et al.; *J. Pharmacol. Sci.;* **2004a**; 96; 229-245.

[64] R.A. Holmes, R.S. Boston, G.A. Payne; *Appl. Microbiol. Biotechnol.*; **2008**; 78; 559-572.

[65] M.A. Passone, S.L. Resnik, M.G. Etcheverry; *J. Appl. Microbiol.*; **2005**; 99; 682-691.

[66] R.A. Norton; *Phytopathology*; **1997**; 87; 814-821.

[67] S.E. Lee, N.E. Mahoney, B.C. Cambpell; *J. Microbiol. Biotechnol.*; **2002**; 12; 679-682.

[68] D.C. Doehlert, D.T. Wicklow, H.W. Gardner; *Phytopathology*; **1993**; 83; 1473-1477.

[69] M.V. Kolomiets, et al.; *Plant Physiol.*; **2000**; 124; 1121-1130.

[70] H.W. Gardner; *Biochim. Biophys. Acta*; **1991**; 1084; 221-239.

[71] P.U.M. Devi, et al.; *Legume Res.–An. Int. J.*; **2005**; 28; 87-93.

[72] A. Sucharitha, et al.; *Int. J. Applied Agric. Res.*; **2010**; 5; 283-290.

[73] P.U.M. Devi, et al.; *Eur. J. Plant Pathol.*; **2000**; 106; 857-865.

[74] S. Parchmann, H. Gundiach, M.J. Mueller; *Plant Physiol.*; **1997**; 115; 1057-1064.

[75] K.P.C. Croft, F. Juttner, A.J. Slusarenko; *Plant Physiol.*; **1993**; 101; 13-24.

[76] H. Weber, et al.; *Plant Cell*; **1999**; 11; 485-493.

[77] D.I. Tsitsigiannis, N.P. Keller; *Trends Microbiol.*; **2007**; 15; 109-118.

[78] C. Rusterucci, et al.; *J. Biol. Chem.*; **1999**; 274; 36446-36455.

[79] L. Ilag, R.W. Curtis; *Science*; **1968**; 159; 1357-1358.

[80] L.V. Roze, et al.; *J. Food Protect.*; **2004b**; 67; 438-447.

[81] E. Graf, K.L. Empson, J.W. Eaton; *J. Biol. Chem.*; **1987**; 262; 11647-11650.

[82] H. Kato-Noguchi, F.A. Macias; *J. Chem. Ecol.*; **2006**; 32; 1101-1109.

[83] J.P. Rao, R.B. Sashidhar, C. Subramanyam; *W. J. Microbiol. Biotechnol.*; **1998**; 14; 71-75.

[84] B.D. Roufogalis, A. Minocherhomjee, A. Aljobore; *Can. J. Biochem. Cell Biol.*; **1983**; 61; 927-933.

[85] J.P. Rao, C. Subramanyam; *Lett. Appl. Microbiol.*; **2000**; 30; 277-281.

[86] J.P. Rao, C. Subramanyam; *Lett. Appl. Microbiol.*; **1999**; 28; 85-88.

[87] J.D. Palumbo, J.L. Baker, N.E. Mahoney; *Microb. Ecol.*; **2006**; 52; 45-52.

[88] T. Kondo, et al.; *J. Antibiot.*; **2001**; 54; 650-657.

[89] T. Yoshinari, et al.; *Microbiology*; **2007**; 153; 2774-2780.

[90] S. Sakuda, et al.; *J. Antibiot.*; **2000**; 53; 1265-1271.

[91] K. Shimizu, et al.; *Genetics*; **2003**; 165; 1095-1104.

[92] C. Fanelli, et al.; *Recent. Res. Devel. Crop. Sci.*; **2004**; 1; 295-317.

[93] K.V. Narasaiah, R.B. Sashidar, C. Subramanyam; *Mycopathologia*; **2006**; 162; 179-189.

[94] M. Reverberi, et al.; *Eukariot. Cell*; **2008**; 7; 988-1000.

[95] T. Jayashree, C. Subramanyam; *Free Rad. Biol. Med.*; **2000**; 10;981-985.

[96] G. Grover, S.G. Kini; *Eur. J. Med. Chem.*; **2006**; 41; 256-262.

[97] D.T. Nguyen, T.H. Le, T.T.T. Bui; *Eur. J. Med. Chem.*; **2012**; 60; 199-207.

[98] R.P. Tenorio; *Quimica Nova*; **2005**; 28; 1030-1037.

[99] R.O.A. Soares, et al.; *Experimental Parasitology*; **2011**; 129; 381-387.

[100] M. Tyagi, S. Chandra, P. Tyagi; *Spectrochim. Acta A*; **2014**; 117; 1-8.

[101] D.X. West, et al.; *Coord. Chem. Rev.*; **1993**; 123; 49-71.

[102] F. Degola, et al.; *Int. J. Food Microbiol.*; **2015**; 2001; 104-111.

[103] H. Beraldo, D. Gambino; *Mini-Rev. Med. Chem.*; **2004**; 4; 31-39.

[104] R. Prabhakaran, et al.; *J. Organomet. Chem.*; **2016**; 821; 1-218.

[105] R. Pedrido, et al.; *Chem. Eur. J.*; **2008**; 14; 500-512.

[106] A.W. Addison, et al.; *J. Chem. Soc. Dalton Trans.;* **1984**; 1349-1356.

[107] L. Korzycka, M. Glowka, J. Janicka, Pol. J. Chem. 1998, 72, 73–77.

[108] R. Noto, et al.; *J. Heterocycl. Chem.*; **1999**; 72; 73-77.

[109] M. Gruttadauria, et al.; *J. Heterocycl. Chem.*; **1993**; 30; 765-770.

[110] J.S. Casas, et al.; *Dalton Trans.*; **2004**; 2019-2026.

[111] R. Gill-Garcia, et al.; *New J. Chem.*; **2013**; 37; 3568-3580.

[112] F. Degola, E. Berni, F.M. Restivo; *Int. J. Food . Microbiol.*; **2011**; 146; 235-243.

RINGRAZIAMENTI

Desidero anzitutto ringraziare il professor Mauro Carcelli così come la professoressa Dominga Rogolino per avermi dato la possibilità di lavorare su questo progetto di dottorato con generosità d'insegnamenti e consigli, oltre che incoraggiante disponibilità e cordialità.

Ringrazio anche il professore Paolo Pelagatti per i chiarimenti e gli aiuti nei momenti del bisogno così come anche il professore Giorgio Pelosi.

Un ringraziamento particolare al Professore P.J.Sadler per avermi ospitata nel suo gruppo di ricerca permettendomi, così, di crescere sia da un punto di vista scientifico che personale.

Come non citare, poi, tutti "i ragazzi dello stanzino": Irene, Davide, Balo, Corrado, Marianna, Vittoria, Stefano. Senza di voi questa esperienza non sarebbe stata cosi positiva.